Nanostructured membranes from polymer-surfactant films

Jaber, Robben

Award date:
2014

Awarding institution:
University of Bath

Nanostructured membranes from polymer-surfactant films

Robben I Jaber

A thesis submitted for the degree of Doctor of Philosophy

University of Bath
Department of Chemistry
March 2014

Acknowledgements

Firstly I would like truly to thank Karen Edler for her guidance and excellent supervision throughout my PhD programme. Without her support and encouragement this work would not have been possible. I also want to thank Prof. Gareth Price and Stephen Roser for being a great co-supervisor, their input was greatly appreciated.

I would also like to thank previous and continuing members of Edler research group who have helped me learn new experimental methods and developed my theoretical understanding over the past years.

I would also like to thank all other members of the University of Bath, Department of Chemistry who have helped me. Also I express my thanks and appreciation to all the scientists outside of the Department of Chemistry at ISIS, ILL, ESRF and Diamond who have helped when performing the several experiments that have given the core of the results throughout this thesis.

Finally on a personal note I would like to thank my amazing father who has always inspired me to do my very best in life and to stay strong through hard times (peace be upon his soul**)**. Also I would like to thank my family for their continued support and encouragement on this journey, particularly my wife Sura, for her patience and encouragement during this graduate program.

Abstract

A new method of preparing solid nanostructured polyelectrolyte films through self-assembly at the air/solution interface was discovered by our group. These films form spontaneously through interactions between water-soluble polymers with polarisable groups, and surfactant micelles with a positive charge. The films have an ordered mesostructure consisting of a surfactant liquid-crystalline phase in a polymer hydrogel matrix. In initial work, micellization of a variety of cationic surfactants in the presence of the film-forming polymer, polyethylenimine, was investigated. Surfactants, which formed robust, well-ordered films, were selected for the subsequent experiments.

The main aim of this thesis was to exploit the mesostructures in these films as templates for polymerization of styrene. The replication of ordered surfactant liquid-crystalline structures into mechanically and chemically stable nanostructured polymer materials could provide a rapid, cheap method to generate intricate nanostructures. As a first step of this project, encapsulation of styrene into cationic surfactant/polymer films was investigated. Deuterated and hydrogenated styrene were used to probe the structure and location of styrene in the micelles and films using small-angle neutron scattering and neutron reflectivity experiments. The results showed that styrene was most effectively encapsulated in the films prepared from cetylpyridinium bromide (CPBr) and benzyldimethylhexadecylammonium bromide (BDHAB). In the films, the high viscosity hydrogel surrounding the swollen surfactant micelles prevents diffusion and micelle rearrangement on short timescales, making them an ideal host for styrene polymerisation to create solid polymer nanostructures within the water-soluble polymer film. Both thermal methods and UV-irradiation were used to initiate polymerization of the encapsulated styrene. The nanostructured polystyrene produced was characterised using a range of techniques.

In the second part of this project, the species 1-(2-Pyridylazo)-2-naphthol (PAN) and pyrene were incorporated in the micelles in the nanostructured hydrogel films to prepare metal ion sensors. PAN is a well-known chelating agent for transition metal ions. When used with pyrene in micellar systems the fluorescence response of pyrene is modified in a quantitative manner when PAN is bound to metal ions. The response of the micellar solution can thus be calibrated and used as a fluorescence sensor. Unfortunately the optical response of the films was poor, but the films were used in an electrochemical cell, demonstrating selective and sensitive detection of metal ions.

Table of Contents

1.	**Introduction**	**1**
1.1	The Aim and Objectives of this Project.	3
1.2	General overview of Surfactants and their Classifications	4
1.3	Critical Micelle Concentration (cmc)	6
1.4	Self-Assembly of Micelles	9
1.5	Temperature effects on ionic surfactant aggregation behaviour	11
1.6	Polyelectrolytes	14
1.7	Polymer Surfactant Interactions	15
1.8	Polymer-Surfactant Films	17
1.9	Solubilisation of Hydrophobic Molecules in Aqueous Solutions of Amphiphiles.	19
1.10	Polymerization of Solubilised Monomer within Templating Lyotropic Mesophases	21
1.11	Surfactant Micelle Based Sensors for Metal Ions	23
1.12	References	25
2	**Theory and Experimental Methods**	**33**
2.1	Small Angle Neutron Scattering (SANS) and Small Angle X-ray Scattering (SAXS)	34
2.1.1	Basic Scattering Theory and Q-Vector Definition	34
2.1.2	Instrumentation and Principle of Small Angle Neutron Scattering (SANS)	37
2.1.3	Instrumentation and Principle of Small Angle X-Ray Scattering (SAXS)	40
2.2	Form and Structure Factor	44
2.3	Reflectivity	47
2.3.1	Neutron Reflectivity Experimental Measurements	49
2.3.2	X-ray Reflectivity Experimental Measurements	49
2.4	Characterization of Crystalline & Liquid Crystalline Structures	50
2.5	Grazing incidence x-ray diffraction (GIXD)	55

2.6	Gel permeation chromatography	57
2.6.1	Experimental Measurement	59
2.7	Cyclic voltammetry (CV)	59
2.7.1	Experimental Measurement	61
2.8	Electron microscopy	61
2.8.1	Experimental Measurements	64
2.9	Other Techniques	65
2.9.1	Determination of Critical Micelle Concentration by Conductivity	65
2.9.2	UV-Vis and Fluorescence spectroscopy	66
2.9.3	Gas Chromatography (GC)	67
2.10	Chemicals and Materials	68
2.11	Synthesis of Quaternary Ammonium Bromide Surfactants	69
2.12	References	72
3	**Micellization Behaviour of Cationic Surfactants in Presence and Absence of Polyelectrolyte**	**76**
3.1	Introduction	76
3.2	Methods and Materials	76
3.3	Results and Discussion	77
3.3.1	Characterization of synthesized surfactants	77
3.3.2	The Critical Micelle Concentration (cmc) Behaviour of Cationic Surfactants in Presence and Absences of Polyethyleneimine (PEI).	78
3.3.3	Micellar volume and aggregation numbers (Nagg) of cationic Surfactants in presence and absences of polyethyleneimine (PEI).	86
3.4	Conclusion	97
3.5	References	98
4	**Encapsulation of Monomers into Cationic Surfactant Micelles**	**101**
4.1	Introduction	101
4.2	Study of Solubilisation of Styrene in Cationic Surfactant Solutions By Using UV-Vis Spectroscopy.	102

4.3	Study of encapsulation of styrene monomer into cationic surfactant micelles using SANS.	105
4.3.1	Contrast SANS study of the location of encapsulated styrene monomer inside cationic surfactant micelles.	107
4.3.2	Effects of PEI on Cationic Surfactant micelle Solutions Encapsulating Styrene.	113
4.4	Extent of Encapsulated Styrene in Cationic Surfactant micelle Solutions with and without PEI	116
4.5	Encapsulation of Monomers into Cationic Surfactant Films	128
4.5.1	Aliphatic Cationic Surfactant/PEI Films Encapsulating Hydrophobic Monomers.	129
4.5.2	Effects of Surfactant Headgroup on the Polymer/Surfactant Films	133
4.5.3	Effects of Surfactant Chain Length on PEI/Surfactant Films	136
4.6	Kinetic Study of Polymer/Surfactant Films Solubilising Styrene.	143
4.6.1	C14 Hydrocarbon Chain Surfactant/PEI Films	144
4.6.2	C16 Hydrocarbon Chain Surfactant/PEI Films	148
4.7	Extent of Styrene Incorporation into Cationic Surfactant Films	152
4.8	X-ray Reflectivity and Grazing Incidence X-ray Diffraction.	156
4.9	Conclusions	164
4.10	References	167
5.	**Polymerization of Encapsulated Styrene in Polyelectrolyte / Surfactant Films**	**173**
5.1	Gas chromatography (GC) Studying the Conversion Percentage of Styrene in Cationic surfactant/PEI Solution.	174
5.2	Thermal and Photopolymerization of Encapsulated Styrene in Cationic Surfactant/PEI Films.	176
5.2.1	Effects of High Flux Synchrotron X-ray Energy on Styrene Monomer Encapsulated in Surfactant/PEI Films	178
5.2.2	Thermal Polymerization of Styrene Encapsulated in	

Cationic Surfactant/PEI Films. 180
5.2.3 Photopolymerization of Styrene Encapsulated in Cationic Surfactant/PEI films. 192
5.2.3.1 Time-Resolved Measurement of the Photopolymerization 193
5.2.3.2 Effect of UV Irradiation Time and Wavelength 199
5.2.3.3 Effect of PEI Molecular Weight 202
5.2.3.4 Effect of Surfactant Chain Length 203
5.1 Characterization of Polymerized Polystyrene in Organized systems. 205
5.1.1 NMR, FT-IR and GPC used to identify and study polystyrene. 205
5.1.2 Electron microscopy studies of polystyrene 211
5.2 Conclusion 214
5.3 References 216
6. PAN-Pyrene-Micelle Based Sensors for Metal Ions 222
6.1 Study of PAN and Pyrene Encapsulation in Micelles Using SANS 224
6.1.1 Encapsulation of PAN and Pyrene 226
6.1.2 Incorporation Metal Ions into Surfactant/PAN/pyrene Micelle Systems. 233
6.1.3 SANS Study Using Contrast Variation to Study Surfactant Micelles Solubilising Pyrene 238
6.2 Incorporation of PAN/Pyrene Swollen Micelles in Cross-Linked Polyelectrolyte Films 244
6.2.1 Solubilisation of Pyrene in Surfactant/PEI Films. 245
6.2.2 Solubilisation of PAN in Surfactant/PEI Films. 248
6.2.3 Solubilisation of Combinations of PAN/Pyrene. 251
6.2.4 Cross-Linking of Surfactant/PEI Films Solubilising PAN/Pyrene. 254
6.2.5 Effects of Metal Ions on Cross-Linked Films Solubilised PAN/Pyrene. 257
6.3 Grazing Incidence X-ray Diffraction of Cationic Surfactant/PEI Films Solubilising PAN and Pyrene 260
6.4 Characterization of cationic surfactant/PEI films solubilising PAN/Pyrene. 264
6.4.1 Surfactant/PEI/PAN/Pyrene films as an electrochemical metal ion sensor. 264

6.4.2 Fluorescence and UV-Vis of surfactant/PEI/PAN/Pyrene films. 268
6.5 Conclusion 274
6.6 References 276
7 Conclusions and Future Work 285
Appendix A: Chemicals used in this thesis. 294

1. Introduction

Many investigations have been carried out in the past few decades, with the target to synthesize nanomaterials systems and to control their physical properties. Most of these studies have presented the great efforts and versatility of the synthetic methods [*1-3*].

Nanostructured materials, or nanomaterials, indicate materials that have relevant dimensions on the nanometer length scales (1nm equals 10 Å equals 10^{-9}m) and exist in states between isolated atoms or molecules and bulk matter. These materials have distinctive physical and chemical properties that are different from bulk materials. Their size-dependent properties, their sensitivity to surface phenomena, and how they are spatially arranged present a significant challenge to our fundamental understanding of how these materials should behave [*4*]. Nanoscale materials, the foundation of nanoscience and nanotechnology, have become one of the most popular research topics in a very short period of time. The intense interest in nanotechnology and nanoscale materials is supported by the huge economical, technological, and scientific impact anticipated in several areas [*5*]. Nanomaterials have demonstrated great potentials for applications in electronics, photovoltaics, catalysis, sensors, detectors etc [*5, 6*]. The advances in these areas will affect our daily life from how we design a faster computer, to how we use and conserve energy, preserve the environment, and how we diagnose and treat disease. The research and development in nanomaterials involves three key aspects: assembly and synthesis of the nanomaterials, characterization of their properties, and exploration or implementation of their applications [*7*]. The nanostructured material system is of increasing significance in our technology-dominated economy and this suggests the need for a large amount of research to improved methods of synthesis [*7-9*].

Self-assembly has become one of the most important effective and promising approaches to synthesize a wide range of novel nanoscale materials [*10, 11*]. In the self-assembly processes, atoms, molecules, particles, and other building blocks organize themselves into functional structures as driven by the energetics of the system [*12, 13*]. Self-assembly also involves that if the system is taken apart into the appropriate subunits, these subunits can then be mixed to reform the whole structure under favourable conditions. The most important driving force for self-assembly is the

interaction energies between the subunits, whether they are atoms, molecules, or particles [*8, 14*].

It is worth noting that at present, the huge efforts are directed to establish suitable techniques to assemble nanoparticles in 1D, 2D, and 3D architectures that have importance in many applications for instance biotechnology, sensor, and intelligent responsive nanostructured materials [*13*].

Amphiphilic molecules (molecules containing both hydrophilic and hydrophobic groups), such as surfactants, copolymers, and proteins, play a critical role in a wide range of self-assembly phenomena. Due to these self-assembly mechanisms into ordered nanostructures at interfaces and in bulk solution the amphiphilic molecules are frequently used to structure other materials. For example a range of amphiphiles/polyelectrolyte materials can precipitate having a highly ordered nanoscale structures, when a mixture of solutions of amphiphiles or surfactants are mixed with polyelectrolyte of opposite charge [*15-18*]. These combinations consist of a surfactant liquid-crystalline phase with the polyelectrolyte intercalated into the spaces between surfactant headgroups. In general, many factors control the polymer/surfactant nanostructures shape such as the charge on each species, polymer:surfactant ratio, surfactant headgroup area and the presence of additives such as salts and other small molecules [*19-22*].

Polyelectrolyte/surfactant mixtures have proven to provide the basis for new materials with extraordinary properties that make them interesting and important from the viewpoints of academic research, as well as industrial applications. Recently polyelectrolyte/surfactant research has increased, not only because of their importance in essential polymer physics/biophysics but also because of their great possible application to engineering, pharmaceutics, and noanocomposite material sciences [*23-25*]. The numerous useful properties of these complexes result from the highly ordered structures formed by the self-assembly of surfactant molecules through the aggregate behaviour. Solid-state polyelectrolyte/surfactant complexes are one of the most interesting topics as a new class of materials with special electrical, optical, and mechanical properties [*23, 26-30*]. They have extraordinarily diverse mechanical properties ranging from elastomers to crystalline solids. Solid nanostructured polyelectrolyte/surfactant films can be promising hosts for many applications such as drug delivery [*31*], nanostructured polymer materials [*32*] and metal ion sensors [*33, 34*].

1.1 The Aim and Objectives of this Project.

The major aims of this thesis are:

1- To achieve an understanding of the cationic surfactant and polyelectrolyte interactions responsible for forming particular nanoscale structures in free-standing polymer amphiphile films. This step was achieved by studies of polyethyleneimine/surfactant films varying the chain length and headgroup of the surfactant, where both the interactions in polyelectrolyte-cationic surfactant solutions and the relationship between these and the materials properties of the films were investigated. The polymer/surfactant solutions were characterised by using small angle neutron scattering (SANS), X-ray and neutron reflectivity and conductivity. These data are mainly discussed in Chapter 3.

2- To investigate the effect of incorporation of polymerisable species such as styrene and methyl methacrylate to create solid polymer nanostructures within the polymer hydrogel film. The incorporation of monomers both in solution and in films was probed using neutron and X-ray reflectivity, small angle scattering and spectroscopic techniques. Neutron scattering measurements, in particular, enable polymer and surfactant structures to be distinguished by using deuterated and hydrogenated surfactants and monomers in order to change the sample contrast without altering the chemical interactions. These contrast experiments assist in locating the hydrophobic species unambiguously within the solutions and films formed from them (Chapter 4).

3- To polymerise templated encapsulated hydrophobic monomers within nanostructured polyelectrolyte/surfactant films, resulting in formation of solid polymer nanostructures. Also to investigate the effect of thermal and photoinitiated polymerisation of these monomers on the film structures in a controlled atmosphere maintained during measurements. *In situ* polymerisation measurements were achieved by using grazing incidence x-ray diffraction (GIXD) (Chapter 5).

4- To incorporate metal ion sensor species such as 1-(2-Pyridylazo)-2-naphthol (PAN) and pyrene into the micelles in polymer/surfactant films forming a fluorescence sensor system. When used in combination with PAN in micellar systems the

fluorescence response of pyrene is modified in a quantitative manner in the presence of the chelating agent, and when it is bound to metal ions. The response can thus potentially be calibrated and used as a fluorescence sensor. Such films deposited on a surface e.g. as a dip stick, could provide a simple and sensitive method of monitoring metal ion content in aqueous samples so the concept was tested in this thesis (Chapter 6).

1.2 General Overview of Surfactants and their Classifications

Surfactants play essential functions in many applications in chemical industries, for example detergents, paints, dyestuffs, paper coatings, inks, plastics and fibres, personal care and cosmetics, agrochemicals, pharmaceuticals, food processing, etc. In addition, they play very important role in the oil industry, e.g. in enhanced and tertiary oil recovery, oil slick dispersion for environmental protection [*35*].

The name "surfactant" is derived from surface active agents although they are also known as amphiphilic molecules. Basically they consist of a non-polar hydrophobic part, usually a straight or branched hydrocarbon chain containing from 8 to18 carbon atoms, which is attached to a polar or ionic part (hydrophilic). The hydrophilic part can, therefore, be non-ionic, ionic or zwitterionic. The hydrocarbon chain hydrophobic part, is generally readily soluble in oil but sparingly soluble or insoluble in water, and the hydrophilic (or polar) part, is sparingly soluble or insoluble in oil but readily soluble in water. However, the cooperative action of dispersion and hydrogen bonding between the water molecules tends to fold the hydrocarbon chain out of the water and hence these chains are referred to as hydrophobic. The stability between hydrophobic and hydrophilic parts of the molecule gives these systems their unique properties, e.g. accumulation at different interfaces and association in solution to form micelles [*36, 37*]. The concentration where surfactants aggregate to form micelles in solution is called the critical micelle concentration (cmc).

Surfactants are classified according to hydrophilic part (headgroup); i.e., surfactants with a negatively charged headgroup are referred to as anionic surfactants, whereas cationic surfactants contain polar headgroups with a positive charge. Uncharged surfactants such as those with an oligo(ethylene oxide) headgroup are generally referred

to as nonionic, whereas zwitterionic surfactants contain both a negatively charged and a positively charged group. In addition, a fourth class of surfactants, usually referred to as polymeric surfactants, has long been used for the preparation of emulsions and suspensions and their stabilization [*36, 38*].

Anionic surfactants are the most widely used class of surfactants in industrial applications [*35*] due to their relatively low cost of manufacture and they are used in practically every type of detergent. For optimum detergency the hydrophobic chain is a linear alkyl group with a chain length in the region of 12–16 carbon atoms. The most commonly used hydrophilic groups are carboxylates, sulphates, sulphonates and phosphates.

The main classes of cationic surfactants are the ordinary amine salts, quaternary ammonium compounds, and amine oxides. There are two major categories of cationic surfactants that differ mainly in the nature of the nitrogen-containing group. The first consists of the alkyl nitrogen compounds such as ordinary ammonium salts containing at least one long-chain alkyl group and one or more amine hydrogen atoms, and quaternary ammonium compounds in which all amine hydrogen have been exchanged by organic substituents. The amine substituents may be either long-chain or short-chain alkyl, alkylaryl, or aryl groups [*39*]. The counter ion could be a halide, sulphate, acetate, or similar compound. The second category contains heterocyclic or aromatic materials like pyridinium, morpholinium, and imidazolinium derivatives. Cationic surfactants are generally water soluble when there is only one long alkyl group. Generally they are stable to pH changes, both acid and alkaline. They are usually precipitated with most anionic surfactants, but they do not precipitate with nonionics. These cationic surfactants are insoluble in hydrocarbon oils. In contrast, cationics with two or more long alkyl chains are soluble in hydrocarbon solvents, but they become only dispersible in water (sometimes forming bilayer vesicle type structures). They are generally chemically stable and can tolerate electrolytes. The critical micelle concentration of cationic surfactants is close to that of anionics with the same alkyl chain length [*39, 40*]. The most important behaviour of ionisable amphoteric surfactants is their dependence on the pH of the solution in which they are dissolved. Amphoteric surfactants become positively charged and behave like a cationic surfactant in acid pH solutions, whereas in alkaline pH solutions they acquire a negative charge and behave like an anionic species.

A specific pH can be defined at which both ionic groups show equal ionization. They are soluble in water, but the solubility shows a minimum at the isoelectric point. Amphoterics show excellent compatibility with other surfactants, forming mixed micelles. They are chemically stable both in acids and alkalis. The surface activity of amphoterics varies widely and depends on the distance between the charged groups, showing maximum activity at the isoelectric point. Wetting, detergency, foaming, and other physical properties of amphoteric surfactants are strongly affected by changing the pH of their solution [*38, 41*].

Ethylene oxide surfactants are the most common nonionic surfactants. Some categories can be distinguished: fatty acid ethoxylates, alkyl phenol ethoxylates, alcohol ethoxylates, monoalkaolamide ethoxylates, sorbitan ester ethoxylates, ethylene oxide propylene oxide copolymers and fatty amine ethoxylates. Another essential category of nonionics is the multihydroxy products such as glucosides , polyglucosides, (glycol, glycerol, polyglycerol) esters and sucrose esters. Amine oxides and sulphinyl surfactants represent nonionics with a small head group [*42*].

1.3 Critical Micelle Concentration (cmc)

The behaviour of surfactants in dilute aqueous solution is almost similar to normal electrolytes, but at higher concentrations they behave in a different way [*43*]. The variation in solubility of hydrophilic (head group) and hydrophobic (hydrocarbon chain or tail) parts of surfactant molecule drives the alkyl chains to avoid energetically unfavourable mixing with polar solvents, and the hydrophilic parts to maintain interactions with polar solvents. As a consequence of this behaviour the surfactants at higher concentrations associate with each other to form larger units. These associated units are called micelles (self-assembled structures) [*35*]. The primary aggregation usually starts with a spherical shape. The surface tension decreases rapidly with increasing surfactant concentration (Figure 1.3.1). At a certain concentration, micelle formation begins and this point is called the critical micelle concentration (cmc)

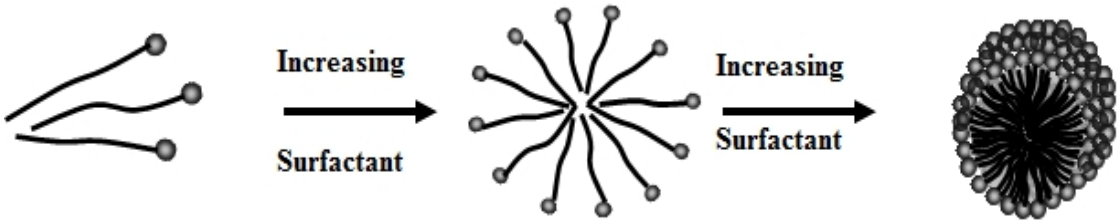

Figure 1.3.1: Surfactant association in aqueous solution during increase of the surfactant concentration.

This point can be measured by different techniques where unusual changes are recorded. Self-diffusion and equivalent conductivity start to decrease while light scattering starts to increase. Surface tension and osmotic pressure take on an approximately constant value (Figure 1.3.2). The interior of the surfactant micelle has properties similar to liquid hydrocarbons. This property is confirmed by the high mobility of the alkyl chains and the ability of the micelles to solubilize many water-insoluble organic molecules, e.g. dyes and agrochemicals [*44*].

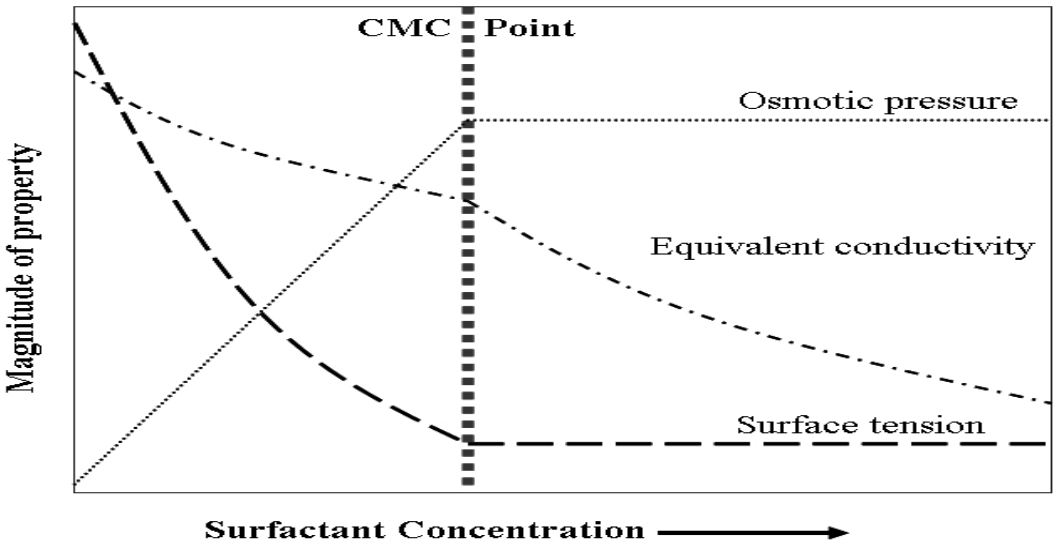

Figure 1.3.2: Changes in behaviour of physical properties during increasing surfactant concentration.

In general, chemical properties of surfactants, such as the hydrocarbon chain length and category of head group have a strong effect on cmc and their physical properties. Physical feature such as temperature, pressure, and the presence and nature of additives have variable effects on cmc. Adding electrolyte or increasing the pressure usually

decrease the cmc value whereas the effects of temperature depends on the nature of the surfactant and its concentration and solubility [*43*].

Above a certain temperature, termed the Krafft point (T_k), the solubility of the surfactant monomer increases to the point at which aggregate formation may begin, and the aggregated micelle becomes the thermodynamically favoured or predominant form in solution (Figure 1.3.3). Below the Krafft point the concentration of the surfactant is too low for micellization and solubility alone determines the surfactant monomer concentration [*43, 44*].

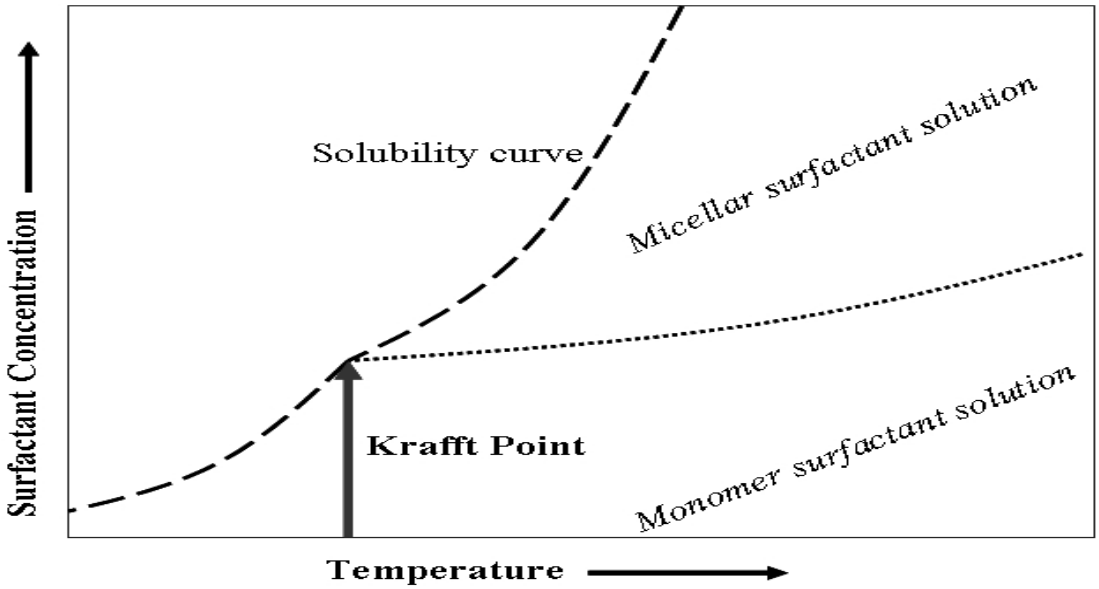

Figure 1.3.3: The relation of surfactant solubility, micellization behaviour and temperature effects in terms of Krafft point.

The solubility increases as temperature increases, until at T_k the cmc is reached. At this temperature the surfactant can be dispersed in micelles and solubility increases greatly. Above the Krafft point, a maximum reduction in surface interfacial tension occurs at the cmc and the value of the cmc determines the remaining surfactant monomer concentration.

Non-ionic surfactants do not show Krafft points. Since the solubility of non-ionic surfactants decreases with increasing temperature, the surfactants begin to lose their surface active properties above a transition temperature referred to as the cloud point.

1.4 Self-Assembly of Micelles

As surfactant concentrations increase above the cmc, micelles in solution will begin to pack together in ways that depend on the geometry of the individual micelles. Close-packed arrangements of micelles are called liquid crystals [*45*].

Surfactant micelles and bilayers are the building blocks of most self-assembled structures. Surfactant liquid crystals can be classified in two main groups; the first is limited self-assemblies, which may be characterized in general as spherical, prolate or cylindrical. The second category is unlimited self-assemblies, which the aggregates are associated over macroscopic distances in one, two or three dimensions [*46*]. For instance the rod-like or cylindrical phase is an example of a one-dimensional structure, the lamellar phase of two-dimensional structure, whereas the bicontinuous cubic phases and the sponge phase are examples of three-dimensional structures (Figure 1.4).

Pure, dry surfactants, like most materials, can be made to crystallize relatively easily. Because of their amphiphilic nature, however, the resulting structures are always lamellar with alternating head-to-head and tail-to-tail arrangements. Liquid-crystalline structures of surfactants behave as fluids and are usually viscous but it is also apparent that they are more ordered than ordinary liquids [*8, 37*].

The liquid-crystalline structures of surfactants depend mostly on the chemical structure of the surfactant molecule, the total bulk-phase composition, and the environment of the system (temperature, pH, co-solutes, additives, etc.) [*47-51*]. For example 2D hexagonal and lamellar liquid crystals are formed by the packing together of cylindrical micelles and lamellar micelles, respectively. With an increase in the concentration of the surfactant, a tendency can exist for surfactant micelles to change from spherical to cylindrical, and then to lamellar. Consequently 2D hexagonal liquid crystals are usually encountered at lower surfactant concentrations than lamellar phases. The cubic phases can occur either at lower or higher concentrations than 2D hexagonal depending on the type of cubic phase and the micelle shapes. Certainly the lamellar phase occurs at the highest concentrations [*42, 52, 53*].

The 2D hexagonal phase consists of long cylindrical micelles ordered in a hexagonal pattern, with each micelle encircled by six other micelles (figure 1.4.D). The radius of the circular cross-section is close to the surfactant molecule length [*54*].

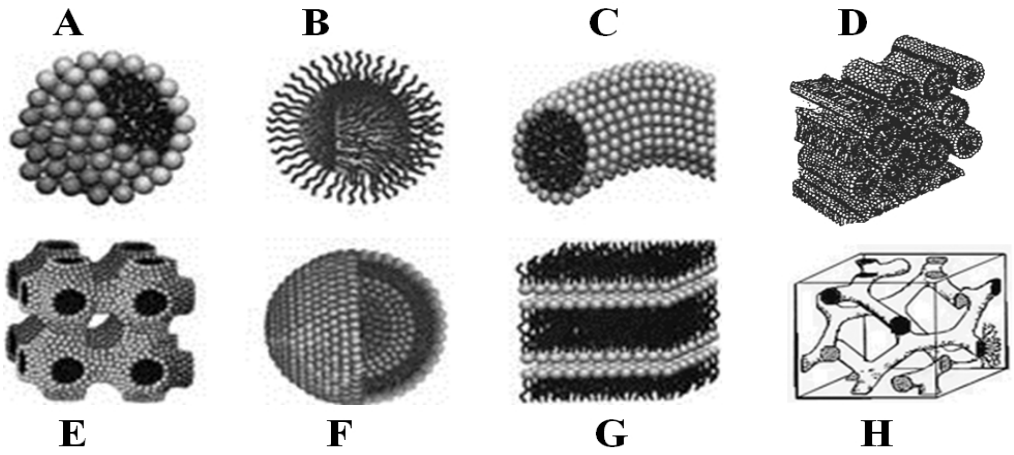

Figure 1.4: The most popular 1D, 2D and 3D Self-assembly liquid crystalline structures of surfactants. (A) Normal micelle, (B) Reverse micelle, (C) Cylindrical phase, (D) 2D Hexagonal Phase, (E) Bilayer cubic phase, (F) Vesicle phase, (G) Lamellar phase and (H) Branched cubic gyroid phase. Reprinted with permission from ref [55].

The micellar cubic phase consists of normal packing of small micelles, which have properties similar to those of small micelles in the solution phase. However, the micelles are short prolates rather than spheres since this allows a better packing [*56*]. Usually the cubic micellar phase is highly viscous.

There are different structures of bicontinuous cubic phases, where the surfactant molecules form aggregates that penetrate space, forming a porous linked structure in three dimensions. They can be considered as structures produced by involving rod-like micelles (branched micelles) (Figure 1.4.H) or bilayer structures (Figure 1.4.E) [*57*].

The lamellar phase consists of layers of surfactant molecules alternating with water layers (figure 1.4.G) [*54*]. The thickness of the bilayers is roughly lower than twice the surfactant molecule length. The thickness of the water layer can vary over wide ranges, depending on the nature of the surfactant. The surfactant bilayer can vary from being robust and planar to high flexible and meandering.

In the case of inverted structures like reversed micelles the polar groups of the surfactants are concentrated in the interior and the lipophilic groups extend towards and into the nonpolar solvent (figure 1.4.B). Likewise, the different structural phases have a reversed counterpart in which the polar and non-polar parts have changed roles, except for the lamellar phase, which is symmetrical around the middle of the bilayer [*58*], For instance an inverse 2D hexagonal phase consists of hexagonally packed water cylinders encircled by the polar head groups of the surfactant molecules and a continuum of the hydrophobic parts.

1.5 Temperature effects on ionic surfactant aggregation behaviour

The effect of temperature on the surfactant micellization performance in aqueous medium is complex, where the cmc value at relatively low temperature appears to decrease as the temperature increases, however at high temperature the cmc values start to increase (displaying a U-shaped trend) [*59*]. On the other hand, increasing the temperature causes an increase in dehydration of the hydrophilic group, which favours micellization, whereas an increase the temperature also causes disruption of the structured water surrounding the hydrophobic group, an effect that disfavours micellization [*60*]. The compromise between these two different effects consequently determines whether the aggregation increases or decreases over a particular temperature range.

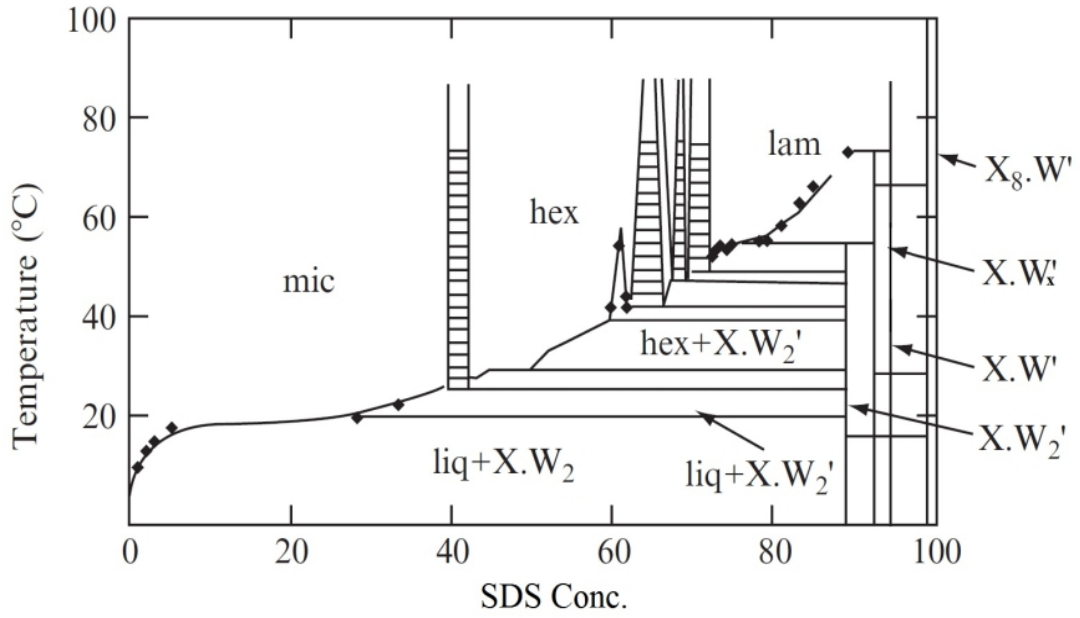

Figure 1.5.1: Temperature/concentration phase diagram of sodium dodecyl sulphate (SDS). The main liquid crystalline phases are the hexagonal and lamellar, while the other phase notations refer to less common intermediate liquid crystalline phases and to crystalline hydrates. The X.W` refers to the water content in SDS phases [61].

For example an anionic surfactant such as SDS has a relatively high Krafft temperature where above of the Krafft temperature, SDS illustrates a wide micellar region, which extends to ~40 wt% SDS. Above 40 wt% up to ~60 wt% SDS concentration, a hexagonal phase appears at the temperatures above the Krafft point (Figure1.5.1). A

mixture of liquid crystalline phases was seen over a narrow concentration range, after which the lamellar phase appears, followed by a solid phase at much higher SDS concentration. Overall different solid phases were predominant at ambient temperatures due to the high Krafft temperature of SDS [*61*].

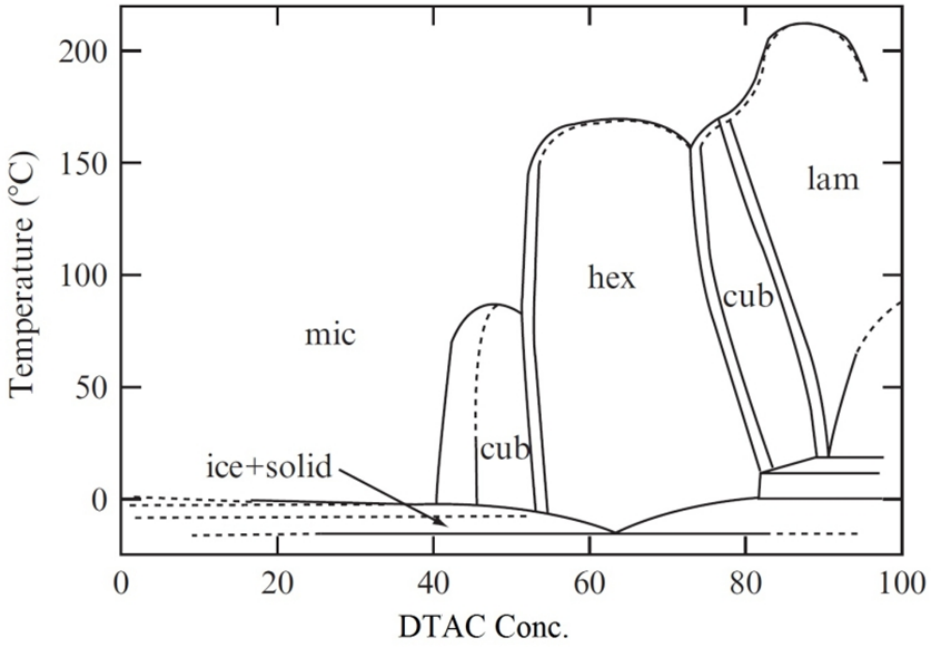

Figure 1.5.2: Temperature/concentration phase diagram of dodecyltrimethylammonium chloride (DTAC). The liquid crystalline phases hexagonal, cubic and lamellar form at relatively high DTAC concentrations, while isotropic micellar solutions exist at lower surfactant concentrations and higher temperatures [62].

Cationic surfactants show different temperature/concentration phase diagram behaviour (Figure 1.5.2-3). The phase diagram of dodecyltrimethylammonium chloride (DTAC) shows a relatively low Krafft point and solid phases have very little role to play. An isotropic micellar phase exists at room temperature up to high concentrations ~40 wt%, where the cubic phase built up of separate micelles appears. Between the two phases there is a two-phase region where the two phases coexist. At high volume fractions the micelles deform and become elongated to form finally a hexagonal phase, due to the difficulty of packing globular micelles. By increasing the DTAC concentration, transformation to a second cubic phase was seen, where a bicontinuous cubic phase appears at the temperature above that of the Krafft point. Lamellar and solid hydrated surfactant phases were predominant at very high concentration. The sequence of phases found in this case is typical of rather hydrophilic surfactants. At higher temperatures, the stability relations between the different phases change. The first cubic phase

disappears and at very high temperatures the lamellar phase is the only liquid crystalline phase, forming also for the neat surfactant. At very high temperature but lower concentrations, there are only isotropic solutions, with changes in aggregate structures as the composition changes [*62*].

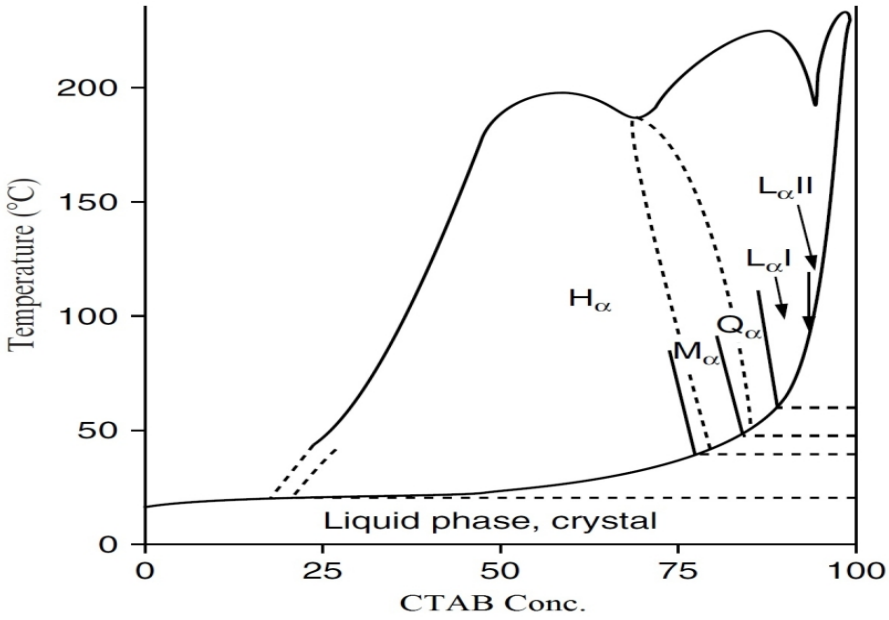

Figure 1.5.3: Temperature/concentration phase diagram of cetyltrimethylammonium bromide (CTAB). I, Hα, Mα, Qα, and Lα refer to isotropic micellar phases, hexagonal close packed cylinders and monoclinic hexagonal, cubic Ia3̄d, and lamellar phases, respectively [63].

However that both CTAB and DTAC have similar headgroup, nevertheless hydrocarbon tail and counterion could change the temperature/concentration phase diagram of these surfactants. CTAB is the one of the most common cationic surfactants and was used in this thesis. As illustrated from the phase diagram isotropic micelles and a two-dimensional hexagonal close packed structure can be formed at room temperature (Figure 1.5.3). Whereas the three phases, 3D hexagonal structure, *Ia3̄d* cubic and lamellar phase can be formed at relatively high temperatures and high concentrations of CTAB. This is the typical sequence of ordered phases observed for binary surfactant solutions. Mainly a region of *Ia3̄d* bicontinuous phase exists in the CTAB/water phase diagram at high concentrations of CTAB, where *Ia3̄d* structure always occurs in a phase diagram between 2D hexagonal and lamellar [*63*].

1.6 Polyelectrolytes

Polyelectrolytes are polymers that have the capability to dissociate charges in polar solvents, so occur as charged polymer chains (macroions) and mobile counterions.

Polyelectrolytes can be classified into natural such as nucleic acids, modified natural such as cellulose or chitin derivatives, and synthetic polymers such as poly(ethyleneimine) or poly(diallyldimethylammonium chloride). In the category depending on their charge, they can be divided into polyanions, polycations, and polyampholytes. There is further classification depending on the charge density and acidity of the functional groups. Strong and weak polyelectrolytes are defined related to high or low charge density [*64*] and the extent of counterion dissociation.

Polyelectrolytes play an essential part in nature and find various applications in industrial processes and daily life. Since they are both macromolecules and electrolytes they form a unique class of polymer. The special properties of these polymers are determined by their electrochemical and macromolecular parameters and their chemical structure. Charge density and charge strength result in variable long-range electrostatic interactions, which are mainly responsible for the physicochemical properties of polyelectrolytes and their behaviour in aqueous solution [*65*]. These interactions and the formation of complexes driven by attractive Coulomb forces between charged macromolecules and oppositely charged macroions, surfactants, colloid particles, or solid surfaces are of central importance in the life sciences and in most technical applications. However, the general properties of polyelectrolytes do not depend completely on the electrostatic forces. Differences between the flexibility of the polymer chain and, particularly, a molecular architecture supporting the formation of H-bonds or hydrophobic interactions also play a significant role in questions of scientific interest and practical importance [*66*].

In general the strength of the electrostatic interactions may be moderated by increasing the concentrations of added salt, which results in a screening effect by the small ions, but high concentrations of salt may also affect the solvent quality.

Substantial theoretical and experimental efforts have been made over the past few decades for example in understanding the origin of domains or clusters in semidilute polyelectrolyte solutions or counterion binding phenomena but several of them have not yet found a satisfactory theoretical explanation [*65, 67, 68*].

1.7 Polymer-Surfactant Interactions

The recent studies of polymer-surfactant interaction in dilute solutions shows there are two critical concentrations, symbolized T1 and T2. T1 indicates the concentration at which interaction between the surfactant and polymer start to appear [*69*]. Some references characterised this behaviour as the critical aggregation concentration (CAC). T2 occurs at the point where free micelles form in solution ie where the polymer is saturated with surfactant, and addition of more surfactant results in an increase in the free surfactant concentration, the surface tension is therefore reduced, until the free surfactant concentration equals the cmc, where free micelles are formed, and the surface tension becomes essentially independent of the surfactant concentration [*70*].

In general there are two main scenarios describing the surfactant/polymer interaction in solutions. The first interaction scenario is in terms of a strongly co-operative association or binding of the surfactant to the polymer chain and the second scenario is in terms of a micellization of surfactant on or in the vicinity of the polymer chain. The binding approach is preferred, in case of polymers with hydrophobic groups, whereas the micelle formation scenario is more ideal for hydrophilic homopolymers [*71*]. There is another scenario proposed a structure in which the aggregated ionic surfactants are surrounded by macromolecules in a loopy configuration [*72*] (Figure 1.7.1).

Polyelectrolyte properties play a very important role for the interactions with surfactants. These factors include chemical composition, linear charge density, location of the charges, and the backbone flexibility of the polymers.

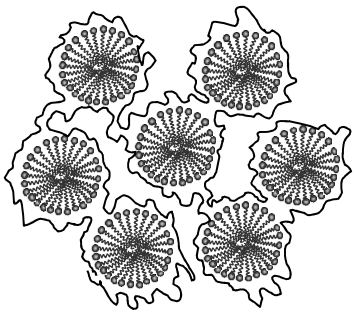

Figure 1.7.1 Schematic illustration the micelles surrounded by macromolecules in a loopy configuration.

The binding of surfactants to polyelectrolytes of opposite charge has been reported to be a highly cooperative process in which the cooperative binding range is restricted to the

early stage of binding. It is known that the presence of polyelectrolytes induces aggregation of the oppositely charged surfactant [*21, 66*]. However, an increase in linear charge density of the polyelectrolyte gives rise to stronger interactions. Studies of polyelectrolytes with similar charge density exhibited that binding parameters can still significantly through charge-dipole or hydrophobicity interaction between the surfactant and the polymer [*73*]. Added salt always reduces the binding affinity between opposite charged polyelectrolytes and surfactants. While added salt decreases the binding affinity, it increases the cooperatively of the interaction [*20*]. The effect of polymer hydrophobicity on cationic surfactant binding shows that for very hydrophobic polyelectrolytes where most repeat units are involved in microdomains, the surfactant aggregation number is proportional to the surfactant concentration (Figure 1.7.2). On the contrary, hydrophilic polyelectrolytes bind surfactants cooperatively above the cac and this binding is nearly independent on the surfactant concentration [*71*].

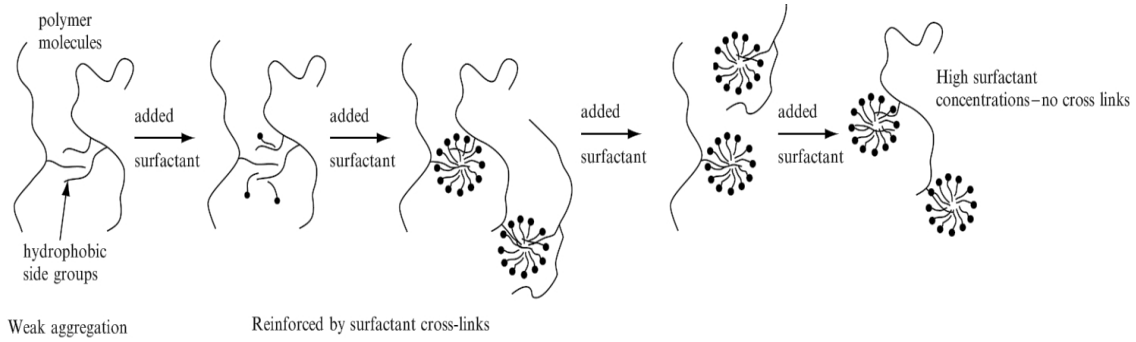

Figure 1.7.2: Polymer/Surfactant interactions during increasing surfactant concentration. Reprinted with permission from Ref. [71].

Above the cmc, polyelectrolytes interact in most cases with oppositely charged surfactants so strongly that irreversible macroscopic phase separation occurs. In the gel phase, polymer gels consisting of a crosslinked polyelectrolyte network are of special interest with regard to their ability to absorb large amounts of water, which could be up to thousand times its own weight [*66*].

The interaction between neutral polymers like poly(ethylene glycol), poly(vinyl pyrrolidone) (PVP), poly(ethylene oxide), etc., and surfactants is not simple. A number of factors control the performance of neutral polymers/surfactant interactions. For instance the polymer hydrophobicity, character of the surfactant head group and the nature of the polar groups embedded in the polymer backbone can change the interactions [*74*]. Mainly, cationic surfactants have relatively less interactions than

anionic surfactants with neutral polymers. Several studies have reported that hydrophobic interactions dominate in the interaction of neutral polymers like hydroxypropyl cellulose poly(vinylmethyl ether) and poly(propylene oxide) with cationic surfactants. In addition electrostatic interactions have been seen between the polar head groups of surfactant and neutral polymers as in the case of hexadecylpyridinium chloride/PVP systems [*75, 76*]. In general hydrophilic and lipophilic phenomena are the main interactions between polyelectrolyte and surfactants.

1.8 Polymer-Surfactant Films

Over the past several years, the electrostatic self-assembly (ESA) technique has been devoted to understanding of a variety of multilayer heterostructures on a solid substrate, particularly ultrathin films and coatings of polymers. A range of these strategies have been employed widely such as the Langmuir Blodgett (LB) technique, self-assembled monolayer (SAM) method, layer-by-layer (LbL) adsorption and spin-coating technique [*77*]. Unluckily, some of these approaches are not always useful for practical application. For example, LB method is a practical way to build-up multilayer structures, but it is restricted due to the requirement for rather expensive instruments and it is not applicable for many kinds of non-amphiphilic material [*78*]. The SAM technique can be applied to a wider range of substances, but it is not a useful process for multilayer fabrication.

Recently Edler's group discovered a new method of preparing solid nanostructured polyelectrolyte films through spontaneous self-assembly at the air-solution interface [*79*]. These films are self-supporting and assemble through interactions between water-soluble neutral polymers with polarisable groups, and surfactant micelles or vesicles having a well-defined range of surface charge [*80-82*]. This system forms films spontaneously at the surface of homogeneous solutions containing both the polyelectrolyte and surfactant and the films can be lifted from the solution surface after cross-linking onto either open mesh as membranes or on a solid substrates.

The thickness of these films (typically about 0.5μm) depends on the solution concentration and polymer molecular weight and the film completely covers the open interface of the container in which it is grown, allowing arbitrarily large films to be

easily prepared. Some well-developed films can be removed from the interface as a single piece and are self-supporting [*83*]. After removal of the film from the solution surface, a new film will form within a few minutes [*82, 83*].

Films formed from a catanionic surfactant mixture with polyethyleneimine raise the exciting possibility of trapping water-soluble as well as hydrophobic species within different regions of the same membrane due to incorporation of vesicle-like structures in the polymer-surfactant membrane. These systems are very promising in wide range of applications such as targeted delivery including as membranes for topical drug delivery for wound dressings and bandages as well as other encapsulation and release systems such as agrochemicals, flavour components, odorants and nutrients, and also for instrumental application such as sensors and responsive membranes.

Recent work on these films shows that film formation occurs with neutral polymers rather than charged species. This allows composite formation using a different range of polymers from those typically used for polymer-surfactant composites. These films, formed from polyelectrolyte polymers such as polyethylenimine (PEI) templated with surfactant liquid crystalline phases. The surfactant liquid crystalline phase within the films is oriented with respect to the interface rather than randomly distributed as in a precipitated powder and thus is more readily addressable and able to provide macroscopically oriented nanostructures [*48*]. Additionally the polymer phase between micelles is similar to a hydrogel rather than the dense polymer matrix found in precipitated materials. This hydrogel phase can allow facile diffusion of materials though the film raising the possibility of using pH or salt responsive polymers for this component to produce membranes which contract or curl under this stimulus. Cetyltrimethylammonium bromide (CTAB)-polyethylenimine (PEI) films can also be significantly reinforced by cross linking the polymer after the film has formed using ethylene glycol diglycidyl ether (EGDGE). This allows them to be removed from the solution surface on an open mesh. When mixed catanionic surfactant systems are used, the membrane is sufficiently thick that no further cross-linking of the polymer phase is required. After drying both cationic and catanionic surfactant-polymer films retain a significant degree of nanoscale structure which corresponds to the structure present in the in situ films. The general observation of initial experiments in this film shows that it is possible to prepare films with a variety of nanostructures ranging from lamellar, to 2D hexagonal to cubic depending on the surfactant, the polymer and the degree of polymer cross-linking used [*50, 82, 84, 85*].

1.9 Solubilisation of Hydrophobic Molecules in Aqueous Solutions of Amphiphiles.

The high ability of aqueous surfactant solutions to solubilise organic materials is a phenomenon that has enormous established applications in many scientific and technological areas. Recently more intensive experimental and theoretical work has been concerned to develop an understanding of the structural requirements to obtain optimum solubilisation criteria [*86*]. Solubilisation is defined as a spontaneous process leading to a thermodynamically stable, isotropic solution of a substance (the hydrophobic molecules) normally insoluble or only slightly soluble in a given solvent produced by the addition of one or more amphiphilic compounds, including polymers, at or above their critical micelle concentration. Since solubilisation is temperature dependant, therefore the maximum concentration of hydrophobic molecules (solute) that can be incorporated into a given system with preservation of a single isotropic solution (saturation concentration or maximum solute concentration) is achieved by using the same methods for measurement of solubility of any compound in a given solvent [*87*]. This can expressed as the concentration of solute versus concentration of surfactant or as ratio of solute dissolved per gram of surfactant versus surfactant concentration.

There are several factors can determine or affect the solubilisation process such as nature of solutes, amphiphile structure and temperature. The nature of solutes has complicated effects on thesolubilisation process. Polarisability, polarity, chain length and branching, molecular size and shape of solute can change significantly the solubility of solute. The polarity of the solute is the most major influence. Many researchers have reported that the extent of solubilisation increases with increasing the alkyl chain length of surfactant [*88*]. On the other hand solubilisation increases in the order: anionic < cationic < non-ionic in the case of the same length of the surfactant hydrocarbon chain [*89*].

As mentioned earlier the effect of temperature on the micellization of ionic surfactants is not a simple relationship, therefore it is to be expected that the effects on solubilisation will be correspondingly more complex. Temperature is known to affect some of the important solute characteristics (size, shape, ionic nature, etc.). In addition, temperature can affect the intermolecular interactions between solvent and solutes, such

as hydrogen bonding; therefore the solvent properties of the liquid for both the surfactant and the solute may be significantly changed [*90*].

Addition of most electrolytes causes a reduction in the CMC and they may increase the aggregation number and size of the micelle. This can lead to an increase in solubilisation.

The major location of hydrophobic molecules solubilised in micelles depends on the hydrophobicity of the solute and its interactions with the surfactant. There are four possible locations for solubilized molecules inside the micelle. The first possibility is that the hydrophobic molecules are located in the central region of the micelle, second is in the region between the tail and the headgroup of micelle, third is in the headgroup area which is the interface between the micelle and the surrounding bulk water and the fourth possibility is that these molecules are attached or adsorbed at the surface of the micelle [*88*]. The shape and size of the micelles and the location of these solubilised molecules can be studied by a number of experimental techniques, such as small-angle neutron scattering (SANS), small-angle X-ray scattering (SAXS), dynamic light scattering (DLS) steady-state fluorescence quenching (SSFQ), time-resolved fluorescence quenching (TRFQ), pulsed gradient spin-echo NMR (PGSE NMR) and cryo-transition electron microscopy (Cryo-TEM). Each of these method gives its own contribution to the clarification of the final micellar/solute structure [*91*].

1.10 Polymerization of Solubilised Monomer Within Templating Lyotropic Mesophases

As stated earlier, lyotropic liquid crystals are self-assembling structures consisting of a typically polar solvent and surfactant having low viscosities and the long range order of crystalline materials [*92*]. Through changing the surfactant concentrations, numerous lyotropic liquid crystal structures with simple and complex geometries can be observed, such as spherical micelles, hexagonal arrangements of rod-like structures, and bilayer aggregates of the lamellar phase. In addition at appropriate concentration, temperature and surfactant geometry extra phases can form including, discontinuous cubic, bicontinuous cubic, and the inverse of the above stated phases [*55*].

Polymerisation of micelles swollen with monomer in these lyotropic phases is a very promising approach to synthesis nanostructured polymers. However polymerisation of solubilised monomer in lyotropic liquid crystalline solutions can be difficult to control due to of rearrangement of the surfactant template due to temperature and composition changes through interdroplet diffusion and droplet exchange which occur faster than the polymerisation reaction [*93*]. Polymerization of monomer within well-organized system, such as microemulsions, vesicular solutions or dispersions, or lyotropic mesophases has been studied using several polymerisation techniques. However monomer segregation and diffusion are still been reported during the polymerization of these systems, due to micelle rearrangement on short timescales, which allows the encapsulated monomer to move [*94, 95*].

Recently, several synthetic methods displaying enhanced control of organic polymer nanostructured have been established. For example polymerization within microemulsions [*96*], liquid-crystalline gel phases of surfactants [*97*], block copolymers [*98*] or polymerization of polymerizable amphiphiles molecules [*99*] has been achieved to synthesis reproducible nanostructure polymers.

A template is a structure directing agent; therefore the templated material can be a 1:1 copy of the template structure. Templating using self-assembled surfactant in aqueous or organic solvent media is one of the most promising approaches towards the synthesis of nanomaterials, such as nanostructure particles, mesoporous spheres and porous bulk polymers as, for instance, nanofiltration membranes [*100*].

The complexity of lyotropic liquid crystals morphology enables their potential use for templated synthesis not only of nanoparticles, but also of bulk materials with isotropic

or anisotropic morphologies. However, most studies deal with the synergistic templating of lyotropic mesophases by polymerization of surfactants [*101*]. Nevertheless, polymerization of monomers in a surfactant template has significant advantages over polymerization of amphiphilic monomers. This is due to the fact that the phase behaviour of common surfactants is known or relatively easy to control. For instance it is easy to modify identified mixtures to produce the most wanted template. The second reason is the effect of added monomers mainly can be predicted and relatively easily be manipulated by changing phase behaviour parameters such as temperature. Finally, the cost of particularly synthesized polymerizable surfactants is such that large scale applications will be restricted [*102*].

In the last few years several studies have been directed towards polymerisation in various surfactant phases [*103*]. However the vast numbers of these researchers investigate microemulsion phases, while just a few successful examples have been reported on polymerisations in other phases. One of these promising examples is polymerisation of a thermosetting epoxy resin within a hexagonally ordered block-copolymer phase without experiencing any change of phases by using a templating approach to the synthesis of ordered polymer morphology [*104*]. Forney et al. demonstrated nanostructured polyacrylamide hydrogels formed through photopolymerization in lyotropic templates using certain concentrations of polymerizable surfactant [*105*]. Another example reported polymerisation of styrene and methyl methacrylate in cubic phases formed from didodecyldimethylammonium bromide, which appeared to yield a cubic polymer mesostructure [*106, 107*].

In general many techniques have been used to synthesise ordered nanostructured polymers which attempt to avoid phase separation behaviour through either thermodynamic or kinetic parameters [*102*]. Some of these approaches described one-to-one polymerization by using different strategies such as thermodynamic adjustment of the surfactant/monomer/polymer system. Other methods used polymerization within templates with long rearrangement times such as concentrated lamellar, hexagonal and cubic phases. Stabilization of the polymerization process was achieved by using surfactants with slower exchange dynamics such as amphiphilic block copolymers [*108-110*]. Finally cross-linking of the polymer matrix to balance the entropy loss produced by synthesising the polymer matrix in a controlled nanostructure can also help form the templated polymer structure. Monomers with a high number of reactive entities per

molecule can be fully cross-linked at low conversions faster than micelle re-arrangement occurs [*111-114*].

1.11 Surfactant Micelle Based Sensors for Metal Ions

Fluorescent sensors are becoming increasingly popular due to their easy use in solution as well as their high sensitivity and selectivity for some essential trace metal ions and various harmful metal species in drinking water [*115-118*]. Recently chemistry developed for fluorescent sensors has been merged to micelles with many advantages in terms of synthetic simplification, low cost and ease of use in aqueous solutions. In addition, developing micelle-based fluorescence sensors for the measurements of molecular properties are useful, for instance in drug design, drug delivery and the lipophilicity of pharmaceutically interesting molecules [*119*]. Fluorescent sensor has been developed using aqueous micelles solubilising hydrophobic fluorophore and a lyophilized receptor [*120*]. These two molecular components are combined together by a preferential solubilisation inside the intramicellar region without any covalent bonding involved. When the target metal ion interacts with solubilised receptor on the surface of the micellar container a metal-receptor complexation results inside the micelle. The intramicellar photo-electron transfer or energy transfer mechanisms between the excited fluorophore and the metal complex causing changes in the fluorescence signal. Several papers reported solubilising different molecules interacting in the same micelle can be considered classics of surfactant chemistry [*121*]. Some of these studies used the micellar incorporation of hydrophobic fluorophore and hydrophobic quencher, and their interactions in the flash photolysis timescale, to study the diffusion rates of the fluorophore inside the micelle [*122*]. A indole–quinolizine- based sensor for Cu^{2+} [*123*], off-on-off window-shaped fluorescent sensor for pH [*124*], fluorescent logic operation gate based on H^+ and Na^+ inputs [*125*] and sensor for the inositol triphosphate anion [*126*] examples used the intramicellar energy and electron transfer between a fluorophore and metal-ion complex of a solubilised receptor to obtain fluorescent micellar sensors for cationic metals.

In general micelles can be advantageously used as nanosized containers for the self-assembling of fluorescent sensors for anions or cations amphiphilic molecules. This

technique is characterized by high flexibility, as the components (or the system) can be changed without the need for particularly complicated synthetic effort such as transforming a fluorescent sensor. For instance, changing selectivity for sensing from Cu^{2+} into a sensor for Hg^{2+} by simply varying the binding unit appended to a long *n*-alkyl chain [*126*]. On the other hand properties of a micellar device can be controlled by changing simple structural features of the molecular components included, for instance acting on their lipophilicity and structure to getting different size or volume of micellar incorporation. This allows one to regulate the type of response of the sensor (e.g. changing an ON–OFF into an OFF–ON sensor or its working pH range, or even its signalling efficiency [*127, 128*].

In this work the PAN/Pyrene combination was used together to develop solid micelle based metal-ion sensors [*129, 130*]. The species 1-(2-Pyridylazo)-2-naphthol (PAN) is a well-known chelating agent for broad range of transition and lanthanides metal ions [*131-134*]. When used with pyrene in micellar systems the fluorescence response of pyrene is modified in a quantitative manner. When PAN is bound to metal ions the response can therefore be calibrated and used as a fluorescence sensor. The aim is to develop micelle-based metal ion sensors using the PAN/pyrene system by incorporate micelle solubilised PAN/Pyrene species into robust surfactant-polyethylenimine films.

1.12 References

1. Hosokawa, M. (2007) *Nanoparticle technology handbook*, Elsevier, Amsterdam, Netherlands; Boston [Mass.].
2. Xu, J., Wang, Z., and Chen, M. (2014) Research progress of controllable syntheses of nanomaterials constructed from coordination complexes, *Chemistry Bulletin / Huaxue Tongbao 77*, 30-36.
3. Li, X., Wepasnick, K., Tang, X., Fairbrother, D. H., Bowen, K. H., Dollinger, A., Strobel, C. H., Huber, J., Mangler, T., Luo, Y., Proch, S., and Gantefoer, G. (2014) A new nanomaterial synthesized from size-selected, ligand-free metal clusters, *J Appl Phys 115*.
4. Turco Liveri, V. (2006) *Controlled synthesis of nanoparticles in microheterogeneous systems*, Springer, New York.
5. Vizirianakis, I. S. (2014) Handbook of personalized medicine advances in nanotechnology, drug delivery, and therapy, Pan Stanford, Boca Raton.
6. Kleijn, S. E. F., Lai, S. C. S., Koper, M. T. M., and Unwin, P. R. (2014) Electrochemistry of nanoparticles, *Angewandte Chemie - International Edition 53*, 3558-3586.
7. Gerrard, J. A. (2013) Protein nanotechnology : protocols, instrumentation and applications.
8. Zhang, J. Z., and NetLibrary, I. (2003) Self-assembled nanostructures, Kluwer Academic/Plenum Publishers, New York.
9. Ahmed, S. P. N. A. A. U. H. K. D. K. D. V. M. (2014) Impact of the Substrate Material on the RF Performance of Carbon-Nanotube Transistors, *IEEE transactions on nanotechnology. 13*, 123-135.
10. Ma, S. Y., and He, D. H. (2014) Novel self-assembled nano-antimicrobial peptides and antimicrobial peptide drugs, *Chinese Journal of New Drugs 23*, 203-209.
11. Zhang, S. Y., Regulacio, M. D., and Han, M. Y. (2014) Self-assembly of colloidal one-dimensional nanocrystals, *Chemical Society Reviews 43*, 2301-2323.
12. Messina, P. V., Besada-Porto, J. M., and Ruso, J. M. (2014) Self-assembly drugs: From micelles to nanomedicine, *Curr Top Med Chem 14*, 555-571.
13. Chen, X. (2013) Mechanical self-assembly science and applications, Springer, New York, NY.
14. Zhang, J., Song, Y. F., Cronin, L., and Liu, T. B. (2008) Self-Assembly of Organic-Inorganic Hybrid Amphiphilic Surfactants with Large Polyoxometalates as Polar Head Groups, *Journal of the American Chemical Society 130*, 14408–14409.
15. Thunemann, A. F. (2002) Polyelectrolyte-surfactant complexes (synthesis, structure and materials aspects), *Progress in polymer science 27*, 1473-1572.
16. Kotz, J., Kosmella, S., and Beitz, T. (2001) Self-assembled polyelectrolyte systems, *Progress in polymer science 26*, 1199-1232.
17. Peng, B., Han, X., Liu, H., Berry, R. C., and Tam, K. C. (2013) Interactions between surfactants and polymer-grafted nanocrystalline cellulose, *Colloids and Surfaces A: Physicochemical and Engineering Aspects 421*, 142-149.
18. Bahramian, A., Thomas, R. K., and Penfold, J. (2014) The adsorption behavior of ionic surfactants and their mixtures with nonionic polymers and with

polyelectrolytes of opposite charge at the air-water interface, *J. Phys. Chem. B 118*, 2769-2783.
19. Li, Y. J., Dubin, P. L., Dautzenberg, H., Luck, U., Hartmann, J., and Tuzar, Z. (1995) Dependence of Structure of Polyelectrolyte/Micelle Complexes Upon Polyelectrolyte Chain-Length and Micelle Size, *Macromolecules 28*, 6795-6798.
20. Wang, Y., Kimura, K., Huang, Q., Dubin, P. L., and Jaeger, W. (1999) Effects of Salt on Polyelectrolyte-Micelle Coacervation, *Macromolecules. 32*, 7128-7134.
21. Wang, Y., Kimura, K., Dubin, P. L., and Jaeger, W. (2000) Polyelectrolyte-Micelle Coacervation: Effects of Micelle Surface Charge Density, Polymer Molecular Weight, and Polymer/Surfactant Ratio, *Macromolecules 33*, 3324-3331.
22. Romsted, L. (2014) Surfactant science and technology retrospects and prospects, CRC Press, Taylor and Francis, Boca Raton, FL.
23. Ober, C. K., and Wegner, G. (1997) Polyelectrolyte-surfactant complexes in the solid state: Facile building blocks for self-organizing materials, *Advanced Materials 9*, 17-31.
24. Kötz, J., Kosmella, S., and Beitz, T. (2001) Self-assembled polyelectrolyte systems, *Progress in Polymer Science (Oxford) 26*, 1199-1232.
25. Habibi, N., Pastorino, L., Sandoval, O. H., and Ruggiero, C. (2013) Polyelectrolyte based molecular carriers: The role of self-assembled proteins in permeability properties, *J Biomater Appl 28*, 262-269.
26. Bandyopadhyay, R. (2013) Novel experimentally observed phenomena in soft matter, *Pramana - Journal of Physics 81*, 3-34.
27. Carmona-Ribeiro, A. M., and de Melo Carrasco, L. D. (2013) Cationic antimicrobial polymers and their assemblies, *Int J Mol Sci 14*, 9906-9946.
28. Smith, G. N., and Eastoe, J. (2013) Controlling colloid charge in nonpolar liquids with surfactants, *Phys. Chem. Chem. Phys. 15*, 424-439.
29. Gao, C., Shi, J., and Zhao, F. (2014) Successful polymer flooding and surfactant-polymer flooding projects at Shengli Oilfield from 1992 to 2012, *Journal of Petroleum Exploration and Production Technology 4*, 1-8.
30. Shamsijazeyi, H., Miller, C. A., Wong, M. S., Tour, J. M., and Verduzco, R. (2014) Polymer-coated nanoparticles for enhanced oil recovery, *Journal of Applied Polymer Science 131*.
31. Li, L., Wang, L., Shao, Y., Ni, R., Zhang, T., and Mao, S. (2013) Drug release characteristics from chitosan-alginate matrix tablets based on the theory of self-assembled film, *Int J Pharm 450*, 197-207.
32. Xia, M., Liu, S., Wang, Y., Zhang, Y., Wu, Y., and Zhu, M. (2013) Preparation and properties of nanocomposite hydrogel by photoinitiated polymerization, pp 499-506.
33. Peinetti, A. S., Méndez De Leo, L. P., González, G. A., and Battaglini, F. (2012) A polyelectrolyte-surfactant complex as support layer for membrane functionalization, *J. Colloid Interface Sci. 386*, 44-50.
34. Shi, J., Lu, C., Yan, D., and Ma, L. (2013) High selectivity sensing of cobalt in HepG2 cells based on necklace model microenvironment-modulated carbon dot-improved chemiluminescence in Fenton-like system, *Biosensors and Bioelectronics 45*, 58-64.
35. Canselier, J. P. (2007) Applied Surfactants, *Macromolecular chemistry and physics. 208*.

36. Rhein, L. D. (2007) *Surfactants in personal care products and decorative cosmetics*, CRC Press, Boca Raton.
37. (2005) *Surfactant Science and Technology*, John Wiley & Sons Inc.
38. Malmsten, M. (2002) *Surfactants and polymers in drug delivery*, Marcel Dekker, New York.
39. Cross, J., and Singer, E. J. (1994) *Cationic surfactants : analytical and biological evaluation*, M. Dekker, New York.
40. Rubingh, D. N., and Holland, P. M. (1991) *Cationic surfactants : physical chemistry*, M. Dekker, New York.
41. Tadros, T. F. (2005) *Applied surfactants : principles and applications*, Wiley-VCH, Weinheim; [Great Britain].
42. Wendt, P. L., and Hoysted, D. S. (2009) *Non-ionic surfactants*, Nova Science Publishers, Hauppauge, NY.
43. Rehage, H. (2008) Giant Micelles, Properties and Applications, *Macromolecular chemistry and physics. 209*.
44. Schramm, L. L. (2005) *Emulsions, foams, and suspensions : fundamentals and applications*, Wiley-VCH, Weinheim; [Great Britain].
45. Guerin, C. B. E., and Szleifer, I. (1999) Self-assembly of model nonionic amphiphilic molecules, *Langmuir 15*, 7901-7911.
46. Camesano, T. A., and Nagarajan, R. (1998) Micelle formation and CMC of gemini surfactants: a thermodynamic model, In *72nd ACS Colloid and Surface Science Symposium*, pp 165-177, University Pk, Pennsylvania.
47. Nagarajan, R., and Ruckenstein, E. (1991) THEORY OF SURFACTANT SELF-ASSEMBLY - A PREDICTIVE MOLECULAR THERMODYNAMIC APPROACH, *Langmuir 7*, 2934-2969.
48. Edler, K. J., Wasbrough, M. J., Holdaway, J. A., and O'Driscoll, B. M. D. (2009) Self-assembled films formed at the air - Water interface from CTAB/SDS mixtures with water-soluble polymers, *Langmuir Langmuir 25*, 4047-4055.
49. O'Driscoll, D., Fernandez-Martin, C., Wilson , D., Knott, J., Roser, J., and Edler, J. (2007) Macroscopic, mesostructured cationic surfactant/neutral polymer films: structure and cross-linking, *Langmuir 23*, 4589-4598.
50. Edler, K. J., Fernandez-Martin, C., Brennan, T., and Roser, S. J. (2007) A tale of two mechanisms: comparing mesostructure formation in cationic and non-ionic surfactant-templated silicas, *Stud. Surf. Sci. Catal. 170B*, 1763-1769.
51. Edler, K. J. (2006) Nanoscum: solid nanostructured films at the air-water interface, *Soft Matter 2*, 284-292.
52. Abe, M., and Scamehorn, J. F. (2005) *Mixed surfactant systems*, Marcel Dekker, New York.
53. Hirst, L. S. (2013) *Fundamentals of soft matter science*, CRC Press, Boca Raton.
54. Fontell, K. (1981) Liquid crystallinity in lipid-water systems, *Molecular Crystals and Liquid Crystals 63*, 59-82.
55. Lindman, B., and Alexandridis, P. (2000) *Amphiphilic block copolymers : self-assembly and applications*, Elsevier, Amsterdam; New York.
56. Khan, A., Fontell, K., and Lindman, B. (1985) Some observations on liquid crystallinity in barium surfactant systems, *Prog. Colloid Polym. Sci. 70*, 30-33.
57. Evans, D. F., and Wennerström, H. (1994) *The colloidal domain : where physics, chemistry, biology, and technology meet*, VCH, New York,N.Y.
58. Cochran, H. D., Salaniwal, S., Cui, S. T., and Cummings, P. T. (2000) Self-assembly of reverse micelles by molecular dynamics simulation, In *1st*

International Conference on Molecular Modeling and Simulation (Cummings, P. T., and Westmoreland, P. R., Eds.), pp 183-186, Keystone, Co.
59. Noudeh, G. D., Housaindokht, M., and Bazzaz, B. S. F. (2007) The effect of temperature on thermodynamic parameters of micellization of some surfactants, *Journal of Applied Sciences 7*, 47-52.
60. Shah, S. S., Jamroz, N. U., and Sharif, Q. M. (2001) Micellization parameters and electrostatic interactions in micellar solution of sodium dodecyl sulfate (SDS) at different temperatures, *Colloids and Surfaces A: Physicochemical and Engineering Aspects 178*, 199-206.
61. Laughlin, R. G. (1994) *The aqueous phase behavior of surfactants*, Academic Press, London; San Diego.
62. Balmbra, R. R., Clunie, J. S., and Goodman, J. F. (1969) Cubic mesomorphic phases, *Nature 222*, 1159-1160.
63. Auvray, X., Petipas, C., Anthore, R., Rico, I., and Lattes, A. (1989) X-ray diffraction study of mesophases of cetyltrimethylammonium bromide in water, formamide, and glycerol, *Journal of Physical Chemistry 93*, 7458-7464.
64. von Ferber, C., and Lowen, H. (2004) Polyelectrolyte-surfactant complex: phases of self-assembled structures, In *Meeting on Self-Organising Polymers*, pp 389-405, Leeds, ENGLAND.
65. Schmidt, M. (2003) *Polyelectrolytes with defined molecular architecture. Volume II*, Springer, Berlin; London.
66. Koetz, J., and Kosmella, S. (2007) Polyelectrolytes and nanoparticles, Springer, Berlin; New York.
67. Schmidt, M. (2004) *Polyelectrolytes with defined molecular architecture. Volume I*, Springer, Berlin; New York.
68. Hara, M. (1993) *Polyelectrolytes : science and technology*, Marcel Dekker, New York.
69. Aidarova, S., Sharipova, A., Kragel, J., and Miller, R. (2014) Polyelectrolyte/surfactant mixtures in the bulk and at water/oil interfaces, *Advances in Colloid and Interface Science 205*, 87-93.
70. Capalbi, A., and La Mesa, C. (2001) Polymer-surfactant Interactions, *Journal of Thermal Analysis and Calorimetry 66*, 233-241.
71. Holmberg, K. (2003) *Surfactants and polymers in aqueous solution*, John Wiley & Sons, Chichester, West Sussex, England; Hoboken, NJ.
72. Cabane, B. (1977) Structure of some polymer-detergent aggregates in water, *J. Phys. Chem. 81*, 1639-1645.
73. O'Driscoll, B. M. D., Fernandez-Martin, C., Wilson, R. D., Roser, S. J., and Edler, K. J. (2006) Effect of micelle composition on the formation of surfactant-templated polymer films, *J. Phys. Chem. B 110*, 5330-5336.
74. Bakshi, M. S. (2000) Interactions between cationic mixed micelles and poly(vinyl pyrrolidone), *Colloid and Polymer Science 278*, 524-531.
75. Penfold, J., Thomas, R. K., and Taylor, D. J. F. (2006) Polyelectrolyte/surfactant mixtures at the air-solution interface, *Current Opinion in Colloid & Interface Science 11*, 337-344.
76. Hentze, H.-P., Niederberger, D., Willax, H., Burger, J., and Pascual Gienap, D. (2008) Polyelectrolyte-modified crosslinked polymer microcapsules, pp 39-52, (Basf Aktiengesellschaft, Germany).
77. Ariga, K., Hill, J. P., and Ji, Q. M. (2007) Layer-by-layer assembly as a versatile bottom-up nanofabrication technique for exploratory research and realistic application, *Phys. Chem. Chem. Phys. 9*, 2319-2340.

78. Maenosono, S., Okubo, T., and Yamaguchi, Y. (2003) Overview of nanoparticle array formation by wet coating, *Journal of Nanoparticle Research 5*, 5-15.
79. Edler, K. J., Goldar, A., Brennan, T., and Roser, S. J. (2003) Spontaneous mesostructured film growth in polyelectrolyte-surfactant solutions, *Chem. Commun.*, 1724-1725.
80. O'Driscoll, B. M. D., Milsom, E., Fernandez-Martin, C., White, L., Roser, S. J., and Edler, K. J. (2005) Thin Films of Polyethylenimines and Alkyltrimethylammonium Bromides at the Air/Water Interface, *Macromol. 38*, 8785-8794.
81. O'Driscoll, B. M. D., Fernandez-Martin, C., Wilson, R. D., Roser, S. J., and Edler, K. J. (2006) Influence of Micelle Charge on the Formation of Mesostructured Polymer/Surfactant Films at the Air/Water Interface, *J. Phys. Chem. B 110*, 5330-5336.
82. O'Driscoll, B. M. D., Fernandez-Martin, C., Wilson, R. D., Knott, J., Roser, S. J., and Edler, K. J. (2007) Macroscopic, Mesostructured Cationic Surfactant/Neutral Polymer Films: Structure and Cross-Linking, *Langmuir 23*, 4589-4598.
83. O'Driscoll, B. M. D., Nickels, E. A., and Edler, K. J. (2007) Formation of Robust, Free-standing Nanostructured Membranes from Catanionic Surfactant Mixtures and Hydrophilic Polymers, *Chem. Commun.*, 1068 - 1070.
84. O'Driscoll Benjamin, M. D., Hawley Adrian, M., and Edler Karen, J. (2008) Incorporation of sparingly soluble species in mesostructured surfactant-polymer films, *J. Colloid Interface Sci. 317*, 585-592.
85. O'Driscoll Benjamin, M. D., Fernandez-Martin, C., Wilson Roland, D., Roser Stephen, J., and Edler Karen, J. (2006) Effect of micelle composition on the formation of surfactant-templated polymer films, *J Phys Chem B 110*, 5330-5336.
86. Torchilin, V. P. (2007) Micellar nanocarriers: Pharmaceutical perspectives, *Pharm Res 24*, 1-16.
87. Yalkowsky, S. H. (1981) *Techniques of solubilization of drugs*, M. Dekker, New York.
88. Rangel-Yagui, C. O., Pessoa, A., Jr., and Tavares, L. C. (2005) Micellar solubilization of drugs, *8*, 147-165.
89. Rangel-Yagui, C. O., Hsu, H. W. L., Pessoa Jr, A., and Tavares, L. C. (2005) Micellar solubilization of ibuprofen - Influence of surfactant head groups on the extent of solubilization, *Revista Brasileira de Ciencias Farmaceuticas/Brazilian Journal of Pharmaceutical Sciences 41*, 237-246.
90. Tehrani-Bagha, A. R., and Holmberg, K. (2013) Solubilization of hydrophobic dyes in surfactant solutions, *Materials 6*, 580-608.
91. Christian, S. D. S. J. F. (1995) *Solubilization in surfactant aggregates*, M. Dekker, New York.
92. Sarkar, B., Ravi, V., and Alexandridis, P. (2013) Micellization of amphiphilic block copolymers in binary and ternary solvent mixtures, *J. Colloid Interface Sci. 390*, 137-146.
93. Yan, F., and Texter, J. (2006) Polymerization of and in mesophases, *Advances in Colloid and Interface Science 128*, 27-35.
94. DePierro, M. A., and Guymon, C. A. (2006) Photoinitiation and monomer segregation behavior in polymerization of lyotropic liquid crystalline systems, *Macromolecules 39*, 617-626.

95. Bucknall, D. G., Higgins, J. S., Penfold, J., and Rostami, S. (1993) Segregation behavior of deuterated poly(styrene-block-methyl methacrylate) diblock copolymer in the presence of poly(methyl methacrylate) homopolymer, *Polymer 34*, 451-458.
96. Peinado, C., Bosch, P., Martin, V., and Corrales, T. (2006) Photoinitiated polymerization in bicontinuous microemulsions: Fluorescence monitoring, *J. Polym. Sci., Part A: Polym. Chem. 44*, 5291-5303.
97. Forney, B. S., Baguenard, C., and Allan Guymon, C. (2013) Improved stimuli-response and mechanical properties of nanostructured poly(N-isopropylacrylamide-co-dimethylsiloxane) hydrogels generated through photopolymerization in lyotropic liquid crystal templates, *Soft Matter 9*, 7458-7467.
98. Zhang, Y., Tajima, K., Hirota, K., and Hashimoto, K. (2008) Synthesis of all-conjugated diblock copolymers by quasi-living polymerization and observation of their microphase separation, *Journal of the American Chemical Society 130*, 7812-7813.
99. Qiao, W.-h., Chen, M., Liu, H.-z., Zhao, X.-s., and Cao, C. (2010) Synthesis and application of several series of polymerizable surfactants in emulsion polymerization, pp 315-341, Nova Science Publishers, Inc.
100. Hentze, H. P., and Antonietti, M. (2001) Template synthesis of porous organic polymers, *Curr. Opin. Solid State Mater. Sci. 5*, 343-353.
101. O'Brien, D. F., Armitage, B., Benedicto, A., Bennett, D. E., Lamparski, H. G., Lee, Y.-S., Srisiri, W., and Sisson, T. M. (1998) Polymerization of Preformed Self-Organized Assemblies, *Acc Chem Res 31*, 861-868.
102. Hentze, H. P., and Kaler, E. W. (2003) Polymerization of and within self-organized media, *Current Opinion in Colloid & Interface Science 8*, 164-178.
103. Summers, M., Eastoe, J., Heenan, R. K., Steytler, D., and Grillo, I. (2001) Polymerization of cationic surfactant films in microemulsions, *J. Dispersion Sci. Technol. 22*, 597-607.
104. Hillmyer, M. A., Lipic, P. M., Hajduk, D. A., Almdal, K., and Bates, F. S. (1997) Self-assembly and polymerization of epoxy resin-amphiphilic block copolymer nanocomposites, *Journal of the American Chemical Society 119*, 2749-2750.
105. Forney, B. S., Baguenard, C., and Guymon, C. A. (2013) Effects of controlling polymer nanostructure using photopolymerization within lyotropic liquid crystalline templates, *Chem. Mater. 25*, 2950-2960.
106. Ström, P., and Anderson, D. M. (1992) The cubic phase region in the system didodecyldimethylammonium bromide-water-styrene, *Langmuir 8*, 691-709.
107. Anderson, D. M., and Ström, P. (1989), 204.
108. Hentze, H.-P., and Kaler, E. W. (2003) Polymerization of and within self-organized media, *Current Opinion in Colloid & Interface Science 8*, 164-178.
109. Yang, J. L., and Wegner, G. (1992) Polymerization in Lyotropic Liquid-Crystals .1. Phase-Behavior of Photo-Cross-Linkable Ethylene-Oxide (Peo)-Dimethylsiloxane (Pdms) Triblock Copolymers Peo-Pdms-Peo in Aqueous-Solution, *Macromolecules 25*, 1786-1790.
110. Paleos, C. M. (1985) Polymerization in Organized Systems, *Chemical Society Reviews 14*, 45-67.
111. Wadekar, M. N., Pasricha, R., Gaikwad, A. B., and Kumaraswamy, G. (2005) Polymerization in surfactant liquid crystalline phases, *Chem. Mater. 17*, 2460-2465.

112. Pindzola, B. A., Jin, J., and Gin, D. L. (2003) Cross-linked normal hexagonal and bicontinuous cubic assemblies via polymerizable gemini amphiphiles, *Journal of the American Chemical Society 125*, 2940-2949.
113. Sisson, T. M., Lamparski, H. G., Kolchens, S., Elayadi, A., and Obrien, D. F. (1996) Cross-linking polymerizations in two-dimensional assemblies, *Macromolecules 29*, 8321-8329.
114. Yang, J., and Wegner, G. (1992) Polymerization in lyotropic liquid crystals. 1. Phase behavior of Photo-cross-linkable Ethylene Oxide (PEO)-dimethylsiloxane (PDMS) triblock copolymers PEO-PDMS-PEO in aqueous solution, *Macromolecules 25*, 1786-1790.
115. Hirano, T., Kikuchi, K., Urano, Y., Higuchi, T., and Nagano, T. (2000) Highly zinc-selective fluorescent sensor molecules suitable for biological applications, *Journal of the American Chemical Society 122*, 12399-12400.
116. De Silva, A. P., Fox, D. B., Huxley, A. J. M., and Moody, T. S. (2000) Combining luminescence, coordination and electron transfer for signalling purposes, *Coordination Chemistry Reviews 205*, 41-57.
117. Amendola, V., Fabbrizzi, L., Licchelli, M., Mangano, C., Pallavicini, P., Parodi, L., and Poggi, A. (1999) Molecular events switched by transition metals, *Coordination Chemistry Reviews 190-192*, 649-669.
118. Huang, S. T., Shi, Y., Li, N. B., and Luo, H. Q. (2012) Fast and sensitive dye-sensor based on fluorescein/reduced graphene oxide complex, *Analyst 137*, 2593-2599.
119. Bandyopadhyay, P., and Ghosh, A. K. (2011) Recent developments in micelle-induced fluorescent sensors, *Sensor Letters 9*, 1249-1264.
120. Diaz-Fernandez, Y., Perez-Gramatges, A., Rodriguez-Calvo, S., Mangano, C., and Pallavicini, P. (2004) Structure and dynamics of micelle-based fluorescent sensor for transition metals, *Chem. Phys. Lett. 398*, 245-249.
121. Thomas, J. K. (1980) Radiation-induced reactions in organized assemblies, *Chem Rev 80*, 283-299.
122. Grätzel, M., and Thomas, J. K. (1973) On the dynamics of pyrene fluorescence quenching in aqueous ionic micellar systems. Factors affecting the permeability of micelles, *Journal of the American Chemical Society 95*, 6885-6889.
123. Mallick, A., Mandal, M. C., Haldar, B., Chakrabarty, A., Das, P., and Chattopadhyay, N. (2006) Surfactant-induced modulation of fluorosensor activity: A simple way to maximize the sensor efficiency, *Journal of the American Chemical Society 128*, 3126-3127.
124. Diaz-Fernandez, Y., Foti, F., Mangano, C., Pallavicini, P., Patroni, S., Perez-Gramatges, A., and Rodriguez-Calvo, S. (2006) Micelles for the self-assembly of "off-on-off" fluorescent sensors for pH windows, *Chemistry - A European Journal 12*, 921-930.
125. Uchiyama, S., McClean, G. D., Iwai, K., and De Silva, A. P. (2005) Membrane media create small nanospaces for molecular computation, *Journal of the American Chemical Society 127*, 8920-8921.
126. Pallavicini, P., Diaz-Fernandez, Y. A., Foti, F., Mangano, C., and Patroni, S. (2007) Fluorescent sensors for Hg2+ in micelles: A new approach that transforms an ON-OFF into an OFF-ON response as a function of the lipophilicity of the receptor, *Chemistry - A European Journal 13*, 178-187.
127. Pallavicini, P., Pasotti, L., and Patroni, S. (2007) Residual and exploitable fluorescence in micellar self-assembled ON-OFF sensors for copper(II), *Dalton Transactions*, 5670-5677.

128. Díaz-Fernández, Y., Rodríguez-Calvo, S., Pérez-Gramatges, A., Pallavicini, P., Patroni, S., and Mangano, C. (2007) Effect of surfactant structure on the residual fluorescence of micelle-based fluorescent probes, *J. Colloid Interface Sci. 313*, 638-644.
129. Díaz-Fernández, Y., Péres-Gramatges, A., Rodríguez-Calvo, S., Mangano, C., and Pallavicini, P. (2004) Structure and dynamics of micelle-based fluorescent sensor for transition metals, *Chem. Phys. Lett. 398*, 245-249.
130. Perez-Gramatges, A., and Chatt, A. (2006) Preconcentration neutron activation analysis of lanthanides by cloud point extraction using PAN, *Journal of Radioanalytical and Nuclear Chemistry 269*, 491-497.
131. Jaggi, S., and Gupta, U. (2013) Solid phase extraction and preconcentration of Ni(II) using 1-(2-pyridylazo)-2-naphthol) (PAN) modified β-cyclodextrin butanediol diglycidyl ether polymer as a solid phase extractant, *Macedonian Journal of Chemistry and Chemical Engineering 32*, 57-67.
132. Safari, Z., Gholivand, M. B., and Hosseinzadeh, L. (2011) Spectrophotometric study of complex formations between 1-(2-pyridylazo)-2-naphthol (PAN) and some metal ions in organic solvents and the determination of thermodynamic parameters, *Spectrochimica Acta Part A: Molecular and Biomolecular Spectroscopy 78*, 1606-1610.
133. Pramanik, K., and Adhikari, B. (2010) 1-(2′-Pyridylazo)-2-naphtholate (PAN) complexes of rhodium(III): Synthesis, structure and spectral studies, *Polyhedron 29*, 1015-1022.
134. Kobylecka, J., and Skiba, E. (1993) Spectrophotometric analysis of solubilization of Cu(II), Zn(II), Cd(II) and Co(III) complexes with 1-(2-pyridylazo)-2-naphthol by using quaternary ammonium salts, *Chem. Anal. (Warsaw) 38*, 599-605.

2 Theory and Experimental Methods

This chapter describes the analysis techniques used in this thesis to characterise materials on molecular and nanometer length scales. Techniques such as gel permeation chromatography, conductivity, UV-Vis and fluorescence spectroscopies, gas chromatography and cyclic voltammetry were used to characterise molecular properties while electron microscopies, small-angle scattering, reflectivity and grazing-incidence diffraction were used to characterise larger length scale structures. The basis of each of these techniques will be described in turn.

It is very important to understand the mechanisms of how nanoscale systems behave and to know the details of nanostructures, such as the particle size, the size distribution, the shape, the charge and the dimensions of adsorbed layers. There are a wide range of methods and techniques available for this purpose. Small-Angle Neutron Scattering (SANS) and Small-Angle X-ray Scattering (SAXS) are the most common and powerful tools for nanostructure and nanoscale analysis since the scattering experiments can supply excellent detailed information [*1, 2*]. Transmission Electron Microscopy (TEM) and Scanning Electron Microscopy (SEM) have also been recently used to provide useful information about the architectural organization of nanostructures in dry samples. However the resolution and accuracy of techniques used to characterize the size and shape are very important but the main factor to determining the choice of a technique is the length scale of the structure being examined [*3, 4*]. Figure 2.1 shows wide range of techniques used to characterise size and structures of materials. This chapter covers the theory behind the main characterisation techniques used in this thesis.

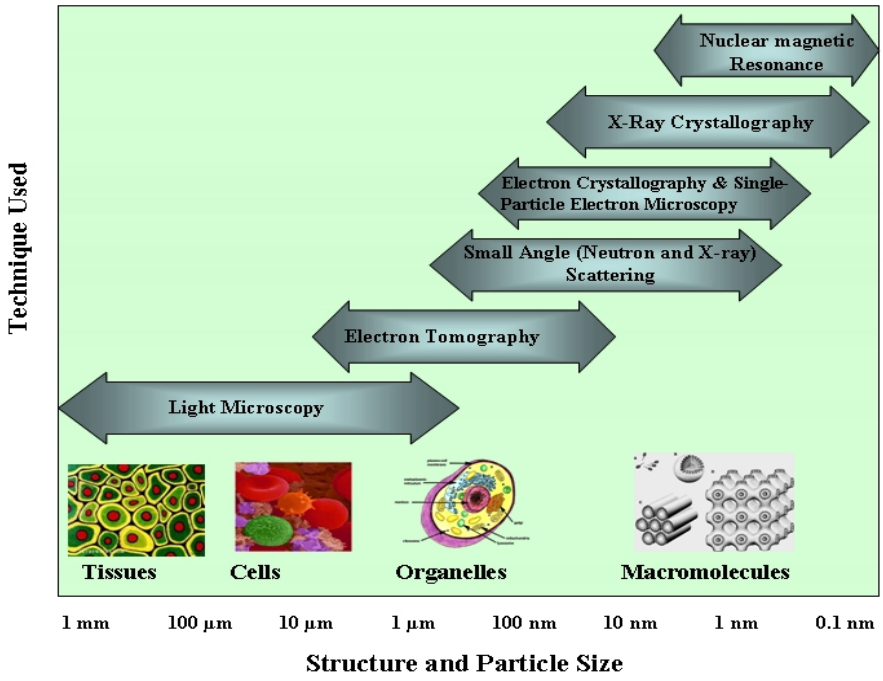

Figure 2.1: Techniques used to determine particle size or structural information.

2.1 Small-Angle Neutron Scattering (SANS) and Small-Angle X-ray Scattering (SAXS)

Neutron and x-ray scattering techniques have become established as a versatile probe for the determination of the structure of nanocomposite materials. Thus small-angle neutron scattering (SANS) and small x-ray scattering (SAXS) can give accurate details of the size, shape concentration, surface area and dispersion of very small particle systems. Both SANS and SAXS are non-destructive techniques which are applicable to various systems such as solid, liquid and gas samples under a range of temperatures and pressures [*5*].

2.1.1 Basic Scattering Theory and Q-Vector Definition

The main types of radiation used in scattering studies of materials are light, neutron and x-rays. Although the mechanism of scattering is different in all three cases, the basic aspect that unites and ultimately makes them so important in the study of soft matter is the concept of interference and its relation to the structure of the substances in a medium. X-rays are scattered by the electrons surrounding the nucleus of an atom. That

means light atoms like oxygen or hydrogen scatter x-rays less efficiently than heavy atoms with many electrons like mercury. Neutrons have no charge, and their electric dipole moment is either zero or too small to be measured by the most sensitive techniques. Consequently, neutrons can go through matter much further and deeper than charged particles. Additionally, neutrons interact with atoms via their nuclei rather than electrons thus different isotopes of the same element will have different neutron scattering properties. The scattering phenomena occur when radiation incident on a small volume of the sample is scattered from the direction of the incoming beam. The scattering is then observed a large distance from the sample, usually as a function of the scattering angle. In general the magnitude of the scattered wave for coherent scattering at a given time depends on the interference between waves scattered by the different scattering centres in the scattering medium [*6*].

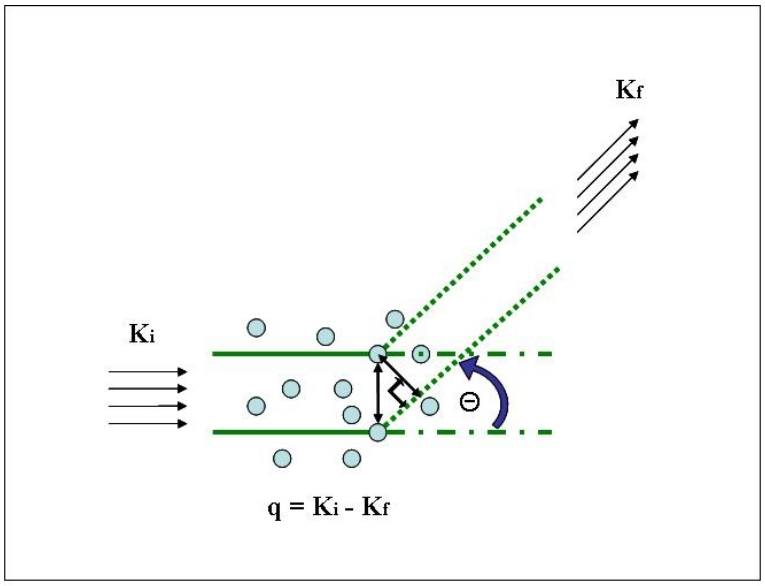

Figure 2.1.1: Schematic of scattering method. The incident radiation wave with vector K_i is scattered by the two scattering centres. The radiation is observed at a scattering angle Θ. The scattered wave has propagation vector K_f.

The scattering centres are characterized by circles. In the figure 2.1.1 two scattering centres are shown scattering radiation in a given direction, along which the detector is placed. This detector is usually a square law detector which means the response of detector is proportional to the square of the amplitude of the scattered wave. Practically this is proportional to the number of photons (X-rays or light) or neutrons. In case of ideal waves scattering (no interfering or overlapping between waves), the secondary

radiation that arrives at the detector from the two scattering centres arrives with different phases because the path lengths are different [*7, 8*]. For example, the radiation scattered from the lower particle travels a longer distance to the detector compared to that from the higher particle. The perpendicular line in the figure above indicates the distance between two particles. The phase difference δ between the secondary wavelets is the extra distance d travelled by one of them divided by the wavelength of the radiation and multiplied by 2π, i.e., $\delta = 2\pi d/\lambda$ this phase difference is usually written in terms of the positions of the particles and the q vector defined in figure 2.1.1. The vectors K_i and K_f are the propagation vectors of the incident and scattered radiation, respectively. They are vectors in the direction of propagation of the incident and scattered radiation and have lengths given by $2\pi/\lambda$. (assuming that the radiation wavelength is not particularly changed by the scattering.) A geometrical argument shows that

$$\delta = q.(r_i - r_j) \qquad (1)$$

where r_i and r_j indicate the positions of the scattering centres measured relative to an arbitrary coordinate system and the length of q is related to the scattering angle θ (defined in the figure 2.1.1),

$$q = 4\pi / \lambda \sin(\theta / 2) \qquad (2)$$

The scattering vector $q = K_i - K_f$ is central to scattering theory. That means, it may, when multiplied by $h/2\pi$ (Planck's constant divided by 2π) be interpreted as the momentum transferred to the system by the photons. It should be noted that the letter *q* is usually used to indicate the scattering vector or the negative of the scattering vector.
By definition, the angle between K_f and K_i is called 2θ. The magnitude of q quantifies the lengths in the reciprocal space and is expressed in $Å^{-1}$ or nm^{-1} in this case

$$q = \frac{4\pi}{\lambda}\sin\theta \qquad (3)$$

Applying the latter equation in the Bragg law, gives:

$$q = \frac{2\pi}{d} \qquad (4)$$

The dimension for q is reciprocal distance and it is related to the distance scale (d) probed by $d = 2\pi/q$. The SANS experiment provides a scattering profile consisting of the scattered intensity, $I(q)$ vs. q. This can be thought of as the Fourier transform of the radial distribution profile for the system, resulting from both the particle itself, and the distribution of particles in space [*7-9*]. Further details on analysis of small-angle scattering data are given below in section 2.2.

2.1.2 Instrumentation and Principle of Small-Angle Neutron Scattering (SANS)

scattering was discovered in the late 1930s by Guinier during X-ray diffraction experiments on metal alloys. The development of SANS experiments started in the 1960s [*10, 11*]. The increase of interest was related to the pioneering work of Sturhmann et al [*12*], who used contrast variation experiments to demonstrate that neutrons were a powerful tool to investigate materials. Difference of scattering length densities between isotopes and more precisely between hydrogen and deuterium atoms is at the basis of most experiments. Moreover, neutrons are non-destructive. neutron scattering (SANS) can give accurate information about shape and the structures, averaged in time, of particles or aggregates dispersed in a variety of media under a range of conditions. SANS has a wide application range for instance, small colloidal particles (silicates, suspensions, nanotubes), surfactant aggregates (micelles, lamellar, hexagonal, cubic, or sponge phases), polymers and all derivatives, liquid crystals, model membranes, proteins in solution, etc [*12, 13*].

The two main sources of neutrons are reactors and spallation sources. In the reactor, neutrons are continuously produced by fission processes whereas in spallation, a pulsed neutron beam (typically with 25 or 50 Hz frequency) is generated by the collision of high-energy protons with a target.

The time-of-flight method is used on the instruments on a spallation source to analyse the neutrons arriving on the detector. The wavelength is selected through a mechanical velocity selector, which consists of a rotating drum with helically curved absorbing slits at its surface. The wavelength can be varied depend on the rotation speed of the velocity selector. The selector is mounted on ball-bearings and forbidden frequencies of rotation exist to minimize vibrations and resonance. After the selector, a set of vertical and

horizontal slits are mounted. They define the size of the beam. The closure of the slits to reduce the beam size is used when a higher instrument resolution is necessary. Then neutrons pass through a low efficiency detector, called a monitor. The integrated counts during the time of the measurement are used for data normalization. To focus neutrons beam and remove other electromagnetic radiation like light or X-rays, a series of waveguides are used, called collimation [*14, 15*].

In the SANS instrument on LOQ at TS1 at ISIS, UK, the beam passes through a super mirror Soller bender which removes wavelengths less than 2Å, a first aperture, a disk chopper with variable openings, and a frame overlap mirror to cut the wavelengths higher than 12Å (Figure 2.1.2). The neutrons fly through a 3 meter evacuated guide. A second aperture is placed at the end of the final collimation and defines the sample beam size. The sample position is at around 11.1 meters from the moderator. The sample transmissions are measured by inserting a monitor just after the sample after reducing the beam diameter to 1 mm between the sample and the monitor [*16-18*].

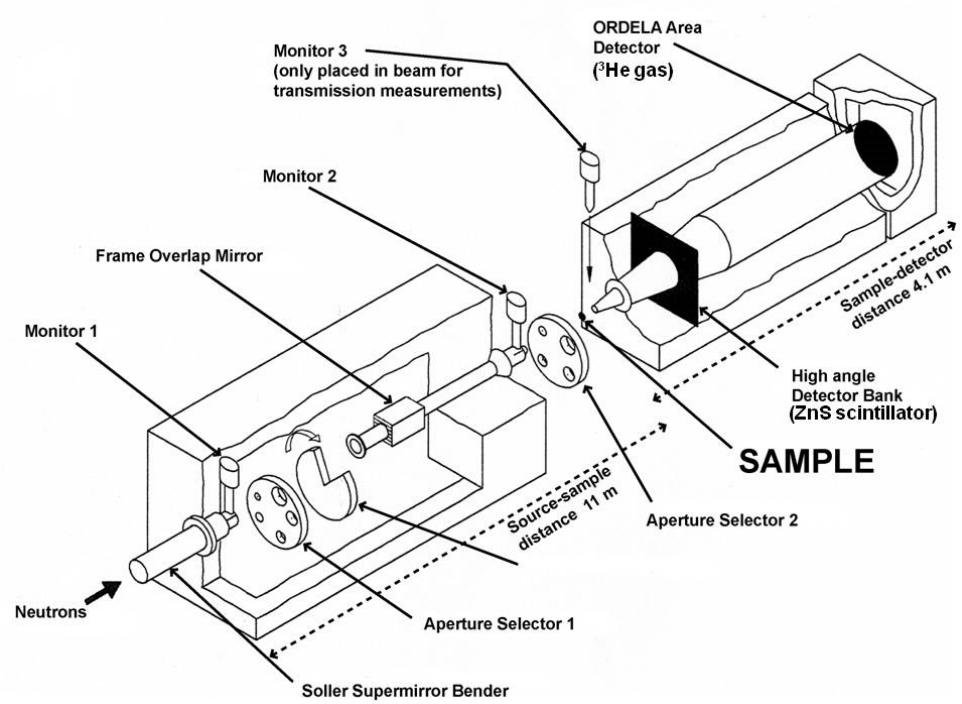

Figure 2.1.2 Schematic illustration of the LOQ diffractometer at the ISIS Facility, Didcot, UK [18].

The main detector is located at 4.1 meters from the sample in a vacuum tube. The active area is 64 cm^2 with 128 × 128 pixels (5 mm resolution) and 100 time channels for the different wavelengths. The high q region can be measured at the same time using a second detector set at a fixed and close position to the sample. The main advantage of conducting SANS experiments at ISIS is that a white incident beam is combined with time-of-flight detection technique to give a very large dynamic range in scattering vector, accessible in a single measurement without any need to reconfigure the instrument. In addition, the 25 Hz disc chopper selects wavelengths from 2.2 to10 Å, which are used together by time-of-flight. For fixed geometry instruments working in time of flight mode, different wavelength neutrons scattered at a same angle have different *q* values and arrive on the detector at different times. The broader the incoming wavelength range, the wider the *q*-range of the instrument. The data are saved in a 3D array with two dimensions for the pixels of the detector and the third for the time axis. The range of scattering vectors for time-of-flight instruments is similar to the range for steady-state instruments. The main advantage of time-of-flight instruments is that the full q-range is covered by only one instrument setting [*18*].

Since the neutron is an uncharged subatomic particle, secondary effects are needed to detect the neutron activities. Gas proportional counters are the technique most used in SANS detectors. The neutron absorption by a target isotope molecule like ^3He, induces a fission reaction and emission of two charged particles, a proton (^1H) and, in the opposite direction, a triton (T) with a total kinetic energy of 760 keV ($^1n+^3He\rightarrow{}^1H+^3T$) which induces the primary ionization in the gas. The electrons are accelerated to get more ionization and to amplify the signal near the anode wire, where the electric field is very high. The ions produced by the electron move away from the anode and cause a current in the cathode which is measured. SANS detectors are mainly filled with CH_4 or CF_4 as the stopping gas which plays an important role to reduce the path length of the electrons for good position resolution and to minimize wall effects. Mixtures of $^3He/(CH_4$ or $CF_4)$ also have a low sensitivity to gamma and X-rays in an environment of high photon background [*6, 8, 19*].

In this research all small-angle neutron scattering (SANS) experiments were performed at LOQ at the ISIS Pulsed Neutron and Muon source, Rutherford Appleton

Laboratories, Chiltern, England. The incident wavelength range of 2.2 - 10.0 Å at 25 Hz, gave rise to a *Q* range of 0.009-0.249 $Å^{-1}$. Measurements were made at 30°C. All samples were made up in either 100% or 70% of D_2O and run in 1 mm thick double stopper quartz Hellma cells. Each raw scattering data set was then corrected for the detector efficiencies, sample transmission and background scattering and converted to scattering cross-section data ($\partial\Sigma/\partial\Omega$ vs Q) using the instrument-specific software in Mantid, provided by ISIS [*18*].

2.1.3 Instrumentation and Principle of Small-Angle X-Ray Scattering (SAXS)

X-ray scattering (SAXS) is a well-established technique to study the nanoscale size and structure of ordered and disordered systems. More detail of the theory behind this technique can be found in several textbooks [*20-22*] but an overview is given here. X-rays are electromagnetic radiation with short wavelengths of about 0.01 to 10 nm. Usually 0.15 nm generated from a copper x-ray tube is a suitable wavelength to study nanostructures in soft matter. The X-ray radiation interacts with matter by scattering from distributions of electron density [*23*].

The use of X-ray scattering has been broadened in soft matter research due to high power advanced synchrotron X-ray sources. Enhancements of photon flux and collimation have made SAXS a very powerful scattering technique in terms of angular and time resolution, small sample volume, etc. For instance, very fast time-resolved experiments can be done even with dilute and low contrast samples. In addition, SAXS can be carried out alongside different thermophysical and rheological techniques [*24*].

The first generation of X-rays were established in the laboratory by using a filament tube. In 1913 Coolidge [*25*] used accelerated electrons released from a hot tungsten filament on a metal target in an evacuated tube to generate X-rays. Usually X-ray tubes are categorized into two types, sealed and rotating anode. Recently, synchrotron radiation sources have been used to generate a high intensity beam and high flux of X-rays.

In an X-ray sealed tube, the filament current heats the tungsten filament and emits electrons into the surrounding vacuum. The filament is sustained at a high negative voltage around 30 kV up to 50 kV, relative to the anode, toward which the electrons are excited and accelerated. The small metal cup surrounding the filament is at the same potential as the filament itself and assists to focus the electron beam to a small area (focal spot) on the surface of the target metal bonded to the anode. The excited electrons induce emission of x-rays, which then exit the tube through a small glass window. In a rotating anode X-ray tube, the power of the incident electron beam is extended over a circular ring. Thus it is possible to increase the power of the tube to about 100 kW without melting the anode metal. However rotating anodes are less robust than x-ray sealed tubes [*7, 25*].

In a synchrotron, a beam of electrons is accelerated to nearly the speed of light in a closed circular orbit in a storage ring under high vacuum. The closed orbit is made by bending the path with a series of bending magnets placed along the ring circumference. The boundary of the storage ring at Diamond is 560m while at the ESRF it is 844 metres, and the electron beams are accelerated typically to energy on the order of GeV. Electrons orbiting in a magnetic field lose energy continually in the form of electromagnetic radiation (photons) emitted tangentially from the orbit. This light is called synchrotron radiation. The radiation emitted by the orbiting electrons covers a broad range of the electromagnetic spectrum [*7, 26*].

The quality and resolution of X-ray data can be affected by several factors, for instance, the intensity of the x-ray radiation, sample thickness and category of detector resolution. A range of detectors are used in X-ray scattering instruments. In general CCD detectors have become popular in scattering instruments due to many advantages like robust remote operation, short read-out time, high spatial resolution, automatic internal compensation of non-uniform detector response and removal of cosmic-ray spikes [*7*].

Image plates are mainly used in laboratory x-ray instruments. The detection procedure is similar to photographic film or a medical x-ray image. Image plates can be read out after exposure to scattered x-rays from the sample. Time of exposure depends on sample concentration and thickness. These plates are sensitive to both mechanical damage and x-ray overexposure [*27*]. In general they have high spatial resolution and are robust but cannot be operated remotely. Commercially available plates are composed of extremely fine crystals of $BaFBrEu^{+2}$ where X-rays excite an electron of Eu^{+2} into the conduction

band, and then it is trapped in an F-centre of the barium halide with a subsequent oxidation of Eu^{+2} to Eu^{+3}. The image plate scanner needs to read 16-bit TIFF data image. The image plate can be erased by exposing them to light [*28-30*].

Gas-filled detectors are popular as X-ray detectors in synchrotron facilities since it has many advantages. This detector is based on the principle of a gas ionization chamber where the electronic noise can be discriminated. Typically, the detector consists of a drift chamber a few millimetres thick filled with a mixture of noble gas (Ar or Xe) and a polyatomic quenching gas. The anode is made up of a grid of fine wires (diameter 10–20 mm and spaced 1–2 mm apart) and the two-dimensional position sensitivity is obtained by two layers of cathode strips on either side of the anode perpendicular to each other (X and Y). Gas-filled detectors have many advantages, including constant dead time after each pulse, non-uniform detector response, capability to carry out energy discrimination of elastically scattered photons and a close relationship between a count in the electronics and an incident photon [*25, 31*]. However recently, hybrid pixel X-ray detectors such as PILATUS-100K (used in Diamond -I07) become very available detector due to fast readout time and the absence of readout noise. The operation technology of PILATUS based on single-photon-counting mode. The hybrid pixel detectors offer precise measurement of the diffraction pattern around the very intense direct beam with high spatial resolution [*32, 33*].

In a SAXS experiment a highly collimated and monochromatic X-ray beam of wave length (λ) impinges on a sample and the scattered intensity in the forward direction is recorded by a detector. The transmitted primary beam is fully absorbed by the beam stop placed in front of the detector and the entire flight path before and after the sample is in vacuum to avoid absorption and scattering by air.
The basic theory of scattering is similar for light, neutrons and X-rays. The important difference is in the interaction of the radiation with the scattering medium. The scattering of light originates from refractive index variations while neutrons are scattered by atomic nuclei. As a result, these scattering techniques are very complementary [*7*].

The number of photons scattered as a function of the scattering angle (θ) is measured. For a given sample, the amount of recorded photons varies with the number of incident

photons per second per unit area (photon flux) and the sample to detector distance (Figure 2.1.3). Therefore, the quantity that can be compared in different experiments is the number of photons scattered into unit solid angle normalized to the incident photon flux. For X-rays, the scattering originates from electrons, which is nearly independent of λ except in the close vicinity of the absorption edge of the constituent elements.

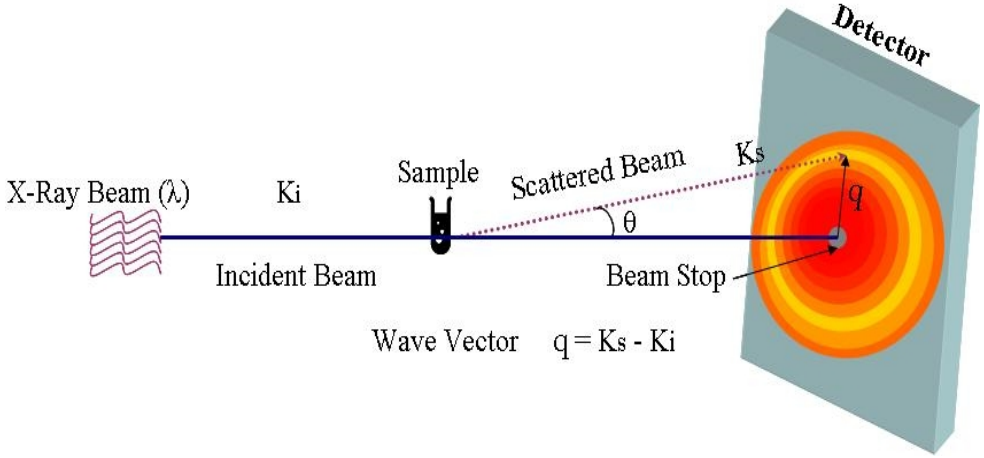

Figure 2.1.3 Schematic of X-ray scattering and the definition of the scattering vector (q)

The scattering at small-angles is fully elastic because of the high energy of the radiation as compared to typical excitations in the sample. In synchrotron SAXS, the *q* range covered can be three orders of magnitude, typically $0.006 < q < 6$ nm^{-1} corresponding to real space dimensions of 1 mm down to 1 nm [*7, 25*].

Two types of SAXS instruments were used in this study, an Anton Parr SAXSess instrument and the I22 beamline at the synchrotron x-ray facility, Diamond . The SAXSess Small-Angle X-Ray Scattering instrument from Anton Paar, located in the Chemistry Department at Bath University was used for low-flux X-ray scattering using a PANalytical PW3830 X-ray generator. Copper anode X-ray radiation (λ = 1.5406 Å) at 40 kV and 50mA were used to record x-ray scattering patterns in the region of 0.08–28nm^{-1} [*34*]. The flexibility of sample holder in the SAXSess allowed measurement of solid and liquid samples. Liquid solutions were measured by using a 1.0 mm quartz capillary sample holder and solid samples by using sellotape to hold powders, mounted in a sample holder. Backgrounds from solid or liquid sample holders were subtracted from sample measurements. The temperature of the sample holder was managed by using an electronic temperature controller and was usually set at 28°C to prevent

crystallization of the surfactant solutions. Imaging plates were used to record scattering patterns with a linear dynamic range of five orders of magnitude. A Perkin Elmer Cyclone Plus Storage Phosphor system was used to scan the imaging plates. Scanned images were processed by using mathematical programs supplied by Anton Paar to convert the image into a 1D scattering curve and to correct for the beam shape.

In the case of non-crystalline diffraction beamline I22 at Diamond, the accelerator storage ring, which is 561m in circumference, is the source of synchrotron X-rays. The beam energy used was 15 KeV and the fight path was 3.2m [*26*]. This high intensity of x-rays provides high flux, high resolution tuneable energy and minimum beam divergence. Liquid solutions were measured by using a 1.0 mm quartz capillary sample holder. A Gas detector containing multi-wire electrode grid in a gas chamber were used to record scattering patterns [*18*].

2.2 Form and Structure Factor

The interactions of particle in a dilute system containing a number of homogeneous particles per unit volume are very weak therefore the intensity *I(q)* for the most part depends only on the shape and size of the particles.

$$I(q) = N\left|F(q)\right|^2 \qquad (5)$$

where *F(q)* is the coherent sum of the scattering amplitudes of the individual scattering centres within the particle given by the Fourier transform of the distribution of those scattering centres in space. The scattering is described as coherent to indicate the relationship between the phase of different scattered waves and their accumulated amplitudes [*35*]. The scattering centres are characterised by the scattering length, b, of the atoms in the particle volume.

Typically in small-angle scattering, the scattering length density, ρ, is substituted instead of the scattering length, $\rho=b_M/V_M$, where b_M is the sum of b for all the atoms in a molecule and V_M is the corresponding molar volume. For neutrons b varies by isotope, while for X-rays $b = n_e \times = 2.81\times10^{-13}$ cm, where n_e is the number of electrons

in the atom. In scattering, the contrast or the relative scattering length density ($\Delta \rho = \rho - \rho_M$) is the parameter that specifies the difference between the scattering power of the particle and the medium in which it is contained, Therefore a consistent spherical particle of radius, R_S, and volume, V_S, gives a scattering amplitude of:

$$\left|F(q)\right|^2 = V_s^2 \Delta\rho^2 \left(\frac{3\left[\sin(qRs) - qRs\cos(qRs)\right]}{(qRs)^3}\right)^2 = V_s^2 \Delta\rho^2 P(q, Rs) \quad (7)$$

where V the volume of the particle, $N V_S$ is the volume fraction of the particles and the shape of the particle is described by the Bessel function (the equation inside the brackets) so that $P(q, R_S)$ is the square of the scattering form factor for a sphere. Pedersen listed comprehensive of $P(q, R)$ scattering functions for different particle shapes typically found in soft matter systems.

In this thesis the main models used to fit the small-angle scattering was uniform ellipsoid with the Hayter Penfold mean spherical approximation for charged spheres as the structure factor [*36*].Calculates the form factor for a monodisperse ellipsoid (ellipsoid of revolution) with uniform scattering length density. The form factor is normalized by the particle volume such that P(q) = scale*<f*f>/Vol + bkg, where f is the scattering amplitude and the < > denote an average over all possible orientations of the ellipsoid. The function calculated for the prolate ellipsoid is [*37*]

$$P(q) = \frac{scale}{v_{ell}}(p_{ell} - p_{solv})^2 \int_0^1 f^2 [qr_b(1 + x^2(v^2 - 1))^{1/2}]dx + bkg \quad (8)$$

$$f(z) = 3v_{ell}\frac{(\sin z - z\cos z)}{z^3} \quad (9)$$

$$v_{ell} = \frac{4\pi}{3} r_a r_b^2 \quad (10)$$

where $f(z)$ is the scattering amplitude and $z=qr_b[1+x^2(v^2-1]^{1/2}$, r_a is the short axis of the ellipsoid, r_b is the long axis, is the ratio of the short axis to the long axis, $x = R^2_g \ q^2$, and V_{ell} is the volume of the ellipsoid, where Rg is the radius of gyration of the scattering particle.

The structure factor S(q) mainly describes correlation between three components, surfactants hydrocarbon chain, surfactant headgroup and a counter ion. The Haytere Penfold structure factor model describes a correlation between charged micelles which can be calculated from the interparticle potential that determines the equilibrium arrangement of charged micelles. The interaction between identical charged spherical micelles of radius R_3 can be described by a screened coulomb interaction potential U(r) as follows [*36, 38, 39*] :

$$U(r) = \frac{Z_m^2}{4\pi\varepsilon_0\varepsilon(1+kR_3)} \exp[-k(r-2R_3)]/r \qquad (11)$$

where r is a centre-to-centre distance. z_m is the charge on the micelle, ε_0 is the permittivity of free space, ε is the dielectric constant of the solvent, and k is the Debye-Huckel inverse screening length. The structure factor of charged spherical micelles is calculated for a given micellar charge and ionic screening using the mean spherical approximation given by Haytere-Penfold when a volume fraction of scattering objects is sufficiently large [*40*].

At high particle concentrations the scattered rays from different particles will interfere. This interference term or the structure factor, S(q), is a complex function. It is an oscillatory function and it can be used to determine how closely the particles pack together. In a dilute system where there are no interacting particles, $S(q) \approx 1$. For particles with spherical symmetry and a narrow size distribution, I(q) is given as

$$\boldsymbol{I(q) = N V^2 \Delta_p^2 p(q) S(q)} \qquad (12)$$

Where *S(q)* is the scattered intensity from the microstructure described through the pair correlation function, g(r). The partial structure factors and scattering amplitudes depend on the orientation of the particles. In the case of size polydispersity for spherical particles with small anisotropies and low volume fractions, the interactions can be considered to be independent of the orientation which leads to an analogous decoupling approximation. Then the averaging is applied over the orientation distribution of anisotropic particles. For spherical particles, the effect is less pronounced in *S(q)* as compared to that in *P(q)* at low polydispersities [*41-43*].

2.3 Reflectivity

In recent years there has been growing interest in studying surfaces and interfaces with nanostructures. Neutron and x-ray reflection from surfaces provides an important means to investigate the nature of surfaces and interfaces, as these techniques offer the ability to see deep inside nanofilms and thin layers. Several books have covered the theory of reflectivity in detail [*6, 44, 45*] but a summary is given here to assist understanding of the work reported in this thesis.

The intensity of scattering in reflectivity, is similar to that in the in the method described above and follows the Porod law asymptotically as the scattering vector *q* is increased. The absolute value of the intensity is proportional to the total area of interfaces within the sample. In addition, study of any deviation of the observed intensity curve from the Porod law can evaluate the diffuseness of the interfaces. The method of reflectivity measurement can be evaluated as an extension of the Porod law method to surfaces that are fundamentally flat and interfaces that are close to exposed surfaces and parallel to them. Small-Angle scattering and reflectivity at small *q* are measured where the radiation hits the surface at a small glancing angle and is reflected (or scattered) from the surface [*6*].

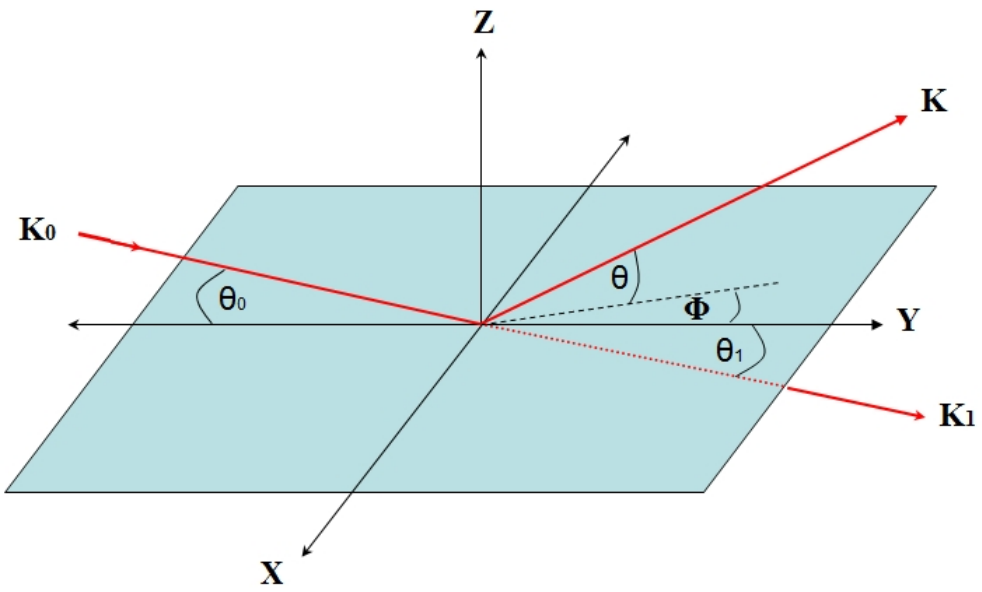

Figure 2.3.1 Schematic to explain the surface scattering; the wave vectors K_0, K, and K_1 indicate incident, reflected and refracted rays respectively.

The vector perpendicular to the surface is designated as the z axis; the incidence plane is defined as the plane including Z and K_0. In general K and K_1 are not in the plane of incidence. Thus the angle Φ between the Z axis and the projection of K on the XY plane

is not necessarily equal to zero. The detector is located to measure the reflected beam in the direction of K, where the scattering vector *q* is equal to K - K_0. In the plane (figure 2.3.1) where the angle of Φ equals zero and θ is equal to θ_0, the reflection referred to as the specular reflection. The wave vectors K_0 and K are then associated to each other since the reflected beam mirrors the incident beam of light.

When the surface is completely flat and there is no difference in the scattering length density in the X and Y directions in the layer of material below the surface, only specular reflection is observed. The ratio of the reflected beam energy to the incident beam energy (reflectivity R), is then measured as a function of the magnitude of q while its direction is maintained normal to the surface (ie q_z). Changes in q can be accomplished either by varying the angles θ_0 and θ (=θ_0) ie of incidence and reflection at the same time or by changing the wavelength λ while keeping the geometry of the scattering fixed. The result of measurement of R as a function of q_z is then analysed to find information about the variation in the scattering length density, *p*(z), in the material as a function of depth Z from the surface. In general most studies of X- ray and neutron reflectivity are focused on the measurement of such specular reflectivity [*6, 24*]. Specular reflectivity data of this type is normally analysed using a layer (or slab) model consisting of defined layers with different scattering length densities arranged parallel to the surface. However this type of scattering was not analysed in this thesis so no further detail is given here.

The off-specular or diffuse scattering occurs when the surface is not perfectly flat or when the material near the surface contains some inhomogeneities in scattering length density in the direction parallel to the surface. The scattering vector q in such a diffuse scattering measurement also contains a q_x or q_y component. The scattering is then analysed to get information about the surface topology or scattering length density inhomogeneities in the x or y direction [*6*].

Solutions of surfactants or polymer/surfactants systems demonstrate a range of one and two dimensionally ordered structures such as lamellar and hexagonal lyotropic phases. Reflectivity measurements can be used to characterize the structure and the degree of order in these complex systems near interfaces, by considering the position and intensities of diffraction peaks in R(q). From *R(q)* intensities and the position relationship of Bragg peaks it is possible to determine the crystallographic symmetries of these ordered system. The assignment of structures using Bragg peaks is discussed in more detail below in section 2.4.

2.3.1 Neutron Reflectivity Experimental Measurements

Neutron reflectivity measurements of the films grown at the air/water interface were performed on SURF and CRISP instruments (Target Station I) at the ISIS Pulsed Neutron Source facility within the Rutherford Appleton Laboratories. Both SURF and CRISP instruments have been established for the study of surfaces using specular neutron reflectivity. The neutrons wavelengths used were 0.55 - 6.8 Å in pulses at 50 Hz to give a q range of 0.048 - 1.1 $Å^{-1}$. A hydrogen moderator at 25 K is used to cool the neutrons in each pulse prior to travel down a flight path with a series of four slits, two before and two after the sample. An optical laser is used to aid alignment of the sample height that is controlled on a sample stage with 0.05 mm accuracy. The incident angles used for the reflectivity experiments described here was 1.5^{o} and 0.5^{o}. The detector is a He^{3} gas detector [*18*]. The solvent for all neutron reflectivity experiments was D_2O. The samples were poured in to sample holders (Teflon troughs) with dimensions of 152mm, 42mm, 3mm which hold 20 - 30ml of solution with a meniscus well above the side of the trough. These sample holders sit within the facilities own heat controlled sample holders allowing temperature control of the solution during each experiment. The temperature was maintained at 35^{o}C for the experiments described in this work, to ensure the surfactants remained in solution.

2.3.2 X-ray Reflectivity Experimental Measurements

X-ray reflectometry experiments were performed in the I07 beamline at the Diamond Light Source in Oxford UK, and on ID10B Troika II beamline at the European Synchrotron Radiation Facility in Grenoble, France. The solvent for all x-ray reflectivity experiments was H_2O. The films grown at the air/water interface were poured in to sample holders (Teflon troughs) with dimensions of 152mm, 42mm, 3mm and hold 20- 30ml of solution with a meniscus well above the side of the trough. All samples measurements were recorded at 35ºC.

The ID10B beamline is a high-brilliance undulator beamline at the ESRF designed for high resolution X-ray scattering and surface diffraction [*46*]. ID10B used photons with an energy range of 8 keV provided by a diamond double-crystal monochromator. Studies of film formation at the air-liquid interface were performed using time-resolved X-ray reflectometry as the flux of the synchrotron radiation was sufficient to allow short scans to be collected. Time-resolved experiments were able to cover a Q_z range of 0.085

– 0.25 A^{-1} by using a linear detector with a vertical orientation to collect data over a range of reflected angles [*46*]. X-ray reflectometry and grazing-incidence diffraction experiments were performed after film formation. X-ray reflectometry patterns were collected over a Q_z range of 0.0014 – 0.3535 A^{-1} and grazing-incidence diffraction patterns were collected over a Q_z range of 0.0014 – 0.89 A^{-1} and a Q_{xy} range of 0.0 – 0.2 A^{-1}. A linear detector with 1024 channels and with a vertical alignment was used to collect data during grazing-incidence diffraction experiments and was rotated incrementally in *XY* plane. Grazing incidence diffraction patterns were calibrated using the known straight through beam position, measured number of pixels per degree and the motor positions during the measurements.

Diamond Light Source beamline I07 is a high-resolution X-ray diffraction beamline for investigating the structure of surfaces and interfaces of the films grown at the air/water interface and on silicon wafers.

Grazing indicence diffraction patterns were collected with a Q_z range of 0.0 - 0.55 $Å^{-1}$ and Q_{xy} range of 0 - 0.25 $Å^{-1}$ at an incident angle of 0.25 º, using an energy of 12.5 or 12.2 keV. X-rays were detected using a two-dimensional pixel detector (Pilatus 2M, 195 X 487 pixels with a size of 172 X 172 μm each) [*26*]. Sample-to-detector distance was calculated using the image of silver behenate powders spread on a silicon wafer, taken in reflection mode. The peak positions were well described the expected diffraction pattern of the silver behenate lamellar structure.

2.4 Characterization of Crystalline & Liquid-Crystalline Structures

The science of crystallography is based on the diffraction of x-ray or neutron beams by a crystalline material. These analytical techniques can provide, with high certainty, the structure of a given compound in a crystalline state. The theory of crystallography can be found in many books, including [*47-51*], and only a brief description is given here. Diffraction can be explained using an analogy to light being refracted by microscope lenses, when a sample is examined under a microscope. Neutron or x-ray diffraction is concerned with the study of systems containing arrangements of atoms, molecules or particles in an ordered array, the composition of which can be found by interpretation of their diffraction pattern. This orderly arrangement in a crystalline material is known as

the crystal structure, with the term "unit cell" used to describe the smallest structure that repeats itself by translation through the crystal.

Therefore crystallography is concerned with describing and discovering the organized structures. Each crystalline material has a specific diffraction pattern. The number of observed peaks is related to the symmetry of the unit cell. The *d*-spacings of the observed peaks are related to the repeating distances between small repeating planes of atoms or molecules in the structure. The intensities of these peaks are related to the number of repeating units [*50*].

X-ray or neutron diffraction is affected by the conditions for constructive interference. Powder diffraction patterns are typically plotted as the intensity of the diffracted beam against the angle 2θ. Once constructive interference is at a maximum the peaks rise in the diffraction pattern at 2θ values. Vectors and atomic planes in a crystal lattice can be described by a three-value Miller index notation (*h k l*):

$$\underline{\boldsymbol{r}}_{hkl} = h\underline{\boldsymbol{a}}^* + k\underline{\boldsymbol{b}}^* + l\underline{\boldsymbol{c}}^* \qquad (13)$$

The integers *h, k* and *l* are the Millar indices of the crystal plane under consideration and $\underline{a}^*$, $\underline{b}^*$ and $\underline{c}^*$ are the vectors defining the reciprocal lattice, i.e. $\underline{a}^* = \underline{a}^{-1}$ $\underline{b}^* = \underline{b}^{-1}$ and $\underline{c}^* = \underline{c}^{-1}$. Here $\underline{a}$, $\underline{b}$ and $\underline{c}$ are the lattice vectors of the crystal.

At $I(\underline{q}) = (F_{hkl})^2$ peaks can only occur for $\underline{\boldsymbol{q}} = \underline{\boldsymbol{r}}_{hkl}$. According to the Bragg's law the diffraction angle 2θ the interplanar distance *d* and wavelength λ are linked with each other by:

$$\lambda = 2\,d\sin\theta \qquad (14)$$

Where *d* is the distance between two parallel units and θ is half of the incidence angle of the plane of the X-ray beam with wavelength λ. Calculation of *d*-spacing for each diffraction peak can be achieved by measuring the 2θ values for each diffraction peak. The peak positions can be used to find the *lattice parameters* for a given unit cell. Unit cells in three-dimensional repeating structures have different shapes based upon the symmetry of the structure [*52*]. The different shapes arise depending on restrictions placed on the lengths of the three edges (*a*, *b*, and *c*) and the values of the three angles α, β, and γ as shown in figure 2.4.1.The seven possible unit cell shapes, also known as crystal systems are identified by their unit cell parameters. The unit cell shapes range

from a cubic cell, with the highest possible symmetry, to a triclinic unit cell, with the lowest possible symmetry.

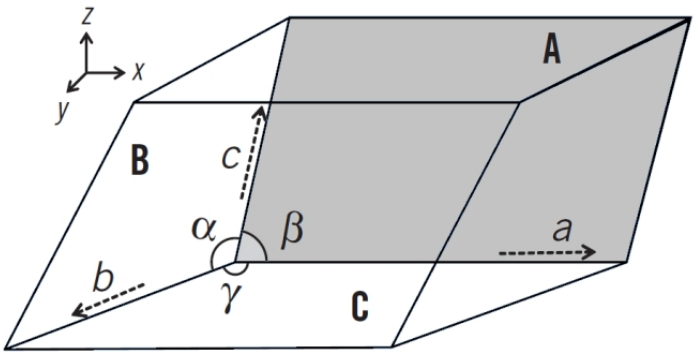

Figure 2.4.1: The unit cell parameters

Each peak in a diffraction pattern arises from a distinctive set of repeating planes in the structure. These sets of planes are oriented in all different directions in three-dimensional space where the diffraction peaks rises from a specific set, the planes must be oriented relative to the incident x-ray beam. Therefore, X-ray powder diffraction relies on a large number of crystallites in random orientations in order to detect the most diffraction peaks. Sometimes diffraction from a particular set of planes may not be detected or the peak intensity could be low due to the crystalline symmetry. Since Miller indices relate the peak positions or *d*-spacings to the lattice parameters, refining the lattice parameters of the unit cell from diffraction data requires to assign the Miller indices (*h k l*) for each diffraction peak [*53*]. This process is known as indexing or assignment of the diffraction pattern. For well-known sample, the assignment process is done by comparing the data to that reported in the literature or in a database of diffraction patterns known as the JCPDS [*54*]. Otherwise, the peak indexes are used to calculate the relationship between peaks, to determine the symmetry of the unit cell. For instance the relationship of peak spacings in a monoclinic unit cell structure with lattice parameters a, b and c is expressed in equation (15)

$$\frac{1}{d_{hkl}^2} = \frac{h^2}{a^2 \sin^2\beta} + \frac{k^2}{b^2} + \frac{l^2}{c^2 \sin^2\beta} - \frac{2h\cos\beta}{ac\sin^2\beta} \qquad (15)$$

where *hkl* are the Miller indices categorizing the repeating planes causing the diffraction peak with spacing d_{hkl}. All of monoclinic unit cell axes are dissimilar lengths with only

the angles of α and γ equal to 90° ($a \neq b \neq c$, where α =γ = 90°; β≠ 90°). The primitive (P) and the single-face-centred (C) type of Bravais lattice can be found for this unit cell type. Both the body-centred (I) and the face-centred (F) Bravais lattice types can also occur in the monoclinic crystal system; however, as they can also be represented as C-type Bravais lattices, they are usually not considered separately. In the case of orthogonal unit cells, all the axes are dissimilar, while all angles are 90° so it is analogous to a rectangular box. The types of Bravais lattice that arise for the orthogonal cell are the primitive-type lattice (P), the body-centred lattice (I), and the face-centred lattice (F), with points on all faces and centred on a single face, the A, B, or C faces ($a \neq b \neq c$ while α =β = γ = 90°). The unit cell relationship for an orthogonal structure is expressed in equation (16)

$$\frac{1}{d_{hkl}^2} = \frac{h^2}{a^2} + \frac{k^2}{b^2} + \frac{l^2}{c^2} \qquad (16)$$

In the case of a cubic unit cell, all axes are of equal length and all angles are 90°. The cubic shape with no other lattice points is the primitive lattice type (P). It is also possible within this unit cell type to identify other lattice types: the body-centred lattice (I); and the face-centred lattice (F; with points on all faces). These give rise to the different Bravais lattices for the cubic unit cell ($a = b = c$, while α =β = γ = 90°). Therefore the unit cell relationship for a cubic unit cell simplifies to equation (17)

$$\frac{1}{d_{hkl}^2} = \frac{h^2 + k^2 + l^2}{a^2} \qquad (17)$$

In crystal systems with angles not equal to 90˚, the equation includes terms involving the angles as well. Thus just one peak position in a cubic system can be used to determine the lattice parameter provided the Miller indices can be assigned. However to obtain accurate lattice parameter, the entire peak positions that can be indexed are used to refine the lattice parameters using a number of data points and regression analysis. Hexagonal unit cells, occur where both top and bottom faces are hexagonal with the *a* and *b* axes of equal lengths and linked by a *c*-axis of a different length. The primitive-type (P) of Bravais lattice is found in the hexagonal unit cell. The angles α and β are 90°, while the angles on the hexagonal face are 120° ($a = b \neq c$, and α =β = 90°; γ = 120°). The relationship between peaks and the structure of the hexagonal unit cell can be expressed as:

$$\frac{1}{d_{hkl}^2} = \frac{4}{3}\frac{h^2 + k^2 + hk}{a^2} + \frac{l^2}{c^2} \qquad (18)$$

In a tetragonal unit cell, only the *a* and *b* axes are of equal length, with all angles at 90°. The only two types of Bravais lattice that occur for this cell type are the primitive-type lattice (P), and the body centred lattice (I) ($a = b \neq c$, while $\alpha = \beta = \gamma = 90°$). The tetragonal unit cell equation relating diffraction peaks with different h,k,l values can be written as:

$$\frac{1}{d_{hkl}^2} = \frac{h^2 + k^2}{a^2} + \frac{l^2}{c^2} \qquad (19)$$

The trigonal unit cell is close to the hexagonal unit cell; the axes *a* and *b* are of equal lengths and linked by the *c* axis of a different length. The angles where the faces meet, *a* and *b* are 90°, while the γ angle on the trigonal face is 120°. Only the primitive-type (P) of Bravais lattice is found in the trigonal unit cell ($a = b \neq c$, while $\alpha = \beta = 90°$; $\gamma \neq 120°$). The relationship between diffraction peaks in a trigonal unit cell is expressed in equation (20)

$$\frac{1}{d_{hkl}^2} = \frac{(h^2 + k^2 + l^2)\sin^2\alpha + 2(hk + kl + hl)(\cos^2\alpha - \cos\alpha)}{a^2(1 - 3\cos^2\alpha + 2\cos^3\alpha)} \qquad (20)$$

The triclinic unit cell has the least symmetry compared with the other crystal systems. The axes are all different and no angle is equivalent to 90° [*49, 50, 54*].

The main objective of x-ray and neutron diffraction pattern indexing process is the geometrical rebuilding of the three dimensional reciprocal space from the one-dimensional distribution of the observed *d* values. The term of indexing corresponds to the fact that the unit cell determination step is related to assigning the appropriate triple of Miller indices to each observed inter-planar distance [*55*]. The first practical indexing was proposed by Runge [*56*]. For accurate assignment of mesostructures using X-ray or neutron diffraction patterns, a minimum of four peaks are required to state with any confidence the symmetry aspect. Table 2.4.1 illustrates some of well-known lyotropic mesophases and their ratio of spacing between Bragg diffraction features for particular lattices [*57*].

Table 2.4.1: The most recognized lyotropic mesophases and their ratio of spacing between lattices Bragg diffraction features.

Categories	Mesophases	Symmetry (dimensionality)	The most intense reflections peak ratios
Smectic	Lamellar	Smectic (1D)	1:2:3:4. . ., etc.
Mesh	Rhombohedral	(1D)	1:2:3:4. . ., etc.
		R$\bar{3}$*m* (3D)	(003), (101), (012). . . (006)
	Tetragonal	(1D)	1:2:3:4. . ., etc.
		I422 (3D)	(002), (101), (110) . .(103), . . (004)
Sponge	Bicontinuous cubics	*Im*$\bar{3}$*m* (3D)	√2:√4:√6:√8:√10…etc.
		Pn$\bar{3}$*m* (3D)	√2:√3:√4:√6:√8…etc.
		Ia$\bar{3}$*d* (3D)	√6:√8:√14:√16:√18:√20…etc.
Columnar	Hexagonal	*p6m* (2D)	√1:√3:√4:√7:√12…etc.
	Ribbon	cmm (2D)	(11):(20):(22):(31):(40):. . .etc.
Micellar	Discrete cubic	bcc packing *Im*$\bar{3}$*m* (3D)	√2:√4:√6:√8:√10..…etc.
		fcc packing *Fm*$\bar{3}$*m* (3D)	√3:√4:√8:√11:√12..…etc.
		Pm$\bar{3}$*n* (3D)	√2:√4:√5:√6:√8..…etc.
		Fd$\bar{3}$*m* (3D)	√3:√8:√11:√12:√16..…etc.

2.5 Grazing-Incidence X-ray Diffraction (GIXD)

Grazing incidence diffraction is a scattering geometry combining the conditions for x-ray total external reflection from crystal surfaces with the Bragg condition. The GIXD provides better characteristic information for studies of thin surface layers as compared to the other diffraction techniques, since GIXD provides morphological information from the Angstrom length scale to micrometres scales. The detailed theory of GIXD can be found in references [*58-61*] and a simplified description is given here to correspond with the measurements made in this work. Grazing incidence x-ray diffraction is non-destructive and can be applied in various types of environment from ultra-high vacuum to gas atmospheres, on both solid and liquid interfaces. It is also applicable during chemical reactions, in situ and in quasi real time when reactions are involved such as

growth of films or during a polymerization reaction. In addition GIXD offer the ability to investigate from surface to buried interfaces as well as the bulk of the sample by varying the depth of x-ray incident angle [*58*].

The principle of X-ray scattering from nanostructures is similar to regular X-ray diffraction, however a synchrotron X-ray radiation source is very necessary because the investigated volume of matter is small and the incident X-ray wave-vector K_i is kept at a grazing angle with respect to the sample surface to minimize the unwanted background scattering such as elastic and inelastic waves emanating from the bulk, and to improve the near surface scattering [*62*]. Figure 2.5.1 illustrates the diagram of grazing incident scattering geometry measurements, in which the incident angle θ_i is generally small and stays constant, mainly close to the angle of total external reflection θ_f.

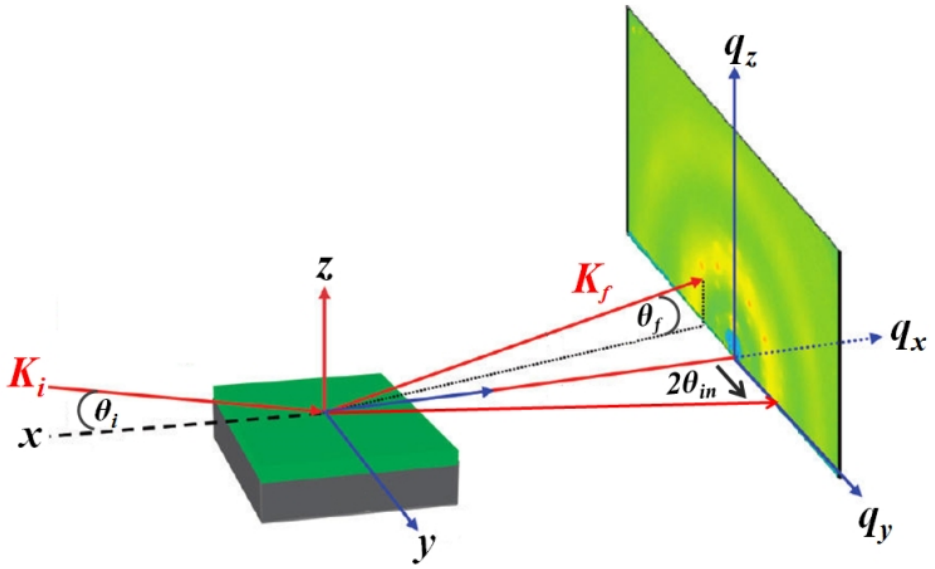

Figure 1.17.: Schematic of grazing incidence diffraction where θ_i incident angle of grazing beam (K_i) and θ_f the angle of scattered beam (K_f). The $2\theta_{in}$ is corresponds to the in-plane diffracted angle.

The scattered beam, of wave vector K_f , makes the scattering angle 2θ with the incident wave vector. It is detected at a direction defined by slits, and makes an angle θ_f with the sample surface and in-plane, the angle 2θ is related to the transmitted beam. The wave-vector transfer is defined as $q = K_f - K_i$. The absolute value of q is a function of θ_i and θ_f, where $|q| = q_z = K_0 [\sin(\theta_f) + \sin(\theta_i)]$ where $K_0 = |K_f| = |K_i| = 2\pi/\lambda$ is the elastically conserved wave vector modulus [*60, 62*]. The λ is the X-ray wavelength. In GIXD, the angular coordinates are correlated to the wave-vector transfer coordinates according to:

$$q_x = K_0[\cos(2\theta)\cos(\theta_f) - \cos(\theta_i)] \quad (21)$$

$$q_y = K_0[\sin(2\theta)\cos(\theta_f)] \quad (22)$$

$$q_z = K_0[\sin(\theta_f) + \sin(\theta_f)] \quad (23)$$

$$k_0 = 2\pi/\lambda. \quad (24)$$

When all angles are small, the wave-vector transfer is also small, typically between 0 and $1nm^{-1}$, and therefore big dimensions are explored in real space. The analogous technique to grazing incidence diffraction [*58, 60, 62, 63*] is X-ray reflectivity (XRR), in the specular geometry, used to characterize the density profile perpendicular to the surface. The off-specular geometry is used to characterize the large lateral electron density correlations along q_x, while grazing incidence small-angle scattering is used to characterize the morphology parallel with the surface along q_y and perpendicular to it along q_z, at intermediate length scales typically between a few nm and a few hundreds of nm.

GIXD patterns taken during this work were analysed in ImageJ and Igor Pro to visualise diffraction rings and spots. Data for ordered mesostructured samples were then analysed using the assignment of these peaks to crystalline unit cells as described above in section 2.4.

2.6 Gel permeation Chromatography

Size exclusion chromatography (SEC) is the one of well-known techniques for the determination of average polymers molar mass and molecular weight distributions. The gel permeation chromatography (GPC) more specifically refers to a separation column filled with cross-linked polymer that is swollen by the employed solvent [*64*]. This stationary phase is the most common type in GPC; however other substrates, such as glass beads, are also used. Typically each analysis column contains only a small range of pore size, such that it separates over a limited range of molecular size. A sequence of columns in series is required for separation over a wide range of molecular size, generally from 2 to 4 columns are used. At the start of a run a small amount of polymer solution is injected into the start of the column, where the sample solution is introduced into a sample loop, by a syringe. The flow by-passes the loop, but by operation of a sample injection valve the sample stream can be diverted into the sample loop, pushing

the polymer solution into the sample column set as seen in figure 2.6.1. The reference column set consists of a series of columns similar to those of the sample set. Ideally solvent should take the same time to reach the detector via the reference column set as via the sample set. The separation process depends on the preferential penetration of smaller molecules into the pores of the column packing material, so that larger particles or molecules elute first followed by smaller species [*65*].

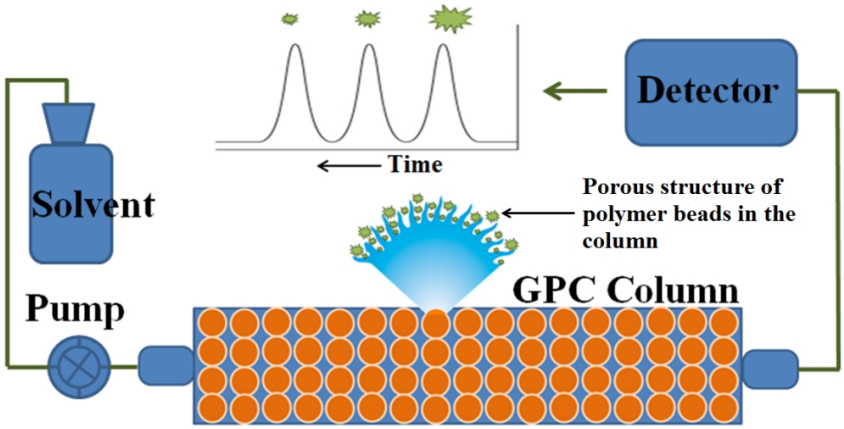

Figure 2.6.1: A simple schematic of gel permeation chromatography.

This may be due to either the inability of large molecules to enter certain regions of the gel due to their size or the larger diffusion coefficients of smaller molecules. To provide quantitative results, the relation between molecular weight and volume of solvent that has passed through the detector since sample injection (also known as the elution volume) must be established by calibration with monodisperse polymer standards Calibration is necessary in order that the elution volume of chromatograms can be related to polymer molecular weight. It is performed most simply by using very narrow distribution fractions of the same polymer as that under investigation. In this case, the peak elution volume of the narrow chromatogram is assumed to correspond to the known polymer molecular weight. Although separation in GPC is ruled by the size of solute molecules in solution, solutes of similar hydrodynamic volume but different molecular weight will elute at the same retention volume. The detector is placed at the outlet of the column. The common detectors used in GPC are differential refractometers, which measure the difference in refractive index between pure solvent and the polymer solution leaving the column, and ultraviolet or infrared detectors, which can be used if the polymer contains some group that absorbs the radiation [*66*] eg styrene.

2.6.1 Experimental Measurement

In this study, polystyrene was first extracted from the polyethylenimine-surfactant matrix where it was polymerised. The extracted polystyrene samples were dissolved in tetrahydrofuran (THF) to a concentration of 0.25-0.30 g/L. The resulting solution was then analysed in a GPC to obtain the average molecular weight as well as the molecular weight distribution. The measurement was performed on a PL-GPC 50 Plus, Integrated GPC System from Polymer Laboratories (A Varian Inc. Company) equipped with a detection system consisting of a refractive index (RI) [*67*]. The system was equipped with PL-gel-5micro mixed-C (300×7.5mm) columns. The mobile phase was THF and the sample was injected via a PL-AS RT GPC Autosampler at a flow rate of 0.1 mL/min. The sample was analysed using software Cirrus GPC version 3.2. The PL-GPC 50 Plus was calibrated with 12 polystyrene standards with M_{ns} ranging from 1060 - 2650000.

2.7 Cyclic Voltammetry (CV)

Cyclic voltammetry (CV) is the most valuable electroanalytical technique for the study of electroactive species [*68, 69*]. It is a widely used technique for obtaining qualitative information about electrochemical reactions; also it is a very sensitive and accurate method for quantitative detection of species such as inorganic complexes, organic molecules and metal ions. Cyclic voltammetry is the first experiment performed in an electrochemical study of a material or an electrode surface [*68, 69*]. Cyclic voltammetry typically uses the principle of potential sweep. The current is recorded while the electrode potential is changed linearly with time between two values. The initial potential ($E_{initial}$) is generally the point where there is no electrochemical activity and the final potential (E_{final}) is the point where the reaction is mass transport controlled. The scan stops at E_{final}, since at this point the sweep direction is reversed, the potential reaches E_{final} and the potential is reverted to $E_{initial}$ (Figure 2.7.1).

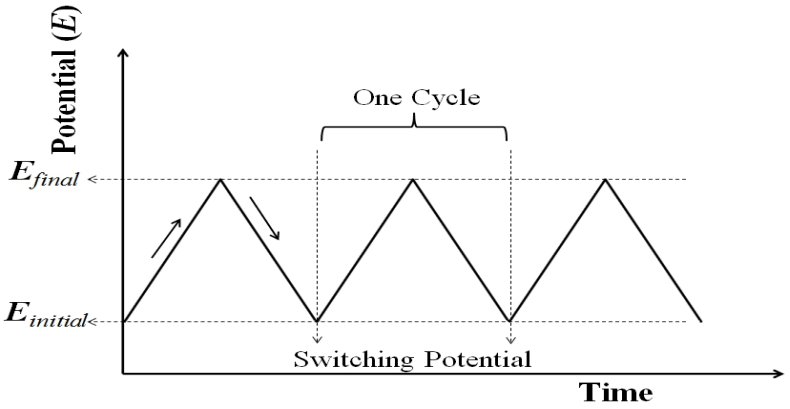

Figure 2.7.1: Schematic of waveforms used in linear sweep cyclic voltammetric experiment.

Usually multiple cycles are recorded for kinetic studies such as molecular diffusion into the films. The starting and reversal potential points define the driving force for electron transfer and the oxidation state of the species involved. In addition by choosing the suitable potentials can determine whether a species is formed or consumed, and whether the reaction is under kinetic or mass transport control. The potential scan rate sets the timescale of the experiment and can determine whether intermediates are formed or consumed. Figure 2.7.2 demonstrates the cyclic voltammogram which is the name of the current/potential plot. The cyclic voltammogram is a time-dependent function of a large number of physical and chemical parameters. As the potential is scanned in the negative direction the current increases to a peak and then reduces in a regular manner. The current depends on two steps in the overall process, the movement of electroactive material to the surface and the electron transfer reaction. The electron transfer rate constant for a reduction process is a function of potential [*69, 70*].

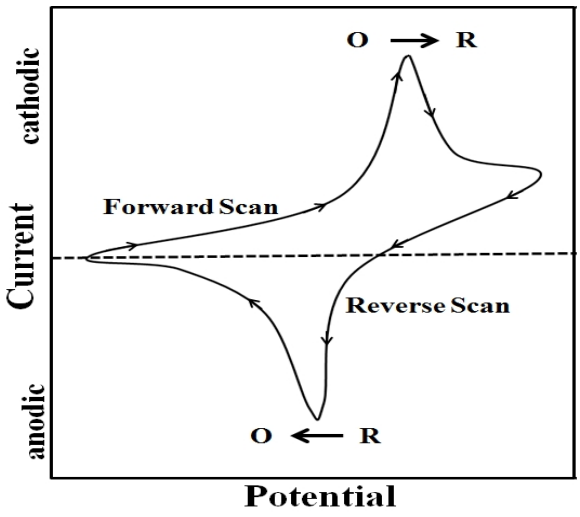

Figure 2.7.2 Typical cyclic voltammogram for a reversible redox process.

2.7.1 Experimental Measurement

The three-electrode cell used in the CV experiments in this thesis consists of a working electrode prepared from tin-doped indium oxide (ITO) coated glass slides. The spontaneously self-assembled film formed from BDHAB/SPEI solubilising 2.0mM and 4.0mM of PAN/Pyrene cross-linked by EGDGE was deposited on a 1cm x 1cm ITO glass slide. A platinum (Pt) wire was used as counter electrode while a silver/silver chloride (Ag/AgCl, 3 M KCl) was used as reference electrode. Two metals ions (Fe^{+3} and Cu^{+2}) as chloride salts dissolved at 10 ppm final concentration were investigated. The metals salts were dissolved in 10mM H_2SO_4 as the electrolyte solution. The electrochemical measurements were implemented by an electrochemical analyser microAutolab II potentiostat system (EcoChemie, Netherlands) with GPES software [*71*]. All scans were conducted at room temperature. The potential was scanned between −0.95 and 0.95 V with a potential scan rate of 30 mV s^{-1} for 9 scan cycles or between −0.12 and 1.25 V with a potential scan rate of 30 mV s^{-1} for 10 scan cycles.

2.8 Electron microscopy

Electron microscopy is used in either a reflection or transmission approach. A typical scanning electron microscope (SEM) relies on the reflected electrons that are used to build up a three-dimensional image of the sample surface giving information on the sample surface features, texture and topography. This style of electron microscopy can covers the magnification range between the lower resolution limit of optical microscopy (~1μm) and the upper practical limit around 5nm of transmission electron microscopy (TEM). The main important difference between these two techniques of instrument is that an image from a scanning electron beam instrument is built up by scanning a focused, highly convergent electron probe over an area of the sample and measuring a signal generated from the interaction of the electron beam with the specimen. In the case of transmission electron microscope a parallel beam of electrons used enlightening an area of the sample and forming an image using several electrons which penetrate through the specimen [*72*].

The scanning electron microscopy techniques mainly using a focused electron beam incident on a sample. The size of the electron probe depends on the electron source configuration and the magnitude of current in the electron probe. This electron probe is hit across an area on a sample and reflected signals from the sample surface can be measured. Interactions between the sample and the electron probe generate many types of signal including secondary electrons, backscattered electrons and characteristic x-rays. The most important signals are those genarated by secondary electrons (SE) with most probable exit energies of 2–5 eV and by backscattered electrons (BSE) with energies that range from the energy of the primary electrons to about 50 eV. The secondary electron produced and the backscattering coefficient depend on the angle of electron incidence (topographic contrast), the mean atomic number (material contrast), the crystal orientation (channeling contrast), and electrostatic and magnetic fields near the surface (potential and magnetic contrast). The resolution for BSEs and x-ray images is dependent on the size of the electron interaction volume, which is a function of the accelerating voltage, and the average atomic number and density of the sample. For SE imaging, resolution is usually dependent on the size of the electron probe and the inherent contrast of the sample. For SEM techniques, samples fits into the instrument stage at high-vacuum system and electrically conductive, where samples that are not electrically conductive can be coated with a thin electrically conductive layer such as evaporated amorphous carbon or have a metal such as gold, platinum, palladium, or chromium sputtered onto the surface. The samples for transmission electron microscopy are necessary to be thin enough that electrons with energies of 100 keV or higher can pass through the sample to provide a magnified image of the sample or an electron diffraction pattern [*72-74*].

The TEM is capable of giving information on an atomic scale, by direct lattice imaging. The high resolution TEM instrument can give information on the crystallographic arrangement of atoms in the specimen and their degree of order; detection of atomic-scale defects in areas a few nanometers in diameter, and can be used to index crystalline materials. In principle, the resolution in the TEM is given by the capability to accelerate electrons, so the higher voltage used to accelerate electrons, the better resolving power of the TEM [*72, 74*], although also the greater the likely damage to the specimen being studied. Electrons emitted from electron gun (filament) are accelerated through high voltage. Their wavelength is related to the accelerating voltage, V by the equation:

$$\lambda = h(2meV)^{-1/2} \qquad (25)$$

where e is the charge and m is the mass of the electron. In the case of TEM the condenser lens is used to control the size and the angular spread of the electron beam that is incident on the sample. The electrons are emitted by a cathode filament. The electrons are then attracted towards the anode, which causes their acceleration. The electron beam is focused by two successive condenser lenses into a beam with a spot size around 5 nm. The beam passes through an objective lens and strikes the surface of the sample as shown in figure 2.8.1. The practical resolving limit is governed by the imperfection of the lenses and for a current microscope is in the range 1 -2 Å. Typically electromagnetic lenses are used in electron microscopy to focus the electron beam. The contrast in electron microscopy is based on the relative difference in the observed intensities between areas filled with atoms with different scattering behaviour. Heavy elements have high electron density so scatter electrons strongly and so appear darker in the TEM bright-field image, the image taken when the directly transmitted electron beam is recorded.

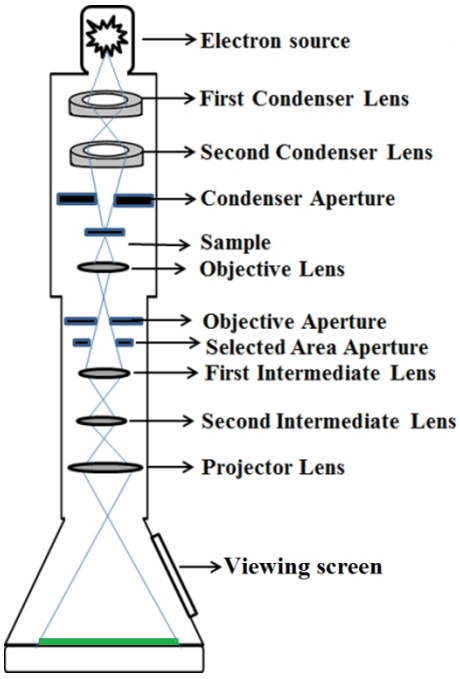

Figure 2.8.1 Schematic image of the components of a transmission electron microscope.

TEM can also provide diffraction data with very high spatial resolution for individual crystals when the diffracted rather than transmitted beam is selected to be recorded. The electron wavelengths are much smaller than the X-ray wavelengths used in typical

diffraction experiments, as a result the diffracted beams are concentrated into a narrow cone cantered on the non-diffracted beam. The area of illumination that is chosen for diffraction can be selected by appropriate lenses giving rise to the selected-area diffraction that is very important for polycrystalline materials [*73*].

2.8.1 Experimental Measurements

The scanning electron microscopy images of recovered templated polystyrene structures were taken at the Centre for Electron Optical Studies at the University of Bath using a Japanese Electron Optics Laboratory JEOL JSM6480LV scanning electron microscope [*75*]. SEM images were collected with an operating voltage of 20 kV and to prevent charging of the samples they were sputter coated with gold prior to imaging in the SEM. The transmission electron microscopy images were taken in two places: first at the Centre for Electron Optical Studies at the University of Bath. Images were collected using a Japanese Electron Optics Laboratory JEOL 1200 EX transmission electron microscope operated at 120 kV. Instrument settings and images were established using the fluorescent screen of the TEM instrument before final collection using a CCD camera. Samples were prepared for TEM study by dispersing the purified polystyrene powder in deionised water by agitating the test tube for one minute. A clean pipette was then used to place a drop of this dispersion onto a copper EM grid with a holey carbon film, and excess solution was blotted with a filter paper, leaving thus a thin sample film spanning the holes in the carbon film.

The second location where TEM images were taken was in the Physical Chemistry Division in the Department of Chemistry, Lund University, Sweden. These micrographs were recorded using a JEOL 3000F (300 kV) microscope. The film samples were frozen under liquid nitrogen to make them brittle, and were crushed in a cold mortar into fragments. The fragments were deposited from the liquid nitrogen onto a copper EM grid with a holey carbon film. The grid was placed into the microscope at room temperature on a stage which was then cooled using liquid nitrogen for 2 hrs before measurement, as well as during imaging.

2.9 Other Techniques

2.9.1 Determination of Critical Micelle Concentration by Conductivity

The charged surfactant such as quaternary ammonium cations behaves as an electrolyte and therefore follows Ohm's Law. This means that when a voltage (V) is applied across a cell containing the cationic surfactant solution the current (I) that flows is proportional to V. Ohm's Law can be written in two equivalent ways : $V = IR$ or $I = VG$, where R is the resistance and G (=1/R) the conductance of the solution. The conductance of the solution mainly depends on the cell dimensions and the nature of the solution. The conductance of a solution contained in a cell of length l and area A is expressed as:

$$G = (A/l) * \kappa \quad (26)$$

where κ is the conductivity of the solution and is independent of the shape of the cell. Conductivity has the units Ω^{-1} m^{-1} or S m^{-1} where S is the SI unit of conductance (Siemens) [*76*]· For a solution of concentration c mol m^{-3} the molar conductivity, Λ with units S m^2 mol^{-1} can be written as: $\Lambda = \kappa c$. Molar conductivity is a very suitable way of measuring conductivity due to highlights the properties of the electrolyte. Overall the molar conductivity decreases with increasing concentration due to the influence of concentration on interactions between electrolyte ions or on an ionic dissociation process. The molar conductivity of an electrolyte depends on the extent to which the electrolyte dissociates into ions. Strong electrolytes such as sodium chloride are almost completely ionised, whilst weak electrolytes are ionised to only a small extent. Therefore conductivity is a convenient instrument to detect the cmc point of ionic surfactants. That is due to below the cmc, the addition of surfactant to an aqueous solution causes an increase in the number of charge and thus increase in the conductivity, while above the cmc, and further addition of surfactant increases the micelle concentration while the monomer concentration remains almost constant. Since a micelle is much larger than surfactant monomer it diffuses more slowly through solution and so is a less efficient charge carrier. A plot of conductivity against surfactant concentration is, thus expected to show a variation at the cmc point. Therefore electrical conductivity was used here in this report to measure the cmc of the surfactants using plots of electrical conductivity versus surfactant concentration [*77*].

A Mettler-Toledo model FE30 conductivity meter was used to measure the conductivity of the surfactant solutions. All experimental measurements were performed at 25°C. The LE703 conductivity electrode used in this study was calibrated using potassium chloride aqueous solution. The zero point of the conductivity measurement was taken at 50.0 ml of ultra-pure Milli-Q water. The solution was stirred with a magnetic stirrer and a Metrohm autotitrator model number dosimat-665 used to control surfactant concentration added into blank water. The conductivity reading was taken after each dispense point and stirring for 30 seconds. In the case of L-PEI/surfactant cmc measurements, the surfactants solutions and blank start point were taken in a 1% (w/v) solution of L-PEI without surfactant.

2.9.2 UV-Vis and Fluorescence spectroscopy

UV/Vis spectra for molecules result when a molecule or ion absorbs ultraviolet or visible radiation it undergoes a change in its valence electron configuration. The valence electrons in organic molecules and inorganic anions occupy sigma bonding, σ, pi bonding, p, and nonbonding, *n,* molecular orbitals. Unoccupied sigma antibonding, σ*, and pi antibonding, π*, molecular orbitals often lie close enough in energy that the transition of an electron from an occupied to an unoccupied orbital is possible.

According to Beer's Law absorbance and concentration of affect the absorptivity [*76, 78*] of a solution and the concentration of solute can expressed as:

$$A = abc \qquad (26)$$

where *a* is the analyte's absorptivity with units of cm^{-1} $conc^{-1}$, b is the absorptivity and C is a concentration of solute. When the concentration is expressed using molarity, the absorptivity is replaced by the molar absorptivity, ε (with units of cm^{-1} M^{-1})

$$A = \varepsilon bc \qquad (27)$$

The absorptivity and molar absorptivity give, in effect, the probability that the analyte will absorb a photon of given energy. As a result, values for both *a* and ε depend on the wavelength of the electromagnetic radiation used.

In this work the UV/Vis experiment was carried out using a Hewlett Packard HP spectrometer with linear diode array. Scan measurements were recorded between 200-800 nm^{-1} with the addition of different concentrations of organic and metal ions compounds.

Fluorescence spectrometry is based on the absorption of radiation of a certain frequency, causing the energy transition from the outermost electronic orbitals to a higher energy state and the subsequent deactivation of the excited atoms with the release of radiation [*78*]. In this work fluorescence spectroscopy was used to study surfactant/PEI/PAN/Pyrene system as metal ion sensor.

Fluorescence spectroscopy was performed on a Perkin Elmer LS 50B Spectrometer. The excitation wavelength was used was 300nm and the spectrum was recorded between 350nm and 660nm. Different concentrations of Cu^{+2} as copper chloride ($CuCl_2$) was added gradually to a solution consisting of BDHAB, SPEI, PAN, pyrene and EGDGE at concentrations of 10.0, 1.2, 0.6 and 2.0 mM respectively. The emission wavelength was 337nm ±2nm, where the spectra and the intensity at the maxima (372nm) were recorded.

2.9.3 Gas Chromatography (GC)

GC is used in the separation of sufficiently volatile organic compounds in mixed samples. Current instruments provide several inlet options that can be selected according to the particular sample and matrix. In order to reach maximum sensitivity, either splitless injection or on-column injection is used [*78*]. Here, gas chromatography was used to study the loss of solubilised styrene monomer in surfactant/polymer solutions during thermal and photopolymerization, where the loss of styrene monomer is related to styrene conversion to polystyrene. An Agilent 6890N Network Gas Chromatography System with an Agilent 19091J-413 HP-5 5% Phenyl Methyl Siloxane 300m x 320µm x 0.25µm column was used.

2.10 Chemicals and Materials

1-Bromododecane, 1-Bromotetradecane, 1-Bromohexadecane, Triethylamine 99%, Pyridine, ACHN [1,1′Azobis(cyclohexanecarbonitrile)], Ethylene glycol diglycidyl ether (EGDGE), 1-(2-Pyridylazo)-2-naphthol, Methyl Methacrylate, Tripropylamine, Polyethylenimine (750,000 Mw) - 50 % (w/v) in H_2O, Polyethylenimine (2,000 Mw) - 50 % (w/v) in H_2O, Barium chloride dehydrate, Iron (II) chloride 99% tetrahydrate, Iron (III) chloride hexahydrate 97%, Lithium chloride, Magnesium chloride, Copper (II) chloride, Copper(I) chloride, Cesium chloride 99%, Zinc Chloride and Deuterium oxide were purchased from Sigma-Aldrich. Hexadecyltrimethylammonium bromide, N,N-Dimethylbenzylamine and Styrene 99% were purchased from Acros Organics. n-Dodecyltriphenylphosphonium bromide, Tetradecyltriphenylphosphonium bromide and Hexadecyltriphenylphosphonium bromide were purchased from Alfa Aesar. Silver nitrate was purchased from FLUKA. Cobalt (II) nitrate hexahydrate was purchased from RIEDEL-DE HAEN. Cadmium chloride was purchased from BDH.

Cetyltrimethylammonium bromide - d_{33} (98% D) and Cetyltrimethylammonium bromide - d_{42} were obtained from the Oxford Isotope Laboratory. Styrene-d_8, Pyrene-d_{10} and Methyl Methacrylate-d_8 were purchased from CDN Isotopes. 1-Hexadecylpyridinium Bromide was purchased from Lancaster. Ultra-pure Milli-Q water (18.2MΩ cm resistance) was used for all H_2O solution preparations.

All purchased chemicals were used without further purification except where noted below. Dodecyltriethylammonium bromide, Tetradecyltriethylammonium bromide, Hexadecyltriethylammonium bromide, Dodecyltripropylammonium bromide, Tetradecyltripropylammonium bromide, Hexadecyltripropylammonium bromide, Benzyldimethyldodecylammonium bromide, Benzyldimethyltetradecylammonium bromide, Benzyldimethylhexadecylammonium bromide, 1-Dodecylpyridinium Bromide and 1-Tetradecylpyridinium Bromide were synthesised in our lab using the procedures described below.

2.11 Synthesis of Quaternary Ammonium Bromide Surfactants

Quaternary ammonium salts are the most common cationic surfactants. Basically they formed when a nitrogen atom is attached with four covalent bonds with at least one of these bonds to a long alkyl chain (figure 2.11.1). Mainly alkyl chain lengths in the region of C_{12}, C_{14} and C_{16} carbon atoms are used as surfactants with longer chain lengths are increasingly insoluble. In this study 1-bromododecane, 1-bromotetradecane and 1-bromohexadecane were used as a source to synthesise surfactants with C_{12}, C_{14} and C_{16} alkyl chains respectively.

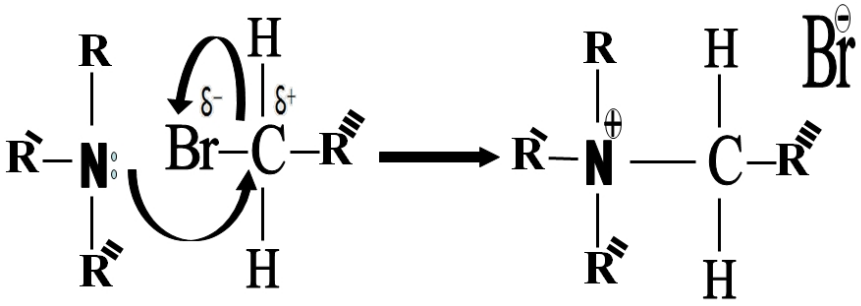

Figure 2.11.1 Nucleophilic substitution of quaternary ammonium salts.

Triethylamine, tripropylamine, pyridine and N,N-dimethylbenzylamine were used to vary the surfactant head groups, see figure 2.11.2. The alkylbromide and trialkylamine were mixed in a one to one mole ratio with excess 10% of trialkylamine to make sure that all of the alkyl chain has been reacted with trialkylamine. 30 ml of absolute ethanol was added to the mixture and heated while being stirred for 12h under reflux conditions at temperature between 100°C and 110°C depending on the chain length and bulkiness of the head group. Ethanol solvent was then evaporated using a rotary evaporator. The remaining mixture was left to cool down at room temperature. Synthesized surfactants were purified from the excess of trialkylamine by a recrystallization process. A minimum amount of chloroform was added to dissolve the mixture. Ethyl acetate was added slowly to this solution while the mixture was stirred until the start of precipitation. To enhance precipitation amount the mixture was cooled in a refrigerator. The resultant precipitate was filtered, washed twice with ethyl acetate, and dried under vacuum at room temperature [*79*]. The same procedure was used to synthesise all of the deuterated surfactants used in this work (Table 2.11.3).

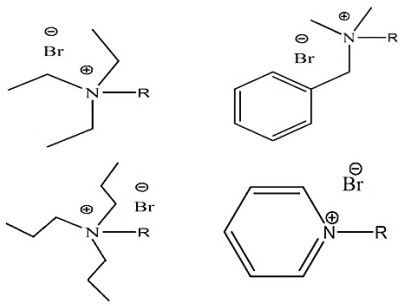

Figure 2.11.2: shows chemical structure of alkyltriethylammonium bromide, alkyltripropylammonium bromide, alkylpyridinium bromide and benzyldimethylalkylammonium bromide respectively where R is a C_{12}, C_{14} or C_{16} hydrocarbon chain.

Table 2.11.1: Abbreviations, molecular formula and SLDs of all surfactants used in this research.

Surfactant Name	***Abbrev.***	**Molecular Formula**	***M. Wt***	**SLDs ($Å^{-2}$)**
Cetyltrimethylammonium bromide	CTAB	$C_{19}H_{42}$ N Br	284.55	-3.40×10^{-7}
Dodecyltriethylammonium bromide	DTEAB	$C_{18}H_{40}$ N Br	350.425	-3.39×10^{-7}
Tetradecyltriethylammonium bromide	TTEAB	$C_{20}H_{44}$ N Br	378.478	-3.35×10^{-7}
Hexadecyltriethylammonium bromide	HTEAB	$C_{22}H_{48}$ N Br	406.532	-3.31×10^{-7}
Dodecyltripropylammonium bromide	DTPAB	$C_{21}H_{46}$ N Br	392.505	-3.35×10^{-7}
Tetradecyltripropylammonium bromide	TTPAB	$C_{23}H_{50}$ N Br	420.559	-3.32×10^{-7}
Hexadecyltripropylammonium bromide	HTPAB	$C_{25}H_{54}$ N Br	448.612	-3.30×10^{-7}
Benzyldimethyldodecylammonium bromide	BDDAB	$C_{21}H_{38}$ N Br	384.442	1.11×10^{-7}
Benzyldimethyltetradecylammonium bromide	BDTAB	$C_{23}H_{42}$ N Br	412.495	7.71×10^{-8}
Benzyldimethylhexadecylammonium bromide	BDHAB	$C_{25}H_{46}$ N Br	440.549	4.82×10^{-8}
n-Dodecylpyridinium bromide	DPBr	$C_{17}H_{30}$ N Br	328.335	2.12×10^{-7}
n-Tetradecylpyridinium bromide	TPBr	$C_{19}H_{34}$ N Br	356.388	1.60×10^{-7}
n-Hexadecylpyridinium bromide	CPBr	$C_{21}H_{38}$ N Br	384.442	1.18×10^{-7}
Dodecyltriphenylphosphonium bromide	DTPhPB	$C_{30}H_{40}$ P Br	511.524	7.08×10^{-7}
Tetradecyltriphenylphosphonium bromide	TTPhPB	$C_{32}H_{44}$ P Br	539.577	6.49×10^{-7}
Hexadecyltriphenylphosphonium bromide	HTPhPB	$C_{34}H_{48}$ P Br	567.631	5.96×10^{-7}

The SLDs values of surfactant are calculated without counterions (Br).

Table 2.11.2: Abbreviations, molecular formula and SLDs of additives, surfactant hydrocarbon chains and polymers were used in this research.

Additives and polymers	***Abbrev.***	**Molecular Formula**	**M. Wt**	**SLDs ($Å^{-2}$)**
Styrene	Styrene	C_8H_8	104.152	$1.22x10^{-6}$
Pyrene	Pyrene	$C_{16}H_{10}$	202.256	$2.61x10^{-6}$
Hexadecane	Hexadecane	$C_{16}H_{33}$	225.44	$-3.53 x10^{-7}$
Tetradecane	Tetradecane	$C_{14}H_{29}$	197.38	$-3.59 x10^{-7}$
Dodecane	Dodecane	$C_{12}H_{25}$	169.33	$-3.67 x10^{-7}$
1-(2-Pyridylazo)-2-naphthol	PAN	$C_{15}H_{11}N_3O$	249.273	$4.24 x10^{-7}$
Low *Mw* of Polyethyleneimine	SPEI	C_2H_5N	~2000	$5.98 x10^{-7}$
High *Mw* of Polyethyleneimine	LPEI	C_2H_5N	~750 000	$5.92 x10^{-7}$

Table 2.11.2: Molecular formula and SLDs of deuterated compounds and solutions were used in this research.

Deuterated compound	**Molecular Formula**	***M. Wt***	**SLDs ($Å^{-2}$)**
CTAB Tail Deuterated	$C_{19}H_9D_{33}$ N Br	397.658	$4.57x10^{-6}$
CTAB Fully Deuterated	$C_{19}D_{42}$ N Br	406.715	$5.74x10^{-6}$
CPBr Head Deuterated	$C_{21}H_{33}D_5$ N Br	389.472	$9.53x10^{-7}$
CPBr Tail Deuterated	C_{21} H_5D_{33} N Br	417.649	$5.65x10^{-6}$
CPBr Fully Deuterated	C_{21} D_{38} N Br	422.680	$6.50x10^{-6}$
BDHAB Tail Deuterated	$D_{33}C_{25}$ H_{13} N Br	473.756	$4.73x10^{-6}$
D_{33}-Hexadecane	$C_{16}D_{33}$	258.643	$6.74x10^{-6}$
D_{29}-Tetradecane	$C_{14}D_{29}$	226.565	$6.66x10^{-6}$
D_{25}-Dodecane	$C_{12}D_{25}$	194.4863	$6.60x10^{-6}$
Styrene-d_8	C_8D_8	112.202	$5.20x10^{-6}$
Pyrene-d_{10}	$C_{16}D_{10}$	212.319	$6.23x10^{-6}$
100% D_2O	D_2O	20.027	$6.36x10^{-6}$
70% D_2O Solutions	$H_3D_7O_5$	97.119	$4.29x10^{-6}$
1.5% S-PEI in 100% D_2O	$C_6H_{21}N_3O_{197}D_{338}$	4068.603	$6.08x10^{-6}$
1.5% L-PEI in 100% D_2O	$C_6H_{21}N_3O_{197}D_{388}$	4068.603	$6.09x10^{-6}$
1.5% PEI in 100%D_2O	$C_{30}H_{75}N_{15}O_{985}D_{1970}$	20373.206	$6.18x10^{-6}$
1.5% PEI in 70%D_2O	$C_{30}H_{665}N_{15}O_{985}D_{1380}$	19779.489	$4.16x10^{-6}$

The SLDs values of surfactant are calculated without counterions (Br).

2.12 References

1. Tsakiroglou, C. D., Ioannidis, M. A., Amirtharaj, E., and Vizika, O. (2009) A new approach for the characterization of the pore structure of dual porosity rocks, *Chem. Eng. Sci. 64*, 847-859.
2. Rizzuti, A., Leonelli, C., Corradi, A., Caponetti, E., Martino, D. C., Nasillo, G., and Saladino, M. L. (2009) Structural Characterization of Zirconia Nanoparticles Prepared by Microwave-Hydrothermal Synthesis, *Journal of Dispersion Science and Technology 30*, 1511-1516.
3. Valentine, K. G., Peterson, R. W., Saad, J. S., Summers, M. F., Xu, X., Ames, J. B., and Wand, A. J. Reverse Micelle Encapsulation of Membrane-Anchored Proteins for Solution NMR Studies, *Structure 18*, 9-16.
4. Broniatowski, M., Dynarowicz-Latka, P., Camacho, L., Martin Romero, M. T., and Muñoz, E. Semifluorinated thiols in Langmuir monolayers, *J. Colloid Interface Sci.*
5. Walker, L. M. (2009) Scattering from polymer-like micelles, *Current Opinion in Colloid & Interface Science 14*, 451-454.
6. Daillant, J., and Gibaud, A. (2008) X-Ray and Neutron Reflectivity Principles and Applications, Springer, New York.
7. Glatter, O., and Kratky, O. (1982) *Small angle x-ray scattering*, Academic Press, London; New York.
8. International Atomic Energy, A. (2006) *Small angle neutron scattering : report of a coordinated research project, 2000-2003*, International Atomic Energy Agency, Vienna.
9. Warner, M., Lovesey, S. W., Smith, J., Science, and Engineering Research Council. Rutherford Appleton, L. (1982) *The theory of neutron scattering from mixed harmonic solids*, Science and Engineering Research Council Rutherford Appleton Laboratory, Chilton.
10. Guinier, A., and Dexter, D. L. (1963) *X-ray studies of materials*, Interscience Publishers, New York.
11. Guinier, A., and Lonsdale, K. (1952) *X-ray Crystallographic Technology (Oversat fra Fransk)*, Hilger and Watts.
12. Grillo, I. (2009) Applications of stopped-flow in SAXS and SANS, *Current Opinion in Colloid & Interface Science 14*, 402-408.
13. Ross Hallett, F., and John, L. (1999) Scattering and Particle Sizing Applications, In *Encyclopedia of Spectroscopy and Spectrometry*, pp 2488-2494, Academic Press, Oxford.
14. Hannon, A. C., and John, L. (1999) Neutron Diffraction, Instrumentation, In *Encyclopedia of Spectroscopy and Spectrometry*, pp 1766-1778, Academic Press, Oxford.
15. Hannon, A. C., and John, L. (1999) Neutron Diffraction, Theory, In *Encyclopedia of Spectroscopy and Spectrometry*, pp 1779-1789, Academic Press, Oxford.
16. Yang, B., Edler, K., Guo, C., and Liu, H. (2010) Assembly of nonionic-anionic co-surfactants to template mesoporous silica vesicles with hierarchical structures, *Microporous Mesoporous Mater. 131*, 21-27.
17. Rogers, S. E., Terry, A. E., Lawrence, M. J., Eastoe, J., Cabral, J. T., and Chan, A. Soft matter at ISIS, *Materials Today 12*, 92-99.

18. http://www.isis.stfc.ac.uk/index.html. (Feb 2010), ISIS Science and Technology Facilities Council Rutherford Appleton Laboratory Harwell Science and Innovation Campus Didcot, OX11 0QX, UK.
19. Borsali, R., and Pecora, R. (2008) *Soft matter characterization*, Springer, New York; [London].
20. Glatter, O. K. O. (1982) *Small angle x-ray scattering*, Academic Press, London; New York.
21. Svergun, D. I. K. M. H. J. T. P. A. M. R. P. (2013) *Small angle X-ray and neutron scattering from solutions of biological macromolecules*.
22. Guinier, A. F. G. (1955) *Small-angle scattering of X-rays*, Wiley, New York.
23. Stribeck, N., and SpringerLink. (2007) X-ray scattering of soft matter, Springer, Berlin; New York.
24. Daillant, J., and Gibaud, A. (1999) *X-ray and neutron reflectivity : principles and applications*, Springer, New York.
25. Tsuji, K., Injuk, J., and Grieken, R. v. (2004) *X-ray spectrometry : recent technological advances*, Wiley, Chichester, West Sussex, England; Hoboken, NJ, USA.
26. http://www.diamond.ac.uk/. (Feb 2010), Diamond Light Source Ltd Diamond House Harwell Science and Innovation Campus Didcot Oxfordshire OX11 0DE UK.
27. Pflugrath, J. W. (1992) Developments in X-ray detectors, *Current Opinion in Structural Biology 2*, 811-815.
28. Li, H. H., Gonzalez, A. L., Ji, H. Y., and Duggan, D. M. (2007) Dose response of BaFBrI : Eu2+ storage phosphor plates exposed to megavoltage photon beams, *Medical Physics 34*, 103-111.
29. Stachs, O., Gerber, T., and Petkov, V. (2000) An image plate chamber for x-ray diffraction experiments in Debye-Scherrer geometry, *Review of Scientific Instruments 71*, 4007-4009.
30. Thoms, M. (1997) The dynamic range of X-ray imaging with image plates, *Nuclear Instruments & Methods in Physics Research Section a-Accelerators Spectrometers Detectors and Associated Equipment 389*, 437-440.
31. Koch, A., Moy, J. P., and Morse, J. (1993) Detectors for Synchrotron X-Ray Topography, *Journal of Physics D-Applied Physics 26*, A19-A21.
32. Mueller, M., Wang, M., and Schulze-Briese, C. (2012) Optimal fine [varphi]-slicing for single-photon-counting pixel detectors, *Acta Crystallographica Section D 68*, 42-56.
33. Wright, G. S. A., Lee, H. C., Schulze-Briese, C., Grossmann, J. G., Strange, R. W., and Hasnain, S. S. (2013) The application of hybrid pixel detectors for in-house SAXS instrumentation with a view to combined chromatographic operation, *Journal of Synchrotron Radiation 20*, 383-385.
34. http://www.anton-paar.com/. (Feb 2010), Anton Paar Ltd. 13 Harforde Court John Tate Road SG13 7NW Hertford United Kingdom.
35. Pedersen, J. S. (1997) Analysis of small-angle scattering data from colloids and polymer solutions: modeling and least-squares fitting, *Advances in Colloid and Interface Science 70*, 171-210.
36. Hayter, J. B., and Penfold, J. (1981) An analytic structure factor for macroion solutions, *Mol. Phys. 42*, 109-118.
37. Kline, S. R. (2006) Reduction and analysis of SANS and USANS data using IGOR Pro, *Journal of Applied Crystallography 39*, 895-900.

38. Hayter, J. B., and Penfold, J. (1981) Self-consistent structural and dynamic study of concentrated micelle solutions, *Journal of the Chemical Society, Faraday Transactions 1: Physical Chemistry in Condensed Phases 77*, 1851-1863.
39. Hiemenz, P. C. R. R. (1997) Principles of colloid and surface chemistry, Marcel Dekker, New York.
40. Hansen, J. P., and Hayter, J. B. (1982) A rescaled MSA structure factor for dilute charged colloidal dispersions, *Mol. Phys. 46*, 651-656.
41. Hsiao, B. S., Lohse, D. J., American Chemical Society. Division of Polymeric Materials, S., Engineering, and American Chemical Society, M. (2000) Scattering from polymers : characterization by X-rays, neutrons, and light, American Chemical Society ; Distributed by Oxford University Press, Washington, DC; [New York].
42. Lindner, P., and Zemb, T. (2002) *Neutrons, X-rays, and light : scattering methods applied to soft condensed matter*, Elsevier, Amsterdam; Boston.
43. Roe, R. J. (2000) *Methods of X-ray and neutron scattering in polymer science*, Oxford University Press, New York.
44. Penfold, J. (1991) Instrumentation for neutron reflectivity, *Physica B (Amsterdam) 173*, 1-10.
45. Grundy, M. J., Richardson, R. M., Roser, S. J., Penfold, J., and Ward, R. C. (1988) X-ray and neutron reflectivity from spread monolayers, *Thin Solid Films 159*, 43-52.
46. http://www.esrf.eu/. (Feb 2010), ESRF 6 RUE JULES HOROWITZ BP 220 38043 GRENOBLE CEDEX 9 FRANCE.
47. Bragg, L. (1968) X-ray crystallography, *Scientific American 219*, 58-70.
48. Hahn, T., Shmueli, U., Wilson, A. J. C., and International Union of, C. (1984) *International tables for crystallography*, D. Reidel Pub. Co. ; Sold and distributed in the U.S.A. and Canada by Kluwer Academic Publishers Group, Dordrecht, Holland; Boston, U.S.A.; Hingham, MA.
49. Guinier, A., Magn, A., and Gunnar, H. (1986) *Advances in powder diffraction crystallography*, Univ. Press, Cambridge.
50. Hammond, C. (2001) *The basics of crystallography and diffraction*, Oxford University Press, Oxford; New York.
51. Hahn, T. (2007) International tables for crystallography A, Space Group Symmetry / Hrsg. Theo Hahn, Springer Netherland, Berlin.
52. Zvelindovsky, A. V. (2007) Nanostructured soft matter experiments, theory, simulation and perspectives, Springer ; In Association with Canopus Pub., Dordrecht, the Netherlands; Bristol, UK.
53. De Graef, M., and McHenry, M. E. (2007) *Structure of materials : an introduction to crystallography, diffraction and symmetry*, Cambridge University Press, Cambridge.
54. Pecharsky, V. K. Z. P. Y. (2005) Fundamentals of powder diffraction and structural characterization of materials, Springer, New York.
55. Ashcroft, N. W. M. N. D. (1976) *Solid state physics*, Holt, Rinehart and Winston, New York.
56. Vand, V., and Johnson, C. G. J. (1968) Indexing of X-ray powder patterns. The theory of the triclinic case, *Acta Crystallographica Section A 24*, 543-546.
57. http://it.iucr.org/. (2013) International Tables for Crystallography.
58. Stoev, K. N., and Sakurai, K. (1999) Review on grazing incidence X-ray spectrometry and reflectometry, *Spectrochimica acta, Part B: Atomic spectroscopy 54*, 41-82.

59. Ree, M., Yoon, J., Heo, K., Jin, K. S., Jin, S., Lee, B., Park, I., Choi, S. C., Kim, G., Kim, H., Oh, W., Park, Y. H., Hwang, Y., Kim, J. S., Kim, J., Kim, K. W., and Chang, T. (2007) Synchrotron grazing incidence X-ray scattering and reflectivity analysis of nano-structures and patterns supported with substrates, pp 1-4.
60. Renaud, G., Lazzari, R., and Leroy, F. (2009) Probing surface and interface morphology with Grazing Incidence Small Angle X-Ray Scattering, *Surface Science Reports 64*, 255-380.
61. Müller-Buschbaum, P. (2013) Grazing incidence small-angle neutron scattering: Challenges and possibilities, *Polym J 45*, 34-42.
62. Birkholz, M., Fewster, P. F., and Genzel, C. (2006) *Thin film analysis by X-ray scattering*, Wiley-VCH ; John Wiley, distributor], Weinheim; Chichester.
63. Daillant, J., and Gibaud, A. (1999) X-Ray and neutron reflectivity: Principles and applications, *Lecture Notes in Physics 58*.
64. Williams, T. (1970) Gel permeation chromatography: A review, *J Mater Sci 5*, 811-820.
65. Striegel, A. M. (2009) *Modern size-exclusion liquid chromatography*, Wiley, Hoboken, N.J.
66. Parvez, H. K. Y. P. S. (1985) *Gel permeation and ion-exchange chromatography of proteins and peptides*, VNU Science Press, Utrecht, the Netherlands.
67. http://www.varian.com/. (2013).
68. Nicholson, R. S. (1965) Theory and application of cyclic voltammetry for measurement of electrode reaction kinetics, *Analytical Chemistry 37*, 1351-1355.
69. Zoski, C. G. (2007) Handbook of electrochemistry, Elsevier, Amsterdam; Boston.
70. Harnisch, F., and Freguia, S. (2012) A basic tutorial on cyclic voltammetry for the investigation of electroactive microbial biofilms, *Chemistry - An Asian Journal 7*, 466-475.
71. http://www.ecochemie.nl/. (2013).
72. Goodhew, P. J. H. F. J. (1988) *Electron microscopy and analysis*, Taylor & Francis, London; New York.
73. Reimer, L. K. H. (2008) Transmission electron microscopy physics of image formation, Springer, New York, NY.
74. Kopp, F., J., H. J., and Diana, K. (1981) *Electron microscopy*, Scientific Publications Division, Carolina Biological Supply Co., Burlington, N.C.
75. http://www.jeol.co.jp/en/. (2013).
76. Bockris, J., Amulya, K., and Maria, E. (1998) *Modern electrochemistry*, Plenum Press, New York.
77. Kabir-ud-Din, Koya, P. A., and Khan, Z. A. (2010) Conductometric studies of micellization of gemini surfactant pentamethylene-1,5-bis(tetradecyldimethylammonium bromide) in water and water-organic solvent mixed media, *J. Colloid Interface Sci. 342*, 340-347.
78. Dean, J. A. (1995) *Analytical chemistry handbook*, McGraw-Hill, New York.
79. Texter, J. (2001) *Reactions and synthesis in surfactant systems*, Marcel Dekker, New York.

3 Micellization Behaviour of Cationic Surfactants in Presence and Absence of Polyelectrolyte

3.1 Introduction

The spontaneous aggregation of surfactant molecules by arranging themselves into organized molecular assemblies at a critical concentration point in a liquid phase system, is called micellization and is one of the most important behaviours of surfactants. Three stages can describe the micellization progression. In the first stage, when the surfactant concentration is low, there are only a few surfactant molecules in the liquid phase and they are far apart from each other. The second stage is when surfactant molecules are starting to aggregate with each other forming micelles, this point is called the critical micelle concentration (cmc). The third stage is above the cmc, where the liquid phase is saturated with micelles and addition of more surfactant molecules in the system increases the micelle numbers with constant free surfactant molecules concentration [*1*].

Conductivity measurements of surfactant concentration can show these phases very clearly, particularly for ionic surfactants. The conductivity measurement of the critical micellar concentration of surfactants has been extensively used to study the free energy of micellization and degree of ionization of the surfactants. SANS experiments has been also used to study the size and aggregation number of cationic surfactants with and without polyelectrolyte. In this study a wide range of cationic surfactants with varied head groups and hydrocarbon chain lengths were used to understand the aqueous micellization behaviours of these cationic surfactants and in addition to study the effects of the bulkiness of the head group and length of hydrocarbon chain in micellization in the presence and absence of a polyelectrolyte, polyethylenimine.

3.2 Methods and Materials

Dodecyltriethylammonium bromide (DTEAB), tetradecyltriethylammonium bromide (TTEAB), hexadecyltriethylammonium bromide (HTEAB), dodecyltripropylammonium bromide (DTPAB), tetradecyltripropylammonium bromide (TTPAB), hexadecyltripropylammonium bromide (HTPAB), benzyldimethyldodecylammonium bromide (BDMDAB), benzyldimethyltetradecylammonium bromide (BTMDAB), benzyldimethylhexadecylammonium bromide (BDMHAB), 1-Dodecylpyridinium

bromide (DPBr) and 1-yetradecylpyridinium bromide (DPBr) were synthesised as part of this thesis as described in chapter 2. Hexadecylpyridinium bromide (CPBr), dodecyltriphenylphosphonium bromide (DTPhPB), tetradecyltriphenylphosphonium bromide (TTPhPB) and hexadecyltriphenylphosphonium bromide (HTPhPB) were purchased. These surfactants were used to prepare solutions in ultra-pure Milli-Q water (18.2MΩ cm resistance) which were used to measure the cmcs for these surfactants as described in Chapter 2. The cmcs were measured with and without polyethylenimine with Mol Wt ~750 000 (LPEI) and ~2 000 (SPEI).

3.3 Results and Discussion

3.3.1 Characterization of synthesized surfactants

Mass spectroscopy, TLC and ^{1}H-NMR were used to confirm the chemical structure and purity of synthesised surfactants. Typical results are shown below. For example figure 3.3.1 shows the positive ionisation mode mass spectroscopy results for dodecyltripropylammonium bromide (DTPAB) where the high intensity peak at 312.36 occurs at the molecular mass of DTPAB. Figure 3.3.2 shows the ^{1}H-NMR of tetradecyltriethylammonium bromide (TTEAB) where at δ = 1.65 ppm the signal indicates the (CH_2) that confirms the joining of the head group and alkyl chain. In general the signal of the alkyl chain (CH_2) at δ = 1.19 ppm increases when the alkyl chain length increases.

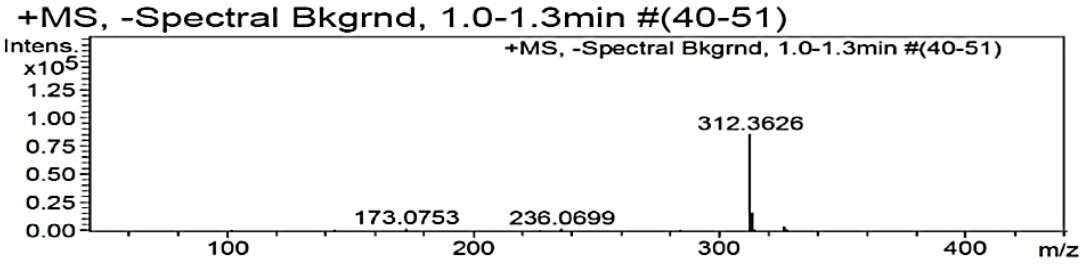

#	m/z	I	I %	Area	S/N
1	144.1750	1167	1.4	26	789.7
2	173.0753	2587	3.0	22	1914.5
3	226.9495	338	0.4	8	183.5
4	236.0699	1863	2.2	35	918.1
5	284.3304	385	0.5	17	175.6
6	312.3626	85303	100.0	4124	10246.1
7	313.3659	16082	18.9	791	1877.3
8	314.3700	1484	1.7	76	168.5
9	326.3784	4141	4.9	216	354.2
10	327.3822	1081	1.3	49	90.5

Figure 3.3.1: Mass spectroscopy analysis of the synthesized dodecyltripropylammonium bromide surfactant where the signal at 312.36 shows the molecular mass of DTPAB after subtraction of the bromide atom.

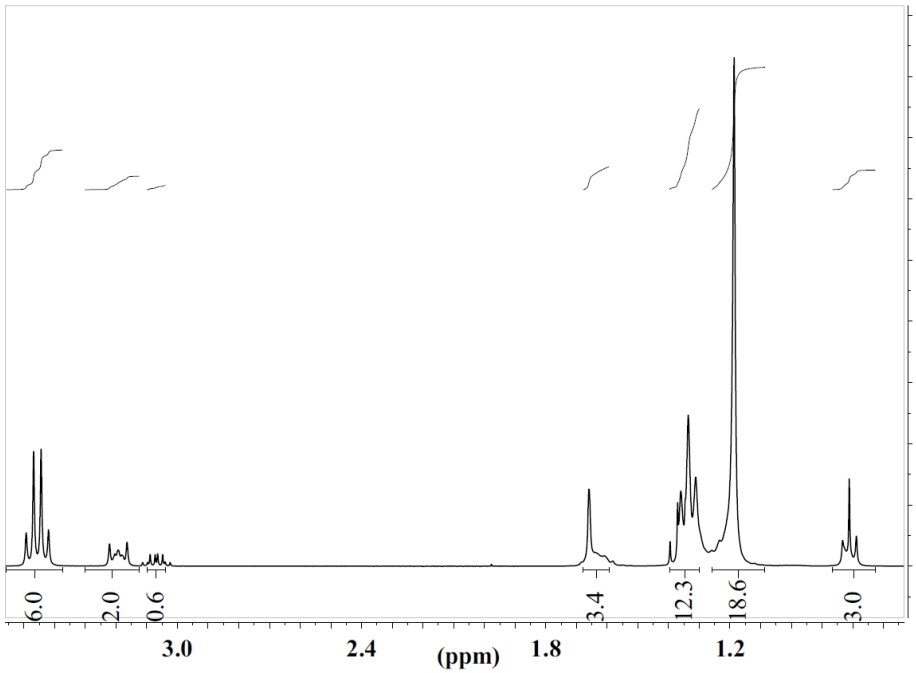

Figure 3.3.2 ^{1}H-NMR of tetradecyltriethylammonium bromide (TTEAB), showing a signal at δ = 1.65 ppm belonging to (CH_2) which gives proof of the head group and alkyl chain interaction.

3.3.2 The Critical Micelle Concentration (cmc) Behaviour of Cationic Surfactants in Presence and Absences of Polyethyleneimine (PEI).

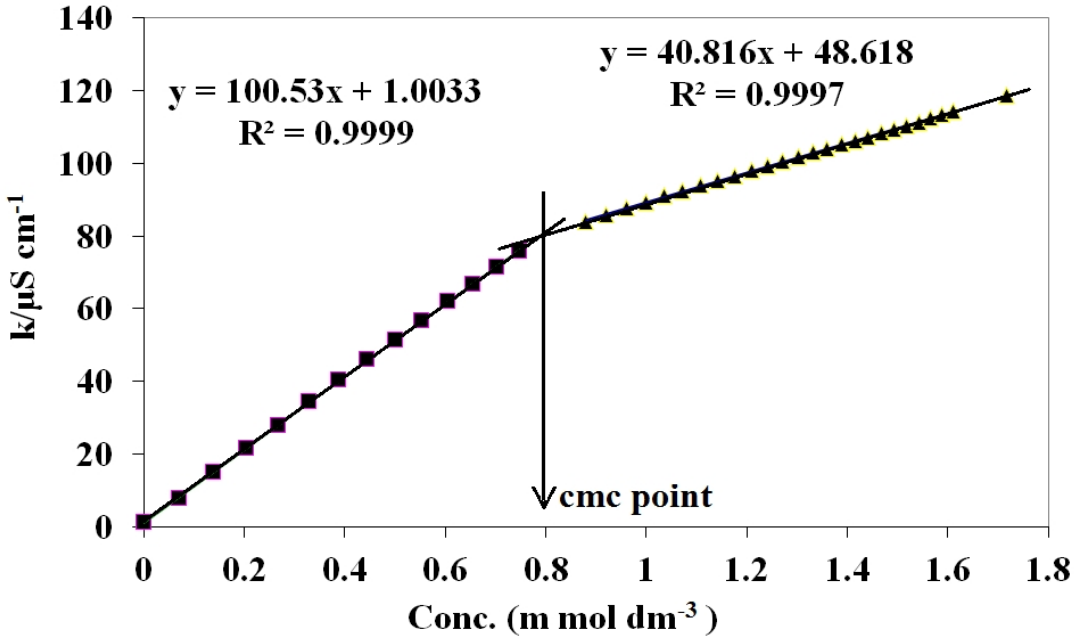

Figure 3.3.3: Plot of HDTEAB concentration versus conductivity measurement where the line shows the cmc point, and the left and right equations show the linearity and regression of the line fitted to the points below and above the cmc.

Conductivity measurements were used to study cmc and degree of ion dissociation β for cationic surfactants [*2*]. The concentrations of surfactants in regions above and below the cmc have a linear correlation with conductivity. The slope of the points above the cmc region is less than the slope value of the points below the cmc region (figure 3.3.3).

Table 3.3.1: The cmc at 25°C (mMol dm^{-3}), degree of counter ion dissociation (β) and Gibbs free energy of micellization $-\Delta°G_m$ (KJ/mol) values for cationic surfactants in water solution and in 1.0% (w/v) L-PEI.

Surfactants name	Solution			1.0% (w/v) L-PEI		
	cmc	β	$-\Delta°G_m$	cmc	β	$-\Delta°G_m$
Dodecyltriethylammonium bromide	13.83	0.215	36.7	13.64	0.391	33.1
Tetradecyltriethylammonium bromide	3.40	0.351	39.7	3.12	0.353	39.9
Hexadecyltriethylammonium bromide	0.80	0.396	44.3	0.29	0.463	46.3
Dodecyltripropylammonium bromide	9.43	0.393	34.6	9.72	0.469	32.8
Tetradecyltripropylammonium bromide	2.42	0.369	40.6	2.06	0.421	39.9
Hexadecyltripropylammonium bromide	0.59	0.451	44.0	0.35	0.518	43.9
Benzyldimethyldodecylammonium bromide	5.39	0.303	38.9	5.37	0.317	38.6
Benzyldimethyltetradecylammonium bromide	1.23	0.353	43.7	0.99	0.387	43.7
Benzyldimethylhexadecylammonium bromide	0.29	0.452	46.7	0.14	0.556	46.3
n-Dodecylpyridinium bromide	11.82	0.266	36.3	11.61	0.271	36.3
n-Tetradecylpyridinium bromide	2.79	0.277	42.3	2.43	0.298	42.3
n-Hexadecylpyridinium bromide	0.70	0.341	46.4	0.41	0.334	48.8
Dodecyltriphenylphosphonium bromide	2.10	0.49	38.1	1.69	0.588	36.4
Tetradecyltriphenylphosphonium bromide	0.67	0.605	39.2	0.26	0.608	42.4
Hexadecyltriphenylphosphonium bromide	0.20	0.616	43.0	0.12	0.862	46.8

The errors in the measured values are ±5% of the reported value.

The intersection point between the two straight lines indicates the cmc value while the ratio between the slopes gives the degree of counter ion dissociation, β. The cmc data obtained from the conductivity measurements versus surfactants concentration plots are shown in Table 3.3.1.

An exponential relationship was found between number of carbons in the cationic surfactant tails and the critical micelle concentration of these surfactants as shown in Figure 3.3.4. This could potentially be used to calculate the theoretical cmc of these surfactants having a similar headgroup but with different hydrocarbon chain lengths. For example from the exponential equation of alkylpyridinum bromides the theoretical cmc calculated for tridecylpyridinium bromide would be 5.8 mMol $dm^{-3}$and pentadecylpyridinium bromide would be 1.4 mMol dm^{-3}. These theoretical values are very close to experimental values found by Skerjanc [*3*] where the cmcs were 5.3 and 1.3 mMol dm^{-3} respectively.

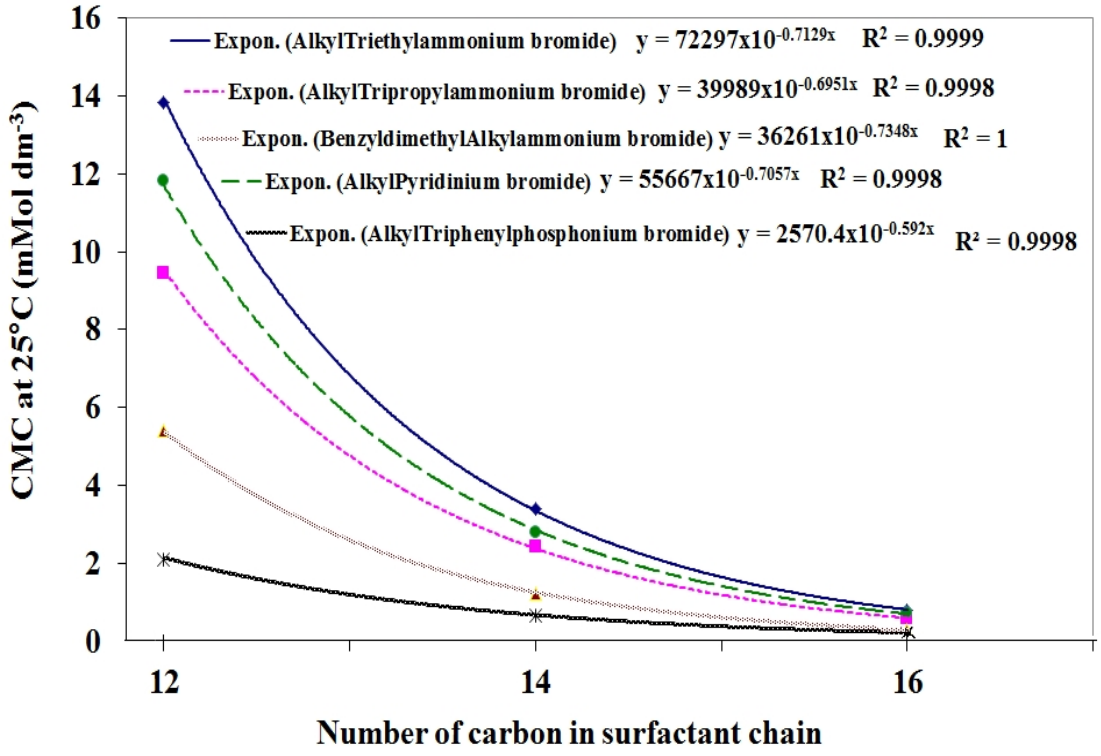

Figure 3.3.4 Number of carbons in cationic surfactants tails correlating exponentially with critical micelle concentration in water solution.

The exponential relationship between micellization behaviour and surfactants tail lengths have been reported by several authors [*4-6*]. For instance Lindman et al.

reported that by increasing the hydrophobic part of the surfactant, the cmc strongly decreased, and that non-ionic surfactants showed more rapid decreases compared with ionic surfactants [*7*]. Attwood et al. suggested that cmc decreases in general by the half when one methylene group was added in the hydrophobic part of ionic surfactants [*8*]. However in some cases the addition of one more methylene group causes the cmc to decrease to one third of its original value. Also a similar relationship has been shown in nonionic and zwitterionic surfactants, where for each two methylene groups added to the hydrophobic chain the cmc decreases by a factor of about 10 from its original value. Several researchers have developed empirical micellization equations based on various structural units in amphiphile molecules and their concentrations. Klevens [*9*] found a relation between the cmc and the number of carbon atoms *N* in the hydrophobic chain and homologous straight-chain ionic surfactants in aqueous medium expressed as:

$$\textbf{Log cmc} = A - BN \quad \textbf{(3.1)}$$

where *A* is a constant for a particular ionic head at a given temperature and *B* is a constant (≈ 0.3) at 35ºC for the ionic surfactants.

Linear regression R^2 values for the cmc values measured in the presence of 1%(w/v) L-PEI / solution indicate that an exponential correlation does not hold as in case of pure surfactant solutions. Instead a polynomial with order 2 is used to show the correlation between number of carbons and the critical micelle concentration of surfactants 1% (w/v) L-PEI solution. The polynomial equation for each surfactant is given in figure 3.3.5.

The cmc performance of surfactants in pure water solution showed different behaviour from that in the surfactant/PEI solutions as shown in Figure 3.4 -3.5. Edler et al, reported hydrophobic interactions between PEI and alkyltrimethylammonium bromide surfactants at high pH solution where highly ordered air/water interface micron thick films are formed [*10, 11*]. Different behaviours of surfactants in pure water and in PEI solution confirm cooperative behaviour between polymer and surfactant when micelles form. This cooperative behaviour starts at surfactant concentrations lower than the critical micellization concentration where a cooperative association occurs between surfactants and polymer due to electrostatic and hydrophobic forces [*12, 13*]. In this case, since the polymer is almost neutral at the pH values used, the only electrostatic forces involved can be weak ion-dipole interactions between the positively charged surfactant headgroup and the lone-pair on the nitrogens of the polymer [*11, 14*].

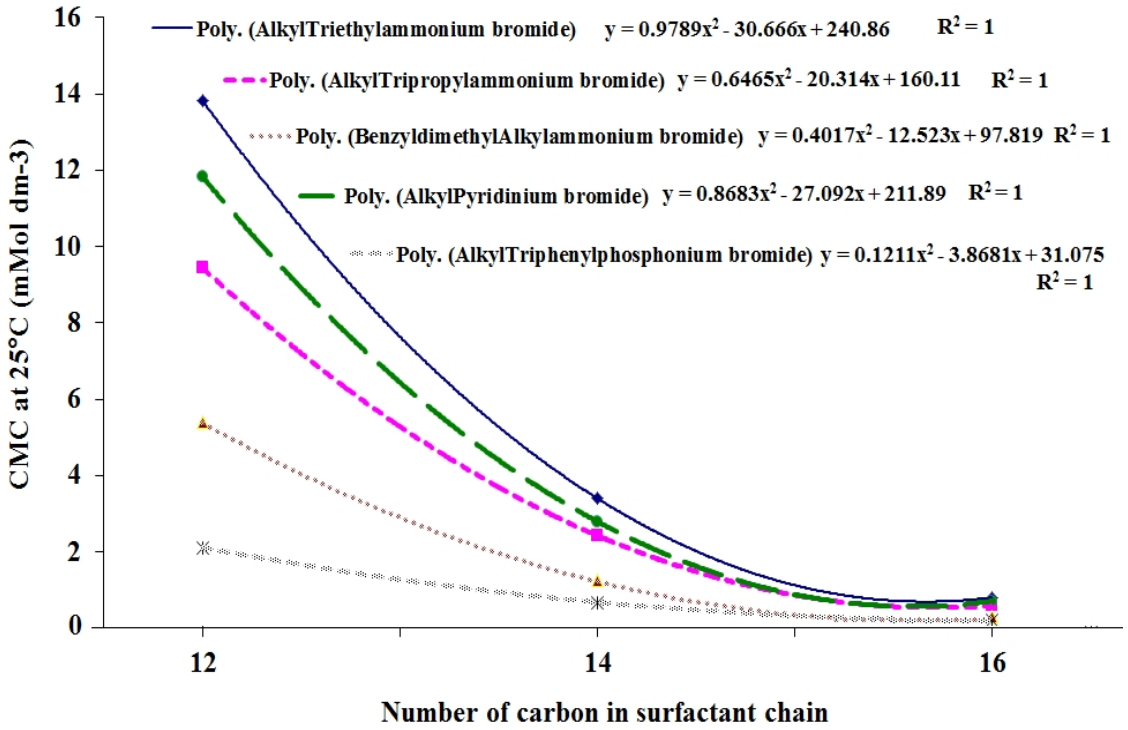

Figure 3.3.5: Number of carbons in cationic surfactants tails correlating polynomially with critical micelle concentration of surfactants in 1 %(w/v) LPEI solution.

From Table 3.3.1 and figures 3.3.4 -3.3.5 the cmc values very obviously show that increasing the hydrocarbon chain length of surfactants decreases the critical micelle concentration point. This behaviour was recorded for both in surfactants/water solution and in surfactants/L-PEI solution. Two categories can be used to classify the surfactants headgroups that were used in this study, the first are aliphatic headgroups like alkyltriethylammonium bromide and alkyltripropaylammonium bromide, and in the second category, aromatic headgroups, where the surfactants contain an aromatic part in their headgroup such as alkylpyridiniumbromide, benzyldimethylalkylammonium bromide and alkyltriphenylphosphonium bromide. The molecular volume in cubic Angströms ($Å^3$) were calculated for triethylamine, tripropylamine, pyridine, (N,N-Dimethylbenzylamine) and triphenylphosphine [*15*]. These compounds represent the head groups of the surfactants used in this study. Table 3.3.2 shows the molecular volume and density for these compounds.

Table 3.3.2: Molecular volumes (A^3) and densities of amine and phosphine compounds.

Compound Name	***Molecular Volume (A^3)***	**Density (gm/cm^3)**
Pyridine	*79.8*	0.98
Triethylamine	*125.5*	0.73
Tripropylamine	*175.9*	0.76
N,N-Dimethylbenzylamine	*146.8*	0.90
Triphenylphosphine	*246.5*	1.10

Molecular Volume (A^3) were calculated from ref. [15] and density values were taken from [16-19].

Table 3.3.2 shows that the bulkiness of tripropylamine is higher than triethylamine and that triphenylphosphine is bigger than N,N-dimethylbenzylamine, while the pyridine has a relatively small molecular volume but high density due to a high packing density of the flat aromatic resonance electron structure. Figure 3.3.6 illustrates the effect of bulkiness of the surfactant headgroup on the critical micelle concentration. This clearly confirms that large bulky headgroups reduce the cmc of the surfactants in both cases ie aliphatic and aromatic headgroups having equal hydrocarbon chain length. This result was also found in surfactant solutions containing 1% (w/v) L-PEI.

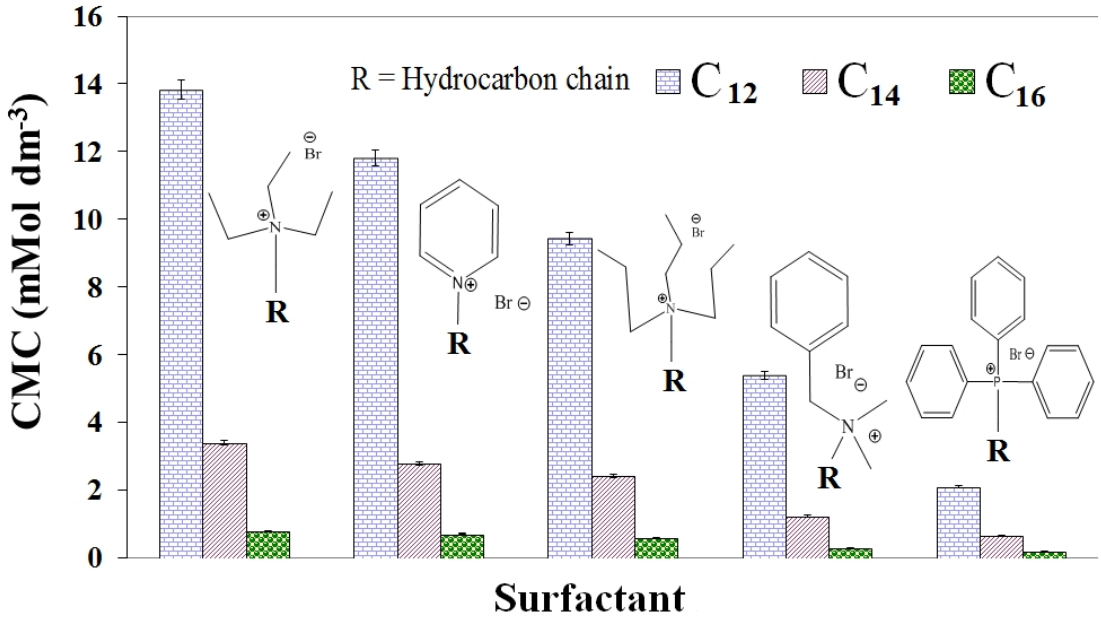

Figure 3.3.6: Effect of the size of the aromatic and aliphatic surfactant headgroups versus critical micelle concentration

In general, the surfactants in 1%(w/v) LPEI solutions show lower cmcs compared to those prepared in water solutions (table 3.3.1), which indicates that the presence of polyelectrolyte is driving the surfactants to form micelles at lower concentration due to interactions between polymer and surfactants. The mechanism of polymer/surfactants interactions still not fully understood particularly for aqueous systems containing similarly charged surfactant and polyelectrolyte. Several studies demonstrated that hydrophobicity and hydrogen bond interactions are dominating in aqueous similarly charged systems [*10, 20*]. However a number of factors control the behaviour of polymer/surfactant interaction. Polyelectrolyte properties such as charge density, flexibility, and degree of branching play essential role in this interaction, while surfactants properties like hydrophobicity, bulkiness, charge type and position of the polar part of surfactant molecules are also significant factors. In general hydrophilic and lipophilic phenomena are the main interactions between polyelectrolyte and surfactants. The lower cmc results of surfactants/PEI solutions compared with surfactants in pure water in this study also agrees with the lower cmc found for the hexadecyltrimethylammonium bromide(CTAB)/PEI system compared to that of CTAB in water solutions found in work by Comas-Rojas et al [*12*].

Assuming a pseudo phase separation model of micelles, the degree of ionization β was calculated from the ratio of the slopes of the intersecting lines on the graph of conductivity measured versus surfactant concentration; see the data summarised in table 3.3.1. In general, the degree of ionization, β, increases as the hydrocarbon chain length increases and as the bulkiness of the surfactant headgroup increases. An exception occurs in DTPAB where β is only a tiny amount higher than TTPAB in both water and L-PEI solutions and in DTEAB in L-PEI solution. Due to rare literature in this field and the simple analysis done on these surfactant / PEI systems no explanation about these variations can be given.

In general the behaviour of degree of ionization result in this work is in good agreement with the study by Shehata [*4*] on quaternary triethyl amines prepared from various long chain alkyl halides. He found that by increasing the length of the alkyl chain, the degree of micelle ionization increased. This behaviour was suggested to be due to the variation in the electronic charge density on the central nitrogen atom, which subsequently depends on the positive inductive effect of the bulkiness of the headgroup and the alkyl group of the cationic part of the surfactant [*4*].

The Gibbs free energy of micellization ($\Delta°G_m$) is the main parameter that can illustrate the thermodynamics of micelle formation [*21*]. The relationship of Gibbs free energy, critical micelle concentration and degree of ionization are given in the following equation:

$$\Delta°G_m = (2- \beta)\, R\, T \ln X_{cmc} \quad (3.2)$$

Where R is the gas constant, T is the absolute temperature, β is the ionization degree of the micelles and X_{cmc} is the critical micelle concentration expressed as a mole fraction. The Gibbs free energies of micellization ($-\Delta°G_m$) were calculated from this equation for surfactant solutions in both water and L-PEI, summarized in table 3.3.1. Figure 3.3.7 demonstrates the correlation between $-\Delta°G_m$ and the surfactant hydrocarbon chain length. Figure 3.3.7 very clearly shows that when the surfactants hydrocarbon tail length increases the negative Gibbs free energy ($-\Delta°G_m$) also increases.

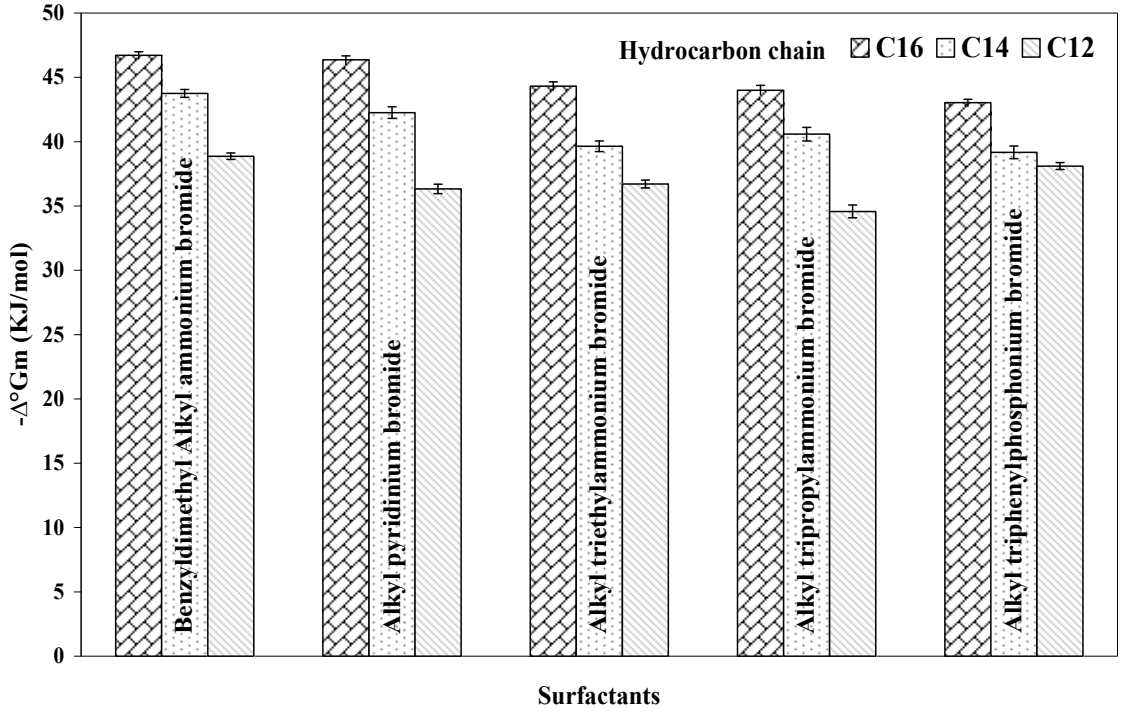

Figure 3.3.7: Negative free energy of micellization ($-\Delta°G_m$) for water/surfactant solution of various surfactants with different hydrocarbon chain lengths.

In other words, thermodynamically, the micellization is stabilized by longer hydrocarbon chain (tail) due to attractive interaction between surfactants hydrocarbon chains with themselves. However although the free energy of micellization can show the effects of hydrocarbon chain length on micelle formation it does not display a clear

effects from the bulkiness of the surfactants headgroups. The thermodynamic differences between pure surfactant solutions and PEI/surfactants solution are not large, showing only a relatively tiny increase in $-\Delta^\circ G_m$ in case of PEI/surfactant solutions. The variation in the value of $-\Delta^\circ G_m$ in PEI/surfactants solutions compared with pure surfactants solutions indicates the variation of interaction strength between PEI and these dissimilar surfactants.

3.3.3 Micellar volume and aggregation numbers (N_{agg}) of cationic surfactants in presence and absences of polyethyleneimine (PEI).

The mechanism of micellization of amphiphile molecules in aqueous solution is very dependent on the hydrophobic interaction between the hydrophobic parts of the molecule which provide the driving force for aggregation and the electrostatic or steric repulsion between the hydrophilic groups which also control the size and shape of self-assembled micelles. The physical properties of the hydrophilic and hydrophobic parts of amphiphile molecules, such as tail length, bulkiness and headgroup charge thus compete and thus play an important role in deciding the micellar shape. The Israelachvili [*22*] concept of a packing parameter, can be used as a qualitative tool to predict aggregate shape. The packing parameter (p) is defined as the ratio of the volume of the tail region of a surfactant molecule to its headgroup area within the micelle:

$$p = v / al \qquad (3.3)$$

where v is the molecular volume, l the hydrocarbon chain length and a the area of surfactant head group. According to Tanford's equation [*23*], the hydrophobic chain volume of the micelle, v, and the critical chain length, l_C, can be obtained from:

$$v = (27.4 + 26.9 n_C) \quad (Å^3) \qquad (3.4)$$

$$l_C = (1.5 + 1.265 n_C) \text{ (Å)} \qquad (3.5)$$

where n_C is the number of carbon atoms in the hydrophobic chain of the surfactant. In this way these equations can be used to predict the micellar geometry. In general, when

p is less than or equal 1/3, the micelles are spherical, if *p* is greater than1/3 and less than 1/2, the micellar shape is suggested to be ellipsoidal or cylindrical. The surfactant aggregates tend to be bilayers for *p* values greater than 1/2 and in suitable cases this results in formation of vesicles [*22*]. It is important to notice that the effective head group area *a* can be altered by changing the solution temperature (for nonionic surfactants which become less soluble as the temperature increases) or by addition of salt to the micellar solution, (where for ionic surfactants the added ions cause screening the charges on surfactant headgroups, allowing them to pack more closely together) which thus changes in micellar shape [*24-27*]. Packing parameter (*p*) calculated for all surfactants were used in this research and summarized in table 3.3.3.

Table 3.3.3: Calculated surfactant packing parameters, p.

Surfactants (headgroup / Tail)	C_{12}	C_{14}	C_{16}
Triethylamine	0.293	0.294	0.294
Tripropylamine	0.240	0.240	0.240
N,N-Dimethylbenzylamine	0.297	0.297	0.298
Pyridine	0.410	0.406	0.407
Triphenylphosphine	0.176	0.176	0.176

Values for *v* and *lc* are calculated using Tanford's formula, while the a_0 values for the surfactants headgroups are taken from refs. [*28-33*],

The calculation of the packing parameters of these surfactants demonstrates that they are all less than 1/2, which is the transition point between spherical and ellipsoidal micelles. Furthermore the packing parameters of alkyl triphenylphosphonium bromide surfactant is less than 1/3, suggesting these micelles should be spherical. Nevertheless all of the cationic surfactants reported here exhibited prolate elliptical micelles, in small angle scattering experiments described in the following section.

SANS experiments were used to investigate the micellar size and aggregation number for all of the cationic surfactants listed in table 3.3.1. The micelle parameters of these cationic surfactants were investigated in the presence and absence of PEI. Low Mw ~2 000 Da SPEI was used at 15g/L. The total surfactant concentration was 0.05M in 100 % or 70 % D_2O. All SANS data were modelled using two contrasts simultaneously, and using a uniform ellipsoid model to calculate the scattering patterns, written by Dr. Steve

Kline at the NIST Centre for Neutron Scattering for the Igor PRO platform (WaveMetrics) [*34*], with the Hayter-Penfold mean spherical approximation for charged spheres as the structure factor [*35*]. This model was chosen for fitting the SANS profiles based on the lowest $\chi 2$ after testing also models for Oblate ellipsoid, Polydisperse spheres, core-shell ellipsoid micelles, cylinder models. The equation for scattering from a uniform ellipse is given in equation 3.3 where the averaging over all orientations has to be done numerically. The ellipse is defined by the semi axes R, R, εR:

$$P_5(q,R,\varepsilon) = \int_0^{\pi/2} F_1^2\left[q, r(R,\varepsilon,\alpha)\right]\sin\alpha d\alpha \qquad \textbf{(3.6)}$$

Where $r(R,\varepsilon,a) = R(\sin^2\alpha + \varepsilon^2\cos^2\alpha)^{1/2}$. The ellipse is rotated about the axis of R_a to define the ellipsoid. If the radius $R_b > R_a$, the object is an oblate ellipsoid (disk-like). If $R_b < R_a$, then the object is a prolate ellipsoid (needle-like). If the two radii are equal, then the ellipsoid is a sphere (figure *3.3.8*). Prolate ellipsoids have one major semi-radius (R_a) and two degenerate minor semi-radii (R_b), the volume of the ellipsoid is consequently equal:

$$\boldsymbol{V_m = (4/3)\,\pi\, R_a R_b^2} \qquad \textbf{(3.7)}$$

Aggregation numbers of surfactant monomer (N_{agg}) [*36*] were calculated based on micelle volume (V_m) and volume of the surfactant molecules (V_{surf}):

$$\boldsymbol{N_{agg} = V_m / V_{surf}} \qquad \textbf{(3.8)}$$

where V_{surf} is the volume of the surfactant molecules calculated based on the calculated density and molecular weight for each surfactant divided by Avogadro's number.

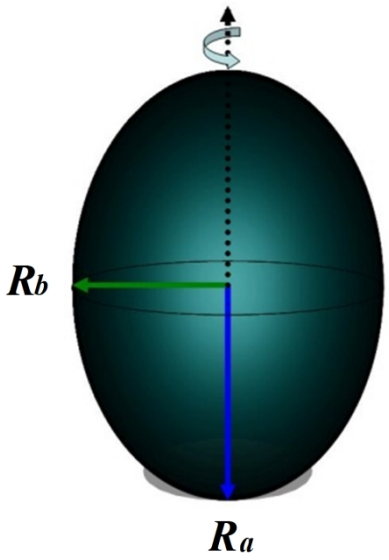

Figure 3.3.8: Schematic of prolate ellipsoid is rotated about the axis of R_a

For the uniform ellipsoid model the values of the SLD contrast were initially calculated for the expected compositions of the solution intermicellar phase and micelle cores, based on the prepared solutions (see table 2.11.1-2.11.2). The temperature was fixed at 308 K and the dielectric constant was held at 78. The monovalent salt concentration was fixed at zero in the case of surfactant solutions without polymer and 0.013M in the case of presence 1.5% (w/v) PEI. The movalent salt concentrations were calculated based on the PEI concentration and the pH of PEI, where the PEI used in this work is only 3% charged. Volume fractions for each surfactant solution were all calculated and fixed based on the concentration and volume of the surfactant molecules added to the solution. The variables fitted were the micelle radii, micellar charge and incoherent background. Figure 3.3.9 shows the simultaneous fitting of SANS data using the charged uniform ellipsoid model for surfactants with C_{12}, C_{14} and C_{16} hydrocarbon chains in presence and absence of PEI.

The SANS data for the surfactants with and without PEI illustrates clearly that SANS profiles of surfactants/PEI have a broader curvature than the SANS profiles of surfactants in the D_2O solution without polymer, suggesting that the correlation between micelles due to intermicellar repulsion is reduced in the presence of the polymer.

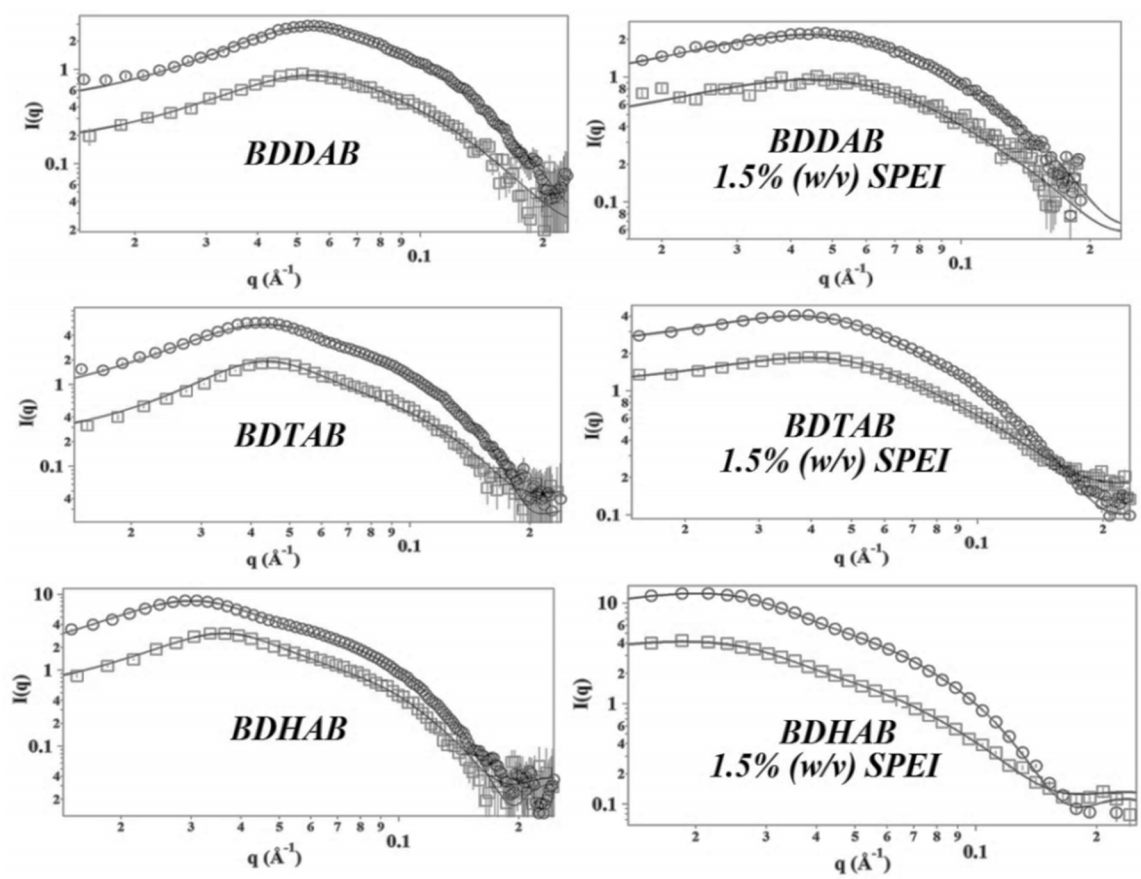

Figure 3.3.9 left: SANS profile for surfactants with C_{12}, C_{14} and C_{16} hydrocarbon chains were dissolved in 100% D_2O (circles) and 70% D_2O solution (squares).The right hand profiles are for the same surfactants with 1.5%(w/v) SPEI. The solid lines are simultaneous fits to the data using the charged uniform ellipsoid model.

Table 3.3.4: Micelle radii, micelle volume, micelle charge and aggregation number (N_{agg}) for cationic surfactants in presence and absence of PEI calculated from fitting SANS data.

Surfactant	***R_a (Å)***	***R_b (Å)***	***Micelle charge***	***Vol. of Ellipse ($Å^3$)***	***N_{agg}***
DTEAB	23	17	6	27516	45
TTEAB	29	20	12	46669	70
HTEAB	33	23	15	72489	100
DTPAB	26	19	9	39839	58
TTPAB	28	19	13	44772	60
HTPAB	33	23	19	70149	87
BDDAB	30	18	11	42597	69
BDTAB	48	20	15	76613	115
BDHAB	73	22	16	149347	209
DPBr	21	18	13	27605	58
TPBr	29	20	15	51250	97
CPBr	35	23	23	75095	130
DTphPB	27	16	12	27071	35
TTphPB	31	19	15	48933	60
HTphPB	34	22	20	65909	76
DTEAB with SPEI	20	20	2	33510	55
TTEAB with SPEI	28	20	4	44867	67
HTEAB with SPEI	33	23	5	70041	97
DTPAB with SPEI	22	21	3	40085	58
TTPAB with SPEI	25	21	4	45443	61
HTPAB with SPEI	30	22	5	62551	78
BDDAB with SPEI	27	23	2	56619	92
BDTAB with SPEI	56	19	4	80426	121
BDHAB with SPEI	142	22	5	287887	402
DPBr with SPEI	17	20	3	27396	57
TPBr with SPEI	29	21	4	53709	102
CPBr with SPEI	40	23	6	89281	155
DTphPB with SPEI	18	17	4	20315	26
TTphPB with SPEI	25	24	4	58086	71
HTphPB with SPEI	74	19	7	111294	129

The errors in micelle radii are ±2 Å, while the errors of the ellipsoid volume and aggregation number (N_{agg}) were ±5% of the measured value. Error in micelle charge is ±3% of the measured value

This result suggests that PEI in some way interacts with these cationic surfactant micelles which subsequently changes their shapes and sizes. Table 3.3.4 shows the micelle radii, micelle volume and aggregation number that were calculated by fitting the SANS data for all of these surfactants in presence and absence of PEI. From table 3.3.4 the relationship between the aggregation numbers with and without PEI and the surfactant hydrocarbon chain length and headgroups was plotted in Figure 3.3.10.

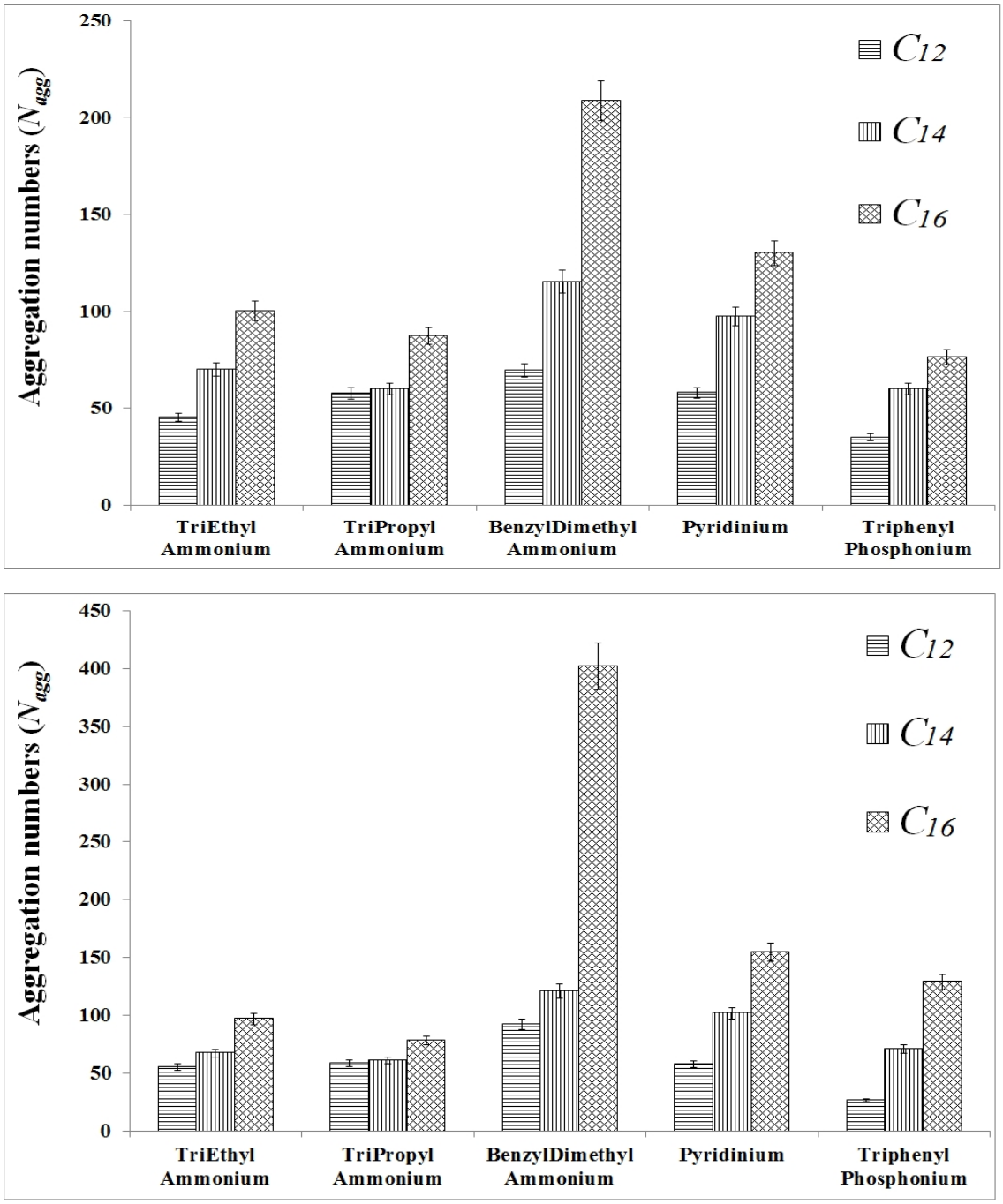

Figure 3.3.10: Effects of surfactant headgroup and hydrocarbon chains on the *aggregation number (N_{agg}) in presence of 1.5% (w/v) SPEI (bottom graph) and in the case of surfactant solutions without any addition of PEI (top graph).*

Figure 3.310 shows clearly that the aggregation number for these cationic surfactants increases as the surfactant hydrocarbon chain length increase, and this result is found in the presence and absence of PEI. Several authors have reported this relationship between N_{agg} and the tail length of amphiphile molecules. In general the micellization process in surfactants solutions is a balance between the steric and electrostatic interactions of the surfactant headgroups and also interactions between the hydrophobic alkyl chins [*37*]. Increasing the length of the hydrocarbon chain has the propensity to decrease the cmc, due to increase the migration of the surfactant molecules to the liquid/air interface, therefor it is speedily covered by surfactant, which that starts formation of the micelle [*4*]. Also increasing the surfactant hydrocarbon chain length causes shifts of the Krafft discontinuity to higher temperature, hence increases the average micellar aggregation number [*38*]. On the other hand increases in the surfactants hydrophobic tail length result in a decrease in the Gibbs free energies of the micellization processes, which subsequently cause a shift toward lower cmc values [*39*]. Oliver et al. suggested that the increases in aggregation number arose from the improved hydrophobic interactions between adjacent surfactant monomers made by the addition to alkyl chain length [*40*].

From the data in Figure 3.3.10, it is apparent that increases in the bulkiness of the surfactant headgroup for both aliphatic and aromatic surfactants headgroups, caused a relative decrease in the N_{agg} for all of these surfactants except benzyldimethyl ammonium bromide. This surfactant shows an extraordinary increase in N_{agg} compared to that found for the other surfactants, particularly for the C_{16} tail. This exceptional behaviour of benzyldimethyl as a headgroup could be related to folding back of the benzyl group into the micelle core when it is neutralised during counterion binding so that it performs as a second hydrophobic tail, which consequently increases the N_{agg} [*41*].

The bulkiness, nature and hydrophobicity of surfactant headgroup, and also the size and type of counterion play an important role in micelle formation. Association of the counterions with the surfactant headgroups significantly changes the micelle growth and their geometry [*42*].

Based on the principle of Israelachvili, the packing parameter demonstrates that bigger surfactant headgroups, with larger headgroup areas decrease the packing parameter and result in smaller aggregate size either by forming spherical or short elliptical micelles

[*23*]. On the other hand counterions also play a very important role in the micellization performance; however the mechanisms of the counterion effects are not fully clear. In solution, counterions stabilize ionic surfactant micelles through binding to the micelle surface and screening the electrostatic repulsions between the ionic headgroups. Therefore the counterion binding affinity influences the bulk self-assembly process [*43, 44*]. For example the cmc of a surfactant with bromide counter ion is less than the same surfactant with chloride counter ions. This is because bromide and chloride ions have different sizes in solution therefore the average number of bound water molecules for the bromide ion is less in comparison to that of the chloride ion [*45*]. Consequently, the hydrated chloride ion is bigger than the hydrated bromide ion and as such the chloride ion is not as closely associated with the cationic head group of the surfactant and will not be as effective as the bromide counter ion at neutralizing the head group charge. This means that for surfactants with the chloride counterion there is an increase of electrostatic repulsion between the head group of the surfactants not only within the micellar aggregates but also between the surfactant aggregates themselves [*45, 46*]. Overall micelle size and structure depends on a balance of the headgroup interactions with themselves and with the counterions, and the hydrophobic interactions between the alkyl groups.

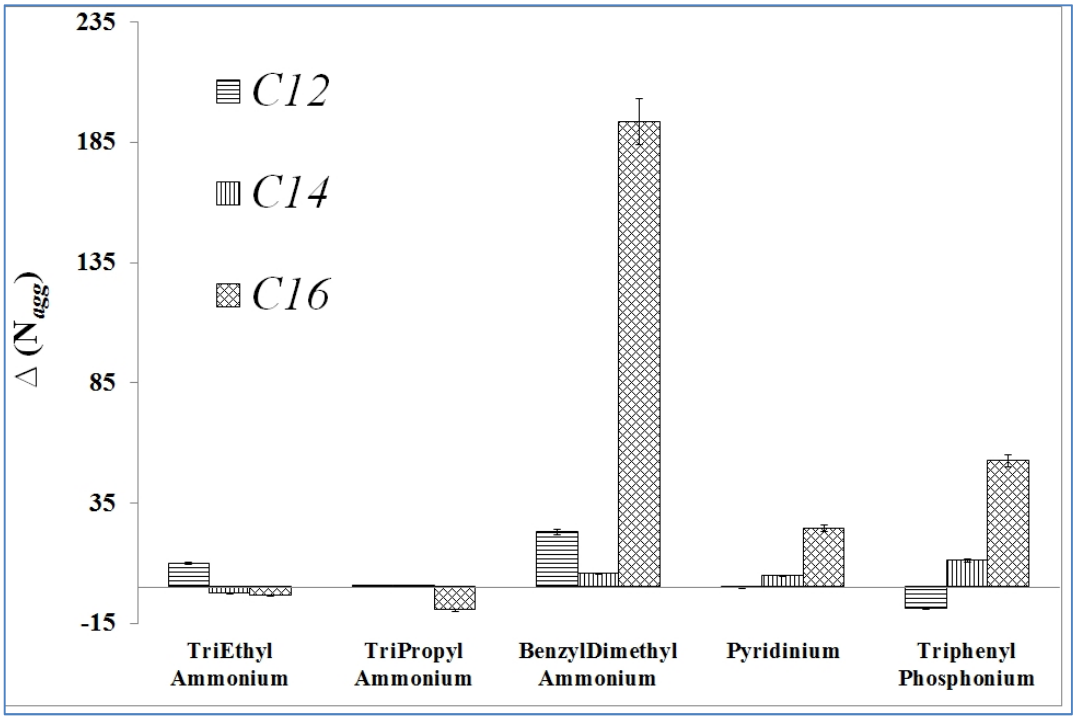

Figure 3.3.11: Variation in the effects of PEI on the micelles aggregation number (N_{agg}) for cationic surfactants in the case of presence and absence of 1.5% (w/v) SPEI.

In general the data in Figure 3.3.11 shows that effect of hydrocarbon chain and bulkiness of surfactants headgroup on micellization for all of these cationic surfactants in presence and absence of PEI was overall consistent in that the micelle size increases as tail length increases. However the effect of PEI for each individual surfactant was dissimilar compared either with the same surfactant headgroup or with equivalent hydrocarbon tail.

As stated in Chapter 1, there are three general proposals which describe surfactant-polymer interactions in aqueous solutions. The first scenario describes co-operative association of surfactant to the polymer chain and the second scenario is that surfactant micelles are located in the vicinity of the polymer chain. A third suggestion proposed a loopy configuration resulting from aggregated surfactant micelles, surrounded by long chain polymers [*47*]. These scenarios will be discussed in more detail in Chapter 4, in the context of film formation. However the effect of PEI on aggregation number can be considered in the light of these models.

Figure 3.3.11 illustrates the change in micelle aggregation number between solutions with and without PEI for these cationic surfactants. In this viewpoint, BDHAB has almost double the N_{agg} value in the case of presence PEI, whereas BDTAB does not show significant change in N_{agg} (figure 3.3.11). In general the change in N_{agg} for surfactants with aliphatic headgroups such as triethyl and tripropyl is smaller than that for surfactants, with aromatic headgroups, particularly for C_{16} tail length which demonstrate the highest effect of PEI addition. The surfactants with aliphatic headgroups and a C_{16} tail decreased in size in the presence of PEI, suggesting perhaps that micellization in this case is largely due to micelles, bound to the polymer chain (which tend to be smaller than free micelles) where the polymer forms part of the hydrophobic region of the micelles. Micelles formed from surfactants with aromatic headgroups however become highly enlarged. This may be due to interactions between the nitrogen lone pair from the PEI interacting with the excess electron density on the aromatic rings, drawing the polymer into the headgroup regions, decreasing electrostatic repulsion between headgroups and thus altering the packing parameter to favour elongated micelles. This variation in N_{agg} suggests that there is a physical interaction between these cationic surfactants and polyethyleneimine; however the influence of PEI on these broad ranges of cationic surfactants was not similar.

The variation between aliphatic and aromatic headgroups are seen in the case of association of PEI with these surfactant micelles it could be related to the hydrophobicity and steric hindrance of aromatic groups in the surfactants headgroup which may lead to extra shields preventing water molecules from penetrating the headgroup region. Thus will leads to decrease the electrostatic repulsion between the headgroup of the surfactants therefore more surfactant molecules can aggregate leading to the formation of bigger micelles [*48, 49*].

Many authors have described the interaction between polyelectrolyte and micelle surfactants as a complex interaction. The term complex is still used to describe this interaction because the fundamental mechanism of this interaction remains ambiguous. However there are several scenarios and trials have been made to solve this question [*49*]. Kudryavtsev et al described the interaction between cationic surfactant and PEI through hydrophobic interaction [*50*]. O'Driscoll et al found cation-dipole interaction between polyethyleneimine and CTAB where the dipole on the branched PEI (amine groups) interacts with the charged part of ammonium CTAB headgroup [*14*]. In aqueous solutions, at pH 7, PEI is partly protonated due to formation of hydrogen bonds with H_2O [*50*] However, in this work the pH of the PEI solutions were not adjusted so remained close to pH values of 9-10 where PEI is less than 3% protonated, meaning the polymer is almost neutral in these experiments. On the other hand the surfactant counterions also associate with the cationic surfactants headgroups. All of these factors and also the balance of interactions between micellar components itself in the aqueous solution makes the interaction between PEI and these cationic surfactants micelles very intricate. However from the data above it illustrates that most likely that these cationic surfactants are interacting physically with PEI through cation-dipole integration.

3.4 Conclusion

The nature and bulkiness of the surfactant headgroup and hydrocarbon chain length all play significant roles in surfactant micellization. From the cmc study for those aromatic and aliphatic headgroup cationic surfactants with three different hydrocarbon chains length an exponential correlation was found between hydrocarbon chain length and critical micelle concentration, where increased surfactant hydrocarbon tail reduced the critical micelle concentration. In addition thermodynamically it is more favourable for longer hydrocarbon chain surfactants to form micelles. On the other hand interaction between polyelectrolyte and cationic surfactants drives the surfactants to form micelles at lower concentration.

Micelle radii, charge, volume and aggregation number for these cationic surfactants in presence and absence of PEI were investigated by using small angle neutron scattering. From this study it was demonstrated that the aggregation number for the wide range of cationic surfactants increases with increased surfactant hydrocarbon chain length, and that this result is observed in presence and absence of PEI. Both aliphatic and aromatic surfactants headgroups illustrates that increases in the bulkiness of surfactants headgroup caused a relative decrease in the N_{agg} . However benzyldimethyl ammonium bromide was showed extraordinary increases in N_{agg} particularly with C_{16} hydrocarbon chain. The large N_{agg} values for this surfactant could be related to fold back of the benzyl group into the micelle core during counterion binding so that it performs as a second hydrophobic tail, therefore increasing the N_{agg}.

In general the influence of hydrocarbon chain and bulkiness of surfactants headgroup on the micellization behaviour for these cationic surfactants was stable in presence and absence of PEI. However growth in N_{agg} was observed overall in the case of addition PEI for these surfactant solutions for aromatic surfactants headgroups while those with aliphatic headgroups decreased in size in the presence of the polymer. This variation in N_{agg} suggests that there is a physical interaction between these cationic surfactants and polyethyleneimine. The influence of PEI on these broad ranges of cationic surfactants was dissimilar which suggested that the combination between these cationic surfactants and PEI was a complex interaction affected by several factors.

3.5 References

1. Holmberg, K. (2003) *Surfactants and polymers in aqueous solution*, John Wiley & Sons, Chichester, West Sussex, England; Hoboken, NJ.
2. Pahi, A. B., Varga, D., Kiraly, Z., and Mastalir, A. (2008) Thermodynamics of micelle formation of the ephedrine-based chiral cationic surfactant DMEB in water, and the intercalation of DMEB in montmorillonite, *Colloids and Surfaces a-Physicochemical and Engineering Aspects 319*, 77-83.
3. Skerjanc, J., Kogej, K., and Cerar, J. (1999) Equilibrium and Transport Properties of Alkylpyridinium Bromides, *Langmuir 15*, 5023-5028.
4. Shehata, H. A., El-Wahab, A. A. A., Hafiz, A. A., Aiad, I., and Hegazy, M. A. (2008) Syntheses and characterization of some cationic surfactants, *Journal of Surfactants and Detergents 11*, 139-144.
5. Ding, W., Liu, K., Liu, X., Luan, H., Lv, C., Yu, T., and Qu, G. (2013) Micellization behavior of ionic liquid surfactants with two hydrophobic tail chains in aqueous solution, *Journal of Applied Polymer Science 129*, 2057-2062.
6. Chen, L. J., Lin, S. Y., and Huang, C. C. (1998) Effect of hydrophobic chain length of surfactants on enthalpy-entropy compensation of micellization, *J. Phys. Chem. B 102*, 4350-4356.
7. Tadros, T. F. (1984) *Surfactants*, Academic Press, London; Orlando.
8. Attwood, D., Elworthy, P. H., and Kayne, S. B. (1970) Membrane osmometry of aqueous micellar solutions of pure nonionic and ionic surfactants, *Journal of Physical Chemistry 74*, 3529-3534.
9. Klevens, H. B. (1953) Structure and aggregation in dilate solution of surface active agents, *J Am Oil Chem Soc 30*, 74-80.
10. Edler, K. J., Goldar, A., Brennan, T., and Roser, S. J. (2003) Spontaneous free-standing nanostructured film growth in polyelectrolyte-surfactant systems, *Chem. Commun. (Cambridge, U. K.)*, 1724-1725.
11. O'Driscoll, B. M. D., Milsom, E., Fernandez-Martin, C., White, L., Roser, S. J., and Edler, K. J. (2005) Thin Films of Polyethylenimine and Alkyltrimethylammonium Bromides at the Air/Water Interface, *Macromolecules 38*, 8785-8794.
12. Comas-Rojas, H., Aluicio-Sarduy, E., Rodriguez-Calvo, S., Perez-Gramatges, A., Roser, S. J., and Edler, K. J. (2007) Interactions and film formation in polyethylenimine-cetyltrimethylammonium bromide aqueous mixtures at low surfactant concentration, *Soft Matter 3*, 747-753.
13. Claesson, P. M., Bergstrom, M., Dedinaite, A., Kjellin, M., Legrand, J. F., and Grillo, I. (2000) Mixtures of cationic polyelectrolyte and anionic surfactant studied with small-angle neutron scattering, *J. Phys. Chem. B 104*, 11689-11694.
14. O'Driscoll, B. M. D., Fernandez-Martin, C., Wilson, R. D., Roser, S. J., and Edler, K. J. (2006) Effect of micelle composition on the formation of surfactant-templated polymer films, *J. Phys. Chem. B 110*, 5330-5336.
15. http://www.molinspiration.com/cgi-bin/properties. (2010), Molinspiration Cheminformatics Nova ulica 61 SK-900 26 Slovensky Grob Slovak Republic.
16. http://www.sigmaaldrich.com/united-kingdom.html. (2010).
17. http://www.alfa.com/en/gh100w.pgm. (2010).
18. http://www.acros.com/. (2010).
19. O'Neil, M. J. (2001) *The Merck index : an encyclopedia of chemicals, drugs, and biologicals*, Merck, Whitehouse Station, N.J.

20. Kosacheva, E. M., Kudryavtsev, D. B., Bakeeva, R. F., Kuklin, A. I., Islamov, A. K., Kudryavtseva, L. A., Sopin, V. F., and Konovalov, A. I. (2006) The aggregation of branched polyethylenimine and cationic surfactants in aqueous systems, *Colloid Journal 68*, 713-720.
21. Moroi, Y. (1992) *Micelles : theoretical and applied aspects*, Plenum Press, New York.
22. Israelachvili, J. N., Mitchell, D. J., and Ninham, B. W. (1976) Theory of self-assembly of hydrocarbon amphiphiles into micelles and bilayers, *Journal of the Chemical Society, Faraday Transactions 2: Molecular and Chemical Physics 72*, 1525-1568.
23. Tanford, C. (1972) Micelle shape and size, *Journal of Physical Chemistry 76*, 3020-3024.
24. Sheu, E. Y., Wu, C. F., and Chen, S. H. (1986) Effects of ion sizes on the aggregation and surface charge of ionic micelles in 1:1 electrolyte solutions, *Journal of Physical Chemistry 90*, 4179-4187.
25. Berr, S. S. (1987) Solvent isotope effects on alkyltrimethylammonium bromide micelles as a function of alkyl chain length, *Journal of Physical Chemistry 91*, 4760-4765.
26. Goyal, P. S., Dasannacharya, B. A., Kelkar, V. K., Manohar, C., Srinivasa Rao, K., and Valaulikar, B. S. (1991) Shapes and sizes of micelles in CTAB solutions, *Physica B: Physics of Condensed Matter 174*, 196-199.
27. Kumar, S., Aswal, V. K., Goyal, P. S., and Kabir ud, D. (1998) Micellar growth in the presence of quaternary ammonium salts, *J. Chem. Soc., Faraday Trans. 94*, 761-764.
28. Wasbrough, M. (2011) Nanostructured hydrogel films for encapsulation and release, University of Bath. , University of Bath, 2011.
29. Mata, J., Varade, D., and Bahadur, P. (2005) Aggregation behavior of quaternary salt based cationic surfactants, *Thermochimica Acta 428*, 147-155.
30. Martín, V. I., Rodríguez, A., Graciani, M. D. M., Robina, I., Carmona, A., and Moyá, M. L. (2011) Physicochemical characterization of bromide mono- and dimeric surfactants with phenyl and cyclohexyl rings in the head group, *J. Colloid Interface Sci. 363*, 284-294.
31. Buckingham, S. A., Garvey, C. J., and Warr, G. G. (1993) Effect of head-group size on micellization and phase behavior in quaternary ammonium surfactant systems, *Journal of Physical Chemistry 97*, 10236-10244.
32. Rosen, M. J. (1978) *Surfactants and interfacial phenomena*, Wiley, New York.
33. Verma, S. K., and Ghosh, K. K. (2011) Micellar and surface properties of some monomeric surfactants and a gemini cationic surfactant, *Journal of Surfactants and Detergents 14*, 347-352.
34. Kline, S. R. (2006) Reduction and analysis of SANS and USANS data using IGOR Pro, *Journal of Applied Crystallography 39*, 895-900.
35. Hayter, J. B., and Penfold, J. (1981) An analytic structure factor for macroion solutions, *Mol. Phys. 42*, 109-118.
36. Peyre, V., Bouguerra, S., and Testard, F. (2013) Micellization of dodecyltrimethylammonium bromide in water-dimethylsulfoxide mixtures: A multi-length scale approach in a model system, *J. Colloid Interface Sci. 389*, 164-174.
37. Tanford, C. (1974) Theory of micelle formation in aqueous solutions, *Journal of Physical Chemistry 78*, 2469-2479.

38. Small, D. M. (1986) *The physical chemistry of lipids : from alkanes to phospholipids*, Plenum Press, New York.
39. Paria, S., and Khilar, K. C. (2004) A review on experimental studies of surfactant adsorption at the hydrophilic solid-water interface, *Advances in Colloid and Interface Science 110*, 75-95.
40. Oliver, R. C., Lipfert, J., Fox, D. A., Lo, R. H., Doniach, S., and Columbus, L. (2013) Dependence of Micelle Size and Shape on Detergent Alkyl Chain Length and Head Group, *8*.
41. Zhang, Y., Qi, Y., and Zakin, J. L. (2005) Headgroup effect on drag reduction and rheological properties of micellar solutions of quaternary ammonium surfactants, *Rheologica Acta 45*, 42-58.
42. Kellaway, L., and Warr, G. G. (1997) The effect of head-group on selective counterion binding to cationic surfactants, *J. Colloid Interface Sci. 193*, 312-314.
43. Aswal, V. K., and Goyal, P. S. (2002) Role of different counterions and size of micelle in concentration dependence micellar structure of ionic surfactants, *Chem. Phys. Lett. 368*, 59-65.
44. Chen, Y. L., Chen, S., Frank, C., and Israelachvili, J. (1992) Molecular mechanisms and kinetics during the self-assembly of surfactant layers, *J. Colloid Interface Sci. 153*, 244-265.
45. Bhat, M., and Gaikar, V. G. (1999) Characterization of interaction between butyl benzene sulfonates and cetyl trimethylammonium bromide in mixed aggregate systems, *Langmuir 15*, 4740-4751.
46. Kötz, J., Kosmella, S., and Beitz, T. (2001) Self-assembled polyelectrolyte systems, *Progress in Polymer Science (Oxford) 26*, 1199-1232.
47. Norwood, D. P., Minatti, E., and Reed, W. F. (1998) Surfactant/polymer assemblies. 1. Surfactant binding properties, *Macromolecules 31*, 2957-2965.
48. Sastry, N. V., and Hoffmann, H. (2004) Interaction of amphiphilic block copolymer micelles with surfactants, *Colloids and Surfaces A: Physicochemical and Engineering Aspects 250*, 247-261.
49. Kotz, J., Kosmella, S., and Beitz, T. (2001) Self-assembled polyelectrolyte systems, *Progress in polymer science 26*, 1199-1232.
50. Kudryavtsev, D. B., Bakeeva, R. F., Kudryavtseva, L. A., Zakharova, L. Y., and Sopin, V. F. (2000) Catalysed hydrolysis of O-alkyl O-p-nitrophenyl chloromethylphosphonates in the cationic surfactant-poly(ethylenimine)-water system, *Mendeleev Communications*, 202-204.

4 Encapsulation of Monomers into Cationic Surfactant Micelles

4.1 Introduction

Self-assembly phenomena of amphiphile molecules in aqueous or organic media open the door to many applications. One of the most common advantages of this phenomenon is the ability of these compounds to solubilise hydrophobic molecules in aqueous solution. Dissolving or dispersion of hydrophobic molecules in aqueous media is very important in many aspects in our daily life such as coatings, adhesives, paints, etc. Therefore solubilisation or encapsulation of molecules in nanoscale systems has started to draw attentions of many recent researchers. Polymer nanoparticles are one of these exciting areas [*1, 2*]. Recently nanostructured polymers have become of worldwide interest since they have applications in many significant practical fields such as selective membranes, catalytic substrates and drug delivery [*3-5*]. A synthesis nanostructured polymer via polymerisation in a liquid crystalline phase is a promising project to make nanostructured polymers. However this type of polymerization is a heterogeneous polymerization which means polymerization in lyotropic liquid-crystalline solutions can be difficult to control because of rearrangement of the surfactant template due to temperature and composition changes through interdroplet diffusion and droplet exchange which occur faster than the polymerisation reaction [*6, 7*]. Therefore here the polymerisation of styrene within a liquid crystalline phase within the polymer films was investigated. Trapping the liquid-crystalline phase in a polymer/surfactant gel phase or film could prevent micelle rearrangement by significantly increasing the viscosity of the surrounding network and improve the ability to achieve polymerisation within micelles before phase changes occur. It will also result in preparation of hydrogel membranes with an insoluble nanoscale polymer network running through the gel phase, forming reinforced films which may have different mechanical properties to the pure hydrogel membranes.

As a first step towards generating these nanoscale reinforced polymer hydrogel membranes, therefore investigation of encapsulation of hydrophobic monomers into cationic surfactant micelles in solution is very important to understand the structure of the micelles formed in these system. It also sheds light upon the interactions in solution which drive formation of the films at the interface, since there is a close relationship between the solution structures and the final structure of the films[*8*]. Therefore the

focus of this chapter is on the ability of cationic surfactants to encapsulate a hydrophobic monomer such as styrene in aqueous solution. The amounts of encapsulated monomer inside these cationic surfactant micelles are quantified, in the presence and absence of polyelectrolyte, and the monomer location inside the micelle geometry is investigated. This data is then compared with neutron and X-ray reflectivity experiments on incorporation of the monomer swollen micelles into the polymer/surfactant films. The next chapter will report *in situ* polymerisation of encapsulated monomer in polymer/surfactant films.

4.2 Study of solubilisation of styrene in cationic surfactant solutions by using UV-Vis spectroscopy.

In this experiment CTAB, CTEAB, CPBr and BDHAB were used to solubilise styrene at four concentrations 0.65, 0.98, 1.31 and 1.63 mM, while all surfactant concentrations were fixed at 0.05M. The solubility of styrene in water is poor (2.97 mM) [*9*] therefore concentration calibration curves were made using styrene solutions from 25 to 300μM in water solution [*10*].

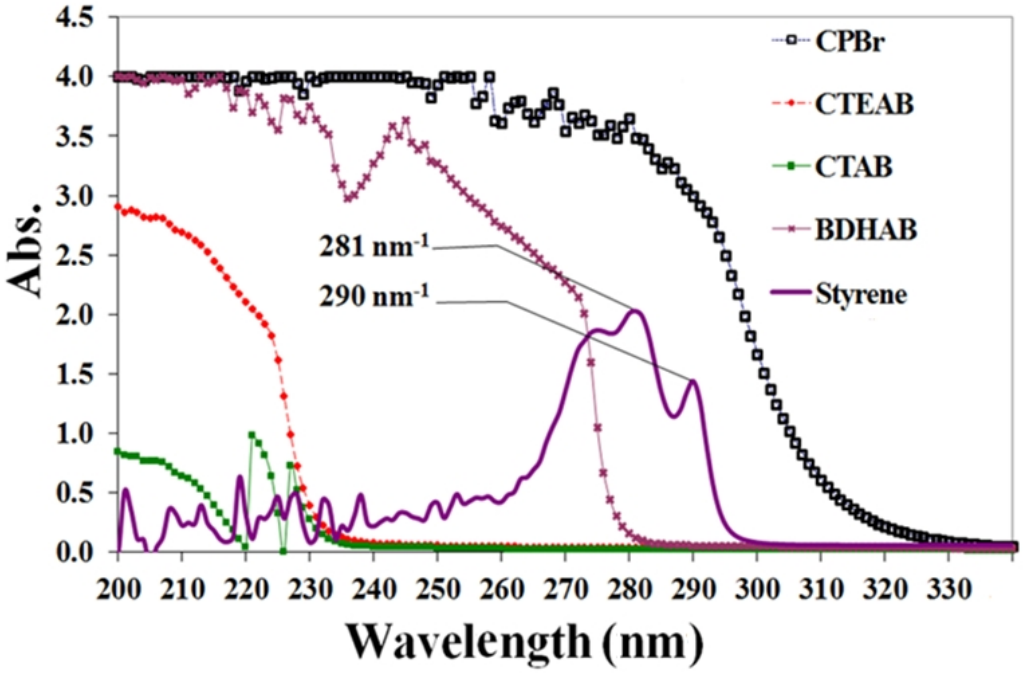

Figure 4.2.1: UV-Vis scans of 0.05M CPBr, CTAB, CTEB, BDHAB and 9μM styrene solution in water where each of these scans measurements were done individually.

The UV-Vis spectroscopy measurements were scanned from 200-400 nm^{-1} for all samples. Figure 4.2.1 shows the overlapping wavelength scans of CPBr, CTAB, CTEAB and BDHAB individually along with that of styrene in water. The UV-Vis scan of styrene in pure water solution illustrates that there are two peaks with λ_{max} at 281 and 290 nm This corresponds to the pattern for styrene commonly found in the literature [*11*]. Overall the UV-Vis measurements for these surfactant solutions without styrene monomer shows there are no overlapping peaks arising from these surfactants with the two λ_{max} of styrene absorption except in the case of CPBr, which shows a relatively high overlap with the styrene peaks. Therefore calculation of the amount of solubilised styrene in these surfactant solutions can be achieved by using UV-Vis except in the case of the CPBr/styrene solutions, due to the huge contribution of CPBr absorption to the measured λ_{max} of styrene. UV-Vis data from surfactant/styrene mixed solutions shows clearly there are shifts in the styrene λ_{max} compared with that found in the styrene/water scan reflecting the hydrocarbon environment of styrene in the micelles. The first peak was shifted from $281nm^{-1}$ to $283nm^{-1}$ and the second λ_{max} shifted from $290nm^{-1}$ to $292nm^{-1}$ (figure 4.2.2).

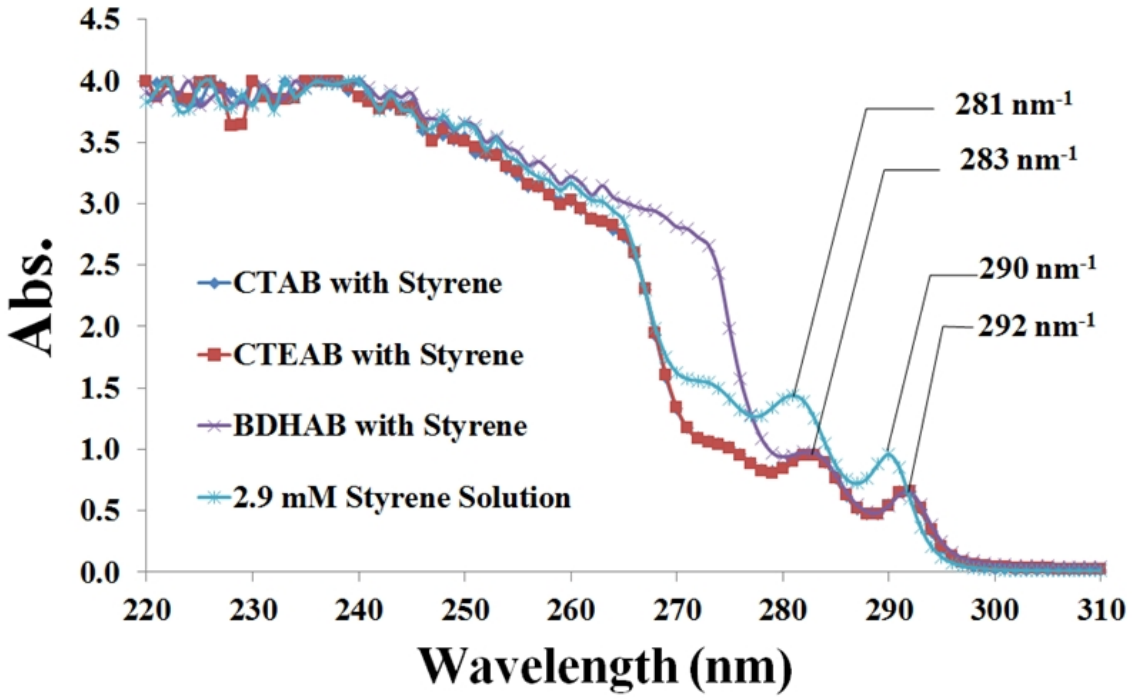

Figure 4.2.2: UV-Vis scans of 0.05M CTAB, CTEAB, BDHAB in solution with 2.9mM styrene in water. Each of these solutions was scanned individually.

Absorption spectroscopy of organic compounds is based on transitions of *n* or π electrons to the π^* excited state. This transition can be measured since the energy of the absorption bands exist within an experimentally measured region of the spectrum. These transitions need an unsaturated group in the molecule to provide the π electrons. In general the λ_{max} of styrene, which occurs due to the $\pi \rightarrow \pi^*$ transition, is shifted due to changes in the molecular environment. This behaviour was observed due to attractive polarisation forces between the surfactant hydrocarbon chain and styrene hydrophobic monomer, which lower the energy levels of both the excited and unexcited states [*12*], compared to those for the same molecule in water.

Table 4.2.1: Percentage of styrene solubilized in 0.05M BDHAB, CTAB and CTEAB micelles.

Surfactant	Theoretical Amount of Styrene (mM)	Calculated Amount of Styrene (mM)	Percentage of solubilised styrene %
BDHAB	0.652	0.782	120
	0.982	1.207	123
	1.304	1.629	125
	1.632	2.137	131
CTAB	0.652	0.684	105
	0.982	1.166	119
	1.304	1.653	127
	1.632	2.122	130
CTEAB	0.652	0.686	105
	0.982	1.131	115
	1.304	1.581	121
	1.632	2.140	131

The error of absorbance, amount of styrene and percentage of solubilised styrene are ±2% of the reported value. The percentage of solubilised styrene was calculation based on styrene solution calibration curve at λ_{max} 283 nm^{-1}.

From the calibration curve was obtained from styrene solution, the amounts of solubilized styrene in surfactant solutions were calculated and reported in Table 4.2.1. The calculated percentage of solubilised styrene in these cationic surfactant micelles shows values of styrene are more than actual amounts of added styrene. This high percentage of styrene, which increases as the concentration of styrene increases indicates that UV-Vis absorbance of styrene in the case of the surfactant/styrene solution was greater than styrene absorptivity in the case of styrene/water solutions. This result is as expected, since styrene is transferred from a highly polar phase (H_2O)

to a less polar medium in the micellar phase (hydrocarbon region); in other words, styrene is solubilized by these surfactant micelles particularly in the hydrophobic phases [*13-17*]. Table 4.2.1 shows that at low concentration of styrene, micelles formed from BDHAB contain the highest percentage compared with the CTAB and CTEAB micelles. This result could be related to a relatively stronger interaction between styrene and BDHAB which favours styrene to solubilisation in BDHAB micelles more fully than in micelles with aliphatic headgroups. At high concentrations of added styrene, the percentage of solubilized styrene for all of these surfactants was used in this experiment is similar. This result suggesting that for surfactants with the same hydrocarbon tail and at this particular concentration of hydrophobic solute, the partition coefficient of hydrophobic molecules between the bulk water and different surfactant micelles tends to be very close [*18, 19*]. This also suggests that hydrocarbon tail interactions are the main influence in the distribution of styrene between the micelle or water phases [*16*]. In general the UV-Vis results suggest that there is interaction between the surfactant hydrocarbon chain and styrene molecules, which produces a shift in the styrene λ_{max} and increase in styrene absorbance values. Subsequently this behaviour indicates that styrene is favoured to encapsulate inside the micelles in the hydrophobic tail region.

4.3 Study of encapsulation of styrene monomer into cationic surfactant micelles using SANS.

The initial work on encapsulation in our group where three related species were studied, cyclohexane, cyclohexanol and benzene,[*20*] found that aromatic species were preferentially solubilised in micelles made from surfactants which also contained aromatic groups. This observation is also supported by the UV-Vis results discussed above. In this experiment hexadecyltrimethylammonium bromide, (C_{16}TAB), benzyldimethylhexadecylammonium bromide (BDHAB) and hexadecylpyridinium bromide (CPBr) were used to compare the relative extent of styrene encapsulation in the micelles with two different types of aromatic headgroup, in the presence and absence of PEI. High Mw ~750 000 Da PEI was used at 15g/L. The total surfactant concentration was 0.05M in 100 % or 70 % D_2O. Tail-deuterated C_{16}TAB (d_{33}-C_{16}TAB) and fully

deuterated $C_{16}TAB$ (d_{42}-$C_{16}TAB$) were used to help determine the monomer location in the micelle. Hydrogenated and deuterated styrene was added at 30, 40 and 50 vol% with respect to the micelle volume (which equivalent to 0.03, 0.06 and 0.09 mM) and the swollen micelles investigated with and without PEI. Figure 4.3.1 shows SANS data for 0.05M CTAB, BDMHAB and CPBr with and without 50% h-Styrene. This data clearly shows, by comparing the surfactants SANS data in the presence and absence of styrene, that deformation of the surfactant micelles structures occurs when styrene is mixed with these surfactants. BDHAB which is the surfactant with a bulky aromatic headgroup shows a greater deformation compared with CTAB and CPBr. Changes in the SANS patterns in the presence and absence of styrene suggests that styrene is encapsulated inside these surfactants micelles, changing their micelles shape or size.

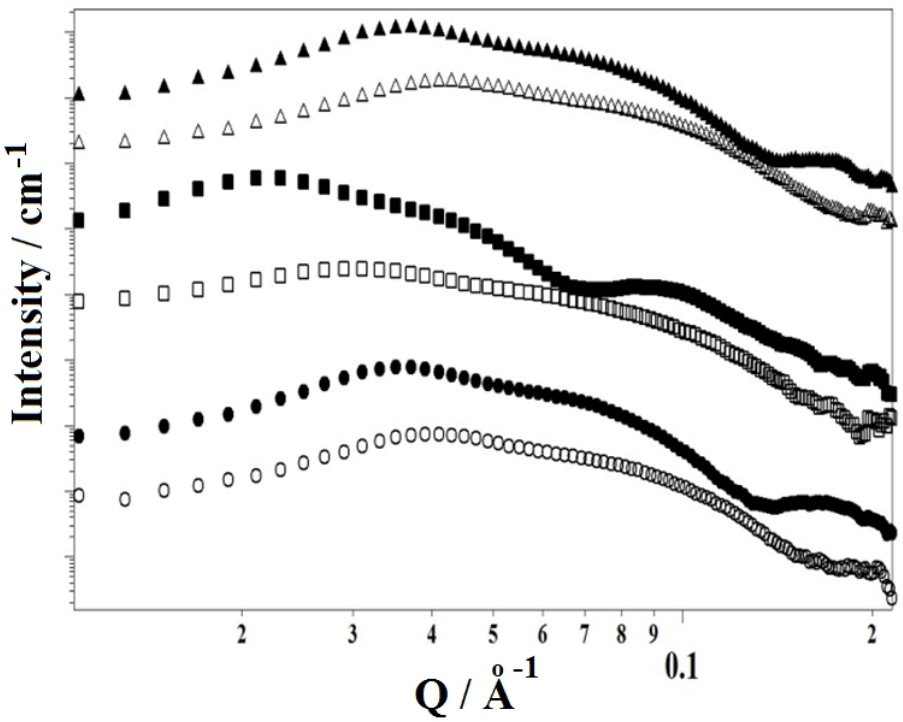

Figure 4.3.1: SANS data for (from bottom to top) 0.05M CTAB, 0.05M CTAB with 50% h-Styrene, 0.05M BDMHAB, 0.05M BDMHAB with 50% h-Styrene, 0.05M CPBr and 0.05M CPBr with 50% h-Styrene. All of these solutions were prepared in 100% D_2O.

4.3.1 Contrast SANS Study of the Location of Encapsulated Styrene Monomer Inside Cationic Surfactant Micelles.

The location of hydrophobic molecules or the position of encapsulated molecules inside amphiphile micelles is not fixed in all solubilisation circumstances. The locations of encapsulated materials depend on various factors such as hydrophobicity of solubilized molecules, the nature of the surfactants and type of solvent [*21*]. In general there are four probable locations for solubilized molecules inside the micelle. The first possibility is that the hydrophobic molecules are located in the central region of the micelle (the core of the micelle), the second is in the region between the tail and the headgroup of micelle (palisade layer), the third is in the headgroup area (shell region) and the fourth possibility is that these molecules are attached or adsorbed at the surface of the micelle. Figure 4.3.2 shows these possibilities for a simple micelle in an aqueous solution [*22*].

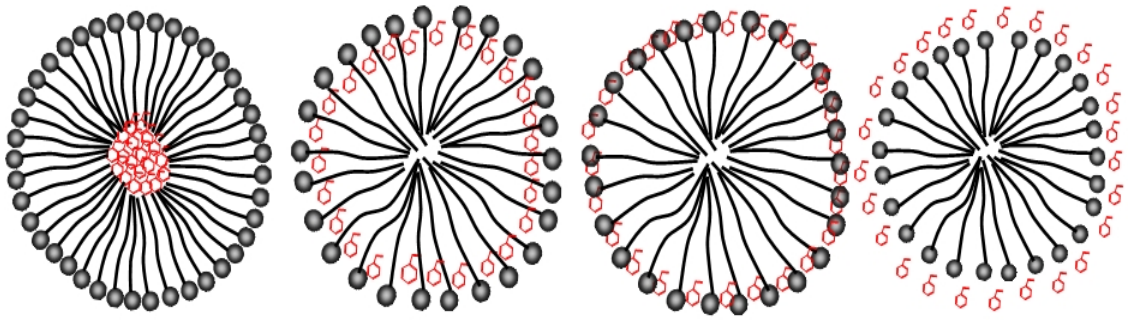

Figure 4.3.2: Locations of encapsulated molecules inside a simple micelle. From left to right encapsulated hydrophobic molecules in the core region, palisade layer, shell region and molecules adsorbed onto the micelle headgroups.

SANS contrast experiments were used to determine the monomer location inside the micelles. Tail deuterated C_{16}TAB (d_{33}-C16TAB) and fully deuterated C_{16}TAB (d_{42}-C_{16}TAB) were used to solubilised hydrogenated and deuterated styrene. Figure 4.3.2 illustrates the scattering length density (SLD) contribution of CTAB micelles with different contrasts in100% D_2O. In the case of fully hydrogenated CTAB the contrast with D_2O comes from both tail and shell of the micelles, while for the headgroup deuterated CTAB the main contrast comes from the core-solvent difference, and for tail deuterated CTAB the main scattering comes from the hydrogenated shell. In case of fully deuterated CTAB, very low scattering is expected since in 100% D_2O there is no significant contrast variation between fully deuterated micelles and D_2O.

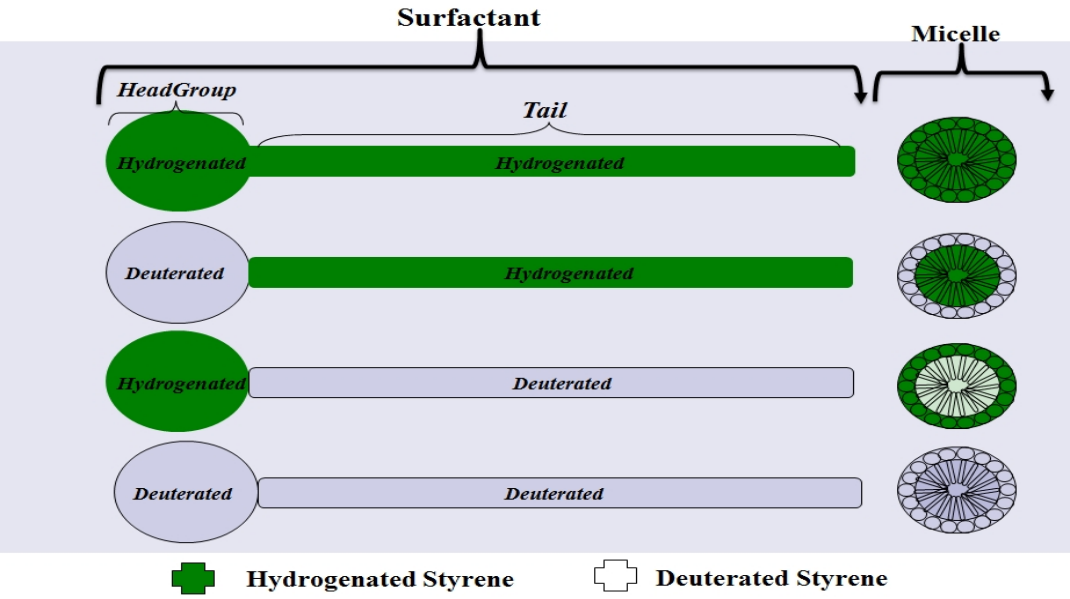

Figure 4.3.2 Schematic of scattering length density contributions to contrast in surfactant micelles in 100% D_2O.

The SANS contrast data from solutions of fully and tail deuterated CTAB show low scattering between Q = 0.131Å^{-1} - 0.213 Å^{-1} compared with hydrogenated CTAB which indicates that this region contains scattering from the CTAB hydrocarbon chain. On the other hand, scattering from solutions of tail deuterated CTAB with 50% of d-styrene emerging between Q = 0.013Å^{-1} - 0.077Å^{-1} indicates the scattering due to the CTAB headgroup. The scattering from a solution of fully deuterated CTAB with 50% of h-styrene indicates that encapsulated hydrogenated styrene itself scatters in the Q region between 0.015Å^{-1} – 0.043Å^{-1}. Fully hydrogenated CTAB micelles with (d or h)-styrene show the highest scattered intensity while fully deuterated CTAB encapsulating h-styrene shows the lowest scattered intensity (figure 4.3.3). In the case of solutions of fully deuterated CTAB encapsulating d-styrene no scattering is observed since there is no big contrast variation between this micelle and D_2O.

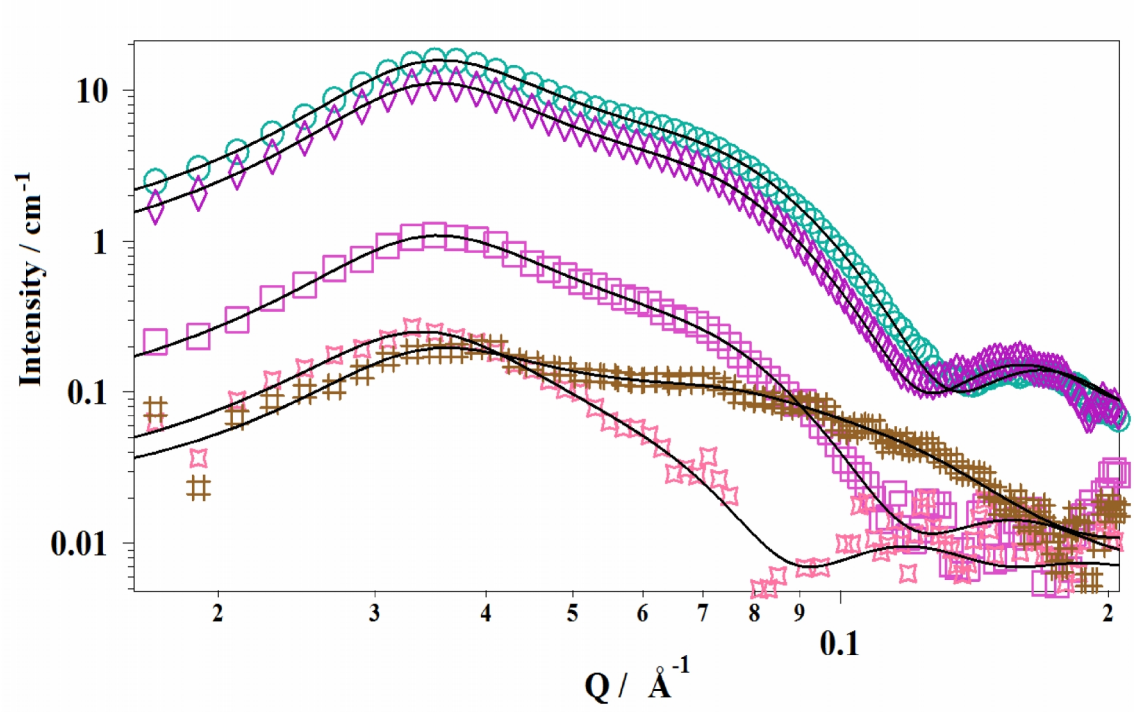

Figure 4.3.3: *SANS data from solutions of (from top to bottom) 0.05M of CTAB with 50% h-Styrene, CTAB with 50% d-Styrene, tail deuterated d_{33}-CTAB with 50% h-Styrene, tail deuterated d_{33}-CTAB with 50% d-Styrene and full deuterated d_{42}-CTAB with 50% h-Styrene. Solid lines show the best fit to a polydisperse core shell sphere model with a Hayter-Penfold structure factor to account for micelle charge.*

A model of a sphere with a polydisperse core and constant shell thickness [*23*] was used to fit the CTAB/styrene data since this model fits the data best. The procedure was written by Dr. Steve Kline at the NIST Centre for Neutron Scattering for the Igor PRO platform (WaveMetrics) [*24*], and used the Hayter-Penfold mean spherical approximation as the structure factor [*25*]. The form factor is normalized by the average micelle volume as shown in equation below:

$$P(q) = scale \times \langle f \times f \rangle / vol + bkg \qquad (4.1)$$

where *P(q)* is the form factor, *vol* micelle volume, $\langle\ \rangle$ is the average over the size distribution, *bkg* incoherent background and *f* is the single micelle scattering amplitude, appropriately averaged over the Schulz distribution of radii [*26*]. To normalize the form factor by the average micelle volume, <V> can written as:

$$\langle v \rangle = 4\pi/3 \langle r^3 \rangle \qquad (4.2)$$

$$\langle r^3 \rangle = (z+3)\,(z+2) / (z+1)^2 \langle r \rangle \qquad (4.3)$$

The z here is the width parameter of the Schulz distribution which equals: $z = (1/p^2) - 1$. The average micelles diameter equal: 2 x (radius + shell thickness).

For the polydisperse core-shell sphere model with Hayter-Penfold structure factor, the values of the SLD contrast in the case of CTAB without styrene were initially calculated for the expected compositions of the surfactants intermicellar phase and micelle cores, based on the prepared solutions (see Chapter 2 Table 2.11.1-2.11.2). Temperature was fixed at 308 K and dielectric constant was 78. The monovalent salt concentration was fixed at zero. Volume fractions for each surfactant solution were all calculated and fixed. The main variables fitted were the average micelle core radius and shell thickness. Global fitting was performed for all of the SANS patterns from hydrogenated and deuterated styrene solubilized in micelles using each of the individual of contrasts CTAB. All of these CTAB/styrene solutions were dissolved in 100% D_2O. The fitted parameters from the global fitting of this SANS data using polydisperse core-shell sphere model is shown in Table 4.3.1.

This table shows a number of interesting results. The SLD value of micelle core of composed of fully h-CTAB encapsulating d-styrene is about 10 times higher SLD than the core of the same contrast CTAB but encapsulated h-styrene. On the other hand the SLD for the shell of fully h-CTAB encapsulating h or d –styrene are very similar to the SLDs of the shell of fully h-CTAB without styrene. In addition the constant shell thickness in the case of full h-CTAB micelles with and without styrene indicates that the styrene does not sit in the shell region. This result agrees with the nature and polarity of both styrene and CTAB headgroup. The CTAB micelles headgroup (which forms the micelle shell layer) is a highly polar region due to the quaternary ammonium group, which gives the CTAB headgroup with a charge of +1. Styrene is also well known as a hydrophobic molecule therefore it is favoured to dissolve in non-polar media such as oily phase in the micelle solution.

The SANS patterns from solutions of fully h-CTAB micelles illustrate clearly that as the styrene concentration was increased from 0% to 50% the micelles core radii were swollen from 19Å to 25Å while the shell layer almost remained stable. Moreover the SLD's of the core of the fully h-CTAB micelles shows significant increases when

comparing the cases of micelles solubilising both h and d styrene, while the SLD's of the shells of fully h-CTAB micelles do not show notable variation in the presence and absence of styrene. From these results it is suggested that styrene is encapsulated inside CTAB micelles, particularly in the hydrophobic region.

Table 4.3.1: Fitting of CTAB contrast data with different amount of styrene using a polydisperse core-shell sphere model with a constant shell thickness and a Hayter-Penfold structure factor.

CTAB contrast	% of Styr.	Core radius (Å)	Shell thick. (Å)	SLD Core ($Å^{-2}$) of h-Styrene	SLD Core ($Å^{-2}$) of d-Styrene	SLD Shell ($Å^{-2}$) of h-Styrene	SLD Shell ($Å^{-2}$) of d-Styrene
Full h-CTAB	0	19	5	-3.53×10^{-7} *	-3.53×10^{-7} *	-5.96×10^{-6}	-5.96×10^{-6}
Full h-CTAB	50	25	6	2.21×10^{-7}	2.67×10^{-6}	-5.85×10^{-6}	-5.84×10^{-6}
Tail d-CTAB	50	23	14	5.24×10^{-6}	7.03×10^{-6}	4.58×10^{-6}	5.12×10^{-6}
Full d-CTAB	50	22	14	3.69×10^{-6}	N/A	6.37×10^{-6}	N/A

The errors of core radii are ± 4 Å, ± 2 Å of shell thickness, errors of SLD core are ± 1.61×10^{-6} $Å^{-2}$ and ± 4.97 $\times10^{-7}$ $Å^{-2}$ of shell thickness. the SLD value was calculated and held.*

The fitting results for both full and tail deuterated CTAB (d_{33}-CTAB and d_{44}-CTAB) micelles solubilising h and d-styrene shows clearly an increase in the micelle shell thickness and at the same time small losses are seen in the micelle core radius. In addition the SLD's of micelle shell layer for both d_{33}-CTAB and d_{44}-CTAB shows significant increases for micelles solubilising styrene compared with fully hydrogenated CTAB solubilising the same amount of styrene. This increasing of shell thickness in the case of d_{33}-CTAB and d_{44}-CTAB solubilising styrene does not mean that styrene is located in shell layer, since the data from the fully hydrogenated CTAB solubilising h and d styrene illustrated very clearly that styrene is located in the oily phases, and not in the shell region. The increase in SLD could be due to the low contrast between the micelles core and D_2O in the case of d_{33}-CTAB and d_{44}-CTAB solubilising styrene, the polydisperse core-shell spheres model cannot distinguish between the palisade layer and shell layer and these are treated as one region. Therefore this variation in shell thickness and core radius could therefore be due to encapsulation and concentration of the styrene molecules inside CTAB micelles in the palisade layer. However these results do not deny that there is also styrene in the core region. The micelles core radius swelling is

seen in the in all CTAB contrasts solubilising styrene compared with CTAB micelle core radii without styrene. However the increases in the SLD's for CTAB contrasts solubilising styrene also suggest that there is some portion of the styrene located in the micelle core as well as some of the styrene in the palisade layer.

O'Driscoll suggested that hydrophobic molecules such as benzene could be favoured to solubilise in the cationic surfactant such as CTAB and be located in the palisade layer due to polarisation charge-dipole which forms a complex with the surfactant headgroups and these solutes [*27*]. This also agrees with earlier UV-Vis results by others which suggested that the aromatic ring of the styrene can sit in the palisade region of the micelles [*10*].

Therefore the resulting model from fitting of SANS contrast data for the CTAB/Styrene system suggest that styrene is encapsulated and located both in the palisade layer which is the region between headgroup and hydrocarbon chain, and at the same time some of encapsulated styrene is in the micelle core, mixed with the surfactant alkyl tails [*28, 29*] as illustrated in figure 4.3.4.

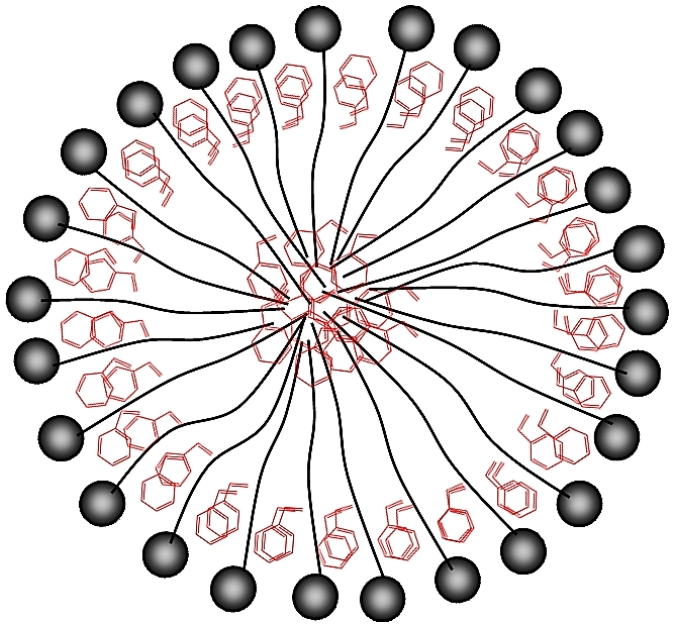

Figure 4.3.4: *Schematic of CTAB micelle encapsulating styrene molecules in aqueous solution based on CTAB contrast SANS data.*

4.3.2 Effects of PEI on Cationic Surfactant Micelle Solutions Encapsulating Styrene.

AS mentioned in chapter one, there are three general scenarios describing the surfactant-polymer interaction in aqueous solutions. The first scenario describes co-operative association or binding of the surfactant to the polymer chain and the second scenario is that surfactant micelles are located in the vicinity of the polymer chain [*30*]. A third scenario proposed a structure in which the aggregated surfactant micelles are surrounded by macromolecules in a loopy configuration (figure. 4.3.5).

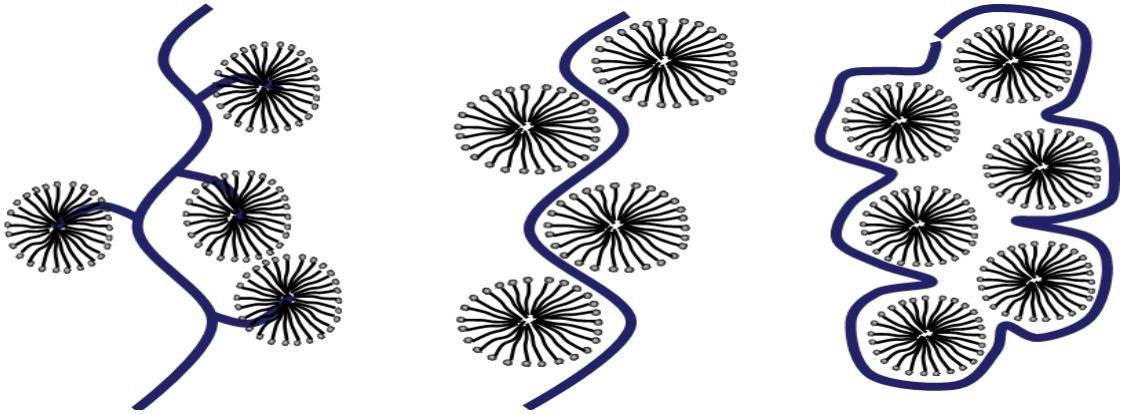

Figure 4.3.5: *Schematic illustrating polymer/surfactant micelles interactions. From left to right, surfactant micelles bound to the polymer chain, surfactant micelles in the vicinity of the polymer chain and aggregated surfactant micelles surrounded by macromolecules in a loopy configuration.*

SANS contrast experiments were used to understand the relationship between cationic surfactant micelles and branched polyethyleneimine (PEI) in mixed solutions. CTAB, tail deuterated C_{16}TAB (d_{33}-C_{16}TAB) and fully deuterated C_{16}TAB (d_{42}-C_{16}TAB) were used to solubilized hydrogenated and deuterated styrene and high Mw ~750 000 Da of PEI was used at 15g/L. A model of a sphere with a polydisperse core and constant shell thickness [*23*] with the Hayter-Penfold mean spherical approximation as the structure factor [*25*] was used to fit the multiple contrast CTAB/LPEI solubilising styrene data simultaneously, as this model fits the data best. Figure 4.3.6 shows the SANS patterns of different contrasts of CTAB micelles with LPEI solubilising styrene. Results from fitting this data for solutions of CTAB with LPEI solubilising different amount of styrene are reported in Table 4.3.2.

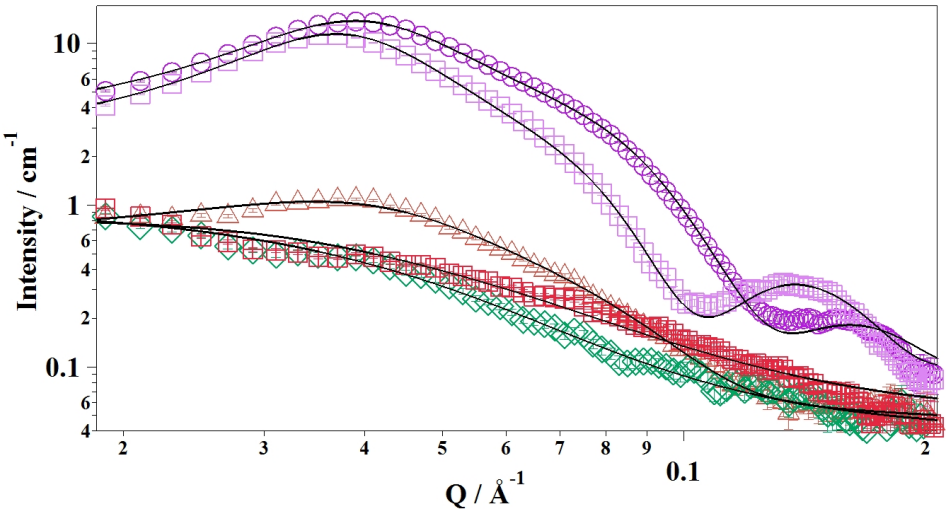

Figure 4.3.6: *SANS data of (from top to bottom)0.05M of CTAB/LPEI with 50% h-styrene, CTAB/LPEI with 50% d-Styrene, tail deuterated d_{33}-CTAB/LPEI with 50% h-styrene, tail deuterated d_{33}-CTAB/LPEI with 50% d-styrene and fully deuterated d_{42}-CTAB/LPEI with 50% h-styrene. Solid lines show the best fit to a polydisperse core-shell sphere model as described in the text above.*

From the data in Table 4.3.1 and 4.3.2 it can be seen in general that the micelle sizes found in solutions of CTAB with LPEI solubilising different amount of styrene are practically close to those found for the CTAB/styrene system without PEI. The CTAB micelle core radius in the presence of PEI was between 21-24 Å, where it was 19-25Å in the case of micelles of CTAB/styrene without PEI.

Table 4.3.2: Results from fitting data from multiple contrasts of CTAB micelles mixed with LPEI, solubilising different amount of styrene. Parameters were calculated from the polydisperse core-shell sphere model with a constant shell thickness and a Hayter-Penfold structure factor.

CTAB contrast	% of Styr.	Core radius (Å)	Shell thick. (Å)	SLD Core ($Å^{-2}$) with h-Styrene	SLD Core ($Å^{-2}$) with d-Styrene	SLD Shell ($Å^{-2}$) with h-Styrene	SLD Shell ($Å^{-2}$) with d-Styrene
Full h-CTAB	0	21	5	-3.74×10^{-7}	-3.74×10^{-7}	-2.80×10^{-7} *	-2.80×10^{-7} *
Full h-CTAB	50	24	5	6.35×10^{-7}	5.08×10^{-6}	-8.37×10^{-7}	-9.41×10^{-7}
Tail d-CTAB	50	22	14	4.14×10^{-6}	6.19×10^{-6}	5.14×10^{-6}	5.61×10^{-6}
Full d-CTAB	50	22	14	3.15×10^{-6}	N/A	5.94×10^{-6}	N/A

*The errors of core radii are ± 4 Å, ± 2 Å of shell thickness, errors of SLD core are ± 1.26×10^{-6} $Å^{-2}$ and ± 9.55 $\times10^{-8}$ $Å^{-2}$ for shell thickness. *the SLD value was calculated and held.*

These results indicate that there is no obvious variation in the micelle core sizes in both cases (CTAB/styrene systems with and without polyelectrolyte). Consequently these results suggesting that possibility of association or binding the surfactant micelles to the polymer chain is not logical. This because theoretically in the case of surfactant micelles binding to the polymer chain the core radius should be swollen compared with micelles not associated or bonded with a polymer chain. On the other hand the stability of the value found in all CTAB contrasts of the micelle shell thickness both in the presence and absence of PEI, suggests that surrounding or wrapping these micelles by the macromolecules is also not compatible with this system, otherwise significant variation in the shell thickness and SLD should be noticed. However no clear variation in shell thickness has been seen in this system. Therefore the second scenario as shown in figure 4.3.5 is the most reasonable scenario applicable to this system. This scenario suggesting that there is interaction between PEI and this cationic micelles but it is not strong enough to interact directly with these surfactant headgroups and wrap around the micelles as occurs in the case of opposite charge polymer/surfactant interactions [*31*]. In other words there is attractive complex interaction between the cationic surfactant micelles system and PEI; which leads to the polyethyleneimine getting closer to the micelle headgroup through electrostatic interaction between PEI amino group and the cationic surfactant micelle headgroup [*32, 33*]. At the same time PEI interacts with water molecules close to the surfactant micelle headgroup, and also with other PEI molecules by hydrogen bonding [*34, 35*]. In addition the Br- counterion from the surfactant will form equilibrium interactions between the cationic surfactant headgroup, water molecules and PEI [*36*].

4.4 Extent of encapsulated styrene in cationic surfactant micelle solutions with and without PEI

Micelles of CPBr and BDMHAB swollen with styrene were also investigated using SANS. For these systems deuterated surfactants were not available, thus the contrasts were limited to h- and d-styrene. Many attempts were made to fit the SANS data for micelles encapsulating styrene and a variety of models were investigated including using prolate and oblate ellipsoids, cylinders, core-shell spheres, core- shell spheres with polydisperse core and other models. However since only two contrasts were available for these solutions a simpler model than that used for CTAB (above) was required, since fitting complex models with many variables is not justified with so few contrasts.

Therefore all SANS data were modelled simultaneously (surfactants solubilising hydrogenated and deuterated styrene) using a uniform ellipsoid model [*24*], with the Hayter-Penfold mean spherical approximation as the structure factor [*25*]. This model was chosen for fitting the SANS profiles based on the fits giving the lowest χ^2 values. During fitting using the uniform ellipsoid model the temperature was fixed at 308 K and dielectric constant fixed at 78. The monovalent salt concentration was fixed at zero in the case of surfactant solution without polymer and 0.013M in the case of presence 1.5% (w/v) PEI, based on the measured charge on the polymer at this pH [*33*]. Volume fractions for each surfactant solution were all calculated and fixed. The SLD contrast for surfactant micelles without styrene were initially calculated for the expected compositions of the surfactants intermicellar phase and micelle cores, based on the prepared solutions as reported in chapter 2 table 2.11.1 and 2.11.2. Hydrogenated and deuterated styrene was added at 30, 40 and 50 vol% with respect to the micelle volume and the swollen micelles investigated with and without PEI. The SANS patterns of 0.05M surfactant solutions with various concentrations of styrene and L-PEI at different contrasts are shown in figure 4.4.1.The micelle radii of BDMHAB, CPBr and CTAB with and without 1.5% L-PEI incorporating different amount of styrene were calculated from the fitting of the uniform ellipsoid model and the results shown in table 4.4.1. Micelles charge and SLD's of those fitting are shown in appendix.

Two methods were used to investigate the amount of encapsulated styrene in these cationic surfactant micelles. Method one is discussed in detail first, followed below by

method 2. The first method depends on using the SLD contrast between hydrogenated surfactant micelles encapsulating either hydrogenated or deuterated styrene.

In this experiment BDHAB, CPBr and CTAB were used to solubilise hydrogenated and deuterated styrene, where all of these cationic surfactants have a C_{16} hydrocarbon chain. Therefore the percentage of encapsulated styrene can be calculated using equation 4.4:

$$SLD_{ellipse} = [(1 - Ps)\, SLD_m + Ps * SLD_{sty}] \qquad (4.4)$$

Where, $SLD_{ellipse}$ is the SLD resulting from fitting the scattering from the surfactant micelles as an ellipsoid encapsulating styrene, SLD_S is the solvent SLD; Ps is the calculated molar percentage of encapsulated styrene; SLD_m is the micelle scattering length density, which is the SLD of the C_{16} surfactant tails; and SLD_{sty} is the SLD of either hydrogenated or deuterated styrene [*27*].

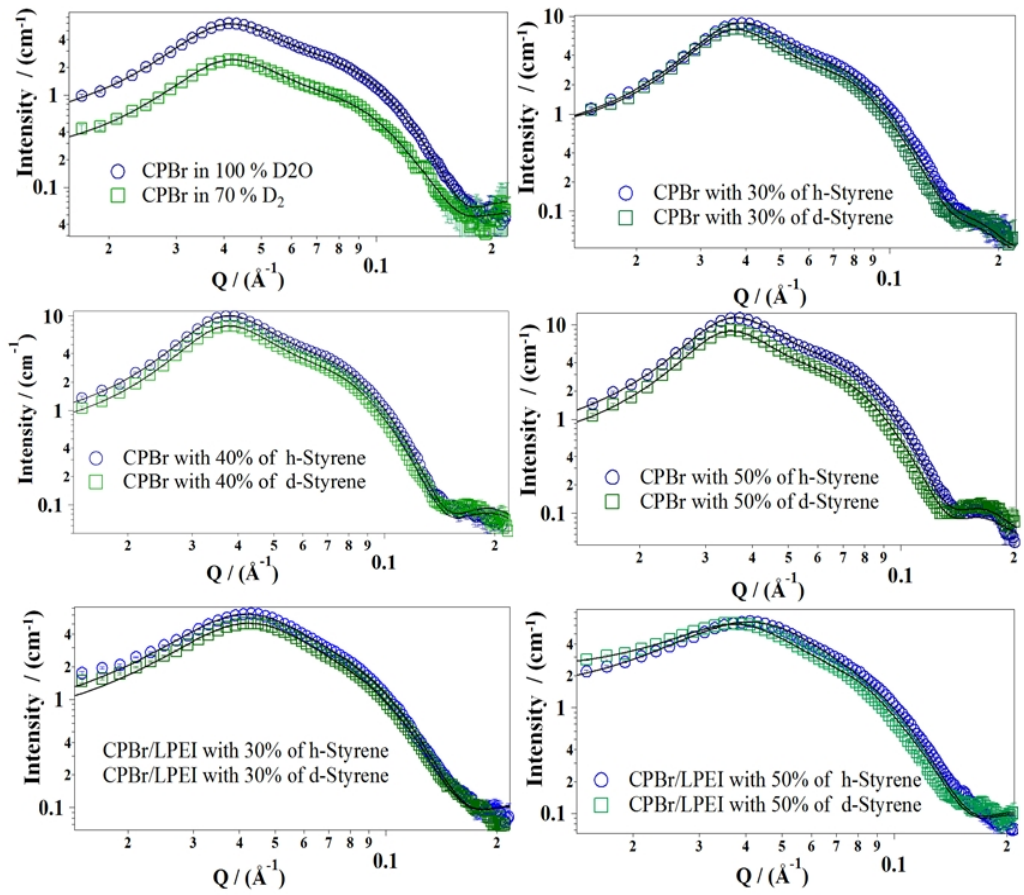

Figure 4.4.1: SANS patterns from solutions of 0.05M CPBr with (0, 30, 40 and 50%) of h&d styrene with and without PEI. Solid lines show the best global fitting to the data using a uniform ellipsoid model with a Hayter Penfold structure factor.

Table 4.4.1: Measured value of encapsulated styrene and micelle radii for BDMHAB, CPBr and CTAB with and without of 1.5% LPEI. Calculated by fitting the SANS data and using method 1.

Solution	Amount of styrene added (vol%)	Ra (Å)	Rb (Å)	Measured encapsulated styrene (vol%)
BDHAB	30	108	25	0
	40	81	60	100
	50	81	59	100
BDHAB/LPEI	30	191	25	7
	50	200	25	19
CPBr	30	42	26	16
	40	42	27	19
	50	44	30	27
CPBr/LPEI	30	42	24	15
	50	44	24	7
CTAB	50	43	32	26
CTAB /LPEI	50	46	32	35

The maximum errors in micelle radii are ± 3Å. The errors in measured values of encapsulated styrene (vol%) are ±5% , where the values less than 0.05% and more than 100% were recorded as 0% and 100% respectively.

The fitting results show, in general, a swelling of the ellipsoidal micelles as the amount of styrene is increased and this relation is, in general, directly proportional to the amount of styrene added (Table 4.4.1). BDHAB shows the highest measured values of encapsulated styrene particularly at 40% and 50% of added styrene. However at 30% of added styrene for the same surfactant of the calculation of styrene content from the fitted SLD values suggests that no styrene was encapsulated. The fitted results for the CPBr micelles show a systematic relationship between increasing amounts of styrene and expansion in R_a and R_b and this relation is also compatible with the increasing percentage of measured encapsulated styrene. However the measured values of encapsulating styrene in the CPBr micelles are less than one third of the actual amounts were added. CPBr micelles with 50% of added styrene showed slight high measured value of encapsulated styrene, despite having different headgroup types and bulkiness. CTAB has an aliphatic and bigger headgroup compared with CPBr which has an

aromatic headgroup but a lower headgroup surface area (the headgroup area of CTAB = 64Å^2 [*37*] while CPBr is 40 Å^2 [*38*]). These results suggest that the cationic surfactant consist of aromatic headgroup have more solubilisation capacity of hydrophobic molecules than aliphatic surfactant headgroups. Dar et al. [*39*] reported that the solubilisation capacity of the cationic surfactant improved by increases in the hydrophobicity of headgroup, such as substitution of a benzyl group in the cationic surfactant headgroups. On the other hand some authors found that there is π-cation interaction between these aromatic solutes and the aromatic part in the surfactant headgroups which subsequently increases the solubilisation amounts [*40-43*].

In the presence of polyelectrolyte both BDHAB and CPBr (surfactants with aromatic headgroup) demonstrate a dramatic drop in the measured values of encapsulated styrene compared with the same surfactant without PEI. However CTAB does not show this behaviour in the presence of PEI. Figure 4.4.2 display the effects of PEI on these cationic surfactants and their encapsulation capacity for styrene, where calculated by method 1 as explained above.

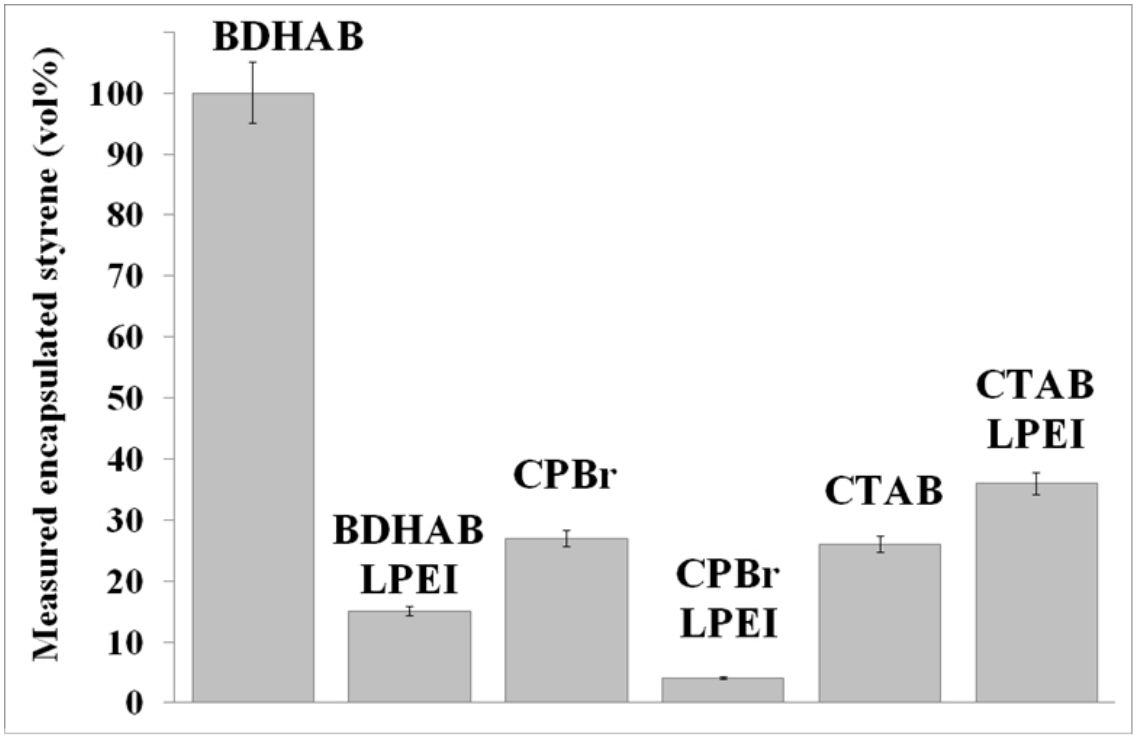

Figure 4.4.2: Measured encapsulated styrene for the 50% (vol.%) of added styrene in 0.05M cationic surfactant solutions in presence and absence of PEI.

This decrease in measured encapsulated amounts of styrene found after adding PEI could be due to the interaction between PEI and these surfactants headgroups, since this interaction will vary for these different surfactant headgroups. However the effects of PEI on the micelles aggregation number (N_{agg}) for cationic surfactants without styrene in Chapter 3 showed that surfactants with aliphatic headgroups did not have large changes in N_{agg} when adding the PEI, while surfactants with aromatic headgroups and consist from C_{16} hydrocarbon chain showed a growth in N_{agg} when PEI was present (Chapter 3 Table 3.3.11). As can be seen from Figure 4.4.2 these surfactants with aromatic headgroups show different behaviour for encapsulation of styrene. These results suggest that the interaction between the PEI and these surfactants micelles are changed when styrene is encapsulated inside these micelles predominantly when these solutes are located in the palisade layer, as suggested for this system [*44*]. Addition of PEI to micelles which are already encapsulating styrene reduces the charge density on the micelle which decreases the micellar curvature thus changing the average distance between the surfactant headgroups [*45, 46*]. The change in micelle curvature is shown by the change in shape of the micelles after addition of PEI. The micelles become longer and thinner when PEI is added, reflecting the decrease in micellar curvature (see Table 4.4.1)

Overall comparing the surfactant micelle radii and increasing amount of styrene added to these surfactant/PEI/styrene solutions with measured values of encapsulated styrene by using the SLD method it seems that there are big variations between the addition of styrene and the measured amount of encapsulated styrene as shown in table 4.4.1. This fluctuation in calculated measured value was also reported by Wasbrough since he used the same calculation method to measure the quantity of cyclohexane and cyclohexanol that were solubilised by cationic surfactants in similar systems [*47*]. On the other hand both Wasbrough [*47*] and O'Driscoll [*27*] observed in general that the calculated amount of these solutes inside cationic surfactant micelles are significantly lower than theoretically expected by using the SLD calculation method. The inaccuracy of this method it could be due to one of several reasons. This method is based on the percentage of SLD contribution from both the micelle core and the additives, so the calculated percentage of additives in the micelle depends on the proportion of each of these, which means that if one of them is present as 30% the other should be present as 70%., assuming ideal mixing, which is often not the case since many papers report that aggregation number of surfactant micelles can change while solubilising some additives

[*48*]. The second reason could be related to the model used to fit the SANS data from encapsulation hydrophobic molecules in cationic surfactants. The model was chosen based on the lowest χ^2 however, that does not mean this model will simulate the reality 100% since there are many factors it does not take into consideration, including the more realistic core-shell structure of surfactant micelles. However since it was only possible to obtain two contrasts for this data, fitting a more complex model with a greater number of parameters is not mathematically justified since the simple model describes the data within the limits of the error.

The second method used to calculate the percentage or the amount of styrene encapsulated inside surfactant micelles uses the differences in the micelle volumes. Since the size of micelles shows a very clear systematic increase as the concentration of additives is increased, in this method, the volumes of the uniform ellipsoids were calculated from the radii calculated in fitting the SANS data for the surfactant micelles without any additives. This volume was then compared with the volume resulting from fitting data for encapsulated styrene in the same surfactant micelles. The differences between the volume of micelles without styrene and the total volume of the micelles after encapsulating styrene is assumed to be the volume occupied by styrene itself. This volume can be divided by the volume of one styrene molecule to give the number of styrene molecules encapsulated in the micelles. The volume of the styrene molecules was calculated to be 190.3Å^3 by using the density of styrene monomer (0.906 g/mL) [*49*]. Table 4.4.2 shows the calculated number of styrene molecules encapsulated in cationic surfactant micelles in the presence and absence of LPEI. Micelle volumes and aggregation number of surfactants were calculated as explained in chapter 3. The encapsulation ratio expresses the number of encapsulated styrene molecules inside surfactant micelle to the number of aggregate surfactant molecules.

As shown from table 4.4.2, BDHAB without PEI has the biggest micelle volume, followed by BDHAB with PEI compared with the other surfactant micelles. Both BDHAB with and without PEI also demonstrate the highest number of encapsulated styrene molecules. This could be related to the hydrophobicity and nature of BDHAB headgroup in which it is likely that the benzyl group performs as a second hydrophobic tail [*50*]. In the case of 0% and 30% of styrene, BDHAB with PEI has bigger micelle volumes and thus the larger amount of encapsulated styrene compared BDHAB without PEI, while in case of 50% it shows the opposite effect. This may be related to the

reforming of BDHAB micelles when encapsulating relatively high amounts of styrene . CPBr shows an almost similar trend as BDHAB.

Table 4.4.2: Calculated volumes of surfactant micelles, encapsulated styrene molecules by using micelle volume variation (method 2), aggregation number (N_{agg}) and the ratio of encapsulated styrene to the number of aggregate surfactant molecules.

Solution	Styrene added (vol.%)	Ra (Å)	Rb (Å)	Calc. Ellipsoid vol. (Å^3)	Calc. number of encapsulated styrene	N_{agg}	Encapsulation ratio
BDHAB	0	72	22	145971	0	204	
	30	108	25	282743	719	395	1.82
	40	81	60	1221451	5653	1706	3.31
	50	81	59	1181075	5440	1650	3.30
BDHAB/ LPEI	0	100	23	221587	0	310	
	30	191	25	500037	1464	698	2.10
	50	200	25	523599	1587	731	2.17
CPBr	0	35	23	80646	0	140	
	30	42	26	119371	204	207	0.98
	40	42	27	129647	258	224	1.15
	50	44	30	162201	429	281	1.53
CPBr/LP EI	0	38	24	94675	0	164	
	30	42	24	101312	35	175	0.20
	50	44	24	109581	78	190	0.41
CTAB	0	39	25	98814	0	157	
	50	43	32	181404	434	288	1.51
CTAB/L PEI	0	36	26	99581	0	158	
	50	46	32	195651	505	310	1.63

The maximum errors of radii were ± 3Å and ± 5 % for the reported values of each micelle volumes, encapsulated styrene molecules, N_{agg} and encapsulation ratio.

CPBr illustrates systematic increases in the micelles volume and number of encapsulated styrene molecules in the case of the presence and absence of PEI, However in the presence PEI at 30%-50% of styrene addition the CPBr micelles had a

lower volume and amount of encapsulated styrene compared with the same system but without PEI. CTAB solutions with and without PEI also showed increases in both micelles volume and in calculated number of encapsulated styrene (as discussed above). The effect of PEI on the encapsulation capacity of styrene using method 1 and 2 in these aromatic and aliphatic surfactants headgroups shows in general a drop in encapsulation capacity in presence of PEI particularly for the surfactants with aromatic headgroups. O'Driscoll et al [*27*] found a significant drop in the aggregation number of CTAB micelles solubilising cyclohexane or decane when this system incorporated PEI (MW~ 25,000 Da). On the other hand Reekmans et al [*51*] reported a decrease in N_{agg} (by more than the half) of a cetyltrimethylammonium chloride micelles solution when anon-ionic polymer was added to a solution with these micelles. Figure 4.4.3 shows this variation in micelles volume in presence and absence of PEI for these cationic surfactant solutions encapsulating different amount of styrene.

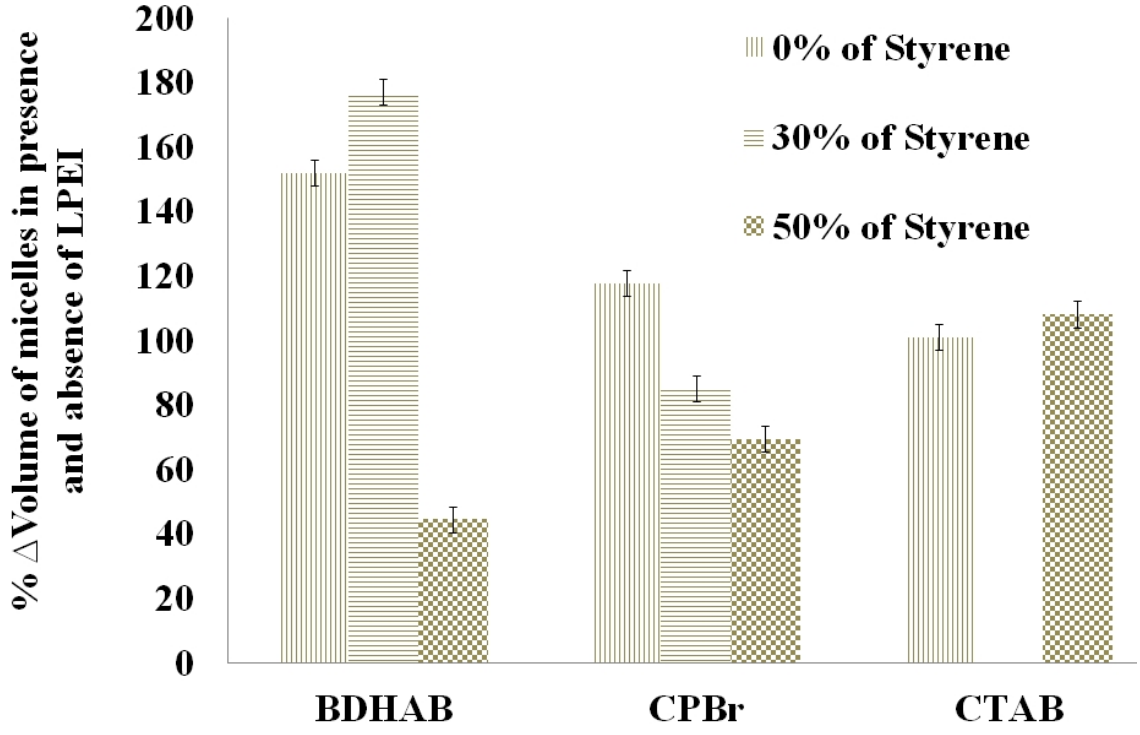

Figure 4.4.3: Percentage of the micelle volume variation for CTAB, CPBr and BDHAB in the case of the presence and absence of PEI for micelles encapsulating different amount of styrene.

Polymer-surfactant interactions without additives were discussed in the previous chapter. In this chapter the suggested interaction model between polyethyleneimine and

cationic surfactant micelles encapsulating hydrophobic monomer has been discussed above. The scattering data in the first part of this chapter suggests that the PEI does not wrap around the CTAB micelles nor do micelles bind to the polymer via their hydrophobic cores. Rather there is a complex interaction between PEI and the outer stern layer of these cationic surfactant micelles and at the same time with the aqueous medium, which distributes the polymer phase between the micelles as a hydrogel network rather than as a dense polymer matrix [*32-36*]. Further information about this point is needed to understand the effects of PEI on the micelles versus concentration of encapsulated hydrophobic monomer molecules. To understand the effects of PEI on the micelles during encapsulation of different amounts of styrene the percentage of micelles volume change was calculated in the case of the presence and absence of PEI for the same styrene concentration in each surfactant micellar system. For example, the volume of CTAB micelles with 1.5% LPEI and 0% of styrene was divided by the volume of CTAB micelles at 0% of styrene and without LPEI then multiply by 100%. The results of these calculations were summarized in figure 4.4.3. Therefore any value above 100% that is means the effects of addition PEI are to expand the micelles volume and vice versa. CTAB in general does not show obvious changes in the micelle volumes before and after addition of PEI and that is seen for the case of encapsulating 50% of styrene. CPBr and BDHAB show a growth in the micelle volume when PEI is added without styrene, however at 30% of added styrene the CPBr micelle volume decreased while that of BDHAB increased about 80% compared with the same BDHAB/styrene system but without PEI. At the 50% of addition styrene and in presence of PEI the micelle volume dramatically diminished becoming around one third of the micelle size in the case of BDHAB and around the half of CPBr micelle size compared with the same system without PEI. However all of these surfactants consist of a C_{16} hydrocarbon chain, consequently PEI effects on these cationic surfactants micelles suggest that the interaction between PEI and the headgroups of cationic surfactants micelle encapsulating hydrophobic molecules is not similar. This means, the surfactants headgroup plays very important role in the micellar volume. Here the surfactant headgroups (nature and hydrophobicity) also can determine the effects of the polyelectrolyte on these micelles encapsulating hydrophobic molecules. Figure 4.4.4 illustrates the suggested effects of PEI on cationic surfactants micelles encapsulating hydrophobic monomer molecules.

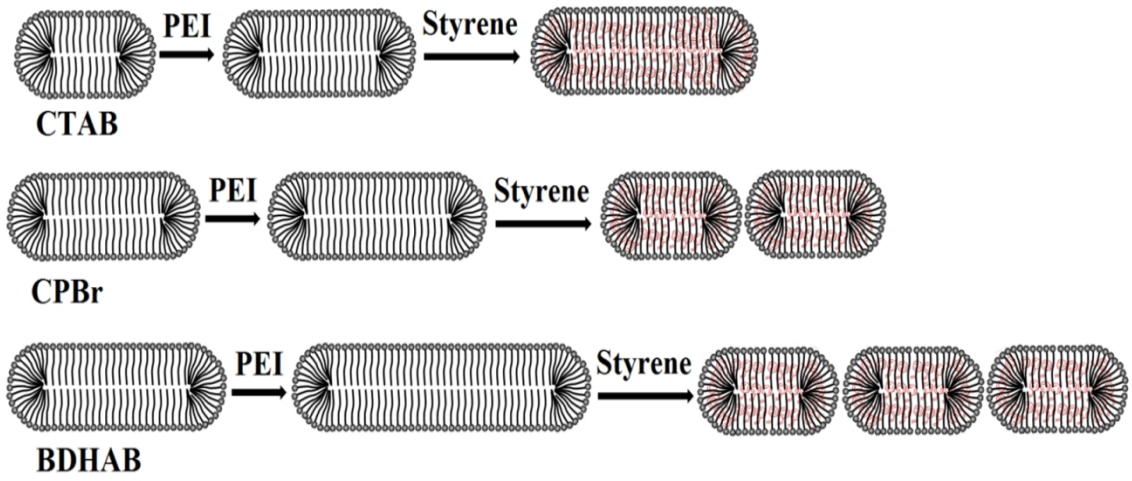

Figure 4.4.4 Schematic suggesting the effects of PEI on the various cationic surfactants micelles encapsulated 50% of hydrophobic monomer.

As mentioned above that BDHAB micelles encapsulating 50% of styrene in the presence of 1.5% L-PEI shows that the micelles volume is a third of the size compared with BDHAB micelles encapsulating the same amount of styrene without PEI. However for CPBr encapsulating 50% of styrene in the presence of 1.5% L-PEI the micelle size is half that of CPBr micelles encapsulating the same amount of styrene without PEI. These results suggests that the BDHAB and the CPBr micelles tends to split or reform themselves into smaller micelles. CTAB, which has an aliphatic headgroup, does not show obvious micellar reforming at the same concentration of styrene. This results suggesting that the influence or the interaction between PEI and these surfactants micelles was the greatest in BDHAB then CPBr while CTAB has shown the smallest effect. These results support the suggestion that more of the styrene is located in the palisade layer in the case of BDHAB and CPBr, since the cationic surfactant micelles with aromatic headgroups have more aptitude to encapsulate hydrophobic molecules than those aliphatic surfactant headgroups [*39*]. In addition these solutes interact with these surfactant micelles headgroup changing the size and morphology of these micelles [*40-43*]. Subsequently, the presence of PEI generally reduce the charge density on the micelle which decreases the micellar curvature therefore changing the average distance between the surfactant headgroups which causing reforming of these surfactant micelles solubilising hydrophobic molecules to accommodate both the styrene and the PEI near the surface of the micelle [*45, 46*].

Since all of the surfactants used in this encapsulation experiment have C_{16} hydrocarbon chain this means the main dominant factor in the encapsulation capacity variation is the headgroup part for these cationic surfactants. Figure 4.4.5 shows the encapsulation ratio for these surfactant micelles in presence and absence of PEI.

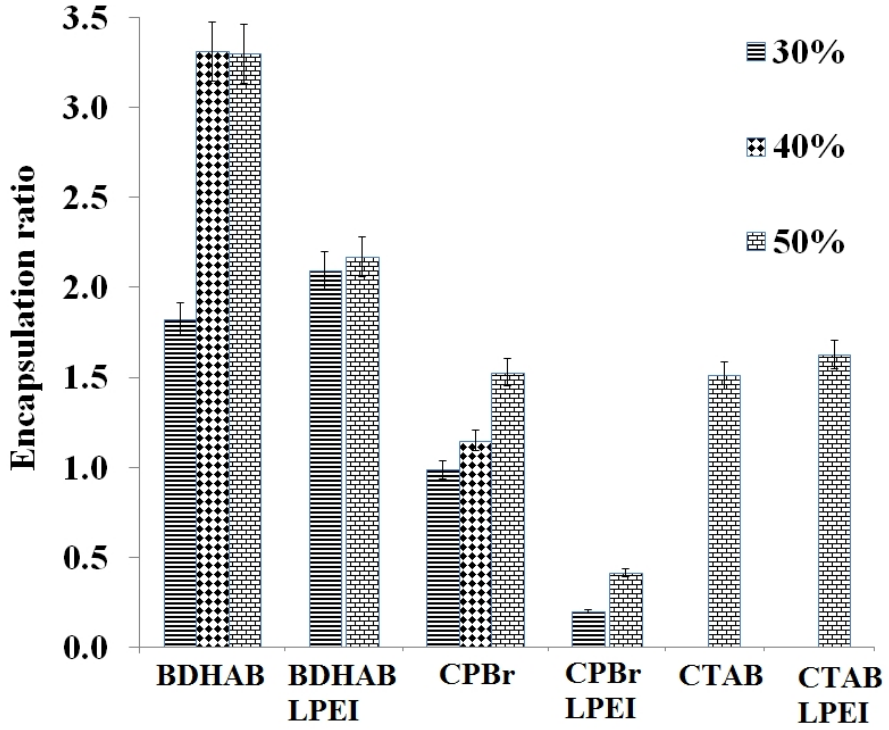

Figure 4.4.5: Encapsulation ratio (number of encapsulated styrene molecules per surfactant monomer) for CTAB, CPBr and BDHAB in presence and absence of PEI.

As shown in Figure 4.4.5, BDHAB with and without PEI has the highest encapsulation capacity compared with other surfactant, which suggest that BDHAB behave different than these surfactants. This could support the theory that the benzyl group in the BDHAB perform as a second hydrocarbon tail subsequently increasing the encapsulation capacity [*50*]. In the case of 40% and 50% of addition styrene, BDHAB without PEI shows almost the same encapsulation ratio (3.3) while at 30% of styrene the ratio was less than 2. This result suggests that these cationic surfactants micelles have tolerant limits of encapsulation capacity of hydrophobic molecules, which after this point it shows phase separation. CPBr shows increases in encapsulation capacity as addition of styrene is increased, and in the range of 30-50% of styrene it doesn't show any limitation in encapsulation ratio. However the encapsulation ratio of CPBr solution solubilising 50% of styrene is only about the half of the BDHAB encapsulation ratio at the same addition amount of styrene. CTAB and CPBr without PEI almost show the

same ratio however in the presence of PEI, the encapsulation capacity of CPBr significantly decreased to a quarter of the CTAB encapsulation ratio value. That it does not mean phase separation had occurred for the CPBr/LPEI solubilising 50% of styrene, since no separation was seen for these solutions;. However this drop happened due to the reforming the CPBr/LPEI micelles encapsulating styrene into smaller micelles as noticed from the variation of N_{agg} for this system before and after addition of PEI. In general these results emphasise that the nature and size of surfactant headgroup plays very important role in the micelle formation (size and geometry) also the micellar performance inside different media [*36*].

4.5 Encapsulation of Monomers into Cationic Surfactant Films

The development of easily reproducible templates to form nanoscale architectures is an on-going area of research in soft matter [*52*]. One of the main obstacles to control ordered nanostructured polymer materials using micelles is the disruption of the morphology of the aggregate during the polymerisation process and partial conversions of the monomer to polymer. To understand whether this was occurring in this system, the first step was to characterise encapsulated hydrophobic monomer in cationic surfactant solutions. This is then followed in this section by studies of these monomers in the surfactant/polymer films which grow at the solution surface. The purpose of the initial SANS experiments on encapsulation of hydrophobic monomer in cationic surfactant solutions was to quantify the amounts of hydrophobic monomer present in the micelles, their location inside these micelles, and also the effects of PEI on these cationic surfactant micelles encapsulating different amounts of styrene. These studies are very important to understand how the individual micelles behave, before going to the final step which is to polymerize these hydrophobic monomers inside the cationic surfactant/polymer films. The second step here is to study the formation of solid polymer/surfactant films at the air-solution interface, from cationic surfactant micelles containing styrene in presence of PEI. The effect of surfactant headgroup variation on film structures and encapsulation of monomer in the films was probed. In addition, the effect of surfactant chain length on the extent of hydrophobic monomer encapsulation and structures in PEI/cationic surfactant films was evaluated. Comparing SANS results from micellar solutions with neutron and X-ray reflectivity from polymer/surfactant films enabled selection of systems with suitable mesostructures in the films in order to direct the subsequent studies of hydrophobic monomer polymerisation within the films.
In these experiments therefore a range of surfactant with aliphatic and aromatic headgroup and three types of hydrocarbon chain length C_{12}, C_{14} and C_{16} were used. Two monomers were used in the initial work; styrene and methyl methacrylate.

4.5.1 Aliphatic Cationic Surfactant/PEI Films Encapsulating Hydrophobic Monomers.

In this section; CTAB, CTEAB and CTPAB were used as cationic surfactants all of which have a C_{16} hydrocarbon chain. Hydrogenated styrene and methyl methacrylate were used as the hydrophobic monomers. Low molecular weight PEI ~2000Da at 15g/L was used at 0.05M surfactant concentration and all solutions were prepared in 100% D_2O. The data was collected using neutron reflectometry on the SURF instrument at the ISIS Pulsed Neutron Source facility [*53*]. Data were collected every 15 min for one hour at 35°C using an incident angle of 1.5°.

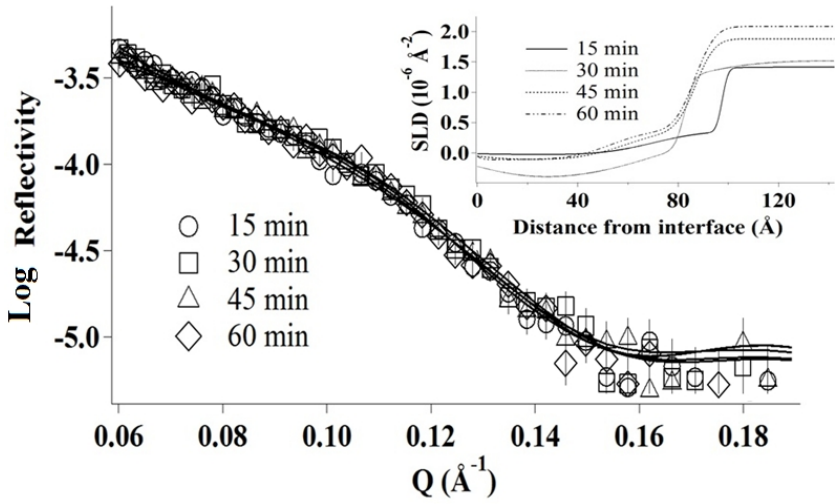

Figure 4.5.1: Neutron reflectivity patterns of CTEAB/SPEI solubilising 50vol% styrene. The pattern collection was started 8 minutes after pouring the solution into the trough. The solid lines are the best model fit to the data using a slab model. The SLD profile used to fit the data is shown in the inset graph.

Figure 4.5.1 shows the initial work on encapsulation of the hydrophobic monomers into cationic surfactant films. The neutron reflectivity data of CTAB, CTEAB and CTPAB with SPEI solubilising different amount of methyl methacrylate or styrene in general show simple curves without any diffraction peaks, which indicates that the structures formed from these solutions are either simple adsorbed layer structures or 2D hexagonal phases oriented with the cylinders oriented parallel to the solution interface [*54*]. The modelling of the data however confirms that only simple layers exist as can be seen from the inset SLD profile in Figure 4.5.1

Several attempts were made to find the best fitting conditions for those data and for equivalent patterns from surfactant solutions with C_{12} hydrocarbon chain. Moreover many suggested models were tested, starting from a single surfactant monolayer to five

alternating layers of solvent/PEI and micelles to find the best model. However the best fit for these patterns suggest a structure composed of three adsorbed layers. This model consists of a first layer corresponding to the surfactant hydrocarbon chain. The second layer of PEI mixed with D_2O and surfactant headgroups, where third layer compose of surfactant micelles as illustrate in figure 4.5.2. This model was chosen to fit these data is close to the suggested model used by a number of other researchers including Taylor et al and others [*55-57*] where they used neutron or X-ray reflectivity to study strongly interacting polymer/surfactant solutions at the water/air interface which are close to our system.

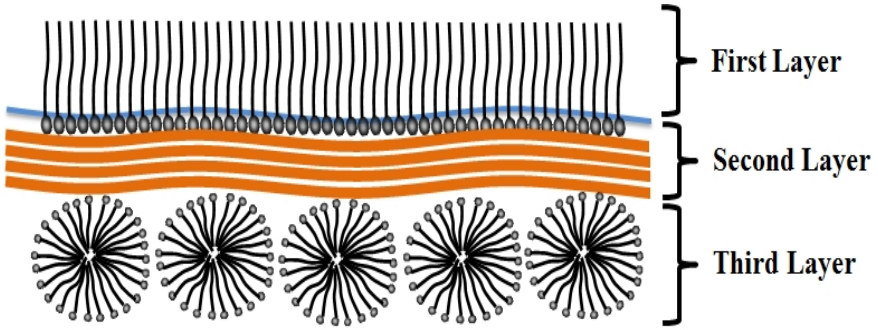

Figure 4.5.2: Schematic of air/D_2O interface of three layers structure where first layer is hydrocarbon chain, second layer is surfactant headgroup and PEI mixed with D_2O. Third layer is surfactant micelle.

Motofit [*58*] was used to fit the neutron reflectivity data. The hydrocarbon chain length and SLD for the first layer were calculated and held. All of the surfactants were used in this experiment have aliphatic headgroups with a C_{16} hydrocarbon chain. Thickness, SLD and roughness were fitted for the second and third layer. The results of fitting these data are given in Table 4.5.1. During fitting, to reduce the number of variables, the thickness, SLD and roughness for the first layer, assumed to be the tail region of the C_{16} surfactant monolayers since it is the hydrophobic part were calculated and held. This approach is commonly used in experimental work from the previous authors. The calculated values were 22Å, -0.353×10^{-6} $Å^{-2}$ and 5Å respectively. The SLD of the subphase was calculated to be $6.08\text{x}10^{-6}$ $Å^{-2}$ and held during fitting.

However, unlike these cases, CTAB/PEI films show a repeating layered structure with Bragg peaks in cases where styrene was solubilized in the film (figure 4.5.3) while showing simple curves without any diffraction peak when methyl methacrylate was solubilised in the films. This suggests that the nature of the solubilised hydrophobic molecules has an important effect on the ability to solubilize the hydrophobic species in the micelles and still form a film resulting from aggregation of these micelles [*48*].

Table 4.5.1: Fitted values of the thickness (Å), SLD (10^{-6} Å^{-2}) and roughness (Å) of second and third layer of films of CTAB, CTEAB and CTPAB with 1.5% SPEI and solubilising either methyl methacrylate or styrene at the air-water interface. The data were collected every 15min for each film.

Surfactant and additives added (vol%)	Parameters	Second Layer				Third Layer			
		15 min	30 min	45 min	60 min	15 min	30 min	45 min	60 min
CTAB with 30% Methyl methacrylate	Thickness	28	27	28	26	34	30	30	32
	SLD	2.06	1.67	1.83	1.45	-0.19	-0.25	-0.19	-0.29
	Roughness	6	8	9	9	6	7	4	4
CTAB with 50% Methyl methacrylate	Thickness	20	16	16	16	32	36	36	37
	SLD	0.98	1.80	1.50	1.44	-0.16	-0.18	-0.18	-0.13
	Roughness	7	8	9	9	8	9	9	9
CTEAB with 30% Methyl methacrylate	Thickness	30	29	22	21	30	31	36	36
	SLD	0.94	1.13	1.66	1.7	-0.25	-0.25	-0.27	-0.26
	Roughness	9	9	9	9	5	6	8	9
CTEAB with 50% Methyl methacrylate	Thickness	30	30	29	27	29	30	31	31
	SLD	0.74	0.81	0.98	1	-0.3	-0.25	-0.14	-0.19
	Roughness	8	9	9	9	6	5	9	7
CTEAB with 30% Styrene	Thickness	20	24	22	22	32	34	34	35
	SLD	2.3	2.2	2.5	2.5	-0.29	-0.29	-0.3	-0.25
	Roughness	8	9	9	9	4	4	4	4
CTEAB with 50% Styrene	Thickness	30	30	27	27	28	29	30	30
	SLD	1.03	1.4	1.7	1.91	-0.24	-0.2	-0.1	-0.12
	Roughness	8	8	9	9	9	8	8	7
CTPAB with 30% Styrene	Thickness	26	29	29	30	30	30	30	30
	SLD	1.1	1	0.87	0.93	-0.16	-0.12	-0.19	-0.1
	Roughness	9	8	9	9	9	9	8	8
CTPAB with 50% Styrene	Thickness	30	30	29	28	34	35	34	34
	SLD	1.80	2.00	2.60	1.90	-0.29	-0.29	-0.20	-0.29
	Roughness	8	9	9	9	5	5	5	5

The error in thickness was ±3Å, SLD ±0.16 ×10^{-6} Å^{-2} and roughness ±2Å.

These films formed from aliphatic surfactant headgroups solubilising either methyl methacrylate or styrene contain in general a second layer which is composed of headgroup, PEI and D_2O, having a thickness from 16Å up to 30Å (table 4.5.1). In the cases of relatively bulky surfactant headgroup such as CTEAB and CTPAB, the second layer was thicker than in the case of CTAB, which has a relatively less bulky headgroup. The second layer is observed to shrink as increasing amount of monomer is added and the second layer in general also shrinks with time. The exceptions to this are the case of CTEAB and CTPAB solubilising 30% of styrene which appear to increase in thickness with time. The micelle layer in general grows and gets thicker with time which indicates increasing incorporation of these solutes inside the micelles layer with time. The theoretical SLD value for these surfactants without monomer is -0.353×10^{-6} $Å^{-2}$ whereas the fitted SLD for the micelle layer overall illustrates higher values than the theoretical SLD value for these surfactants without monomers. Some authors [*59, 60*] found that hydrophobic solutes can also be located in the first layer (Air / hydrocarbon tail of surfactant) and they observed extended chain length by adding these hydrophobic molecules. Therefor this behaviour it could be related to adsorb some of these monomers at the first layer or penetrate some of D_2O in between each micelle due to of not well form a continuous layers. Here in polymer/surfactant systems solubilising different amount of hydrophobic monomer there was no obvious relationship between addition of these monomers and the first layer height therefore the first layer here was held. The other possibility of this growth in the micellar layer is due to reforming of these micelles during evaporation the water molecules from surface of these solutions or it could be equilibrium between both process (encapsulation and micelles growth) which causes variation in SLDs values. In the case of CTAB solubilising methyl methacrylate and CTPAB solubilising styrene the third layer grows as the concentration of monomers is increased from 30vol% to 50vol%. CTEAB films have a thicker third layer in the case of 30% of monomer compared with 50% of addition monomers. This suggests that CTEAB at high concentration of hydrophobic monomers tends to reform itself to form relatively smaller micelles size. Similar behaviour was seen in the fitting of SANS data for CPBr and BDHAB solutions with PEI. Roughness in both the second and third layers is relatively high and this could be due to formation of incomplete micelle layers. In general the second and third layer for PEI films with CTAB, CTEAB and CTPAB solubilising either methyl methacrylate or styrene do not show significant variation in the thickness with time. This it could be related to the fast formation of

these films in the first stage within the first 15 min then it takes some time to repackage or rearrange surfactants micelle and monomer within the layers in a second slower stage [*61*].

4.5.2 Effects of Surfactant Headgroup on the Polymer/Surfactant Films

CPBr, BDHB, CTAB, CTEAB and CTPAB were used as cationic surfactants, all having a C_{16} hydrocarbon chain. These surfactants showed visible and robust films when mixed with polyethylenimine solutions. Hydrogenated styrene was used as a hydrophobic monomer. Low molecular weight PEI ~2000Da at 15g/L was used with 0.05M surfactant concentration and all solutions were prepared in 100% D_2O. The data was collected using neutron reflectometry on the SURF instrument using an incident angle of 1.5°. The data were collected after 60 min at 35°C. Figure 4.5.3 shows the four surfactants with 50% of encapsulated styrene and S-PEI.

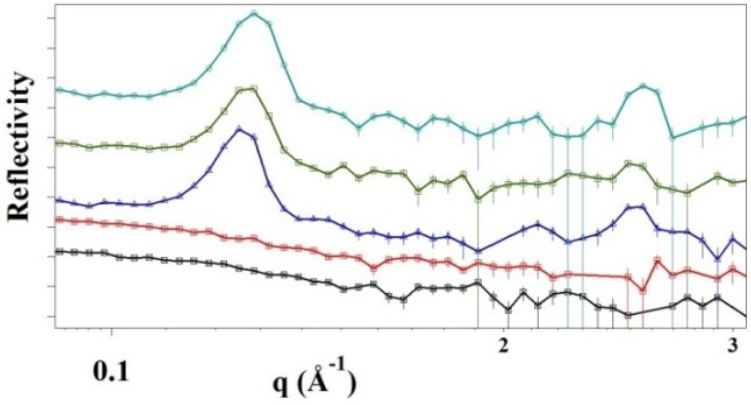

Figure 4.5.3: Neutron reflectivity patterns from films formed of 1.5wt% SPEI with 0.05M (from top to bottom) BDHAB, CPBr, CTAB, CTEAB and CTPAB solubilising 50vol% of styrene. The patterns were collected after 60min of film growth.

BDHAB, CPBr and CTAB films with PEI show a more complex a liquid-crystalline structure while CTEAB and CTPAB show simple adsorbed layer structures. The film formed using BDHAB has peaks at Q values of 0.121 and 0.250 Å^{-1}. The CPBr film shows two peaks at 0.125 and 0.254 Å^{-1} and the CTAB film shows peaks at 0.122 and 0.253 Å^{-1}. The categorisation of the mesostructure of these films and others will be discussed further in the section on GIXD and time resolved formation below. Figure 4.5.3 illustrates in general that the surfactants with aromatic headgroups produce films with a more complex mesophase structure than surfactants with an aliphatic headgroup. CTEAB and CTPAB have bulky headgroups compared with CPBr or CTAB,

nevertheless films grown using CTEAB and CTPAB show no long-range ordered mesostructure. CPBr and CTAB also give patterns containing diffraction peaks in the case of films solubilising styrene however when solubilizing methyl methacrylate even CTAB/PEI films show only adsorbed layers. Crystallite sizes and d-spacing of the intense first peak in these patterns were calculated for these films and given in table 4.5.2.

Crystallite size was calculated from the Scherrer equation, which gives the average crystallite size [*62*], *L*:

$$L = \frac{K\lambda}{\beta \cos\theta} \qquad (1)$$

Where λ is the wavelength of radiation used, β is the peak width of the diffraction peak profile at half maximum height resulting from small crystallite size (in radians) and *K* is a constant related to crystallite shape, normally taken as 0.94. The value of β from the 2θ axis of the diffraction profile must be in radians. The θ can be in degrees or radians, since cos θ corresponds to the same number.

Table 4.5.2: Q vector, d-spacing, crystallite size and number of layers formed of BDHAB, CPBr and CTAB films formed with 1.5wt% SPEI solubilising 50% of styrene after 60min film growth

Surfactant	Q of first intense Peak ($Å^{-1}$)	d-spacing (Å)	Crystallite size from Scherrer Equation (nm)	Number of layers
BDHAB	0.121	52	138	27
CPBr	0.125	50	192	38
CTAB	0.122	52	217	42

Errors in peak positions, crystallite size and number of layers are ±5% of the reported values.

The pattern of the CTAB/SPEI film solubilising 50vol% of styrene shows the highest degree of liquid-crystalline ordering, with 42 layers where these layers consist of a surfactant monolayer on the surface which then interacts with a hydrated polymer layer that is interacting with surfactant micelles that contains the styrene monomer and where the second and third layers are alternating layers as seen in figure 4.5.2. In the case of the CPBr/SPEI film solubilising 50vol% styrene the degree of ordering is lower compared to the CTAB/SPEI film but greater than BDHAB/SPEI films solubilising 50vol% of styrene, where BDHAB/SPEI system shown the smallest crystallite size and

number of layers. These results of cationic surfactant/PEI/styrene films system (from first indication) are unexpected compared with the solutions discussed above. In the solutions micelles of BDHAB/PEI encapsulating 50vol% of styrene were shown to have the largest micelles volume then CTAB/PEI, while CPBr/PEI had the lowest volume. On the other hand BDHAB and CPBr were the most affected by PEI addition compared to CTAB. In the presence of PEI, both BDHAB and CPBr showed micelles reformation while CTAB does not show any obvious micelle volume variation. Therefore BDHAB/PEI films solubilising 50% of styrene were expected to be the thicker film while here the data shows the opposite trend. Edler et al [*63*] reported that the thickness of these cationic surfactant/PEI films is highly dependent on humidity, while O'Driscoll et al [*33*] noticed that these films cannot grow in closed system **(**sealed vials or petri dish taped closed). Even more, if the container in which a film has already formed is covered, and then the film will dissolve and disappear from the surface of solution. These observations are emphasise that humidity or in other words the percentage of water molecules in the surfactant/PEI system plays very important role in these films formation mechanism [*64*]. Therefore this performance variation in the surfactant/PEI solution and water/air solid films could be due to the differences in the surfactant: water molecules: PEI ratio where the water molecules here are related to the number of water molecules in surfactant micelle headgroup layer (number of water molecules per surfactant headgroup). As stated earlier the interaction between these cationic surfactants and PEI is complex interaction in which water molecules between PEI and surfactant headgroups form of this complex interaction. Several authors have demonstrated the relationship between the micelles aggregation number, size and their shapes based on surfactant headgroup/water molecule ratio [*65-67*]. Campbell et al. suggested that water molecules are released by the driving force of the polymer/surfactant interaction which increases entropy. This mechanism accrues due to an ion-dipole interaction between the ammonium part on the surfactant headgroup and the lone pair of electrons on the primary amine group of PEI. Thus this interaction enhances the solid film development at the surface of these solutions due to nonequilibrium evaporation causing the phase separation at the air-liquid interface [*68*]. In addition it is well known that percentage of water molecules in lyotropic system can determine the final structure [*69-71*]. The surfactants used in this section represent different headgroup size, and also aliphatic and aromatic categories where the hydrophobicity of these surfactant headgroups are improve by addition of ethyl or

benzyl groups in their headgroup [*39*]. In addition this bulk and hydrophobic part in the surfactant headgroup have high ability to shield water molecules from micellar headgroup layer. Therefore in the case of water/air films the ratio of (surfactant: water: PEI) has been changed through dehydration of water molecules from the surface of these films. This causes an increase in the charge density on the micelle thus changes in the micellar curvature and average distance between the surfactant headgroups [*45, 46*]. Subsequently the dynamic interactions of PEI with these micelles possibly changed due to loss of water molecules and counterion [*61, 71*]. The results in Table 4.5.2 suggests that the interaction between the second and third layer in the case of CTAB/PEI films was stronger than in the BDHAB/PEI system and this stronger interaction leads the CTAB/PEI system to build thicker films.

However CPBr and BDHAB (both surfactants with an aromatic headgroup) showed thinner films compared with CTAB; nevertheless the surfactants with aromatic headgroups were selected for farther study since these films contained relatively well-ordered mesostructures compared with those having an aliphatic headgroup. The final aim in encapsulation of hydrophobic monomer into cationic surfactants micelles is to prepare a relatively well-organized nanostructured polymer. Therefore styrene was chosen as a hydrophobic monomer for next step because it has less solubility in water and it maintains the crystalline mesostructure in the films compared with methyl methacrylate.

4.5.3 Effects of Surfactant Chain Length on PEI/Surfactant Films

The aim of this section is to evaluate the effect of surfactant hydrocarbon chain length on the styrene encapsulation and structures in PEI/cationic surfactant films. In this experiment six different surfactants with an aromatic head group and with varied tail lengths were used as the cationic surfactants for PEI film formation and to solubilise styrene. DDPBr, TDPBr and CPBr surfactants have pyridinium as the headgroup and BDDAB, BDTAB and BDHAB have benzyldimethyl as the headgroup. Low molecular weight PEI was used (~2000Da) at a concentration of 15g/L in D_2O. Hydrogenated styrene was added at 0, 30 and 50 vol% relative to the micelle volume of the surfactants used. The final concentration of the surfactant was 0.05M. Measurements were made on the reflectometer SURF at ISIS, using an incident angle of 1.5°.

Figure 4.5.4 shows the neutron reflectivity patterns of the surface of solutions containing three different hydrocarbon chain-lengths for either pyridinium or benzyldimethyl as headgroup solubilising 0vol%, 30vol% and 50vol% of styrene. This figure shows very clearly that surfactants with a C_{12} hydrocarbon chain could not developed ordered mesostructures compared with those having C_{14} and C_{16} chains when solubilising different concentrations of styrene. In addition C_{14} and C_{16} surfactant solutions formed robust films on the top of water/air interface solution in the presence of PEI while the C_{12} surfactants do not show an obvious solid film on their solution surface. This performance has been seen for both pyridinium and benzyldimethyl headgroup surfactants. Table 4.5.3 shows the main intense peak positions of surfactant/S-PEI films from those solutions in 4.5.4 which showed clear intense peaks.

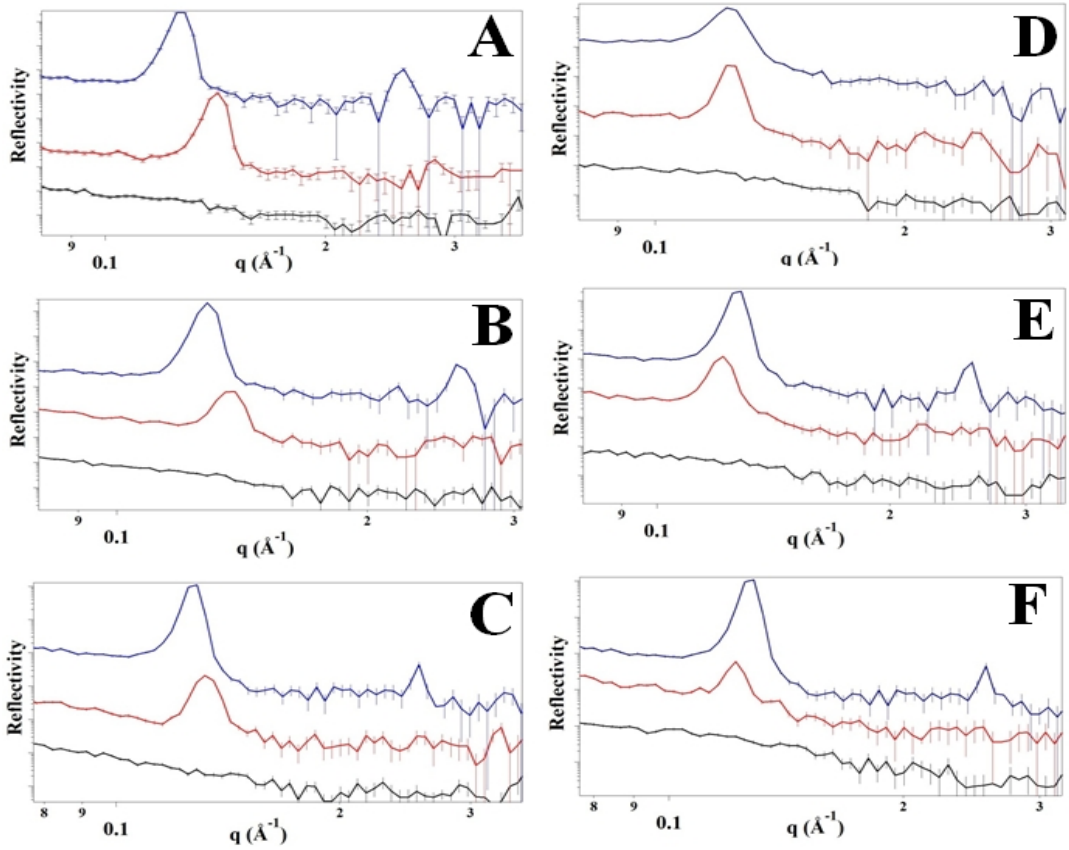

Figure 4.5.4: Neutron reflectivity patterns from the surface of solutions containing 0.05M surfactant with 1.5% S-PEI in D_2O with hydrogenated styrene. The patterns in each graph are corresponds to (from top to bottom) surfactants with a C_{16}, C_{14} and C_{12} hydrocarbon chain respectively. Left hand graphs are correspond to benzyldimethyl as headgroup solubilising 0vol% of styrene (A), 30vol% of styrene (B) and 50vol% of styrene (C). Right hand graphs correspond to pyridinium as headgroup, solubilising 0vol% of styrene (D), 30vol% of styrene (E) and 50vol% of styrene (F). Each of the individual patterns was collected after 15min of film growth time.

The d-spacing for the C_{14} and C_{16} cationic surfactant/PEI films solubilising different amount of styrene were between 48Å to 53Å, however in the case of BDTAB the repeating layers size was less than that for BDHAB which is mainly due to the differences in the hydrocarbon tail length. In the case of TDPB films the d-spacing was higher about 2Å than CPBr when solubilising styrene. This unexpected behaviour for TDPB/PEI system is not clear but it could be related to the TDPB micelles stability. SANS data showed an obvious drop in the volume for CPBr and BDHAB when these micelles solubilised styrene and were then mixed with PEI (possibly due to micelle reformation) (table 4.4.2). It could be that this phenomenon occurs in the BDTAB/PEI system as well as, but not in the case of TDPB/PEI which therefore has larger repeating layers. Overall the d-spacing for these C_{14} and C_{16} cationic surfactant/PEI systems are greater than the width of the micelles calculated from the SANS patterns for both pyridinium bromide and benzyldimethylammonium bromide micelles in solution. This result suggests that PEI is intercalated between the micelles layers, between arrays of rodlike micelles with the long axis of the micelle orientated parallel to the air/water interface [*33*].

Table 4.5.3 Peak positions of the main intense peak, d-spacing, crystallite size and number of layers formed in films of surfactant/SPEI solubilising 50vol% of styrene after 60min film growth.

Surfactant	% of Styrene (vol.)	1st Peak Q ($Å^{-1}$)	d-spacing (Å)	Crystallite size (nm)	Number of layers
BDTAB	0	0.132	48	127	27
	30	0.132	48	120	25
	50	0.132	48	116	24
BDHAB	0	0.118	53	146	28
	30	0.118	53	137	26
	50	0.121	52	138	27
TDPB	0	0.122	52	211	41
	30	0.119	53	212	40
	50	0.119	53	274	52
CPBr	0	0.122	52	182	35
	30	0.125	50	183	36
	50	0.125	50	192	38

Errors in peak positions, d-spacing, crystallite size and number of layers are ±5% of the reported value

The data in table 4.5.3 illustrates very clearly that the number of repeating layers and the film thickness of films containing pyridinium bromide headgroups for both C_{14} and C_{16} hydrocarbon chains are greater than those for films made from benzyldimethylammonium bromide headgroup surfactants when comparing the same tail length. These results confirm the previous results, that the pyridinium headgroup has more attraction interaction to PEI than the benzyldimethylammonium group due to bulkiness and hydrophobicity effects [*72*]. O'Driscoll et al. [*33*] studied the thin film structures formed by polyethyleneimine and alkyltrimethylammonium bromide surfactants (PEI/C_nTAB) at the air/water interface where the alkyl chain was C_{12}, C_{14} and C_{16}. From this study it was observed that at relatively low concentration of PEI the diffraction peaks for C_{12}TAB/PEI and C_{14}TAB/PEI disappeared with time. Modelling of neutron reflectometry data of these films confirmed that there was no obvious mesostructure existing at the interfaces for these solution compositions, where an adsorbed layer instead was found. Here in this experiment, as stated before, C_{12} tail surfactants for both pyridinium and benzyldimethylammonium bromide did not develop obvious solid films or show distinct diffraction peak. However C_{14} surfactants with SPEI for both headgroups did show diffraction peaks. These results suggest that the C_{12} hydrocarbon tail surfactant for both pyridinium and benzyldimethylammonium bromide with SPEI was form only an adsorbed layer rather than forming ordered mesostructures. Also the best modelling fit for these data support this result as reported below. Figure 4.5.5 shows the neutron reflectivity patterns from the surface of a DDPB/SPEI solution solubilising 50vol% of styrene.

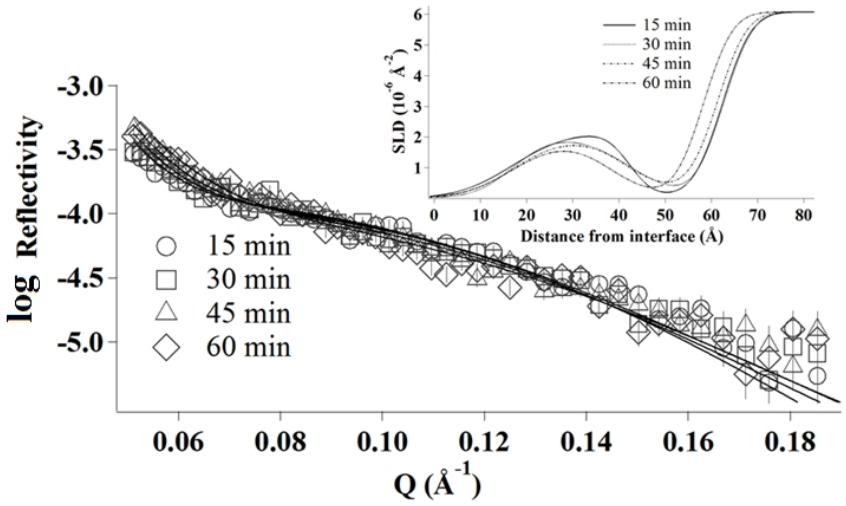

Figure 4.5.5: Neutron reflectivity patterns of 1.5wt% SPEI solutions in D_2O containing 0.05M DDPB with 50% styrene. The patterns were collected 7 minutes after pouring the solution into the trough. The solid lines are the best fit using a 3 layer model.

Surfactants with a benzyldimethylammonium headgroup and C_{16} tail showed thicker films and more repeating layers than those grown with a C_{14} tail. However pyridinium bromide surfactants showed contradictory results compared the benzyldimethylammonium system. This variation could be related to the differences in the packing parameter for these surfactants, thus the micelles re-form in different ways in the moment of forming these solid films. During the film formation process changes in the water molecules/surfactant ratio occur, subsequently changing the surfactant-polymer interaction in these films [*45, 46*]. In other words, polymer/surfactant interaction could be varied by changing the surfactant micelle geometry. O'Driscoll reported that the interaction between C_{16}TAB and PEI was the greatest compared with surfactants having C_{12} or C_{14} hydrocarbon tails, which this increase the interaction surface area corresponding to the long axis of hexagonal array micelles [*33*].

The reflectivity patterns from BDDAB/SPEI and DDPB/SPEI solutions solubilising different amount of styrene were modelled as the previous reflectivity model procedure. The thickness, SLD and roughness for the first layer, assumed to be the tail region of the C_{12} surfactant monolayers since it is hydrophobic part was held as 17Å, -0.367×10^{-6} $Å^{-2}$ and 5Å respectively. The SLD of the subphase was calculated to be 6.08×10^{-6} $Å^{-2}$ and held during fitting. The results from fitting the reflectivity data for the SPEI with C_{12} surfactant solutions solubilising different amounts of styrene are given in table 4.5.4.

The fit results of reflectivity profiles for these solutions illustrates that second layer, which is the layer of headgroups mixed with PEI and D_2O, has an almost stable thickness during the measurements, of between 20 to 25Å for both BDDAB and DDPB at all concentration of styrene. This result in general is less than the thickness of second layers for CTEAB and CTPAB with SPEI solubilising the same amount of styrene (table 4.5.1) which indicates that the percentage of PEI/D_2O at the interfacefor the surfactants with aromatic headgroup is less than in the case of the CTEAB/SPEI and CTPAB/SPEI systems. This supports the previous suggestion that the aliphatic cationic surfactant headgroup has more affinity with PEI than those surfactants with aromatic headgroups. Unfortunately due to the lack of structural information in the layer for these systems the quantitative percentage of D_2O or PEI in the layer was hard to calculate.

Table 4.5.4: Fitted thickness, SLD and roughness of second and third layers for neutron reflectivity patterns from films composed of BDDAB and DDPB solubilising styrene mixed with 1.5% S-PEI. Data were collected every 15min for each film.

Solution	Parameters	Second Layer				Third Layer			
		15 min	30 min	45 min	60 min	15 min	30 min	45 min	60 min
BDDAB with 0vol% of Styrene	Thickness (Å)	21	20	20	20	30	31	30	26
	SLD (10^{-6} Å^{-2})	1.1	1.01	1	1.02	-0.34	-0.34	-0.34	-0.34
	Roughness (Å)	9	9	9	9	6	9	9	9
BDDAB with 30vol% of Styrene	Thickness (Å)	20	20	21	21	35	33	29	24
	SLD (10^{-6} Å^{-2})	1.03	1.08	1.11	1.03	-0.35	-0.33	-0.38	-0.37
	Roughness (Å)	6	8	5	9	7	5	6	5
BDDAB with 50vol% of Styrene	Thickness (Å)	20	20	22	22	31	34	29	27
	SLD (10^{-6} Å^{-2})	2.02	2.08	1.80	1.72	-0.35	-0.13	-0.14	-0.16
	Roughness (Å)	9	8	4	8	4	4	6	6
DDPB with 0 vol% of Styrene	Thickness (Å)	21	21	20	20	25	25	26	27
	SLD (10^{-6} Å^{-2})	2.51	2.14	2.08	2.03	-0.13	-0.24	-0.2	-0.24
	Roughness (Å)	7	5	6	6	6	4	5	5
DDPB with 30vol% of Styrene	Thickness (Å)	20	21	22	21	26	25	28	30
	SLD (10^{-6} Å^{-2})	2.13	1.96	1.98	1.75	-0.25	-0.22	-0.17	-0.2
	Roughness (Å)	6	6	7	6	4	5	5	6
DDPB with 50vol% of Styrene	Thickness (Å)	25	25	21	20	29	26	31	31
	SLD (10^{-6} Å^{-2})	1.8	1.69	1.62	1.51	-0.24	-0.28	-0.1	-0.2
	Roughness (Å)	9	6	8	8	4	8	6	7

Thickness, SLD and roughness *for the first layer were calculated and held as 17*Å, -0.367 $\times 10^{-6}$ Å^{-2} and 5Å respectively. *SLD of solvent and background were calculated and held. The error of thickness was ±3*Å, *SLD* ±0.23 $\times 10^{-6}$ Å^{-2} *and* roughness ±*2*Å.

Overall the second layer had a relativity high roughness (5-9Å) which could be related to the nature of PEI since it is a highly branched polymer [*73*]. The lower micelle layer for both BDDAB and DDPB solubilising different amounts of styrene shows thicknesses from 24 up to 35Å. Therefore the average total layer thickness for these surfactants which consist of an aromatic headgroup and C_{12} hydrocarbon chain is around 70Å. This relatively small thickness of the film in both BDDAB/SPEI and DDPB/SPEI systems is the reason no diffraction peaks are seen, since the crystallite thickness needs to be greater than 200Å in size before peaks could be visible. However,

this layer is still potentially bigger than the expected kinetic equilibrium structure of these films [*74*]. Taylor et al [*55*] reported the total adsorption layer thickness for 0.023M of C_{12}TAB with an oppositely charged polyelectrolyte (poly (styrenesulfonate)) was between 85 and 95 Å. This variation in total adsorption layer thickness between these two systems could be due to the nature of interaction between the polyelectrolyte and the cationic surfactant or it could also be related to the hydrophobicity of the aromatic headgroup in the case of BDDAB and DDPB surfactants with PEI which thus reduces the interaction between these surfactants and the polyelectrolyte [*72*]. The micellar layer in the case of BDDAB surfactant films in general shows a bigger micellar size compared with those for the DDPB surfactant solubilising the same amount of styrene. However the thickness of this layer shrinks with time in the case of BDDAB films while the micellar size in the DDPB layer increased. This neutron reflectivity result is in good agreement with SANS results. SANS results showed that BDHAB has a greater micelle volume (with and without styrene) compared with CPBr (table 4.4.2), while neutron reflectivity shows decreases in the films thickness for benzyldimethyl with both C_{14} and C_{16} hydrocarbon chain over time as presented below. Taylor, Thomas and Penfold [*75*] have studied a wide range of polyelectrolyte/surfactant solutions at the air/water interface and they found the strong electrostatic interactions predominate in these systems and give rise to some significant adsorption behaviour. For instance at low surfactant concentrations the adsorbed layer of polyelectrolyte/surfactant at the air/water interface for those solutions has a thickness of the order of a surfactant monolayer which is approximately from 20Å to 25Å. However, at low concentration polymer tends to desorb from the surface to form aggregates with surfactant micelles in the bulk phase. In contrast at surfactant concentrations above the critical aggregation concentration, strong adsorption at the air/water interface occurred, which raised the adsorbed layer thicknesses to more than 100Å. In that case (at high surfactant concentration with polymer) the best modelling suggested the structure of these solutions consists of an approximate three layers of surfactant with polymer and water contained essentially in the headgroup regions. The concentration of BDDAB and DDPB used here is at least about 4 times greater than the CMC of those surfactants. Therefore the results reported from the above authors are close to the best model found for these solutions by fitting in this work for layers formed using surfactants with a C_{12} hydrocarbon chain. In general the results from benzyldimethylalkylamnim bromide and alkylpyridinum bromide surfactants with PEI suggest that the relatively short

hydrocarbon tail (C_{12}) is the main reason preventing the solid films to form on the top of these solutions and instead it is tends to form an adsorbed layer. Increasing the tail length overall increased the micelles volume thus increased the surfactant/polymer interactions, and consequently enhanced crystallite size [*33, 55*]. However the nature of headgroup of these surfactants still governs the main surfactant/PEI interaction effects [*72*].

4.6 Kinetic Study of Polymer/Surfactant Films Solubilising Styrene.

In the previous section, the effect of the surfactant headgroup type and hydrocarbon chain length on the incorporation of styrene in the films, and on their structure was reported. These results showed very clearly using neutron reflectivity that surfactants with small hydrocarbon chain (C_{12}) give films without long range micellar ordering as no diffraction peaks are visible. On the other hand the films grown with C_{14} tail surfactants in general displayed one intense peak in the reflectivity patterns, while films grown from solutions containing C_{16} tail surfactants showed two very clear diffraction peaks. In addition, the comparison between aliphatic and aromatic surfactant headgroups on solubilisation of styrene showed that surfactants with an aromatic headgroup can develop mesostructured films better than surfactants with aliphatic headgroup. Therefore in this part, the work was focused on surfactants with aromatic headgroups and surfactant with relatively long hydrocarbon chains, since the aim from the previous study was to select surfactants that can solubilise the styrene monomer and form well defined mesostructured films that will ultimately allow to polymerize a well organised system. Kinetic studies of solubilising styrene into cationic surfactant/PEI films and calculation of the extent of incorporation styrene into polymer/surfactant films are investigated in next section using neutron reflectivity and selective deuteration of the styrene component in the films.

4.6.1 C_{14} Hydrocarbon Chain Surfactant/PEI Films

Figure 4.6.1 illustrates time resolved reflectivity patterns from films composed of BDTAB/SPEI and TDPB/SPEI solutions solubilising various amount of styrene. Due to the relatively low neutron flux on the SURF instrument, where this experiment was performed, each pattern was collected every 15min. The kinetic air/water films formation study of these solutions used surfactants with a C_{14} or C_{16} hydrocarbon chain with SPEI and patterns were taken over a period of one hour, since no significant change was seen for these films after 60min. The neutron reflectivity patterns showed in general one peak in the case of TDPB/SPEI films solubilising different amounts of styrene while BDTAB/SPEI films without styrene also show one peak, while in the case of solubilising 30% and 50% of styrene, BDTAB/SPEI films exhibited a second peak at Q = 0.32Å which is double in Q position of the first peak suggesting these films are made up of a repeating layered structure, Thus solubilising styrene in BDTAB/SPEI films overall enhanced the mesostructures of these films.

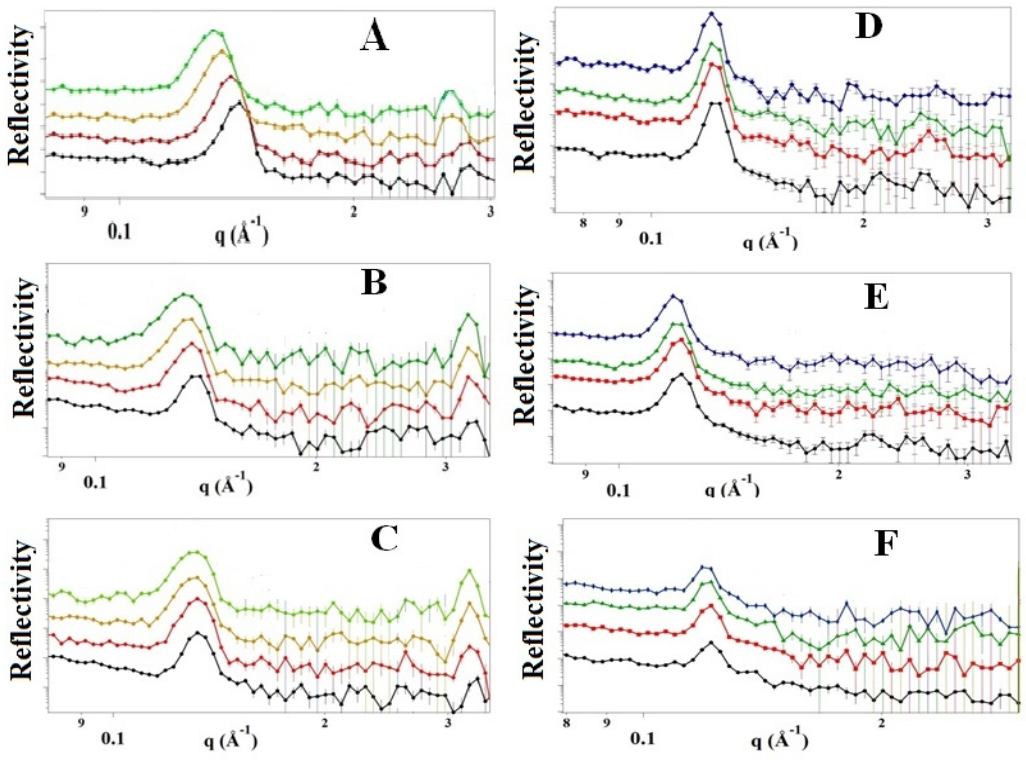

Figure 4.6.1: Time resolved neutron reflectivity patterns of films formed from 0.05M BDTAB with 1.5wt% SPEI (A), BDTAB/SPEI solubilising 30vol% styrene (B), BDTAB/SPEI solubilising 50vol% styrene (C), TDPB/SPEI (D), TDPB/SPEI solubilising 30vol% h-styrene (E) and (F) is TDPB/SPEI solubilising 50vol% h-styrene. The patterns were collected every 15min from bottom to top.

The reflectivity patterns of BDTAB/PEI solubilising different amount of styrene in general show shifts in the peak position toward lower Q. This shift was greater in the case of BDTAB/PEI films without styrene, while BDTAB/PEI films solubilising 50vol% of styrene do not show significant changes in the peak position with time. The TDPB/SPEI system showed the same performance however the shifts were very small. This shift in the peak position for these films indicates restructuring in the polymer/surfactant micelle structure which is mainly due to dehydration of these films. Overall the peaks in the BDTAB/PEI films are much broader than those in the TDPB/SPEI films suggesting greater polydispersity in the layer thickness in BDTAB/PEI system. On the other hand TDPB/SPEI films illustrated relatively thinner diffraction peaks, where the width of these peaks are inversely proportional to the size of the diffracting structure, in this case the number of layers [*76*]. Crystallite sizes and d-spacing were calculated from the intense peak for these films and are summarised in figure 4.6.2.

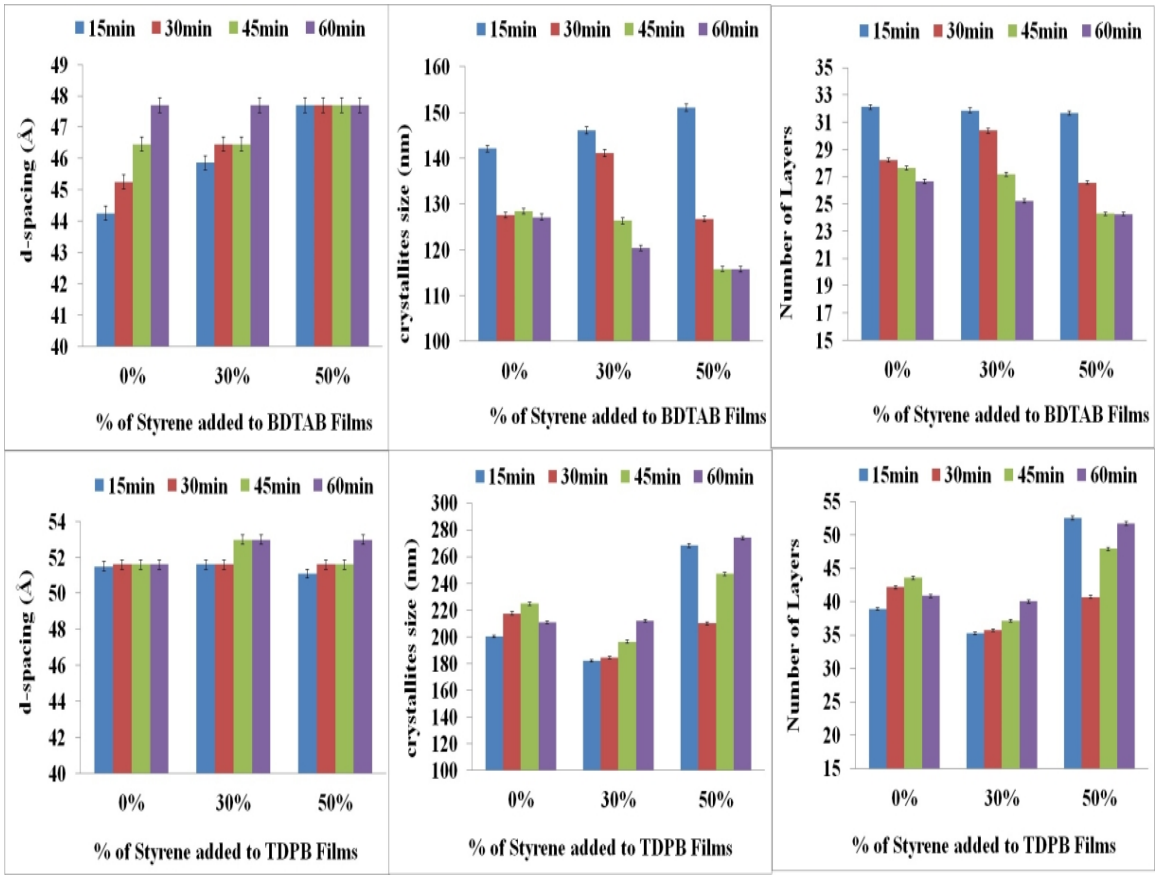

Figure 4.6.2: d-spacing, crystallites size and number of layers of BDTAB/SPEI (top charts) and TDPB/SPEI (bottom charts) films solubilising different amount of styrene during the first 60min of these films formation.

The films formed from BDTAB/SPEI solubilising different amount of styrene in general shows a growth of d-spacing with time, except for those solubilising 50% of styrene for the same film composition, where the d-spacing was constant. However after 60 min the repeating layers thickness of for all of these films was constant (48Å). On the other hand, BDTAB/SPEI films solubilising different amount of styrene overall show a decreases in the total film thickness and number of layers with the time during the film formation time. The average losses of crystallite size for BDTAB/SPEI films solubilising 0vol%, 30vol% and 50vol% of styrene were 3Å, 6Å and 8Å per min respectively. TDPB/SPEI films solubilising different amount of styrene show totally different behaviour compared with BDTAB/SPEI films. In general TDPB/SPEI films solubilising different amount of styrene show a stable d-spacing with the time, however some very small growth (2Å) was seen in the case of films solubilising 30% and 50% of styrene after 60min. The average d-spacing of BDTAB/SPEI films solubilising different amount of styrene was 52Å. The crystallite size and number of repeating layers for the TDPB/SPEI films system shows different trends compared with BDTAB/SPEI films. TDPB/SPEI films solubilising various amount of styrene in general demonstrate an increase of both the number of repeating layers and crystallite size with time. Also as the amount of styrene was increased the crystallite size value and number of repeating layers increased with time. The average growth in crystallite size for TDPB/SPEI films solubilising 0vol%, 30vol% and 50vol% of styrene were 8Å, 9Å and 21Å per min respectively.

However despite the fact that BDTAB films had a relatively bigger headgroup compared with TDPB, nevertheless the average d-spacing of the films in the TDPB/SPEI system (52Å) was bigger than that in the BDTAB/SPEI system (48Å). Both of these values are smaller than d-spacing values that were reported by O'Driscoll for films formed from 0.037M C_{14}TAB and 1.5% (w/v) SPEI, which had a d-spacing of 57Å, for films without additives. These results suggest that the PEI/water ratio between the surfactants micelles inside these films is different. In the optimal condition, BDTAB/SPEI should have the greatest d-spacing value since BDTAB has the bigger micellar volume as seen from the SANS experiment (Table 3.3.4) as well having a bulky headgroup. However, the practical order of repeating layers for these systems was: C_{14}TAB/SPEI > TDPB/SPEI > BDTAB/SPEI. In this case there are two possibilities accountable for this variation. First this variation could be due to either increases or decreases one of these variables; water molecules or PEI. The second

option is a contribution from both of them. As mentioned earlier these films do not form if the atmosphere above the film is saturated with water vapour. Therefore there is loss of water molecules in both cases affecting of the d-spacing during the film formation. However this loss in water molecules shows different d-spacing behaviour in TDPB/SPEI and BDTAB/SPEI systems. On the other hand the maximum d-spacing variation during the films formation was 3Å. This would means that PEI is substituted instead of water molecules between the micelles thus enhancing the repeating layers thickness during the films formation; however this is not reasonable due to the bulkiness of PEI. Therefore the main reason behind this variation must be charge repulsion between micelles affected by the viscosity of the polymer films during the water evaporation process [*77*]. This suggests that the structure of these polymer/surfactant films is essentially determined by the balance between evaporation rates of water molecules at the air/water interface, micelle charge repulsion and viscosity of polymer/surfactant system [*61*].

Åberg et al. [*78*] suggested a theoretical formation mechanism of an ordered phase forming on an open binary aqueous solution at air/water interface. He proposed two mechanisms were predominant forming process of separation phase. The first mechanism is related to the self-assembly processes that occur in bulk solution, particularly when the bulk system is close to a phase separation. This process is governed by equilibrium rate between two factors; the accumulative rate (aggregation of micelles and polymer/surfactant interaction process), while another factor is the re-dissolution rate of these components in the bulk phase. The second mechanism is related to evaporation processes at the top air/water interface. The simple example could explain this phenomenon is the mechanical behaviour of floating ice on the surface of water. The key factor of this process is the density. Likewise these exclusive polymer/surfactant systems are forming a new light and coherent state due to the complex interaction between these two species. This proposal agrees with the previous suggestion about the importance of the micelle geometry in this process. Surfactants with short hydrocarbon tails do not form solid films, while the long tail surfactant was shown to form robust films. However they have the same headgroup nevertheless micellar size and shape was different since the tail length varied. Subsequently polymer/surfactant interaction and overall dimensions of these systems are improved. This mechanism could explain the differences in crystallite growth between TDPB/SPEI and BDTAB/SPEI systems. While the crystallite size of TDPB/SPEI

system showed growth with time, the thickness of BDTAB/SPEI films was decreasing during the film formation process. Based on Åberg's model, this indicates that the dissolution rate of BDTAB/SPEI films was faster than accumulative rate for the same system, which thus causes a loss in the film thickness with time. However the loss in BDTAB/SPEI films thickness was very fast in the first 15min, while after 30min it become slower, then at 60min almost showed equilibrium (accumulative/dissolutions) rate. TDPB/SPEI system illustrated a higher accumulative rate than dissolution rate thus built thicker films with time (figure 4.6.2). This difference between these two systems agreed as well with previous results which suggested that the association between PEI and pyridinium was greater than with the benzyldimethyl headgroup due to the bulkiness and hydrophobicity of benzyldimethyl group [*72*].

4.6.2 C_{16} Hydrocarbon Chain Surfactant/PEI Films

Figures 4.6.3 shows the time-resolved neutron reflectivity patterns of BDHAB/SPEI and CPBr/SPEI films, in which surfactants with C_{16} tails solubilise various amount of styrene. The reflectivity patterns of BDHAB/SPEI and CPBr/SPEI solubilising different amount of styrene in general shows two diffraction peaks, where the first peak (~ 0.12 $Å^{-1}$) was very intense and thinner compared with that seen in the C_{14} hydrocarbon tail surfactant systems.

The reflectivity patterns from BDHAB/SPEI systems showed shifts in the peak position toward lower Q with time, while the peak position in patterns from CPBr/SPEI films was almost constant. BDHAB/SPEI film solubilising 40vol% of styrene shows overlapping diffraction peaks which suggests either that there is a second type of structure forming at the surface of this film or that the film has a structure more complex than the 2D hexagonal phase seen in the other films. After 15min from this film formation, the first peak became very broad and less intense. This broadening suggesting high polydispersity within the structure, which it could be that the micellar ordering in the films becomes less well-defined with time [*68, 79*].

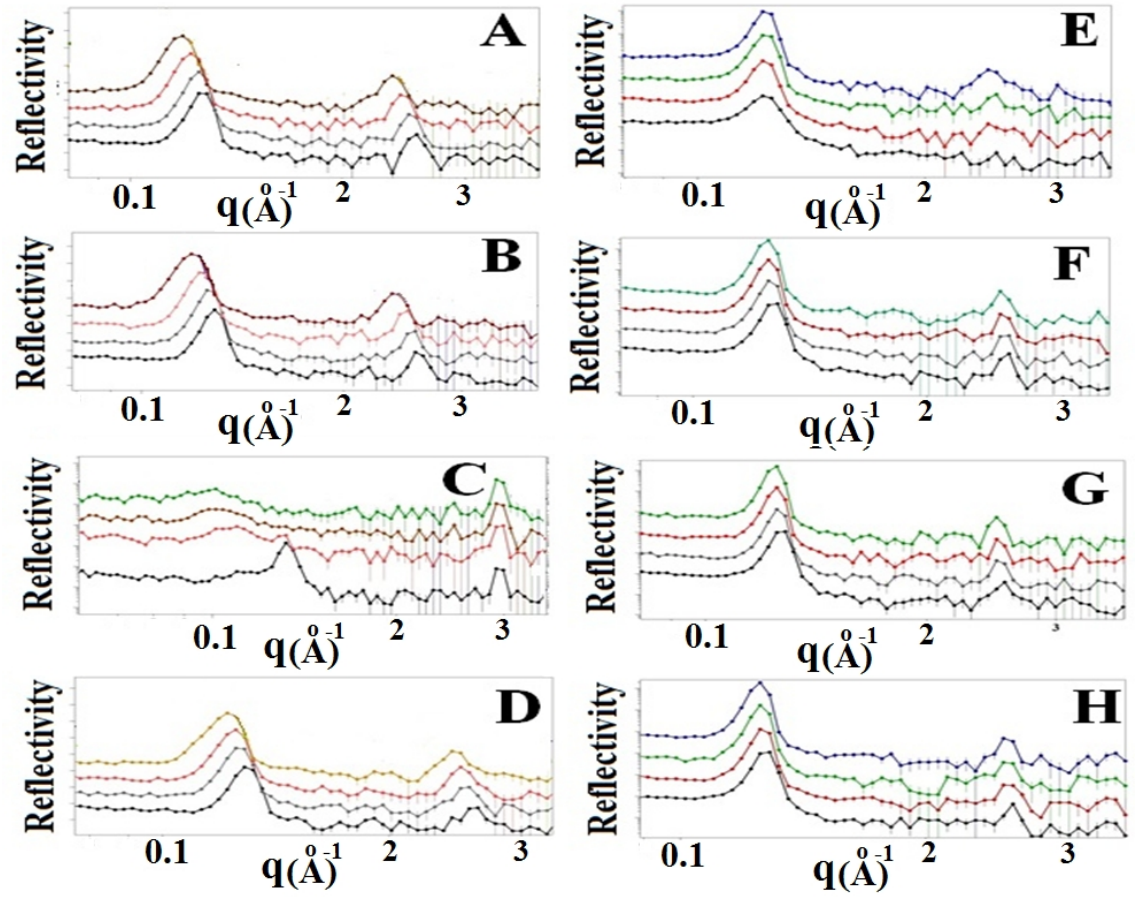

Figure 4.6.3:Time resolved neutron reflectivity patterns of films formed from 0.05M of BDHAB with 1.5wt% SPEI (A), BDHAB/SPEI solubilising 30vol% styrene (B), BDHAB/SPEI solubilising 40vol% styrene (C), BDHAB/SPEI solubilising 50vol% styrene (D), CPBr/SPEI (E), CPBr/SPEI solubilising 30vol% styrene (F), CPBr/SPEI solubilising 40vol% styrene (G) and CPBr/SPEI solubilising 50vol% styrene (H). The patterns were collected every 15min from bottom to top.

Overall the behaviour of reflectivity diffraction peaks for BDHAB/SPEI and CPBr/SPEI are quite similar to those films system formed from surfactants with a C_{14} hydrocarbon chain. Crystallite sizes and d-spacing were calculated from intense peak for these films and reported in figure 4.6.4. This figure shows increases of the number of repeating layers with time in the case of BDHAB/SPEI films solubilising different amount of styrene, while CPBr/SPEI system has a very stable d-spacing size with time. The reason for this behaviour as stated above is due to the variation in interaction between CPBr and BDHAB with PEI which causes more micelles charge repulsion in the case of BDHAB compared with the CPBr/SPEI system [*61*]. The BDHAB/SPEI film solubilising 40% of styrene shows a relatively very big displacement compared with other systems.

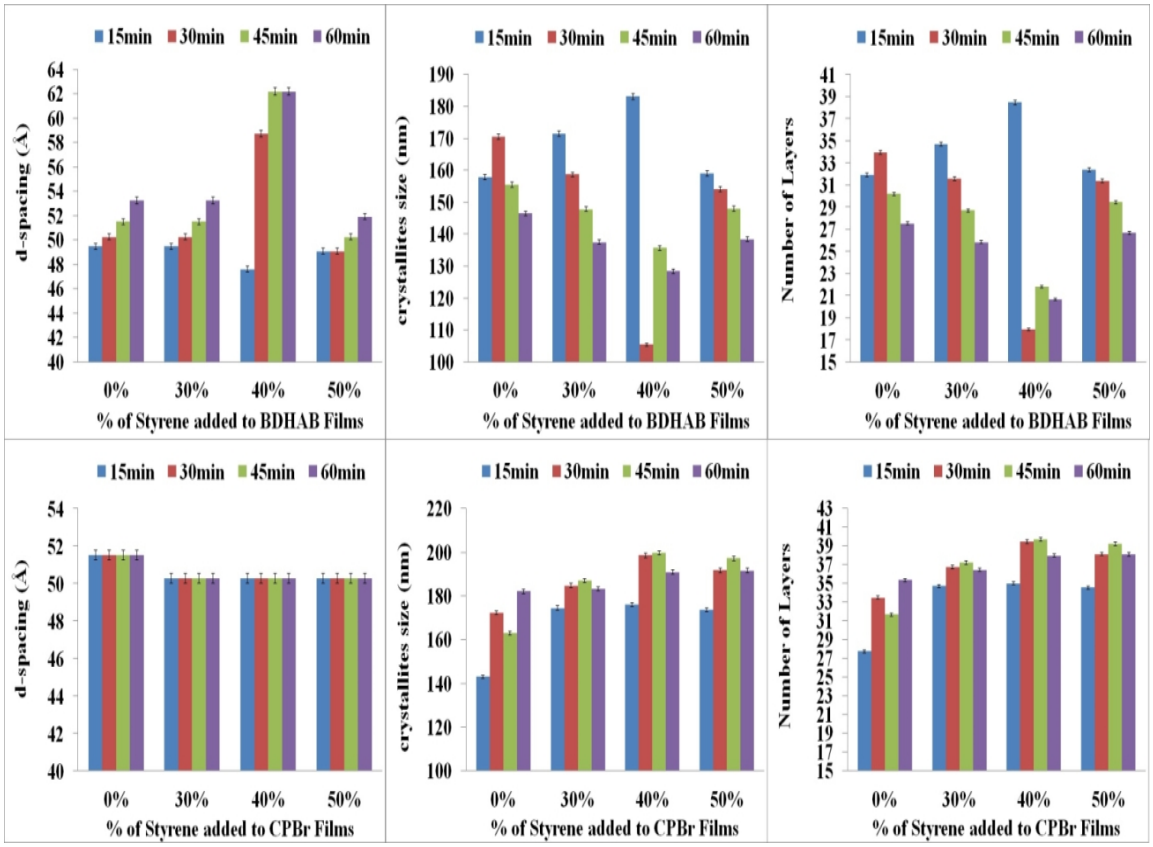

Figure 4.6.4: d-spacing, crystallites size and number of layers of BDHAB/SPEI (top charts) and CPBr/SPEI (bottom charts) films solubilising different amount of styrene during the first 60min of film formation.

This abnormal performance of this film as mentioned before could be due to the high polydispersity within the structure which resulting from forming more than one structure at the same time during the film formation or else due to a phase change from a more complex structure to the 2D hexagonal phase with time. The layers thickness for both BDHAB/SPEI and CPBr/SPEI films without styrene overall were thicker than in of the presence of styrene. This result suggests that solubilising styrene in these films reduces the micellar repulsion which leads to closer packing of these micelles [*33*]. The d-spacing of the BDHAB/SPEI system was bigger by about 5Å compared to the BDTAB/SPEI system and due to the increased hydrocarbon tail length. However the layer thicknesses of the CPBr/SPEI systems solubilising styrene were less than those for the TDPB/SPEI solubilising the same amount of styrene which indicates that polymer/water layer between CPBr/SPEI films were thinner than in the TDPB/SPEI films. The kinetics of BDHAB/SPEI and CPBr/SPEI films formation behaviour was quite similar to that seen for TDPB/SPEI and BDTAB/SPEI systems. The film thickness

and number of layers decreased in the case of benzyldimethyl and increased during time in the case of pyridinium headgroup systems. However the comparison between the same headgroup and different tail length surfactants demonstrates overall that the crystallites size was greater in the case of BDHAB/SPEI compared with BDTAB/SPEI systems. The percentage variation in d-spacing between BDHAB/SPEI and BDTAB/SPEI systems are very close to the percentage variation in crystallites size for these systems, which indicates that the increase in thickness in BDHAB/SPEI films is mainly related to the expansion of the micellar layer. However the difference in d-spacings between CPBr/SPEI and BDTAB/SPEI systems was very small (~2Å), nevertheless BDTAB/SPEI systems showed thicker films compared with the CPBr/SPEI system. This performance of pyridinium surfactant suggests that the interaction between PEI and BDTAB was greater than in the CPBr/PEI system, which emphasises that the geometry of these surfactants micelles plays important role in such kinds of interaction. In general the average d-spacing of BDHAB/SPEI was 53Å while it was 50Å in the case of CPBr/SPEI system. These results are very close to values of repeating layer thickness which were reported by Edler et al for the films formed from 0.037M C_{16}TAB and 6.0% (w/v) SPEI [*63*] and also by Comas-Rojas et al [*77*]. These results indicates that cationic surfactants with relatively long tail and branched PEI mainly form films consisting of alternating layers of polymer and water and surfactant micelles [*63*]. However the films thickness found here for both C_{14} and C_{16} surfactants with aromatic headgroups were greater than the films thickness reported by O'Driscoll for the films formed from 0.037M C_{16}TAB and 0.4%(w/v) SPEI, where it was 1000Å thick [*33*]. Overall the number of layers and the films thickness of films formed using surfactants with benzyldimethyl and pyridinium headgroups with C_{14} and C_{16} hydrocarbon tails solubilising different amount of styrene suggesting that these films are suitable templating media for polymerizing styrene inside these films. However the best ordered structures of these films will be chosen for next polymerization step. The mesostructures of these films will be discussed in more detail in the next section.

4.7 Extent of Styrene Incorporation into Cationic Surfactant Films

SLD contrast variation, one of the main tools used in SANS and neutron reflectivity can give detailed information about structures or additives contained within surfactant micelles [*48, 60*]. Experimental data obtained from SANS or neutron reflectivity, in general can be simulated by programs such as Motofit, within Igor Pro to investigate and understand the compositions of these systems. All reflectivity data from surfactants with aromatic headgroups used in the previous section grown using either C_{16} or C_{14} hydrocarbon chains showed very intense and sharp diffraction peaks. These reflectivity patterns with intense diffraction peaks cannot be fitted very well by using the regular multilayer simulation method. Several attempts by O'Driscoll [*33*] and Wasbrough [*47*] have simulated CTAB/PEI reflectivity data showing intense and sharp peaks and they reported the best fits to this data still were not very accurate. The best simulation for these data proposed by O'Driscoll and Wasbrough suggested a multilayer model, starting from a single surfactant monolayer followed by 20 alternating layers of PEI/water and surfactant micelles with PEI/water. However in reality these polymer/surfactant films compositions have more complicated structures as illustrated in the GIXD section below. A theoretical method was suggested by Wasbrough [*47*] to calculate the amount of encapsulated additives inside these polymer/surfactant films by using neutron reflectivity. This method is based on SLD contrast variation between deuterated and hydrogenated additives. The best fitting for the suggested multilayer model described above was used to simulated the data and then the integrated area under the peak was calculated for the most intense peak by using Motofit procedures [*80*] and TN020-B Peak Areas procedure in IgorPro.

Figure 4.7.1 shows the best simulation of the intense peaks in the reflectivity pattern from a SPEI film BDHAB using Motofit. The purpose of simulation of this pattern is to simulate the real reflectivity peak by estimating the number of repeating layers. The best fitting of those surfactant/PEI films showing sharp and intense peaks suggested the film structure can be modelled as a first surfactant monolayer 25Å thick, 9Å for the second PEI/water layer and 40Å for the third layer of surfactant micelles with PEI and water. The best theoretical diffraction peak resulting from Motofit procedures, simulating the real reflectometry pattern was found when the second and third layers were repeated 35 times. During fitting, to reduce the number of variables the SLD of first layer held as -0.353×10^{-6} Å^{-2} and the second layer calculated and held to be 3.48×10^{-6} Å^{-2} as 1:1

polymer/D_2O mixture ratio, where third layer was fitted . The SLD of the subphase was calculated to be $6.08x10^{-6}$ $Å^{-2}$ and held during fitting. The simulation results for the aromatic headgroup surfactant/PEI system used in this experiment are very close to the best fitting for similar systems suggested by O'Driscoll [*33*] and Wasbrough [*47*].

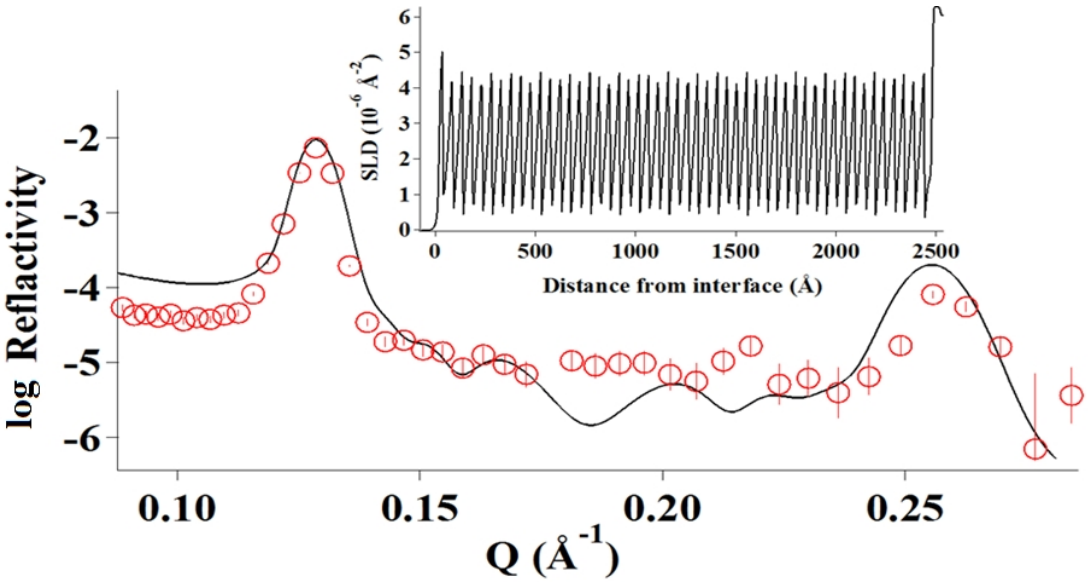

Figure 4.7.1: Multilayer simulation model of reflectivity pattern for BDHAB/SPEI using Motofit. The first layer was a surfactant monolayer, second layer is PEI/water and third layer is surfactant micelle. The second and third layers were repeated 35 times.

To calculate the amount of styrene in the surfactant/PEI films, the area under the peak was calculated for theoretical reflectivity patterns resulting from using simulated the model as shown in figure 4.7.1. Changes in the SLD of the micelle-containing layer in the presence of different amounts of deuterated and hydrogenated styrene were calculated. Then these calculated SLD values were substituted into the model to calculate the area under the peak as the SLD values change, as a result of varying the amount of styrene in the micelle/water and PEI layers. The area under the peak resulting from the calculated patterns using the SLD for both deuterated and hydrogenated styrene was plotted against the amounts of styrene added. Figure 4.7.2 show the linear relationship between SLD variation resulting from addition of deuterated/hydrogenated styrene and the percentage (vol%) of styrene that was added. The area under the peak was the calculated for all of the real neutron reflectivity data where hydrogenated and deuterated styrene was solubilized in these surfactant/PEI films.

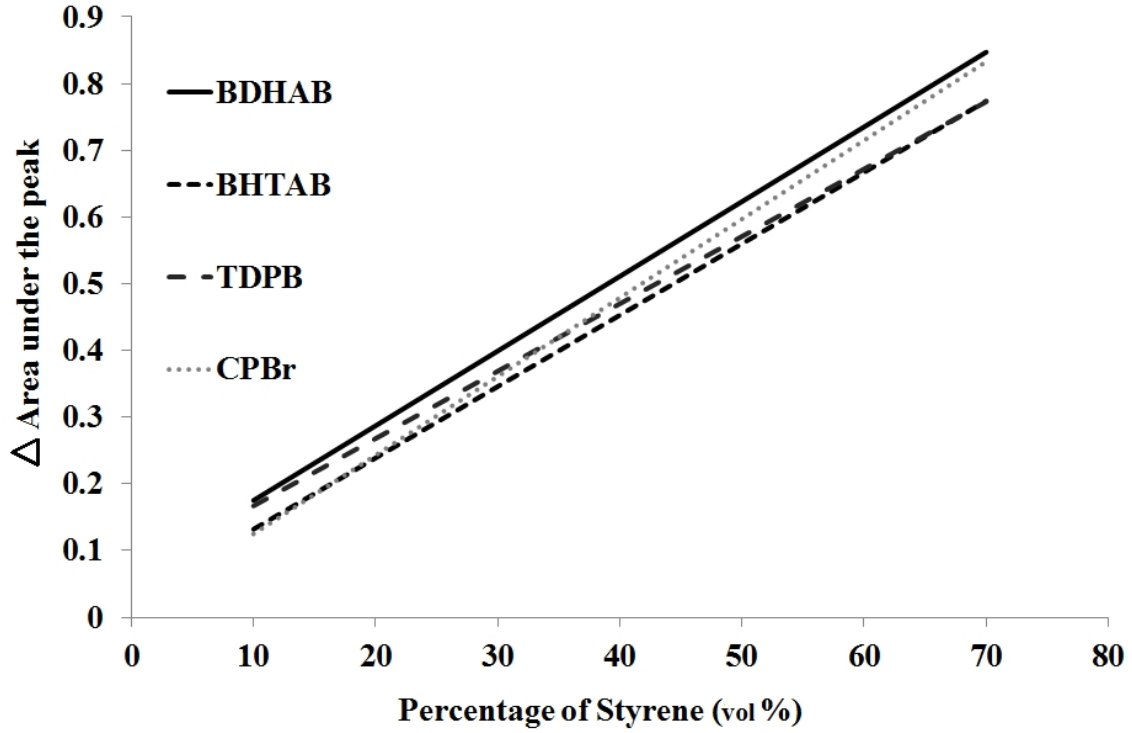

Figure 47.2: Linear correlation from theoretical calculation of area under the peak for a reflectivity pattern calculated incorporating deuterated/hydrogenated styrene into the micelle/PEI/water layer and the percentage of styrene in the micelle. Linear regression was 0.9991 – 0.9996.

Finally the values of the area under the peak for real systems containing hydrogenated/deuterated styrene were matched with the theoretical values in Figure 4.7.1 to estimate the actual amount of styrene in these films. The final results are plotted in figure 4.7.3 illustrating the percentage of calculated styrene inside surfactant/PEI films based on reflectivity measurements with deuterated or hydrogenated styrene. The amounts of encapsulation styrene in C_{14} and C_{16} surfactant/PEI films illustrate a reduction of the amount of encapsulated styrene when the concentration of added styrene is increase. This decrease in the amount encapsulated trend was seen very clearly between 30% and 50% of added styrene, in case of films formed using a surfactant with a C_{14} hydrocarbon chain, and can also be seen between 30% and 40% of added styrene in case of surfactants with a C_{16} hydrocarbon chain. BDTAB/PEI films solubilising 30% and 50% of styrene show after 30 min of film formation, a decrease in encapsulated styrene while TDPB shows increase of encapsulated styrene after 30 min from the film forming. BDHAB/PEI films show a decrease of encapsulation styrene for both 30% and 50% of added styrene. These results agreed with film thicknesses of these systems discussed above, where TDPB/SPEI was thicker than BDHAB/PEI films.

CPBr/PEI films solubilising 40vol% and 50vol% of styrene shows increasing of encapsulation with time, but the 30% of styrene film showed a decrease of encapsulated styrene with time of film forming. The maximum variation in the results of calculation encapsulated styrene was seen in case of BDHAB/PEI films solubilising 40vol% of styrene. This variation as stated before is due to the high polydispersity in the layer thickness in this film. CPBr solubilising 40vol% of styrene showed the lowest percentage of encapsulation compared with other concentrations. This drop in styrene percentage could be due to uncontrolled evaporation processes, since the humidity was not controlled in this experiment. The calculated results of encapsulation of styrene in these films using SLD variation via incorporation of deuterated and hydrogenated styrene show in general almost random positive and negative values and these results do not demonstrate any clear systematic trends.

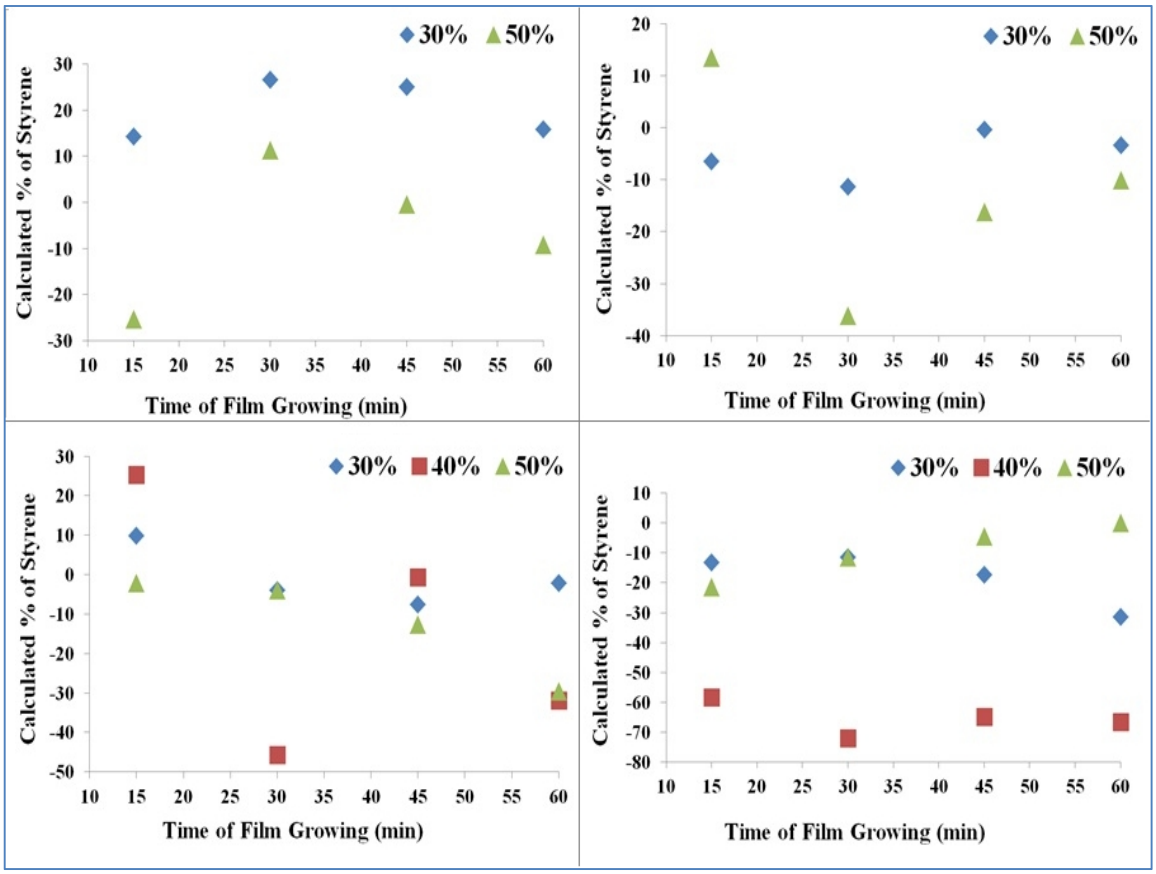

Figure 4.7.3: calculated percentage of encapsulated styrene during film formation for SPEI films grown with BDTAB (left, top), TDPB (right, top), BDHAB (left, bottom) and CPBr (right, bottom). Error of calculated percentage of encapsulated styrene was ±2%

Despite the fact that the theoretical calculation method using contrast SLD variation model showed an accurate linear calibration curve nevertheless the actual data does not match well with the theoretical method. The main explanation suggested by Wasbrough for this variation or inaccuracy by using this calculation method refers to a differential evaporation rate between hydrogenated and deuterated styrene solution samples. The second reason suggested by the same author related to the variation of layers numbers of these surfactant/PEI films which varied between samples depending on evaporation rate, and extent of deuteration of components in the films. The final reason it could be dissimilar amount of roughness between these layers in different films [*47*].

From the previous section on the kinetic study of solubilising hydrophobic monomer into cationic surfactant/PEI films it was shown very clearly that most of these films composition or structures are changing with time which supports the explanation suggested above for the reasons behind inaccuracy of this calculation method. In addition the simulation method used by Motofit assumed that the repeating layers are lamellar structure where the actual structure of these repeating layers could be more complicated.

4.8 X-ray Reflectivity and Grazing Incidence X-ray Diffraction.

In previous the SANS experiments, nine cationic surfactants were used to solubilise hydrophobic monomer. These surfactants represent a wide range of hydrocarbon chains with both aliphatic and aromatic headgroups. As stated before the purpose of these studies was to select an optimal system which can help to achieve our final goal of polymerizing encapsulated monomer in mesostructured films to create insoluble nanostructured polymer. Therefore additional characterisation of the surfactants/PEI systems was carried out on those films, which in the previous section showed relatively improved mesostructures. In this section X-ray reflectivity and grazing incidence X-ray diffraction (GIXD) were used to characterize the final structure of these films. The X-ray reflectivity and GIXD experiments were performed on the Troïka II instrument on the ID10B beam line at the European Synchrotron Radiation Facility (ESRF), Grenoble, France [*79*]. Each sample was investigated in three stages, the first stage was time

resolved off-specular X-ray reflectivity, then after the pattern ceased to evolve, specular X-ray reflectivity and finally by a grazing incidence X-ray diffraction pattern. Figure 4.8.1 show the time-resolved off-specular X-ray reflectivity for a film grown at the air-water interface using 0.05M CPBr with 1.5% SPEI.

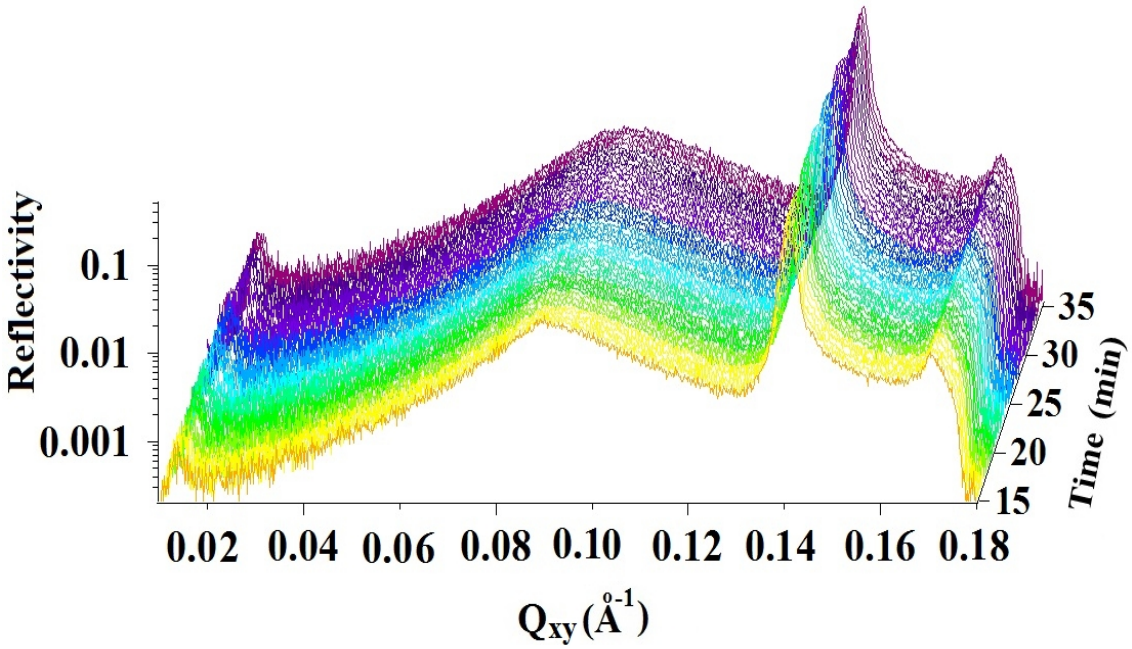

Figure 4.8.1: Time-resolved X-ray reflectivity from a film grown on a solution of 0.05M CPBr with 1.5% SPEI at the air/water interface, taken at an incident angle of 1.27°.

The time-resolved off-specular X-ray reflectivity patterns show small peaks around Q_z 0.014 Å^{-1} and 0.18 Å^{-1} (figure 4.8.1). These peaks are due to enrichment of the reflected beam at the critical angle, which originates from the coherent combination between the incident, reflected and transmitted X-ray at the sample surface causing a phenomenon called the Yoneda wing [*81, 82*]. The intensity of Yoneda wing related to the roughness at the surface of the film [*76*]. When the detector is located such that the specular reflectivity peak rises near the centre of the detector, diffraction peaks appear on either side, flanking the reflectivity peak being the first and second order respectively. The very broad peak at Q_z 0.09 Å^{-1} results from the specularly reflected peak which occurs at the same angle as the incident angle. The low intensity and broad width of this peak are due to surface roughness in the film [*76*]. Also later neutron reflectivity patterns of equivalent samples show some emerging diffraction peaks around this Q region which can also cause the specularly reflected peak to be obscured. Neutron reflectivity patterns of films grown on solutions of CPBr with 1.5% SPEI had two peaks at 0.122 Å^{-1} and

0.244 $Å^{-1}$ (figure 4.8.2). The high intensity peak shown in the X-ray time-resolved reflectivity of CPBr/SPEI films emerged at Q_z 0.140 $Å^{-1}$ (figure 4.8.1). This means there is a shift of 0.018 $Å^{-1}$ in peak position compared with neutron reflectivity for the same sample. This variation between neutron and X-ray reflectivity have also been reported by Wasbrough [*47*] studying the CTEAB/SPEI system. Most surfactants used in this research were hydrogenated surfactant therefore solutions were usually prepared in 100% of D_2O as a solvent in neutron reflectivity or SANS experiments to obtain greatest contrast between the sample and solvent. In the case of X-ray reflectivity or SAXS experiments H_2O was used as a solvent since it is cheaper and there is no great contrast variation between hydrogenated or deuterated samples in X-ray experiments. Since the shift in peak positions were noticed between neutron and X-ray reflectivity experiments it could be related to solvation effects since several authors have reported different effects from changes in isotopic solvation on the final structure [*83, 84*]. In addition H_2O and D_2O have slightly different effects at different temperature [*85*]. The change in peak position could also be due to growing the films under different conditions of humidity. In general, most of the off-specular X-ray time-resolved reflectivity data in this experiment showed only one real peak, therefore there is no further information to be obtained from this peak compared with the time resolved neutron reflectivity discussed in the previous section.

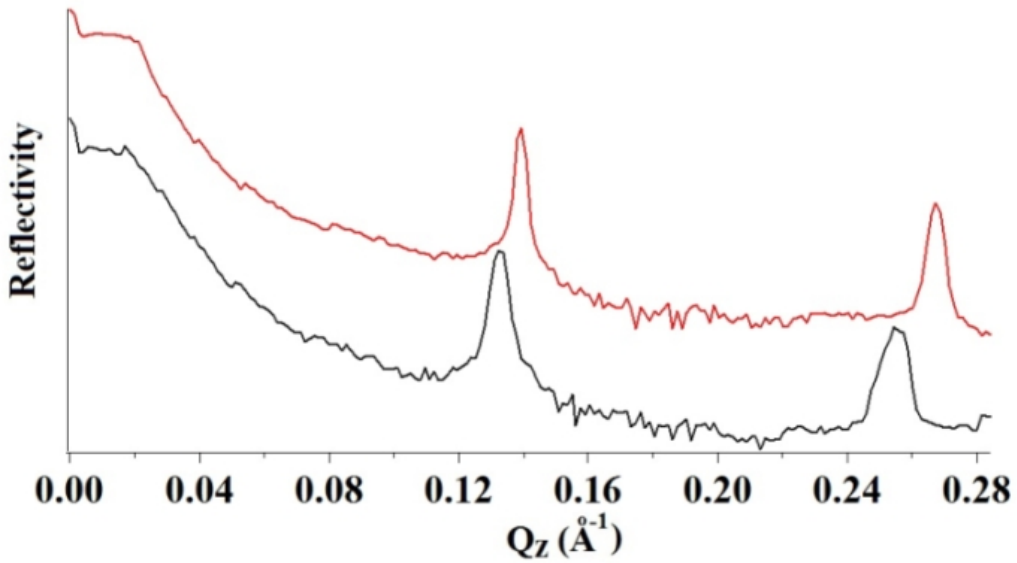

Figure 4.8.2: X-ray reflectivity patterns of films composed of BDTAB/SPEI (top pattern) and BDTAB/SPEI solubilising 50vol% styrene (bottom pattern).

The specular X-ray reflectivity patterns for C_{14} and C_{16} hydrocarbon chain surfactants with aromatic headgroups used in this experiment, in general show the same trends as shown in neutron reflectivity. However the patterns for some samples in neutron reflectivity show clear diffraction peaks where in X-ray reflectivity either it does not show clear diffraction peaks or it shows very low intensity peaks for the same sample. The real reason behind this variation for these samples is not very clear, however it is possibly related to evaporation rate of the sample solutions since the surfactant/PEI films are very sensitive to humidity and the humidity was not controlled in either the neutron or X-ray reflectivity experiments. Another possible reason as mentioned above is this variation of isotope effect due to stronger hydrogen bonding in D_2O compared to H_2O [*86*]. Figure 4.8.2 shows the X-ray reflectivity patterns of films of BDTAB/SPEI and BDTAB/SPEI solubilising 50% styrene. The BDTAB film shows very clear shift of the Bragg peaks toward low Q_z when the amount of styrene solubilized in the film is increased which illustrate good agreement with neutron reflectivity. The d-spacing and crystallite size of BDTAB/SPEI and BDTAB/SPEI films solubilising 50vol% styrene resulting from X-ray reflectivity overall are close to neutron reflectivity results (figures 4.8.3)

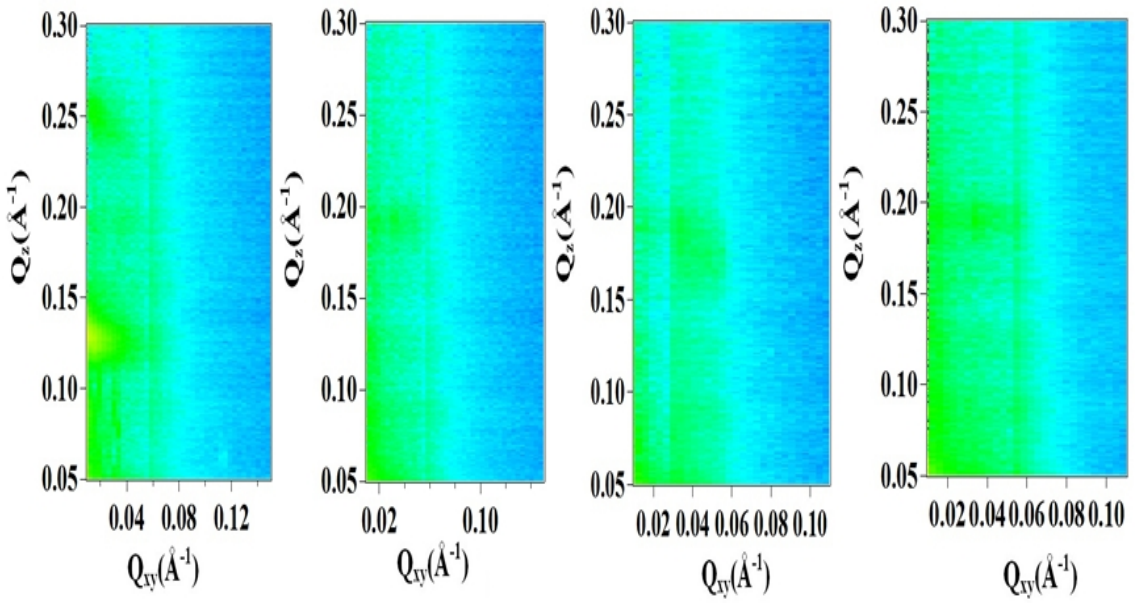

Figure 4.8.3: GIXD patterns collected from air/water interfacial films made from 0.05M C_{14} hydrocarbon chain surfactant/SPEI using an incident angle of 0.13°. From left to right, BDTAB, BDTAB encapsulating 50vol% styrene, TDPB, and TDPB encapsulating 50vol% styrene.

Figure 4.8.3 shows grazing incidence X-ray diffraction of C_{14} hydrocarbon chain surfactant/S-PEI films with and without styrene. In general the scattering from films prepared using SPEI with BDTAB and TDPB solubilising different amount of styrene do not show very clear rings or spots. However GIXD from BDTAB/SPEI films without styrene shows a poorly ordered lamellar structure, while the most of these films show only very broad diffraction features. These broad diffraction features suggest high polydispersity of layers within the structure [*79*]. X-ray and neutron reflectivity show peaks indicating lamellar structures in these films, however the GIXD cannot confirm whether this is truly a lamellar structures or a different mesostructure category. Campbell et al reported that CTAB/SPEI films are not stable with time where the interfacial material could collapse in these films forming adsorbed layers without any mesostructure [*68*].

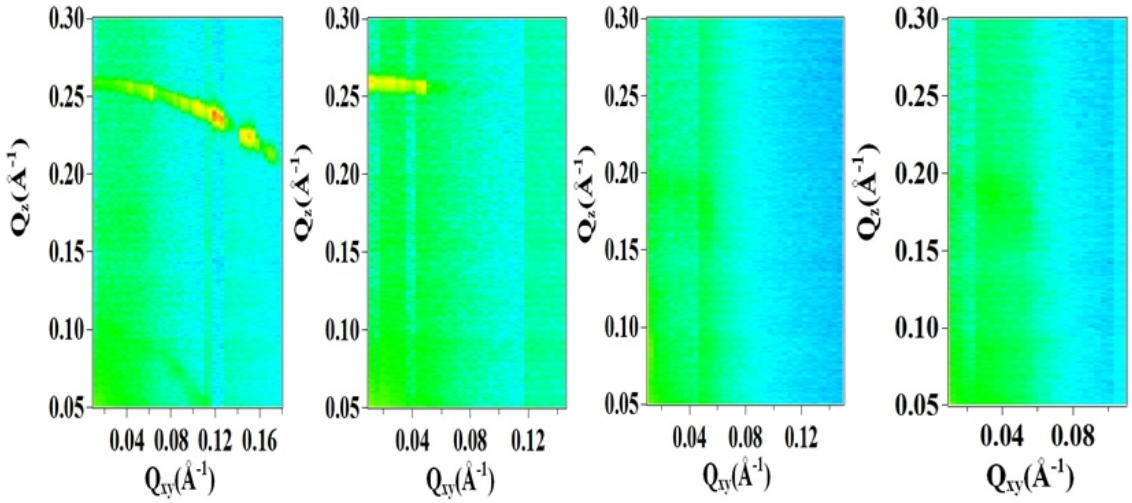

Figure 4.8.4: GIXD patterns collected on air/water interfacial films made from 0.05M C_{16} hydrocarbon chain surfactant/S-PEI. From left to right, BDHAB, BDHAB encapsulating 50vol% styrene, CPBr, and CPBr encapsulating 50vol% styrene.

The C_{16} hydrocarbon chain surfactants BDHAB and CPBr with SPEI solubilising different amount of styrene still show broad diffraction features, particular in films grown using CPBr (figure 4.8.4). BDHAB/SPEI films without styrene showed two rings of spots at Q_z 0.103 and 0.260Å^{-1} while BDHAB/SPEI films solubilising 50% of styrene shown one ring of spots at Q_z 0.25Å^{-1}. The structure assignment for BDHAB/SPEI films without styrene suggests an $Fd\bar{3}m$ structure with a 106Å unit cell size. In general BDHAB and CPBr with S-PEI films do not show very ordered structures but at the same time these spots indicate the final structure is not a lamellar structure.

BDHAB with LPEI films solubilising different amount of styrene show in general well-ordered structures compared with SPEI films (figure 4.8.5). Previous studies by O'Driscoll and Wasbrough on surfactant/PEI films at the air/water interface illustrated well-ordered structures in cases using SPEI while in the case of LPEI GIXD patterns showed broad rings [*27, 79, 87*]. In this work, most BDHAB/LPEI films solubilising different amount of styrene showed a broad ring at Q_z 0.1-0.14 $Å^{-1}$. This broad ring could be either due to high polydispersity within the structure [*79*] or overlapping from more than one ring of diffraction.

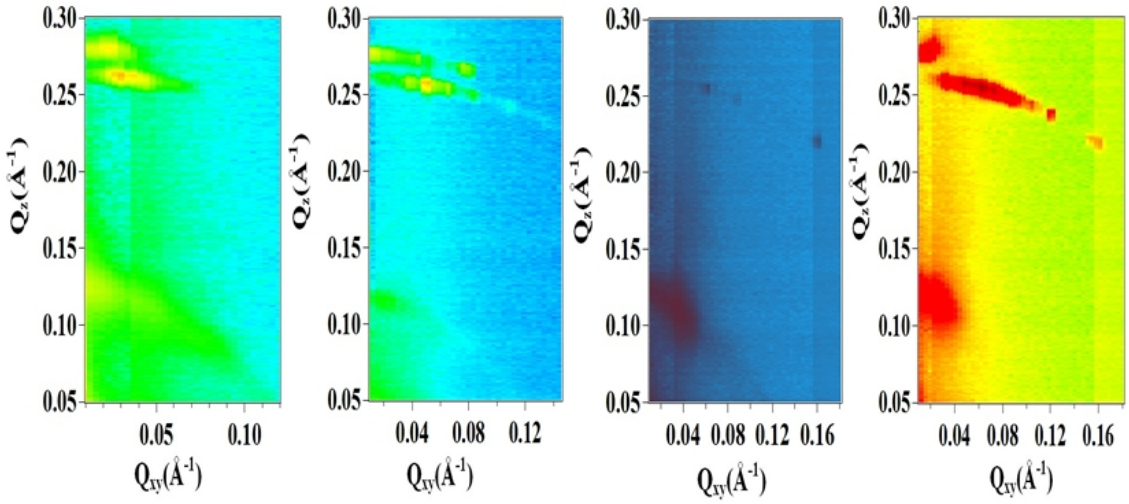

Figure 4.8.5: GIXD patterns collected on air/water interfacial films made from 0.05M C_{16} hydrocarbon chain surfactant/L-PEI. From left to right, BDHAB, BDHAB encapsulating 30vol% styrene, BDHAB encapsulating 40vol% styrene, BDHAB encapsulating 50vol% styrene.

Solubilising different amount of styrene in BDHAB/LPEI films in general does not result in a large variation in the final structure. However BDHAB/LPEI films solubilising styrene show better ordered structures than BDHAB/LPEI films without styrene, which suggests that encapsulating styrene enhances the order of BDHAB/LPEI films mesostructure. This behaviour could be due to π-cation interaction between styrene and the aromatic part in the surfactant headgroups, allowing initially short micelles to become rod-like [*40-43*]. Subsequently, enhanced polyelectrolyte binding to the micelles occurs due to the favourable entropic mechanism of counterion release [*33*] and potentially also optimised headgroup spacing for interaction with PEI. The best structure assignment of BDHAB/SPEI films encapsulating different amount of styrene suggests a cubic $Fd\bar{3}m$ mesostructure with 86Å unit cell size. Another possibility of

these films structure could be a cubic $Pm\bar{3}n$ mesophase with a 70Å unit cell size (figure 4.8.5).

CPBr/LPEI films without styrene show well-ordered mesostructures compared with the same films composition solubilising styrene. By increasing the concentration of styrene in CPBr/LPEI films, the diffraction spots become broader. This indicates an increase of the polydispersity within the CPBr/LPEI films as the concentration of styrene is increased. The best structure assignment of CPBr/SPEI films encapsulating different amount of styrene is suggested to be a cubic $Pm\bar{3}n$ mesostructure with a 168Å unit cell size or possibly could be a cubic $Fd\bar{3}m$ phase with a 218Å unit cell size (figure 4.8.5).

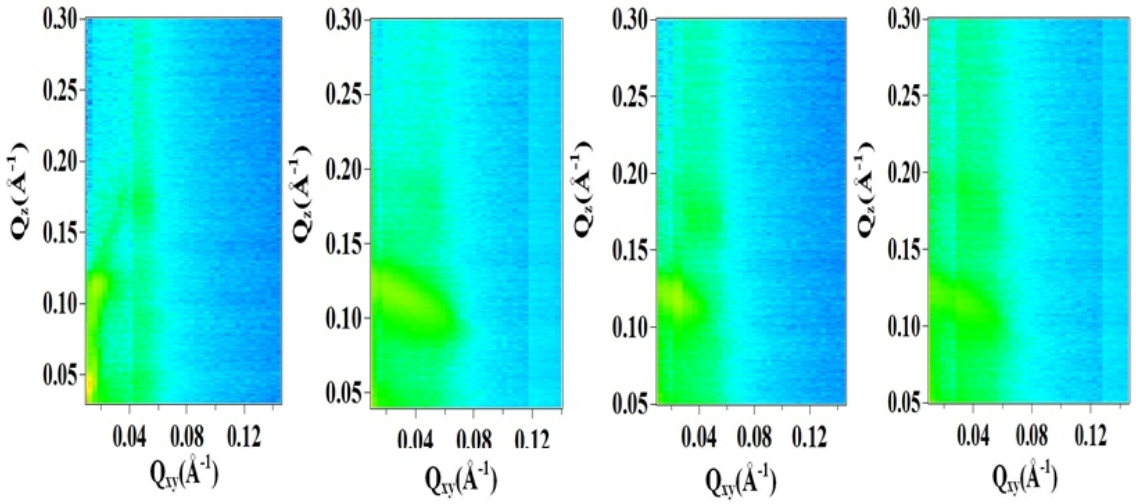

Figure 4.8.6: GIXD patterns collected on air/water interfacial films made from 0.05M C_{16} hydrocarbon chain surfactant/L-PEI. From left to right, CPBr, CPBr encapsulating 30vol% styrene, CPBr encapsulating 40vol% styrene, CPBr encapsulating 50vol% styrene.

GIXD data of surfactants/PEI films solubilising different amounts of styrene showed that the C_{16} hydrocarbon chain for both headgroups (benzyldimethyl and pyridinium) can form more well-ordered structures compared with those formed from surfactants with a C_{14} hydrocarbon chain. In addition BDHDAB/LPEI films at 30vol% and 50vol% of solubilised styrene showed the most highly ordered structures compared with those of the other C_{16} hydrocarbon chain surfactant (figure 4.8.5). However an enhancement of mesoscale structure only occurred when styrene was incorporated into BDHAB/LPEI films whereas CPBr/LPEI films showed an increase in polydispersity as the amount of styrene solubilized increased. SANS experiments showed in general that C_{16} hydrocarbon chain surfactants formed bigger micelles thus enhancing the solubilisation

of styrene inside these micelles, while neutron reflectivity illustrated overall that surfactants with relatively long hydrocarbon chain formed thicker films. These results are in good agreement with results by O'Driscoll which showed that the interaction between C_{16}TAB and PEI was the greatest compared with that for surfactants with a C_{12} or C_{14} hydrocarbon tail. This strong interaction cause elongation of the micelles corresponding to the long axis of hexagonal array of micelles in the films [*33*]. Subsequently this elongation enhances the polyelectrolyte binding to the micelles thus building thick well-ordered mesostructured membranes.

Surprisingly using a high molecular weight of PEI gives better ordered structures in this system compared with low molecular weight PEI in films made using both BDMHDAB and CPBr. This is a different result from previous systems where high molecular weight PEI, although giving thicker more robust films, tended to have poorer ordering in the films while low molecular weight PEI gave highly ordered but thinner films [*27, 79, 87*]. In this system the most robust films are also the most ordered which is a distinct advantage with regard to the final aim to polymerise the styrene within the membranes to make reinforced films for filtration and sensors or to make free standing ordered nanostructured polystyrene structures.

4.9 Conclusions

The aim in this chapter is to select films with well-ordered mesostructures as a first step towards synthesising nanoscale insoluble membranes which could be used as supports for catalysis and selective membranes. Therefore investigation of encapsulation hydrophobic monomers into cationic surfactant micelles in solutions and in solid polymer/surfactant films were investigated to determine the structure of the micelles formed in these system and shed light upon the interactions in solution which drive formation of the films at the interface since there is a close relationship between the solution structures and the final structure of the films.

Solubilisation studies of styrene in cationic surfactant solutions by using UV-Vis spectroscopy illustrated that there are shifts in styrene λ_{max} from surfactant/styrene mixture solutions compared with styrene/water scan. Essentially this λ_{max} shift is due to changes in the $\pi \rightarrow \pi^*$ transitions band due to attractive polarisation forces between the surfactant hydrocarbon chain and styrene hydrophobic monomer, which lower the energy levels of both the excited and unexcited states. This interaction between the surfactant hydrocarbon chain and styrene molecules indicates that styrene preferred to encapsulate inside the micelles at the hydrophobic phase.

SANS study of the location of encapsulated styrene monomer inside cationic surfactant micelles suggest that styrene are encapsulated and located partly in the palisade layer which is the region between headgroup and hydrocarbon chain, and at the same time some of encapsulated styrene exists in the micelle core, intimately associated with the surfactant tails.

The effects of PEI on cationic surfactant micelles solutions encapsulating styrene illustrated that there is an attractive complex interaction between the cationic surfactant micelles and PEI. This leads to polyethyleneimine binding closer to the micelle headgroup through electrostatic interactions between the PEI amino group and the cationic surfactant micelle headgroup. At the same time PEI interact with water molecules close to the surfactant micelle headgroup and also with PEI itself by hydrogen bonding.

Two methods were used to investigate the amount of encapsulated styrene in these cationic surfactant micelles. The first method depends on using the SLD contrast

between hydrogenated surfactant micelles encapsulating either hydrogenated or deuterated styrene. The results were calculated from this methods suggested that the cationic surfactant with aromatic headgroup have more solubilisation capacity for hydrophobic molecules than aliphatic surfactant headgroups. The second method used to calculate the percentage or the amount of styrene encapsulated inside surfactant micelles uses the differences in the micelle volumes. This method shown that BDHAB with and without PEI had the highest encapsulation capacity compared with other surfactants which suggests that the benzyl group in the BDHAB perform as a second hydrocarbon tail subsequently increasing the encapsulation capacity. Overall the SANS results from polymer/surfactant solutions encapsulating styrene showed that the surfactants headgroup plays a very important role in the micellar volume and also can determine the polyelectrolyte/surfactant interaction and its influence on these micelles encapsulating hydrophobic molecules. The greatest influence of PEI on these cationic surfactants encapsulating styrene was seen for BDHAB then CPBr while CTAB showed less effect.

The second part in this chapter is studying the formation of solid polymer/surfactant films at the air-solution interface therefore a range of surfactant with aliphatic and aromatic headgroup and three types of hydrocarbon chain length C_{12}, C_{14} and C_{16} were used to select the best organized templating media.
Cationic surfactant/PEI films encapsulating hydrophobic monomers overall suggest a structure composed of three adsorbed layers. This model consists of a first layer corresponding to the surfactant hydrocarbon chain. The second layer is of PEI mixed with D_2O and surfactant headgroups, while the third layer is composed of surfactant micelles with water/PEI in small gaps between the micelles.

In general cationic surfactants consisting of C_{14} and C_{16} hydrocarbon tails formed robust films on the top of the water/air interface of the solution while C_{12} surfactants do not show any obvious solid films on their solutions surface. Mainly surfactants with a C_{12} hydrocarbon tail for both pyridinium and benzyldimethylammonium bromide with SPEI formed a simple adsorbed layer rather than forming order structures. On the other hand pyridinium headgroup surfactants showed a more attractive interaction with PEI compared with the benzyldimethylammonium group due to the bulkiness and hydrophobicity effects.

Kinetic studies of polymer/surfactant films solubilising styrene showed that the crystallite size of TDPB/SPEI system grew with time while the thickness of BDTAB/SPEI films was decreased during the films formation. These results suggest that dissolutions rate of BDTAB/SPEI films was faster than accumulative rate for the same system, thus causing loss in the film thickness with time. TDPB/SPEI system illustrated higher accumulative rate than dissolution rate, which built thicker films with time.

The layers thickness for both BDHAB/SPEI and CPBr/SPEI films without styrene overall were thicker than in case of presence of styrene. This result suggesting that solubilising styrene in these films reduces the attraction between PEI and micelles which leads to extra packing of these micelles. Overall the number of layers and the films thickness of benzyldimethyl and pyridinium headgroups with C_{14} and C_{16} hydrocarbon tails solubilising different amount of styrene demonstrates that these films are suitable templating media for polymerization styrene inside these films.

X-ray reflectivity and grazing incidence X-ray diffraction has shown that BDHAB with LPEI films solubilising different amount of styrene formed well-ordered structures compared with SPEI films. However BDHAB/LPEI films solubilising styrene show better ordered structures than BDHAB/LPEI films without styrene, which suggests that encapsulating different amount of styrene enhances the order of BDHAB/LPEI films mesostructure. GIXD data for surfactants/PEI films solubilising different amounts of styrene showed that the C_{16} hydrocarbon chain for both headgroups (benzyldimethyl and pyridinium) can form more well-ordered structures compared with those formed from surfactants with a C_{14} hydrocarbon chain

SANS results from micellar solutions and neutron/X-ray reflectivity of polymer/surfactant films propose that surfactant with aromatic headgroup and consist relatively from long hydrocarbon tail could form suitable mesostructures for templating insoluble polymers in the films. Therefore the next chapter (polymerization of encapsulated styrene in these polymer/surfactant films) mainly focused on these systems which were shown to have the best structures and most robust films.

4.10 References

1. Paul, D., and Robeson, L. (2008) Polymer nanotechnology: nanocomposites, *Polymer 49*, 3187-3204.
2. Koo, J. H. (2006) *Polymer nanocomposites : processing, characterization, and applications*, McGraw-Hill, New York.
3. Resmini, M. (2012) Molecularly imprinted polymers as biomimetic catalysts, *Analytical and bioanalytical chemistry*, 1-6.
4. Lau, C. H., Li, P., Li, F., Chung, T. S., and Paul, D. R. (2012) Reverse-selective polymeric membranes for gas separations, *PROGRESS IN POLYMER SCIENCE*.
5. Mandal, B., Bhattacharjee, H., Mittal, N., Sah, H., Balabathula, P., Thoma, L. A., and Wood, G. C. (2012) Core-Shell Type Lipid-Polymer Hybrid Nanoparticles as a Drug Delivery Platform, *Nanomedicine: Nanotechnology, Biology and Medicine*.
6. Yan, F., and Texter, J. (2006) Capturing nanoscopic length scales and structures by polymerization in microemulsions, *Soft Matter 2*, 109 - 118.
7. Jung, M., German, A. L., and Fischer, H. R. (2001) Polymerisation in lyotropic liquid-crystalline phases of dioctadecyldimethylammonium bromide, *Colloid and Polymer Science 279*, 105-113.
8. Edler, K. J., Wasbrough, M. J., Holdaway, J. A., and O'Driscoll, B. M. D. (2009) Self-assembled films formed at the air - Water interface from CTAB/SDS mixtures with water-soluble polymers, *Langmuir Langmuir 25*, 4047-4055.
9. Dean, J. A., and Lange, N. A. (1992) *Lange's handbook of chemistry*, McGraw-Hill, New York.
10. Schulz, P. C., and Morini, M. A. (1997) Styrène solubilization in micelles of dodecyltrimethylammonium hydroxide, *Colloid and Polymer Science 275*, 604-607.
11. Becerra, F., Soltero, J. F. A., Puig, J. E., Schulz, P. C., Esquena, J., and Solans, C. (2003) Free-radical polymerization of styrene in worm-like micelles, *Colloid and Polymer Science 282*, 103-109.
12. Kalsi, P. S. (1995) *Spectroscopy of organic compounds*, Wiley Eastern, New Delhi.
13. Ramachandran, C., Pyter, R. A., and Mukerjee, P. (1982) Microenvironmental effects on energies of visible bands of nitroxides in electrolyte solutions and when solubilized in micelles of different charge types. Significance of effective polarity estimates. Implications for spectroscopic probe studies in lipid assemblies, *Journal of Physical Chemistry 86*, 3198-3205.
14. Warr, G. G., and Evans, D. F. (1988) Spectroscopic determination of the effective dielectric constant of micelle-water interfaces between 15 and 85 °C, *Langmuir 4*, 217-224.
15. Abbott, A. P., Miaw, C. L., and Rusling, J. F. (1992) Correlations between solvent polarity scales and electron transfer kinetics and an application to micellar media, *J Electroanal Chem 327*, 31-46.
16. Hosseinzadeh, R., Gheshlagi, M., Tahmasebi, R., and Hojjati, F. (2009) Spectrophotometric study of interaction and solubilization of procaine hydrochloride in micellar systems, *Cent Eur J Chem 7*, 90-95.

17. Masrat, R., Maswal, M., and Dar, A. A. (2013) Competitive solubilization of naphthalene and pyrene in various micellar systems, *J Hazard Mater 244-245*, 662-670.
18. Khan, A. M., and Shah, S. S. (2008) A UV-visible study of partitioning of pyrene in an anionic surfactant sodium dodecyl sulfate, *Journal of Dispersion Science and Technology 29*, 1401-1407.
19. Enache, M., and Volanschi, E. (2012) Spectroscopic investigations of the molecular interaction of anticancer drug mitoxantrone with non-ionic surfactant micelles, *J Pharm Pharmacol 64*, 688-696.
20. O'Driscoll, B. M. D., Hawley, A. M., and Edler, K. J. (2008) Incorporation of Sparingly Soluble Species in Mesostructured Surfactant-Polymer Films, *J. Colloid Interface Sci. 317*, 585-592
21. Christian, S. D. S. J. F. (1995) *Solubilization in surfactant aggregates*, M. Dekker, New York.
22. Rangel-Yagui, C. O., Pessoa, A., Jr., and Tavares, L. C. (2005) Micellar solubilization of drugs, *8*, 147-165.
23. Bartlett, P., and Ottewill, R. H. (1992) A neutron scattering study of the structure of a bimodal colloidal crystal, *The Journal of Chemical Physics 96*, 3306-3318.
24. Kline, S. R. (2006) Reduction and analysis of SANS and USANS data using IGOR Pro, *Journal of Applied Crystallography 39*, 895-900.
25. Hayter, J. B., and Penfold, J. (1981) An analytic structure factor for macroion solutions, *Mol. Phys. 42*, 109-118.
26. Degiorgio, V. C. M. I. P. S. Physics of amphiphiles : micelles, vesicles, and microemulsions, North-Holland Pub. Co., Amsterdam; New York.
27. O'Driscoll, B. M. D., Hawley, A. M., and Edler, K. J. (2008) Incorporation of sparingly soluble species in mesostructured surfactant-polymer films, *J. Colloid Interface Sci. 317*, 585-592.
28. Kitiyanan, B., O'Haver, J. H., Harwell, J. H., and Osuwan, S. (1996) Absolubilization of styrene and isoprene in cetyltrimethylammonium bromide admicelle on precipitated silica, *Langmuir 12*, 2162-2166.
29. Shi, Y. C., Wu, Y. S., and Li, G. Z. (2004) High resolution NMR study on solubilization behavior of styrene in CTAB microemulsion system, *Acta Chimica Sinica 62*, 424-428.
30. Norwood, D. P., Minatti, E., and Reed, W. F. (1998) Surfactant/polymer assemblies. 1. Surfactant binding properties, *Macromolecules 31*, 2957-2965.
31. Yang, B., Holdaway, J. A., and Edler, K. J. (2013) Robust ordered cubic mesostructured polymer/silica composite films grown at the air/water interface, *Langmuir 29*, 4148-4158.
32. Yang, B., Jaber, R., and Edler, K. J. (2012) Silica-surfactant-polyelectrolyte film formation: Evolution in the subphase, *Langmuir 28*, 8337-8347.
33. O'Driscoll, B. M. D., Milsom, E., Fernandez-Martin, C., White, L., Roser, S. J., and Edler, K. J. (2005) Thin films of polyethylenimine and alkyltrimethylammonium bromides at the air/water interface, *Macromolecules 38*, 8785-8794.
34. Gao, C. Y., Zhang, H., Wu, M., Liu, Y., Wu, Y. P., Yang, X. L., and Feng, X. Z. (2012) Polyethyleneimine functionalized polymer microsphere: a novel delivery vector for cells, *Polymer Chemistry. 3*, 1168-1173.
35. Pangon, A., Tashiro, K., and Chirachanchai, S. (2011) Polyethylenimine containing benzimidazole branching: A model system providing a balance of

hydrogen bond network or chain mobility enhances proton conductivity, *J. Phys. Chem. B 115*, 11359-11367.

36. Mittal, K. L., and Shah, D. O. (2003) Adsorption and aggregation of surfactants in solution, Marcel Dekker, New York.
37. Warr, G. G., Sen, R., Evans, D. F., and Trend, J. E. (1988) Microemulsion formation and phase behavior of dialkydimethylammonium bromide surfactants, *The Journal of Physical Chemistry 92*, 774-783.
38. Gomati, R., Appell, J., Bassereau, P., Marignan, J., and Porte, G. (1987) Influence of the nature of the counterion and of hexanol on the phase behavior of the dilute ternary systems: Cetylpyridinium bromide or chloride-hexanol-brine, *Journal of Physical Chemistry 91*, 6203-6210.
39. Dar, A. A., Rather, G. M., and Das, A. R. (2007) Mixed micelle formation and solubilization behavior toward polycyclic aromatic hydrocarbons of binary and ternary cationic - Nonionic surfactant mixtures, *J. Phys. Chem. B 111*, 3122-3132.
40. Wasan, D. T. G. M. E. S. D. O. (1988) *Surfactants in chemical/process engineering*, M. Dekker, New York.
41. Fuangswasdi, A., Charoensaeng, A., Sabatini, D. A., Scamehorn, J. F., Acosta, E. J., Osathaphan, K., and Khaodhiar, S. (2006) Mixtures of anionic and cationic surfactants with single and twin head groups: Solubilization and adsolubilization of styrene and ethylcyclohexane, *Journal of Surfactants and Detergents 9*, 29-37.
42. Tehrani-Bagha, A. R., and Holmberg, K. (2013) Solubilization of hydrophobic dyes in surfactant solutions, *Materials 6*, 580-608.
43. McCurdy, A., Jimenez, L., Stauffer, D. A., and Dougherty, D. A. (1992) Biomimetic catalysis of SN2 reactions through cation-pi interactions. The role of polarizability in catalysis, *Journal of the American Chemical Society 114*, 10314-10321.
44. Zana, R., Yiv, S., Strazielle, C., and Lianos, P. (1981) Effect of alcohol on the properties of micellar systems. I. Critical micellization concentration, micelle molecular weight and ionization degree, and solubility of alcohols in micellar solutions, *J. Colloid Interface Sci. 80*, 208-223.
45. Luechinger, M., Pirngruber, G. D., and Prins, R. (2004) Solubilization of Aromatic Molecules in Templating Micelles of Mesoporous Silicas Followed by 1H NMR, *J. Phys. Chem. B 108*, 10903-10910.
46. Hedin, N., Sitnikov, R., Furo, I., Henriksson, U., and Regev, O. (1999) Shape Changes of C16TABr Micelles on Benzene Solubilization, *J. Phys. Chem. B 103*, 9631-9639.
47. Wasbrough, M. (2011) Nanostructured hydrogel films for encapsulation and release, University of Bath. , University of Bath, 2011.
48. O'Driscoll Benjamin, M. D., Hawley Adrian, M., and Edler Karen, J. (2008) Incorporation of sparingly soluble species in mesostructured surfactant-polymer films, *J. Colloid Interface Sci. 317*, 585-592.
49. Shipman, J., Wilson, J. D., Todd, A., and Higgins Jr, C. A. (2012) *An introduction to physical science*, Brooks/Cole Publishing Company.
50. Zhang, Y., Qi, Y., and Zakin, J. L. (2005) Headgroup effect on drag reduction and rheological properties of micellar solutions of quaternary ammonium surfactants, *Rheologica Acta 45*, 42-58.
51. Reekmans, S., Gehlen, M., De Schryver, F. C., Boens, N., and Van Der Auweraer, M. (1993) Micellar properties of aqueous solutions of

hexadecyltrimethylammonium salts in the presence of nonionic polymer, *Macromolecules 26*, 687-694.

52. Liu, Q., Song, C., Wang, Z. G., Li, N., and Ding, B. (2014) Precise organization of metal nanoparticles on DNA origami template, *Methods 67*, 205-214.
53. http://www.isis.stfc.ac.uk/index.html. (Feb 2010), ISIS Science and Technology Facilities Council Rutherford Appleton Laboratory Harwell Science and Innovation Campus Didcot, OX11 0QX, UK.
54. Hillhouse, H. W., van Egmond, J. W., Tsapatsis, M., Hanson, J. C., and Larese, J. Z. (2001) The interpretation of X-ray diffraction data for the determination of channel orientation in mesoporous films, *Microporous Mesoporous Mater. 44-45*, 639-643.
55. Taylor, D. J. F., Thomas, R. K., Li, P. X., and Penfold, J. (2003) Adsorption of Oppositely Charged Polyelectrolyte/Surfactant Mixtures. Neutron Reflection from Alkyl Trimethylammonium Bromides and Sodium Poly(styrenesulfonate) at the Air/Water Interface: The Effect of Surfactant Chain Length, *Langmuir 19*, 3712-3719.
56. Monteux, C., Williams, C. E., Meunier, J., Anthony, O., and Bergeron, V. (2003) Adsorption of Oppositely Charged Polyelectrolyte/Surfactant Complexes at the Air/Water Interface: Formation of Interfacial Gels, *Langmuir 20*, 57-63.
57. Vaknin, D., Dahlke, S., Travesset, A., Nizri, G., and Magdassi, S. (2004) Induced crystallization of polyelectrolyte-surfactant complexes at the gas-water interface, *Physical Review Letters 93*, 218302.
58. Lu, J. R., Thomas, R. K., and Penfold, J. (2000) Surfactant layers at the air/water interface: Structure and composition, *Advances in Colloid and Interface Science 84*, 143-304.
59. Lu, J. R., Thomas, R. K., Binks, B. P., Fletcher, P. D. I., and Penfold, J. (1995) Structure and Composition of Dodecane Layers Spread on Aqueous Solutions of Dodecyl- and Hexadecyltrimethylammonium Bromides Studied by Neutron Reflection, *J. Phys. Chem. 99*, 4113-4123.
60. Zarbakhsh, A., Webster, J. R. P., and Eames, J. (2009) Structural studies of surfactants at the oil - Water interface by neutron reflectometery, *Langmuir 25*, 3953-3956.
61. Comas-Rojas, H., Enriquez-Victorero, C., Roser, S. J., Edler, K. J., and Perez-Gramatges, A. (2013) Self-assembly and phase behaviour of PEI : cationic surfactant aqueous mixtures forming mesostructured films at the air/solution interface, *Soft Matter 9*, 4003-4014.
62. Scherrer, P. (1918) Bestimmung der Grösse und der Inneren Struktur von Kolloidteilchen Mittels Röntgenstrahlen, Nachrichten von der Gesellschaft der Wissenschaften, Göttingen, *Mathematisch-Physikalische Klasse 2*, 98-100.
63. Edler, K. J., Goldar, A., Brennan, T., and Roser, S. J. (2003) Spontaneous free-standing nanostructured film growth in polyelectrolyte-surfactant systems, *Chemical Communications 9*, 1724-1725.
64. Comas-Rojas, H., Aluicio-Sarduy, E., Rodriguez-Calvo, S., Perez-Gramatges, A., Roser, S. J., and Edler, K. J. (2007) Interactions and film formation in polyethylenimine-cetyltrimethylammonium bromide aqueous mixtures at low surfactant concentration, *Soft Matter 3*, 747-753.
65. Buckingham, S. A., Garvey, C. J., and Warr, G. G. (1993) Effect of head-group size on micellization and phase behavior in quaternary ammonium surfactant systems, *Journal of Physical Chemistry 97*, 10236-10244.

66. Bales, B. L., and Zana, R. (2002) Characterization of micelles of quaternary ammonium surfactants as reaction media I: Dodeclytrimethylammonium bromide and chloride, *J. Phys. Chem. B 106*, 1926-1939.
67. Bales, B. L., Messina, L., Vidal, A., Peric, M., and Nascimento, O. R. (1998) Precision relative aggregation number determinations of SDS micelles using a spin probe. A model of micelle surface hydration, *J. Phys. Chem. B 102*, 10347-10358.
68. Campbell, R. A., and Edler, K. J. (2011) Growth-collapse mechanism of PEI-CTAB films at the air-water interface, *Soft Matter 7*, 11125-11132.
69. Balmbra, R. R., Clunie, J. S., and Goodman, J. F. (1969) Cubic mesomorphic phases, *Nature 222*, 1159-1160.
70. Auvray, X., Petipas, C., Anthore, R., Rico, I., and Lattes, A. (1989) X-ray diffraction study of mesophases of cetyltrimethylammonium bromide in water, formamide, and glycerol, *Journal of Physical Chemistry 93*, 7458-7464.
71. Leonard, M., and Strey, H. H. (2010) Measurement of phase transition free energies in polyelectrolyte-surfactant complexes, *Macromolecules 43*, 4379-4383.
72. Bakshi, M. S., and Kaur, I. (2003) Aggregates of cationic surfactants and anionic polyelectrolytes influenced by bulky head group modifications, *Colloids and Surfaces a-Physicochemical and Engineering Aspects 224*, 185-197.
73. http://www.sigmaaldrich.com/united-kingdom.html. (2010).
74. O'Driscoll, D., Fernandez-Martin, C., Wilson , D., Knott, J., Roser, J., and Edler, J. (2007) Macroscopic, mesostructured cationic surfactant/neutral polymer films: structure and cross-linking, *Langmuir 23*, 4589-4598.
75. Taylor, D. J. F., Thomas, R. K., and Penfold, J. (2007) Polymer/surfactant interactions at the air/water interface, *Adv Colloid Interface Sci 132*, 69-110.
76. Edler, K. J., Goldar, A., Hughes, A. V., Roser, S. J., and Mann, S. (2001) Structural studies on surfactant-templated silica films grown at the air/water interface, *Microporous Mesoporous Mater. 44-45*, 661-670.
77. Comas-Rojas, H., Fernández-Catá, G., Edler, K. J., Roser, S. J., and Pérez-Gramatges, A. (2009) Multiple thin film formation from dilute mixtures of polyethyleneimine (PEI) and cetyltrimethylammonium bromide (CTAB), *J. Colloid Interface Sci. 339*, 495-501.
78. Aaberg, C., Sparr, E., Edler, K. J., and Wennerstroem, H. (2009) Nonequilibrium Phase Transformations at the Air-Liquid Interface, *Langmuir 25*, 12177-12184.
79. Wasbrough, M. J., Edler, K. J., Hawley, A. M., Holdaway, J. A., and Price, G. J. (2012) Control of mesostructure in self-assembled polymer/surfactant films by rational micelle design, *Soft Matter 8*, 3357-3362.
80. Nelson, A. (2006) Co-refinement of multiple-contrast neutron/X-ray reflectivity data using MOTOFIT, *Journal of Applied Crystallography 39*, 273-276.
81. Perlich, J., Memesa, M., Diethert, A., Metwalli, E., Wang, W., Roth, S. V., Gutmann, J. S., and Müller-Buschbaum, P. (2012) Layer-by-layer fabrication of an anatase titania multilayer with gradual sponge-like morphology, *Colloid and Polymer Science 290*, 119-126.
82. Yoneda, Y. (1963) Anomalous surface reflection of X rays, *Physical Review 131*, 2010-2013.
83. Gittings, M. R., Cipelletti, L., Trappe, V., Weitz, D. A., In, M., and Marques, C. (2000) Structure of Guar in Solutions of H2O and D2O: An Ultra-Small-Angle Light-Scattering Study, *J. Phys. Chem. B 104*, 4381-4386.

84. Chatake, T., Ishikawa, T., Yanagisawa, Y., Yamada, T., Tanaka, I., Fujiwara, S., and Morimoro, Y. (2011) High-resolution X-ray study of the effects of deuteration on crystal growth and the crystal structure of proteinase K, *Acta Crystallographica Section F: Structural Biology and Crystallization Communications 67*, 1334-1338.
85. Jancsó, G. (2006) H2O-D2O solvent isotope effect on excess molar volumes of 3-methylpyridine solutions, *Journal of Solution Chemistry 35*, 991-1005.
86. Pant, D., and Levinger, N. E. (1999) Polar solvation dynamics of H2O and D2O at the surface of zirconia nanoparticles, *J. Phys. Chem. B 103*, 7846-7852.
87. Edler, K., Wasbrough, M., Holdaway, J., and O'Driscoll, B. (2009) Self-assembled films formed at the air-water interface from CTAB/SDS mixtures with water-soluble polymers, *Langmuir 25*, 4047-4055.

5. Polymerization of Encapsulated Styrene in Polyelectrolyte / Surfactant Films

The morphological control of synthesised polymers at the nanometer level is long a pursuit in the studies of polymer materials [*1, 2*]. The formation of nanostructures made from mechanically and chemically stable supramolecular materials can further optimize the properties of materials. Polymerization of trapped monomer in highly ordered dynamic surfactant liquid crystalline structures can provide a rapid and cheap method to generate intricate nanostructures. The development of syntheses for such materials from generic polymers could establish new opportunities to produce materials for chemically and electroactive responsive supports, porous materials for catalysis, nanofiltration and molecular separations, and allow creation of new nanocomposites with improved properties such as ductility and stress dissipation [*3, 4*]. There are several reports where direct templating of micellar phases using inorganic materials such as silica [*5*], to synthesise 1:1 replicas were successful, however these methods have shown to be more challenging for polymers since the time-scales for the polymerization reaction are generally slower than the rate of micelle re-arrangement through interdroplet diffusion and droplet exchange, [*6*] causing in phase segregation of the polymer from the micellar structures.

The initial work on cationic surfactants with polyethyleneimine discussed in Chapter 4 demonstrated well-ordered films form at the surface of these homogeneous solutions. These films contain an ordered array of micelles embedded in a polyethyleneimine hydrogel matrix. Initial experiments on the encapsulation of various hydrophobic species,[*7*] including styrene, demonstrated that the organised nanostructures within this polyelectrolyte-surfactant films can be swollen with monomer. In these films, the high viscosity of the hydrogel surrounding the swollen surfactant micelles prevents micelle rearrangement on short timescales, making them an ideal host for the polymerization of hydrophobic monomers to create solid polymer nanostructures within the water-soluble polymer film. In this chapter, polymerization of the encapsulating styrene monomer is discussed. These polymer networks can reinforce the film making it more robust and suitable for applications requiring unsupported membranes.

The first step in this chapter was to use GC experiments to find out the performance of polymerization of styrene inside cationic surfactant/PEI solutions and thereby allowed to predict the efficiency of polymerization in their films. The effect of high flux synchrotron X-ray energy onto styrene monomer encapsulated in surfactant/PEI films also investigated as the first step to optimize the GIXD parameters. Then two methods were used to polymerize styrene in these polymer/surfactant films. The first method was used thermal polymerization for films prepared by spray coating onto a silicon wafer. The second method used to polymerize these films was UV irradiation (photopolymerization). Finally these films and the templated polystyrene were characterized by using FTIR, NMR, gel permeation chromatography (GPC) and Transmission Electron Microscopy (TEM).

5.1 Gas chromatography (GC) studying the conversion percentage of styrene in cationic surfactant/PEI solution.

Several papers have studied the structures and kinetics of styrene polymerization in organic solvent, emulsions, hydrogels and in polyelectrolyte/surfactant complexes [*8-13*]. Different polymerization techniques and several conditions have been reported to achieve the desired final aim of a polymerized product. In general these reports highlighted some of the common factors which have great influence on the performance of polymerization and final chemical and physical proprieties of these polymers. Temperature, and the nature and amount of initiator were very important factors in the polymerization rate and the properties of final polymer product. The main goal here in this preliminary GC experiment is to find out the performance of polymerization of styrene inside cationic surfactant/PEI solutions and thereby to predict the efficiency of polymerization in the films. Three different concentrations of initiator were investigated in different temperature conditions. The polymerization was achieved by using thermal or UV irradiation under these different conditions. The final concentration of styrene in these solutions was 0.09M which it is equivalent to 50 vol% relative to the micelle volume of the surfactants used. BDHAB and CPBr were used at 0.05M to solubilize the styrene monomer. ACHN [1,1′ Azobis(cyclohexanecarbonitrile)] used as initiator since

this initiator can form a radical compound in either thermal or UV irradiation conditions. The styrene was purified, by removing the inhibitor, by passing the styrene through a column containing activated aluminium oxide. The surfactant/LPEI solutions were degassed prior to making up the solutions to remove any dissolved oxygen. Then the fresh styrene was solubilised in these surfactant/PEI solutions. UV irradiation at 254nm was used to initiate the ACHN at 25ºC. Thermal polymerization was studied at 45 ºC and 60ºC without UV irradiation. The final solutions were tested by GC for three hours, where samples were taken from the solutions every one hour to detect the styrene monomer. The loss of styrene monomer in these solutions is related to styrene conversion to polystyrene. Figure 5.1 displays the conversion of styrene in BDHAB/LPEI solutions under different conditions.

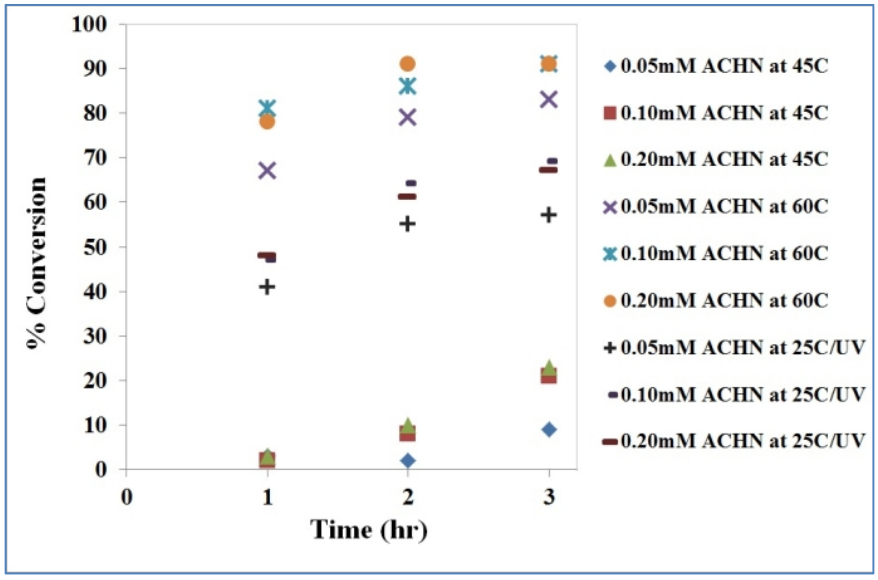

Figure 5.1: Thermal and photoactivation of styrene polymerization within BDHAB/LPEI solutions at three ACHN concentrations. The error in styrene conversion was ±5%.

As can be seen from figure 5.1 above, the thermal polymerization of encapsulated styrene in cationic surfactant micelles gives the highest of polymerization of styrene in these solutions at relatively high temperature (60ºC). The data also shows that polymerization can be successfully achieved in these solutions at room temperature by using ACHN with UV irradiation. The polymerized styrene at 45ºC shows the lowest styrene conversion compared with other conditions. At this temperature the low amount of conversion seen after the first hour then increased with time, and at this temperature

0.05mM and 0.10mM ACHN showed very similar conversion results. The conversion results at 60ºC show that in the first hour of this polymerization condition the relatively high concentrations (0.10mM and 0.20mM) of ACHN give similar conversions, while after three hours these samples improve conversion slightly but still give almost identical conversion results.

Polymerization of styrene in BDHAB/LPEI solutions using UV irradiation at 25ºC shows efficient and systematic conversion of styrene, where after one hour more than 50% of styrene has been polymerized. This is a reasonable result compared with the 45ºC and 60ºC conversion data. In general 0.10mM and 0.20mM ACHN shows similar conversion percentage results. Replacing BDHAB with CPBr does not change the final conversion results. In general these experiments polymerizing encapsulated styrene in cationic surfactant/PEI solutions demonstrated clearly that styrene can be polymerized in these systems using both thermal and photo-irradiation techniques. Furthermore polymerization of styrene in these solutions was successfully shown at room temperature by using UV irradiation. UV irradiation can promote polymerization of styrene in the more viscous solutions found at room temperature, compared with the 45ºC and 60ºC solutions. In other word this method could be used to polymerize styrene in high viscosity hydrogel solutions or films where micelle rearrangement on short timescales can be reduced, which will help to maintain the hosting surfactant/PEI ordered crystalline structures during polymerization process.

5.2 Thermal and Photopolymerization of Encapsulated Styrene in Cationic Surfactant/PEI Films.

The previous chapter illustrated that styrene was most effectively encapsulated in the cationic surfactant micelles with aromatic headgroups, where it was located in the palisade/core region, promoting the formation of rod-like micelles which then improved micelle packing in the films. Moreover studies of solubilised styrene in cationic surfactant/PEI films using neutron, X-ray reflectivity and GIXD proposed that lamellar and cubic structures were formed in those films grown using surfactants with aromatic surfactant headgroups which have a relatively long hydrocarbon chain.

This chapter focuses on the polymerization of encapsulated styrene in cationic surfactant/PEI films, and observing the film structures and their evolution during this process using time-resolved X-ray grazing incidence diffraction. Two methods were used to polymerize styrene in these films. First, free-standing films at the solution surface containing styrene were prepared, and then these films were harvested onto a silicon wafer. Films were allowed to drain excess fluid to ensure they were flat and viscous, before being transferred to a chamber for polymerization (either in the lab or on the beamline). Alternatively the film forming solutions containing styrene were spray coated onto silicon wafers to form solid hydrogel coatings. Recent work on cationic surfactant/PEI films has shown that spray coated films contain identical structures to those grown from the same solutions at the air/solution interface [*4*].

To correspond with previous experiments on cationic surfactant/polymer solutions and films, PEI with either low molecular weight ~2000Da and high molecular weight ~750 000Da were used at a concentration of 15g/L and a surfactant concentration of 0.05M. The final concentration of added styrene in surfactant/PEI solutions were 0.03M or 0.09M which is equivalent respectively to 30 and 50 vol% of styrene relative to the micelle volume of the surfactants used. Surfactants with an aromatic headgroups, CPBr, TDPB, BDHAB and BDTAB were used since these proved to encapsulate styrene and give films containing a relatively good mesostructure as stated earlier, in Chapter 4. The solutions were prepared in water which was degassed prior to making up the solutions. ACHN initiator which is oil soluble (solubilised in the micelles) was used to polymerize encapsulated styrene inside the micelle core region. ACHN initiator was thermally initiated at 40°C or by UV irradiation. These conditions were practical to observe the polymerization process for films on silicon wafers mounted on a temperature controlled base in a nitrogen atmosphere sample holder with an overhead UV lamp. Figure 5.2.1 show the silicon wafer sample holder designed by Diamond I07 to control the temperature and atmospheric above the sample for these polymerization studies using GIXD.

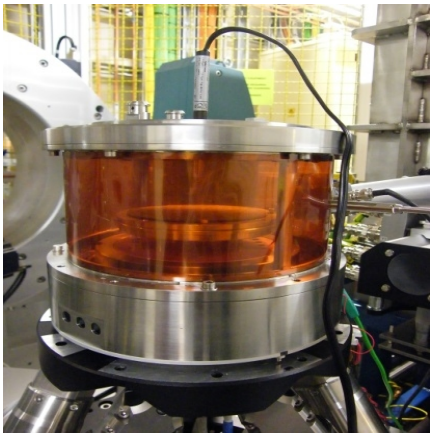

Figure 5.2.1: Sample holder designed with temperature and atmosphere control at Diamond I07 beamline. The temperature was controlled by a peltier heater under the central platform where the silicon wafer was placed. The cell was sealed with Kapton windows, so some samples shown two weak diffraction bands at Q = 0.35 - 0.39 and 0.43 - 0.47 $Å^{-1}$ related to the Kapton windows. A UV lamp was fitted through a hole on top of the metal lid.

5.2.1 Effects of High Flux Synchrotron X-ray Energy on Styrene Monomer Encapsulated in Surfactant/PEI Films

The energy of the X-ray photons used in this experiment was 12.5 keV, which is more than 200,000 times greater than the energy of the neutrons that were used in neutron scattering experiments at ISIS. On the other hand the energy of equivalent bond between two carbons in organic compounds is around 4 eV [*14*]. That means highly collimated synchrotron X-ray energy is easily able to break down the covalent bonds of organic compounds. Several papers [*15-18*] have reported sample damage from X-ray radiation, so it is a common problem that should be taken into account. Therefore the first step of studying polymerization of encapsulating styrene in surfactant/polymer films using GIXD was evaluation of the best X-ray exposure time. A fresh sample of polymer/surfactant film containing encapsulated styrene and initiator was investigated by monitoring the mesostructure changes resulting from different X-ray exposure times. Figure 5.2.2 shows the changes in the GIXD patterns during varied X-ray exposure time on a BDHAB/LPEI film encapsulating 0.09M styrene and 0.1mM ACHN.

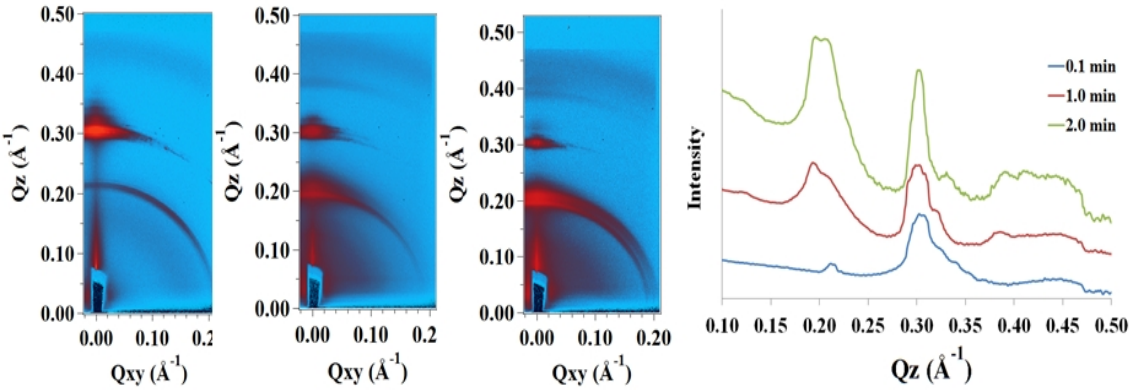

Figure 5.2.2: GIXD of BDHAB/LPEI film encapsulating 0.09M styrene and 0.1mM ACHN. The X-ray exposure time was one second in every 10 seconds at the same spot area at 25ºC. From left to right; first pattern was taken after 0.1 min, the second pattern taken after 1.0 min and the third pattern taken after 2.0 min. The fourth graph shows the Q_z line profiles of these GIXD pattern films taken at Q_{xy} =0.01Å^{-1}.

The main aim of this experiment was to polymerize encapsulated styrene in polymer/surfactant films, then characterise the final structure of these films. Therefore to control polymerization during this study, it was essential to minimize or eliminate the X-ray radiation effects. Despite the fact that the X-ray exposure was not continuous, as these patterns were taken for one second X-ray exposures before waiting 10 seconds for the next image, nevertheless, a very obvious change in the mesostructure was seen after just two minutes of non-continuous X-ray exposure. The variation was significant at Q 0.2 Å^{-1}, where during the first 0.1 min of X-ray exposure time a small peak is seen. After 1.0 min a second peak started growing at Q_z = 0.21Å^{-1} while after 2 min two clear peaks are shown at Q_z = 0.20, 0.21 Å^{-1}. These new peaks were seen during X-ray irradiation so could be from X-ray sample damage or due to the polymerization of encapsulating styrene. Some research suggests that synchrotron X-ray energy can generate free radical compounds which are the key species needed to start the polymerization process [*18*]. Several trials were performed to eliminate the X-ray radiation effects, finally 0.6 second of X-ray exposure time then waiting 30 second for the next pattern was found the best compromise between good signal-to-noise in the patterns and minimal X-ray radiation effects on the samples. The sample composition in Figure 5.2.2 and BDHAB/LPEI film with and without styrene (without initiator) were investigated for more than two hours and they showed a very stable structure with no apparent X-ray damage. To reduce further from the effect of X-ray radiation, the samples were moved horizontally 2 mm away from the initial scan position every 7.5 min.

5.2.2 Thermal Polymerization of Styrene Encapsulated in Cationic Surfactant/PEI Films.

There are usually four fundamental steps in a free-radical polymerization process. The first step is forming free radical molecules which are generated from a non-radical species (initiation). This step could occur by activating the initiator by heat or by photo-irradiation. The second step is radical addition to a substituted alkene (propagation). The third step is chain transfer (similar to the propagation step where a long chain radical alkane loses the radical to another alkene), and the final step is radical termination. The biggest challenge in free radical polymerization is the limited control of molecular weight due to the high reactivity of the radical propagation. Consequently controlling the polymer molecular weight and polymer architectures is very challenging [*19, 20*]. As mentioned before the advantage of the highly viscous organised nanostructures in polyelectrolyte-surfactant films swollen with monomer can prevent the micelle or monomer rearrangement on the short timescales. In other words polymerizing this trapped monomer in a well-ordered structure has potential to control their nanoscale architectures. In this section, polymerization of the encapsulating styrene monomer in polymer/surfactant films was studied by activating thermally the ACHN initiator to produce free-radicals as a first step to polymerize encapsulated styrene monomer in these films. The polymerization of styrene and resulting change in nanostructure within the films was investigated in a time-resolved manner at three different temperatures 45ºC, 50ºC and 60ºC.

Figure 5.2.3 shows GIXD patterns taken during polymerization of a BDHAB/LPEI film encapsulating 0.09M styrene and 0.1mM ACHN at 45ºC. In general BDHAB/LPEI spray coated or free-standing films showed a very broad ring around Q_z =0.30 $Å^{-1}$. Some of these films also showed a second diffraction ring at Q_z= 0.213 $Å^{-1}$ at the beginning of the reaction however this diffraction ring is less broad than the one at Q_z =0.30 $Å^{-1}$, suggesting it belongs to a different structure. On the other hand GIXD diffraction for BDHAB surfactant powder illustrated a diffraction ring at Q_z = 0.30 $Å^{-1}$ but this ring is narrower (nearly half the width) of the diffraction rings in BDHAB/LPEI films encapsulating styrene. However a close zoom onto the broad diffraction ring at Q_z = 0.30 $Å^{-1}$ for BDHAB/LPEI films encapsulating styrene shows intensity from two overlapping diffraction rings, clearly seen in Q_z line profiles for 1.0 min GIXD image (indicated by the arrow in figure 5.2.3). This broad diffraction ring shown at Q_z 0.30 $Å^{-1}$

therefore could be diffraction from both a BDHAB surfactant bilayer structure and from the BDHAB/LPEI mesostructured phase.

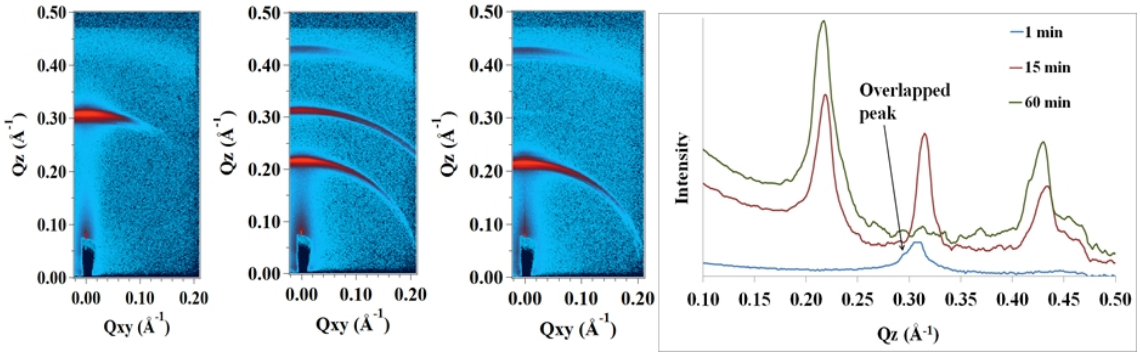

Figure 5.2.3: Time resolved GIXD patterns during thermal 45ºC polymerization of BDHAB/LPEI film encapsulating 0.09M styrene and 0.1mM ACHN. From left to right; first pattern was taken after 1 min, the second pattern taken after 15 min and the third pattern taken after 60 min. The fourth graph shows the Q_z line profiles of those GIXD pattern films taken at 0.01Å^{-1} on the Q_{xy} axis.

Within 15 min of heating at 45ºC the BDHAB/LPEI film encapsulating styrene/ACHN shows three rings at Q_z =0.213, 0.312 and 0.430 Å^{-1} where the position of these rings can be indexed to an *Imɜ̄m* cubic phase (110, 200 and 220).

Although the spray coated or free-standing films appear as a solid layer on the silicon wafer at 25ºC after drying the excess water, most of these solid films transformed to viscous layers at temperatures above 45ºC. This behaviour of these films is due to the physical properties of PEI and the complex interaction of surfactant and PEI in these films. Both branched PEI and these cationic surfactants are hygroscopic materials [*21, 22*], which means that a portion of water molecules still exist in these solid polymer/surfactant films. At temperatures above 45ºC, the PEI and surfactant mixture behaves like a wax with a low melting point. After 37 min of polymerization carried out at 45ºC, the second ring at Q =0.312 Å^{-1} starts disappearing, leaving two rings. The final structure of the polymerized BDHAB/LPEI film encapsulating 0.09M styrene and 0.1mM ACHN at 45ºC is therefore assigned as lamellar. This final polymerized film showed stable lamellar structure for more than 2 hours at 45ºC. The d-spacing of final polymerized film improved about 9Å compared with initial composition of this film. This increasing in d-spacing could be related to reformation of polymer/surfactant micelles due to dehydration of water molecules and the temperature effects on the polymer/surfactant interaction [*23*]. Alternatively the swelling of the d-spacing could

indicate that the viscous liquid film present during the polymerisation of styrene allowed migration of styrene through the structure to form thicker layers than were found in the initial styrene-swollen micelles in the film [*24*].

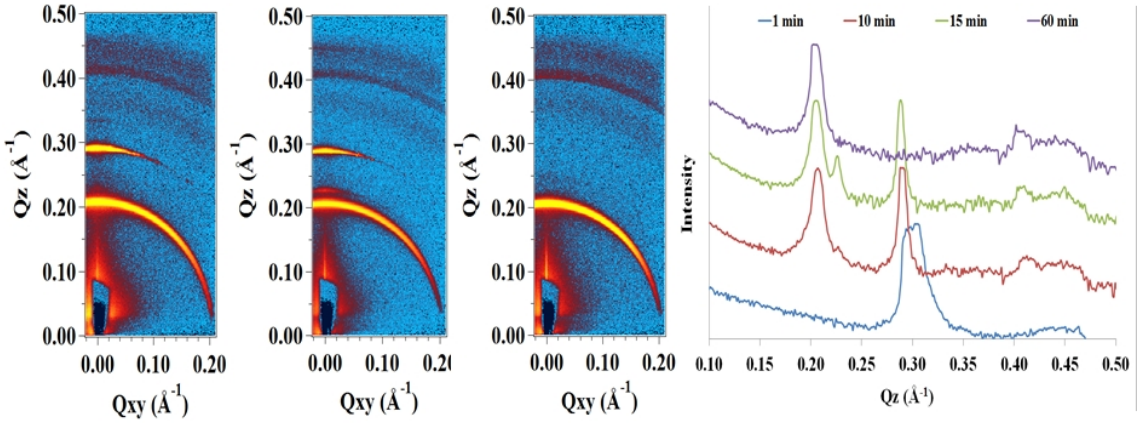

Figure 5.2.4: Time resolved GIXD patterns taken during thermal 50ºC polymerization of a BDHAB/LPEI film encapsulating 0.09M styrene and 0.1mM ACHN. From left to right; pattern taken after 10 min, after 15 min and after 60 min. The fourth graph shows the Q_z line profiles of those GIXD pattern films taken at 0.01Å^{-1} on the Q_{xy} axis.

The polymerization of styrene in a BDHAB/LPEI film encapsulating 0.09M styrene and 0.1mM ACHN at 50ºC (figure 5.2.4) showed similar initial and final structures as found at 45ºC for films polymerized with the same film composition. However the intermediate phase transition seen during polymerization at 50ºC show more diffraction rings compared with the patterns at 45ºC. The phase transition occurring between 10 to 15 min of polymerization of this film at 50ºC had 5 diffraction rings at Q_z 0.207, 0.227, 0.288, 0.408 and 0.450 Å^{-1}. The best structure assignment also suggests that these are the 110, 200, 220, 310 and 222 reflections of an $Im\bar{3}m$ cubic phase. Interestingly Hentze et al observing polymerisation in lyotropic liquid crystalline phases, suggested a mechanism where initially small polymer nanospheres formed during polymerisation which then fused into polymer strands which became lamellar sheets [*25*]. A similar mechanism could be operating here, causing the initial lamellar phase to form polymer particles in a cubic lattice, which then rearrange into the slightly larger lamellar phase found at the end of the reaction.

The polymerization of the same film composition at 60ºC showed different polymerization behaviour than at 45ºC or 50ºC. The intermediate phase transition at 60ºC emerged earlier than at 45ºC and 50ºC. The final structure of BDHAB/LPEI film encapsulating 0.09M styrene and 0.1mM ACHN polymerized at 60ºC shows two

relatively high intensity diffraction rings at Q_z 0.212 and 0.4250 $Å^{-1}$ (figure 5.2.5) which indicate a lamellar structure, however it also shows a low intensity ring at Q_z 0.252 $Å^{-1}$ which along with the two intense peaks can be indexed to either *Fm3̄m or Ia3̄d* cubic structure. The very low intensity ring seen at Q_z 0.252 $Å^{-1}$ at 60ºC does not appear when the same film composition was thermally polymerized at 45ºC while a very low intensity diffraction feature was seen at the same Q_z position in case of polymerization at 50ºC. This suggests that final polymerized structure of the styrene/BDHAB/LPEI films tends to transform from a lamellar to a cubic structure when the polymerization temperature is increased. In future work it could be worthy to investigate the polymerization behaviour of these films composition at even higher temperature.

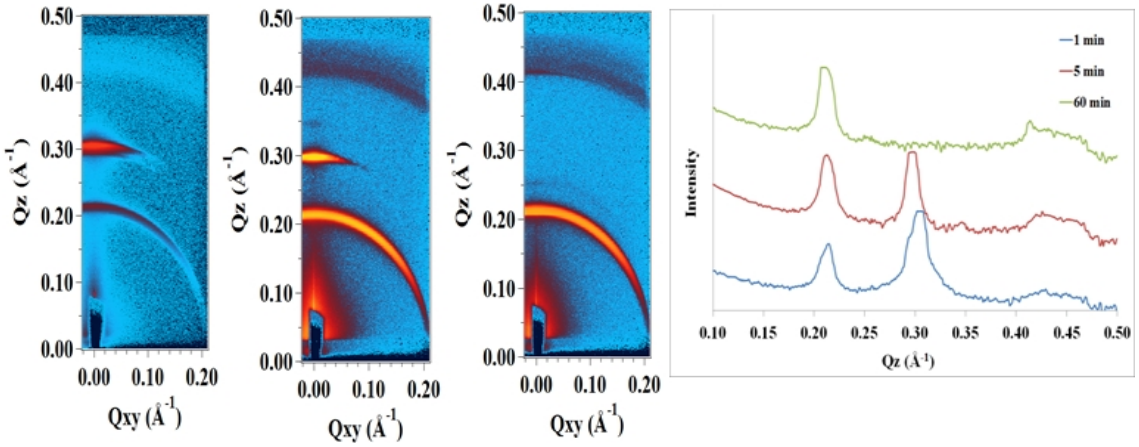

Figure 5.2.5: Time resolved GIXD patterns during thermal 60ºC polymerization of a BDHAB/LPEI film encapsulating 0.09M styrene and 0.1mM ACHN. From left to right; first pattern was taken after 1 min, the second pattern after 5 min and the third pattern after 60 min. The fourth graph shows the Q_z line profiles of those GIXD pattern films at 0.01$Å^{-1}$ on the Q_{xy} axis.

It is important to report that the GIXD patterns of all of the final structures for those polymerized films at 45ºC, 50ºC and 60ºC had a stable structure after 60 min. In addition they show a stable final structure when the film was cooled down to room temperature and no intermediate phase was observed during cooling. This indicates that final structures of polymerized styrene/surfactant/PEI films are stable and non-reversible.

CPBr/PEI films were investigated at the same temperatures and the same concentrations of styrene/ACHN. Figure 5.2.6 shows the GIXD patterns taken during polymerization of a CPBr/LPEI film encapsulating 0.09M styrene and 0.1mM ACHN at 45ºC.

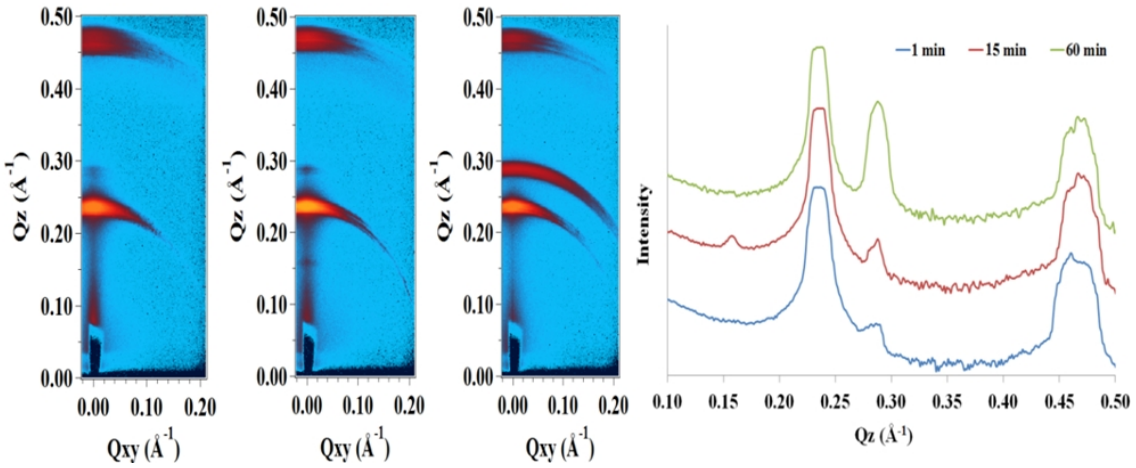

Figure 5.2.6: Time resolved GIXD patterns taken during thermal 45ºC polymerization of CPBr/LPEI film encapsulating 0.09M styrene and 0.1mM ACHN. From left to right; first pattern was taken after 1 min, the second pattern after 15 min and the third pattern after 60 min. The fourth graph shows the Q_z line profiles of those GIXD pattern films at 0.01Å^{-1} on the Q_{xy} axis.

The GIXD pattern of the initial CPBr/LPEI film (Figure 5.2.6) at 45ºC shows a small diffraction spot at Q_z 0.288 Å^{-1} and two very broad diffraction rings at Q_z =0.225-0.250 and 0.451-0.487 Å^{-1}. These very broad diffraction rings were seen also in the surfactant powder and in all CPBr/PEI films. However GIXD patterns of diffraction rings from CPBr powder show narrower diffraction rings compared with CPBr/LPEI films. Zooming in on the rings at Q_z =0.225-0.250 Å^{-1} and 0.451-0.487 Å^{-1} demonstrates that these broad diffraction rings consist of 5-8 small overlapped diffraction rings (figure 5.2.7).

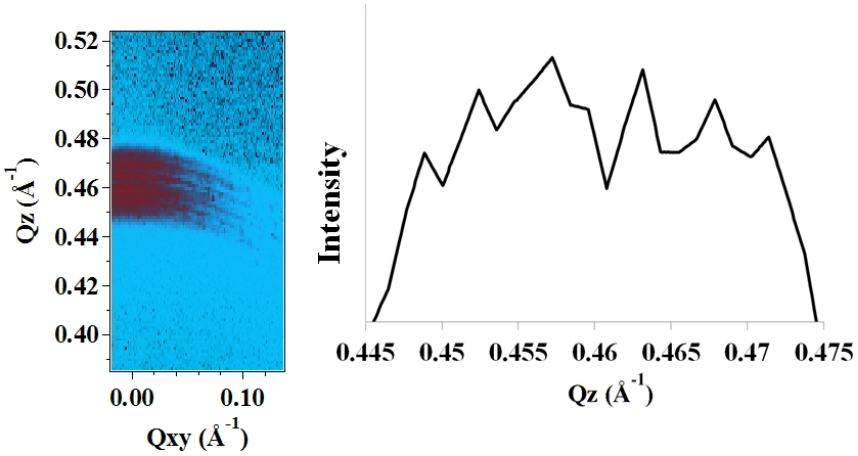

Figure 5.2.7: Magnified GIXD pattern of CPBr/LPEI film at 25ºC and Q_z line profiles of this pattern taken at 0.01Å^{-1} on the Q_{xy} axis.

The Q_z positions of these two very broad diffraction rings overall illustrate a lamellar structure. In lamellar liquid crystalline structures, surfactant bilayers are separated by water layers, where in this polyelectrolyte/surfactant system water and polyelectrolyte form a spacer between the surfactant bilayers. The small overlapped diffraction rings seen at Q_z 0.225-0.250 $Å^{-1}$and 0.451-0.487 $Å^{-1}$ suggest a multilamellar structure with different d-spacings within the same film composition. This could be due to water/polyelectrolyte volume variation within these multilamellar layers. The thickness between two bilayers mainly depends on the amount of water or water/polyelectrolyte present per unit area. In particular in an organized surfactant lamellar structure, the thickness between these bilayers typically is stable within ±0.5 Å [*26*]. However many authors have reported more than one lamellar phase can occur in a single liquid crystalline system [*27-29*]. The second possibility causing this multilamellar structure is a packing variation of the surfactant hydrocarbon chains. The bilayer thickness of surfactant-surfactant hydrocarbon chains generally is 10% to 30% smaller than that calculated from their theoretical free standing chain length [*30*]. However the polydispersity in the layer thickness could arise due to the solubilising of hydrophobic monomer into these cationic surfactant/polymer films which could occur to different extents in different regions of the film.

The intermediate phase observed during polymerization of a CPBr/LPEI film encapsulating styrene/ACHN at 45ºC shows two small diffraction spots at Q_z 0.158 and 0.288 $Å^{-1}$ (middle pattern figure 5.2.6) in addition to the two broad diffraction rings shown in the initial GIXD pattern. These small diffraction spots could be indexed as the 110, 200 and 220 reflections of an $Im\bar{3}m$ cubic phase. After 60 min of polymerization, the two small diffraction spots disappeared and a single relatively broad diffraction ring emerged at Q_z= 0.279-0.300 $Å^{-1}$. The final structure of this film with 2 diffraction rings plus the unchanged initial broad diffraction ring at high Q could suggest formation of two lamellar phases or it could be either 211, 220, 420 and 332 reflections of an $Ia\bar{3}d$ or 111, 200, 311 and 222 reflections of an $Fm\bar{3}m$ cubic phase.

The same film composition was polymerized at 50ºC and 60ºC and showed almost the same performance. However the intermediate phase observed at 60ºC shows more complex diffraction rings than the GIXD patterns for the film that was polymerized at 50ºC. Figure 5.2.8 shows the GIXD patterns taken during polymerization of a CPBr/LPEI film encapsulating 0.09M styrene and 0.1mM ACHN at 60ºC.

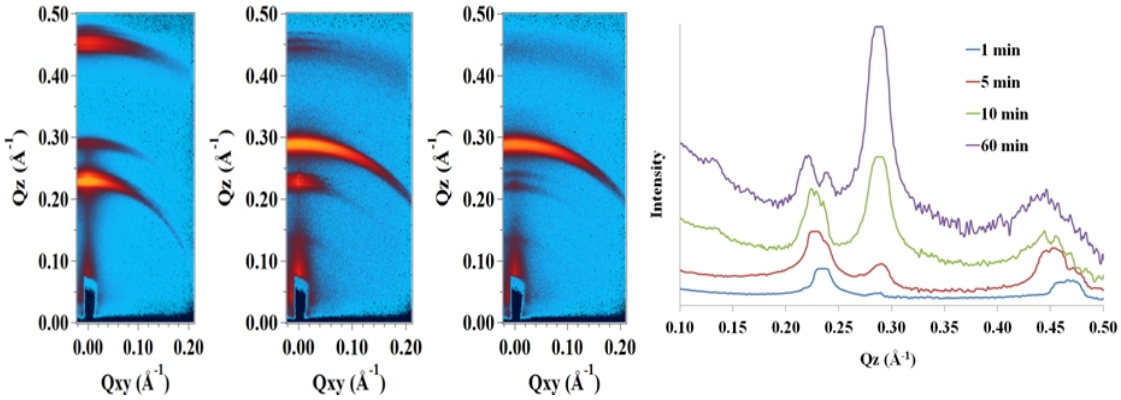

Figure 5.2.8: Time resolved GIXD patterns taken during 60ºC thermal polymerization of a CPBr/LPEI film encapsulating 0.09M styrene and 0.1mM ACHN. From left to right; first pattern was taken after 5 min, the second pattern after 10 min and the third pattern after 60 min. The fourth graph shows the Q_z line profiles of those GIXD pattern films at 0.01Å^{-1} on the Q_{xy} axis.

The intermediate phases seen in the GIXD patterns during polymerization of styrene at 50ºC and 60ºC in both BDHAB and CPBr films emerged earlier than in films that were polymerized at 45ºC. During the first 5 minutes of polymerization the CPBr/LPEI films at 50ºC or 60ºC started developing a diffraction ring at Q_z =0.291 Å^{-1} and this ring became very intense after 60 min. The broad diffraction rings at Q_z 0.225-0.250 Å^{-1}and 0.451-0.487 Å^{-1} after 10 min stared to vanish, leaving two separated small diffraction rings at Q_z 0.222 and 0.241 Å^{-1}, at the end of the polymerization. The final structure of these CPBr/LPEI films polymerized at 50ºC and 60ºC suggest two liquid crystalline structures, where the small intensity diffraction rings can be assigned to the (110) (200) and (210) reflections of a *Pm3̄n* cubic structure while the very intense broad diffraction ring at Q_z 0.270-0.306 Å^{-1} could result from a lamellar structure.

In general most of the mesostructures found during thermal polymerization of these cationic surfactant/PEI films with styrene, are close to the mesostructures that were found by Edler et al [*31*] for CTAB/SDS/PEI films system, where the lamellar structure was found mixed with both *Im3̄m* and *Ia3̄d* cubic structures. However the peak intensities found here in this experiment do not match well with those from the Garstecki and Holyst model [*32, 33*] which was used in the earlier work to fit the data.

Table 5.2.1 summarises the average d-spacing of the first order peak, unit cell dimension and structure assignments for structures formed during thermal polymerization of encapsulated styrene in polymer/surfactant films.

Table 5.2.1: The structure assignments, average d-spacing and unit cell of structures formed during thermal polymerization of encapsulated styrene in polymer/surfactant films.

Surfactant	Time (min)	temp (ºC)	Average d-spacing or unit cell (Å)	Structure assignment
BDHAB/LPEI films encapsulating 0.09M styrene and 0.1mM ACHN	1 to 60	25	21[a]	Lamellar
	1 to 15	45	21[a]	Lamellar
	15 to 37	45	41[b]	*Im$\bar{3}$m*
	37 to 60	45	29[a]	Lamellar
	1 to 10	50	21[a]	Lamellar
	10 to 15	50	46[b]	*Im$\bar{3}$m*
	15 to 60	50	29[a]	Lamellar
	1 to 5	60	21[a]	Lamellar
	5 to 10	60	42[b]	*Im$\bar{3}$m*
	10 to 60	60	30[a] / 51[c] / 72[d]	*Lamellar or either (Fm$\bar{3}$m - Ia$\bar{3}$d)*
CPBr/LPEI films encapsulating 0.09M styrene and 0.1mM ACHN	1 to 60	25	28[a] / 46[c] / 67[d]	*Lamellar or either (Fm$\bar{3}$m - Ia$\bar{3}$d)*
	1 to 15	45	28[a] / 46[c] / 67[d]	*Lamellar or either (Fm$\bar{3}$m - Ia$\bar{3}$d)*
	15 to 30	45	54[b]	*Im$\bar{3}$m*
	30 to 60	45	28[a] / 46[c] / 67[d]	*Lamellar or either (Fm$\bar{3}$m - Ia$\bar{3}$d)*
	1 to 5	50 -60	28[a] / 46[c] / 67[d]	*Lamellar or either (Fm$\bar{3}$m - Ia$\bar{3}$d)*
	5 to 10	50 - 60	28[a] / 46[c] / 67[d]	*Lamellar or either (Fm$\bar{3}$m - Ia$\bar{3}$d)*
	10 to 15	50 -60	46[a]	Mix
	15 to 60	50 - 60	44[a] / 59[e]	*Lamellar and/or Pm$\bar{3}$n*

a is the d-spacing of Lamellar, b is the cell unit value for Im$\bar{3}$m, c for Fm$\bar{3}$m, d for Ia$\bar{3}$d and e for Pm$\bar{3}$n. Errors in the unit cell and layer thickness are 0.5Å for the cubic phases and 0.1Å for the lamellar phases.

The first important observation from thermal polymerization of encapsulated styrene in cationic surfactants films is the relationship between the intermediates phases and the polymerization temperatures. It is clear that variation of the mesostructure of the intermediate phases emerged earlier when the polymerization temperature increased. This change in mesostructure could be due to the polymerization process, where very

fast polymerization would cause polymer networks to form at an earlier stage in the phase separation and may therefore allow a higher degree of liquid crystalline order templated in the final polymer [*34*]. Some authors have also reported mesostructure changes during the polymerization process [*35-37*]. For example DePierro et al [*34*] found three diffraction peaks for the 40 wt % Brij 56 with 25% acrylamide system indexed as cubic structure, before thermal or photo polymerization, while through the polymerization, the primary and tertiary peaks appeared at the same scattering angle as before polymerization, but the secondary peak disappeared completely. However no evidence of phase separation for polymer and surfactant occurred in this system.

The other possibility for this change could be related to the temperature influence on the components of these polymer/surfactant films [*38*]. Both polymerization and temperature could combine to have an impact on these polymer/surfactant films resulting in the observed variation in mesostructure during thermal polymerization. However some changes were also observed in both CPBr and BDHAB films which did not contain any styrene or initiator, at temperature above 45°C. These observed changes were close to the transition phases observed for those films polymerized at 45ºC containing styrene and ACHN.

It is well known that the amount of water (solvent) molecules play an essential role in forming lyotropic liquid crystalline structures. The solvent concentration and nature of the amphiphile molecules define the categories of lyotropic liquid crystal phase that is exhibited. Another crucial factor that has great influence on amphiphile aggregation behaviour is the temperature. Above the Krafft point, transitions between lyotropic mesophases in a surfactant-water system can be observed by changing the temperature [*21, 39, 40*].

Temperature effects on lyotropic mesophases are not simple. However increasing the temperature can cause dehydration of water molecules correlated with the surfactant headgroup. Subsequently depending on the nature of the surfactant, the removal of water molecules from the headgroup can lead to rearrangement of the surfactant micelles. On the other hand the mobility for surfactant molecules will also be increased by increasing the temperature [*41*]. Overall therefore rearrangement and deformation of the surfactant micelles are likely to be the main reason behind the observed intermediate phases. This process is mainly based on the interfacial curvature in the micelle. The

surfactant packing parameter depends on molecular geometry of the surfactant, which defines the surface interfacial curvature of the micelle [*42, 43*].

As mentioned in chapter 1, at relatively high temperature (above 45°C) and at high concentrations of CTAB, $Ia\bar{3}d$ cubic and lamellar structure are the main predominant phases which exist in this region (figure 1.5.3) [*44*]. This is the typical sequence of ordered phases observed for binary cationic surfactant/water solutions such as cetylpyridinium chloride (CPCl) and dodecyltrimethylammonium chloride (DTMAC) [*21*]. However a bicontinuous phase region of $Ia\bar{3}d$ can also be found in these cationic surfactants phase diagram, observed as an intermediate between other ordered structures. Overall the final and intermediate mesostructures of thermal polymerization for these cationic surfactants films encapsulating styrene illustrates good agreement with the temperature/concentration cationic surfactant phase diagrams [*42, 43, 45*].

In general the final structure of thermally polymerized styrene in BDHAB/LPEI films at different temperatures was lamellar. Unexpectedly the d-spacing of these polymerized films increased from 21 Å to 30 Å as the polymerization temperature was increased. Theoretically evaporation of some water molecules existing between surfactant micelles would be predicted upon increasing the temperature. In addition, loss of some of the encapsulated styrene in hydrophobic region could also occur at higher temperatures. Finally conversion of encapsulating styrene monomer to polystyrene should cause micelle shrinkage since the density of styrene monomer is lower than the bulk density of polystyrene [*46, 47*]. Therefore the d-spacing was expected to decrease, unless substantial rearrangement of the styrene occurs during polymerisation. Wadekar et al found substantial increases in lamellar size (from nm to microns) during synthesis of polysiloxanes in nonionic surfactant mesophases [*24*]. Mata et al reported the temperature effects on aggregation number and the cmc behaviour in pure aqueous solution of broad range of cationic surfactants including CPBr [*48*]. In this study, all of the cationic surfactant micelles showed a decrease in aggregation number as the temperature increased, and the cmc increased. However in the PEI/surfactant solutions studied here the aggregation behaviour appears to follow a different trend. SANS and X-ray experiments shown in chapter 3 and 4 demonstrated that the interaction of PEI with BDHAB caused a doubling of the micelle volume, and even CPBr showed a small swelling of the micelle size when interacting with PEI. O'Driscoll et al observed as well an increase of the of CTAB micelle aggregation number when adding SPEI [*7*]. Overall

the mesostructures of these cationic surfactants are highly dependent on the concentration and temperature [*42, 43*], where changing in these parameters causes reorganization from one mesophase to another phase consequently changing the lattice thickness. BDHAB has a bigger micelle volume than CPBr; nevertheless the CPBr containing films have a bigger d-spacing compared with the BDHAB films before and after polymerisation. These results are in good agreement with neutron reflectivity from free standing water/air polymer/surfactant films (chapter 4). As stated in chapters three and four this is due to the various interactions between PEI and the surfactant micelles headgroup, where CPBr/PEI films show a strong interaction with PEI compared with the BDHAB/PEI system, which that leads to thicker PEI/water layers between CPBr micelles. Jung et al [*49*] observed a change in lyotropic liquid-crystalline phases during polymerization of styrene in dioctadecyldimethylammonium bromide (DODAB) solution, where the initial structure of this system was lamellar. In this research they found that the final structure of polymerized styrene inside a lyotropic liquid -crystalline phase at 30°C does not change the initial structure. However when the temperature was increased to 60-70 ºC both $Ia\bar{3}d$ and $Im\bar{3}m$ cubic phases were found as a final polymerized structure. An $Ia\bar{3}d$ phase was found at relatively low concentrations of DODAB while an $Im\bar{3}m$ cubic structure was found at high concentration of the surfactant. These results show good agreement with polymerized styrene in BDHAB/PEI films because both $Ia\bar{3}d$ and $Im\bar{3}m$ cubic structure was seen at high polymerization temperature for this system.

The final polymerized CPBr/LPEI films structure illustrated in general either a lamellar structure or cubic structure $(Fm\bar{3}m$ - $Ia\bar{3}d)$. There are two types of cubic mesophases. The first type is bicontinuous cubic phases. These phases are formed of a continuous bilayer, dividing space into two interwoven networks in a fluid continuum. Bicontinuous cubic phases mostly occur as one possible type of intermediate phase at the transition between layered structures and cylindrical micelles. The second type of cubic mesophases is the discontinuous micellar cubic phases which consist of organized separated spherical micelles [*40, 50-52*]. In general $Ia\bar{3}d$, $Pn\bar{3}m$ and $Im\bar{3}m$ phases are bicontinuous cubic phases whereas $Fd\bar{3}m$ and $Fm\bar{3}m$ are cubic phases formed from micelle aggregation. The $Pm\bar{3}n$ cubic structure is most frequently formed from very close-packed micelles. However in the case of large headgroup cationic surfactants,

with this structural symmetry it can be analogous to the I_1 phases, in other word similar to the bicontinuous cubic structure phases [*53, 54*].

Since the most initial CPBr/PEI films showed a lamellar structure and bicontinuous cubic structures are the most likely structures to form from a lamellae structure, therefore the cubic structure found in the final polymerized film is more likely to be $Ia\bar{3}d$ rather than $Fm\bar{3}m$. In addition, the most commonly observed space group of bicontinuous cubic phases in surfactant and lipid systems is $Ia\bar{3}d$ [*55-57*]. On the other hand SANS and SAXS experiments in chapter 3-4 suggested that styrene was encapsulated in rod-like shaped micelles rather than spherical micelles. The d-spacing of the final CPBr/PEI/styrene films polymerized at temperatures between 25ºC to 45ºC were 28Å while in those polymerized at temperatures between 50ºC and 60ºC the d-spacing jumped from 28Å to 44Å which indicate a critical change in the final mesostructure. This abrupt jump in d-spacing suggests that the final structure of polymerized styrene/CPBr/PEI films at 50ºC or 60ºC could be $Pm\bar{3}n$ micellar cubic rather than a lamellar structure where the $Pm\bar{3}n$ phase most likely derived from the initial lamellar structure by break-up of the sheets into discrete micelles containing polymer particles [*58*].

In general thermal polymerization of both BDHAB/PEI/Styrene and CPBr/PEI/Styrene systems showed changes in mesostructures and intermediate transition phases. These changes in lyotropic phases are most likely due to temperature influence in these cationic surfactant films rather than polymerization effect. As mentioned earlier that the temperature/concentration phase diagram of CTAB and CPCl [*21, 44*] shows cubic and lamellar phases at relatively high temperature and high concentration of these cationic surfactants, and typically BDHAB and CPBr show similar results, as reflected in the structures formed at high temperature observed here.

5.2.3 Photopolymerization of Styrene Encapsulated in Cationic Surfactant/PEI Films.

The previous section on thermal polymerization styrene in polymer/surfactant films illustrated very clearly the influence of temperature on those templated mesostructured films. By increasing the temperature the entropy increases due to the increasingly free mobility of surfactant molecules and encapsulated monomer. Subsequently this free movement of both surfactant and monomer molecules can increase the rate of micelle re-arrangement through interdroplet diffusion and droplet exchange resulting in phase segregation of the polymer from the micellar structures. Therefore in this section the polymerization of encapsulating monomer was done at room temperature by using photo-irradiation to initiate the polymerization which can reduce the effects of temperature on these polymer/surfactant films. Photo-polymerization of trapped monomer in templated well-ordered structure has become very attractive in the polymerization research area. This technique exhibits advantages such as the very fast capability to transform the initiator molecules into free-radicals from non-initiated molecules, so that the rate of polymerization can be controlled by the radiation intensity and photoinitiator concentration [*59-61*]. In addition the most important advantage of this kind of polymerization is that it is independent of temperature which means polymerization in a stable well-ordered structure is easier to control [*62*]. Photo-polymerization is also a useful approach to study the kinetic and the transformation of mesophases during polymerization due to the ability to control and tune the intensity and irradiation time which allow monitoring of the different polymerization processes [*63, 64*]. Time-resolved photopolymerization measurements can provide very important details regarding the structure of templated styrene in polymers/surfactant mesophases during polymerization [*65, 66*]. Figure 5.2.9 illustrates the time-resolved GIXD patterns taken during photopolymerization of BDHAB/LPEI film encapsulating 0.03M styrene and 0.05mM ACHN at 25ºC where the photopolymerization was carried out using UV radiation at 254nm wavelength.

5.2.3.1 Time-Resolved Measurement of the Photopolymerization

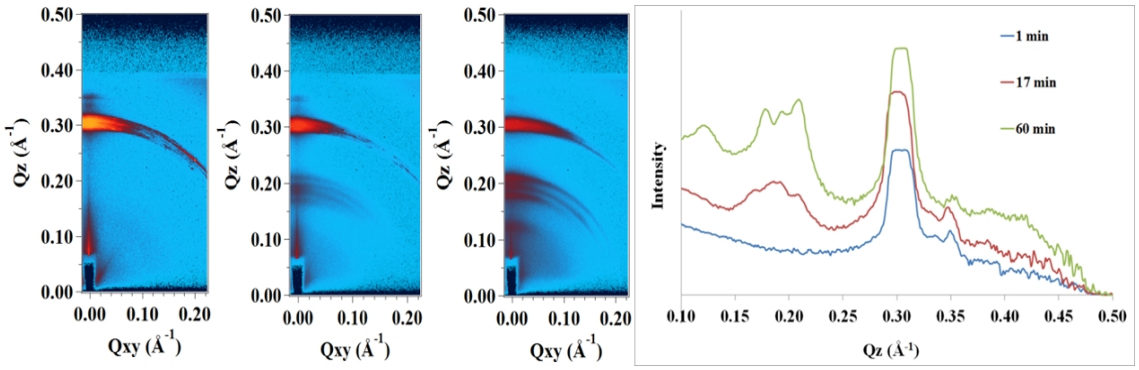

Figure 5.2.9: Time resolved GIXD patterns during photopolymerization at 25ºC of BDHAB/LPEI film encapsulating 0.03M styrene and 0.05mM ACHN. From left to right; first pattern was taken after 1 min, the second pattern after 17 min and the third pattern after 60 min. The fourth graph shows the Q_z line profiles of those GIXD pattern films at 0.01Å^{-1} on the Q_{xy} axis.

The time-resolved photopolymerization of BDHAB/LPEI films encapsulating 0.03M of styrene / 0.05mM ACHN or 0.09M styrene / 0.1mM ACHN showed the same transition phases and final polymerized structure. The difference between these two films was the transition phase in the film containing 0.09M styrene / 0.1mM ACHN occurred earlier than the phase transitions in the film encapsulating 0.03M styrene / 0.05mM ACHN. The final GIXD pattern of these photopolymerized films shown in Figure 5.2.9 shows obvious rings where the first 4 rings can be indexed as the 110, 200, 210 and 211 reflections of a *Pm3̄n* cubic phase (figure 5.2.9).

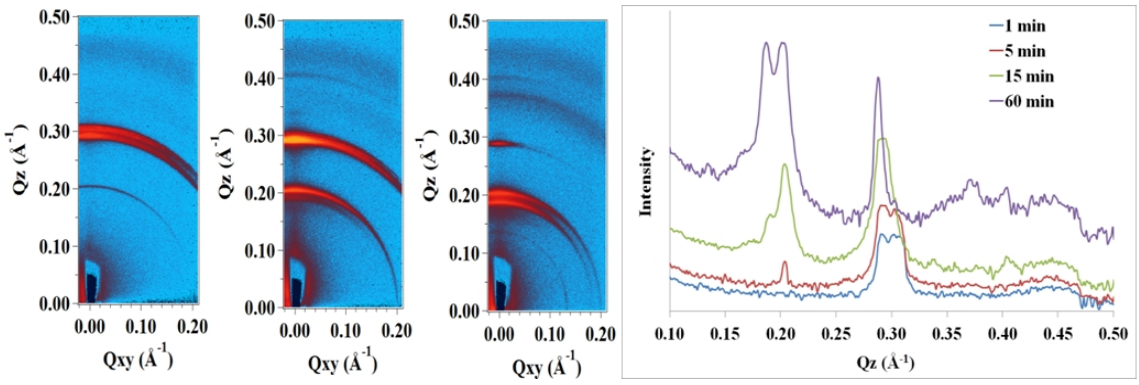

Figure 5.2.10: Time resolved GIXD patterns during photopolymerization at 25ºC of BDHAB/LPEI film encapsulating 0.03M styrene and 0.10mM ACHN at 25ºC. From left to right; first pattern was taken after 5 min, the second pattern after 15 min and the third pattern after 60 min. The fourth graph shows the Q_z line profiles of those GIXD pattern films taken at 0.01Å^{-1} on the Q_{xy} axis. The weak diffraction bands at Q = 0.35 - 0.39 and 0.43 - 0.47 Å^{-1} are related to the Kapton rings.

The time-resolved GIXD patterns that were taken during photopolymerization of BDHAB/LPEI films containing higher relative amounts of ACHN ie those encapsulating 0.03M styrene / 0.10mM ACHN, 0.03M styrene / 0.20mM ACHN and 0.09M styrene / 0.20mM ACHN show similar behaviour but which is different to that of the polymerizations above. After 5 min of UV irradiation, a fine ring appears at Q_z =0.203 $Å^{-1}$. Then after 15min another ring started developing at Q_z =0.190 $Å^{-1}$ while the intensity of the broad diffraction ring at Q_z =0.280-0.307 $Å^{-1}$ began disappearing. The GIXD patterns of the final photopolymerized film structure showed around 6 rings which suggests more than one phase structure is present. The best assignments for those rings indicate a combination of a lamellar with cubic phases. The rings at Q_z =0.136, 0.185, 0.205 and 0.295 $Å^{-1}$ can be indexed as the 110, 200, 210 and 310 reflections of a *Pm3̄n* cubic phase, while the rings at Q_z =0.185, 0.205 and 2.90 $Å^{-1}$ can be indexed as the 111, 200 and 220 reflections of a *Fm3̄m* cubic phase (figure 5.2.10).

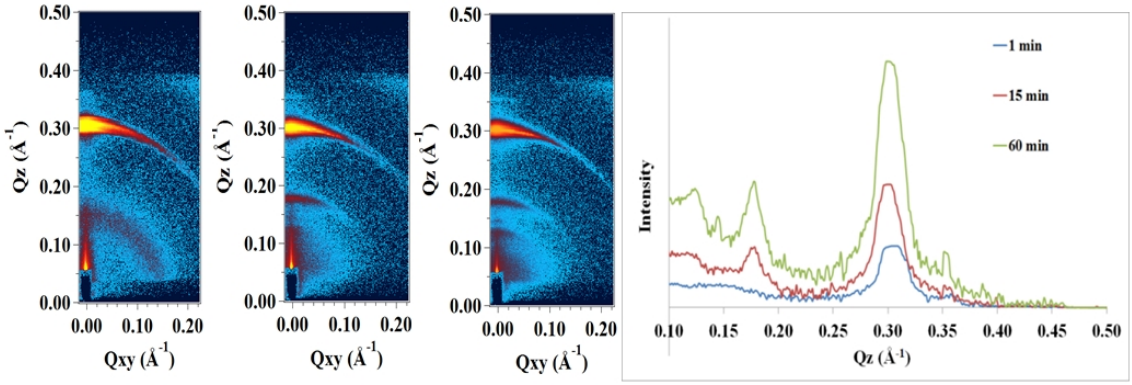

Figure 5.2.11: Time resolved GIXD patterns during photopolymerization at 25ºC of BDHAB/LPEI film encapsulating 0.09M styrene and 0.05mM ACHN at 25ºC. From left to right; patterns taken at 1, 15 and 60 min. The fourth graph is Q_z line profiles of these GIXD pattern films taken at 0.01$Å^{-1}$ on the Q_{xy} axis.

The time-resolved GIXD patterns taken during photopolymerization of a BDHAB/LPEI film with the highest styrene concentration but low amounts of initiator, (0.09M styrene and 0.05mM ACHN) shows three rings growing in at Q_z =0.126, 0.147 and 0.176 $Å^{-1}$ which in the pattern of the final polymerized structure can be indexed as the 110, 111 and 200 reflections of a *Pn3̄m* cubic phase (figure 5.2.11). Similarly photopolymerization of a CPBr/LPEI film also containing relatively high styrene concentrations with low amounts of initiator (0.05M styrene and 0.05mM ACHN), resulted in 3 rings developing at Q_z =0.109, 0.196 and 0.216 $Å^{-1}$ after 15 min UV irradiation. In this case the GIXD pattern of the final polymerized film shows 5 rings at

Q_z = 0.131, 0.180, 0.198, 0.226 and 0.305 $Å^{-1}$ which can be indexed as the 110, 200, 210 and 211 reflections of a *Pm3̄n* cubic phase (figure 5.2.12).

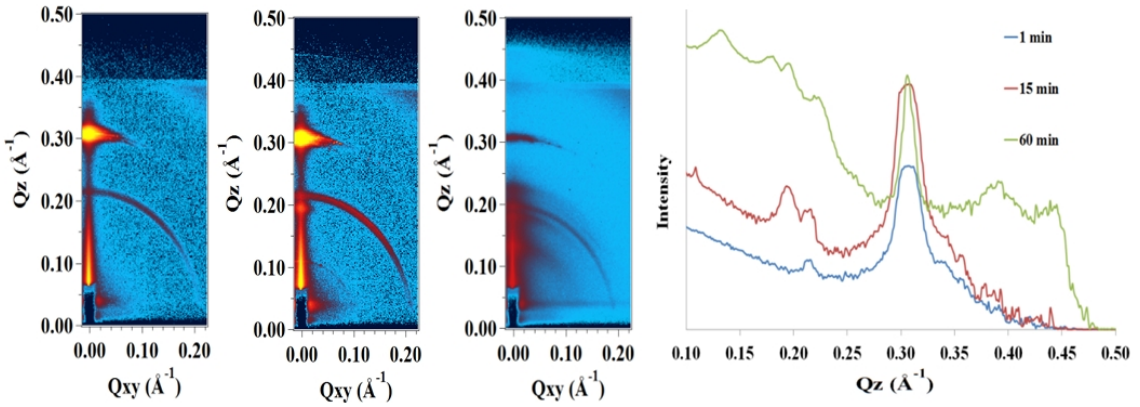

Figure 5.2.12: Time resolved GIXD patterns during photopolymerization of CPBr/LPEI film at 25ºC encapsulating 0.03M styrene and 0.05mM ACHN. From left to right; patterns taken after 1, 15 and 60 min. The fourth graph shows the Q_z line profiles of those GIXD pattern films taken at 0.01$Å^{-1}$ on the Q_{xy} axis.

At higher initiator concentrations and/or higher styrene concentrations CPBr/LPEI films encapsulating 0.05M styrene / 0.1 or 0.20 mM ACHN and 0.09M styrene / 0.05, 0.10 and 0.20 mM ACHN show in general three stable rings in the initial GIXD patterns. The first ring around Q_z =0.165 $Å^{-1}$ became broader with time but the final GIXD pattern of the photopolymerized film can be indexed as showing the 110, 200 and 211 reflections of an *Im3̄m* cubic phase (figure 5.2.13). The final photopolymerized structures for LPEI films containing BDHAB and CPBr with different amount of styrene and ACHN are summarized in table 5.2.2.

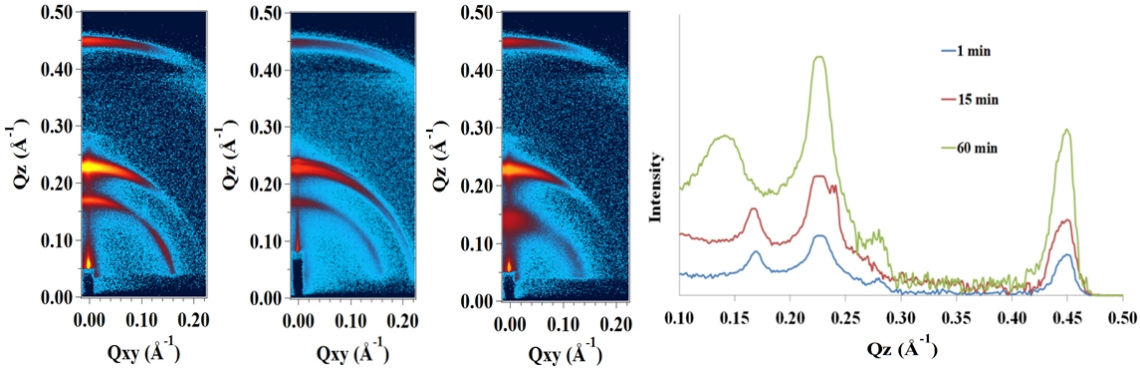

Figure 5.2.13: Time resolved GIXD patterns during photopolymerization of CPBr/LPEI film at 25ºC encapsulating 0.09M styrene and 0.05mM ACHN. From left to right; patterns taken after 1, 15 and 60 min. The fourth graph shows the Q_z line profiles of those GIXD pattern films taken at 0.01$Å^{-1}$ on the Q_{xy} axis.

Table 5.2.2: The average unit cell dimensions and structure assignments of the final photopolymerized films at 60min containing encapsulating styrene in a polymer/surfactant mesophase.

Surfactant	Styrene conc. (M)	ACHN conc. (mM)	Average unit cell size (Å)	Structure assignment
BDHAB/LPEI	0.03	0.05	71	$Pm\bar{3}n$
	0.03	0.10	67[a] / 60[b]	$Pm\bar{3}n$ - $Fm\bar{3}m$
	0.03	0.20	67[a] / 61[b]	$Pm\bar{3}n$ - $Fm\bar{3}m$
	0.09	0.05	72	$Pn\bar{3}m$
	0.09	0.10	82	$Pm\bar{3}n$
	0.09	0.20	74[a] / 62[b]	$Pm\bar{3}n$ - $Fm\bar{3}m$
CPBr/LPEI	0.03	0.05	69	$Pm\bar{3}n$
	0.03	0.10	55	$Im\bar{3}m$
	0.03	0.20	56	$Im\bar{3}m$
	0.09	0.05	55	$Im\bar{3}m$
	0.09	0.10	58	$Im\bar{3}m$
	0.09	0.20	59	$Im\bar{3}m$

a is the Average unit cell for $Pm\bar{3}n$ and b for $Fm\bar{3}m$. The errors in the unit cell sizes are ± 0.5Å

However despite the fact that the initial of BDAHB and CPBr films encapsulating styrene in general shows a lamellar structure, the intermediate phases observed in the photopolymerization of encapsulated styrene in both BDAHB and CPBr films were, in general stable and similar to the final film structure. It is important to notice that mesostructure phases of both BDAHB and CPBr films encapsulating different amounts of styrene but without any amount of initiator (ACHN) did not show any significant or rapid change during UV irradiation, which provides good evidence that the changes in phases during the photopolymerization process are mainly due to polymerization of encapsulating styrene.

Most GIXD patterns taken during the phase transitions for both BDAHB/LPEI and CPBr/LPEI films solubilising different concentration of styrene and ACHN showed gradually increasing numbers of diffraction ring and the intensity of these rings during UV irradiation. These diffraction rings grew at the same Q positions. However structures formed during thermal polymerization showed different intermediate phases compared with their initial or final structure. This constancy in transition intermediate phases indicates stability of the forming mesostructure suggesting it is easier to control photopolymerization compared with thermal polymerization.[*65, 67*].

The formation of intermediate phases occurs earlier when increasing the concentration of initiator for both BDHAB and CPBr systems. This agrees with the GC results reported above (section 5.1) that the polymerization rate was increased by increasing the amount of initiator. However the rate of photopolymerization in liquid crystalline system does not only depend on the initiator type or concentration. Guymon et al. [*68*] found that shape and geometry of nanocomposites hosting the monomer has a great influence on photopolymerization rate and mechanism. This study demonstrated that polymerization rate is highly dependent on the hosting morphology, where the more ordered the nanostructure is, the faster the polymerization rate. Moreover the techniques used to trap monomers within organized systems such as polymer templating in liquid crystals, organized particle templating, linear chain templating or catalytic polymerization, templating of assembled vesicles and molecular imprinting are a very important factor affecting the photopolymerization process [*65, 69*]. In general differences in polymerization rate are mainly due to diffusional limitations on propagating chains of polystyrene. In the case of BDHAB and CPBr films, even though the styrene is embedded in solid state films, the photopolymerization for those films showed stability after 60min. Also conversion percentage of styrene in solution experiment (section 5.1) showed that more than 50% of styrene polymerized after 120min by using UV radiation. This relatively fast polymerization of styrene in solid state films suggests that the styrene is encapsulated in well-ordered mesostructured films and the templating method used to solidify the nanostructured system worked very well with photopolymerization technique.

The final structure resulting from photopolymerization of films containing styrene in BDHAB/LPEI at different concentration of styrene and ACHN was in general a $Pm\bar{3}n$ structure, while the photopolymerization of styrene in LPEI/CPBr films resulted in $Im\bar{3}m$ cubic structures. However the initial structures of these films were in general a lamellar structure. Therefore these phases seen in the final photopolymerized films for both BDHAB and CPBr developed from lamellar phases. This is possibly due to a change in the packing parameter of surfactant micelles, resulting from changes in styrene density during of polymerization process [*70*]. The intermediate transition phases and final photopolymerized films showed in general different structures compared with those formed during the thermal polymerization process. This variation suggests that the mechanisms of structure re-arrangement during the

photopolymerization process are different compared with thermal polymerization technique [*71*]. In thermal polymerization the most influence on the change of transition phases was the temperature, while photopolymerization occurred at 25°C. Some of BDHAB/Styrene/LPEI photopolymerized films encapsulating relatively high concentration ratio of ACHN had a proposed structure combining two structures. Based on the micelle surface curvatures and degree of freedom which can allow surfactant micelles to rearrange and deform in close packed structures, El Safty and Hanaoka suggested that both the micellar $Fm\bar{3}m$ and $Pm\bar{3}n$ cubic phase structures could occur in one film. In addition the cubic $Fm\bar{3}m$ and $Pm\bar{3}n$ geometries are found as stable phases in structures formed from surfactants with a relatively long hydrocarbon chain [*72*].

At low concentrations of encapsulating styrene (0.03M), the final photopolymerized structure of the surfactant/styrene/LPEI systems for both BDHAB and CPBr show in general, a decrease in average unit cell size through increasing the amount of initiator (table 5.2.2). However at relatively high concentration of encapsulating styrene (0.09M), the average unit cell shown for both LPEI films containing BDHAB or CPBr increased when increasing the amount of initiator. This behaviour could be related to the propagation of the polystyrene chain during of the photopolymerization process. Photopolymerization rate and conversion are affected by surfactant/monomer concentration as reported by DePierro *et al* [*71*]. The photopolymerization rate increases at higher surfactant concentrations as initiator becomes more diffusely dispersed in the system and the initiator radicals have more potential to initiate the polymerization process. Faster photopolymerization rate typically results in a decrease in the polymer molecular weight which could be causing re-arrangements of the micelles as well as affecting the micelles size [*73*]. Another possibility is related to the re-formation of both BDHAB and CPBr micelles demonstrated by the observed volume change at relatively high concentration of styrene in the presence of PEI as shown in chapter 4.

The final photopolymerized films of styrene/LPEI/BDHAB show bigger mesostructure spacings compared with final structures in the CPBr/styrene/LPEI films. This result shows good agreement with results on the amounts of encapsulating styrene in polymer/surfactant films and solutions reported in chapters 4. As mentioned before the reason behind this variation is due to the differences in polyelectrolyte/surfactant and surfactant/styrene interactions.

In the previous chapter in polymer/surfactant films containing encapsulated styrene monomer a disordered structure was found for the case of CPBr/LPEI films as the concentration of styrene was increased, while in the case of BDHAB/LPEI/styrene films an enhancement in ordered structures emerged by increasing the styrene concentration. However photopolymerization of styrene/CPBr/LPEI films showed that the diffraction ring at Q_z 0.165 $Å^{-1}$ split into more than one ring at the same Q position which indicates formation of a more ordered structure during the photopolymerization process (figure 5.2.13).

5.2.3.2 Effect of UV Irradiation Time and Wavelength

The effect of exposure time on the photopolymerization reaction was investigated by changing the UV irradiation time. All of previous photopolymerization samples were exposed to 245nm UV radiation from the beginning to the end of photopolymerization run. Figure 5.2.14 shows time-resolved GIXD patterns for the photopolymerization of BDHAB/LPEI film encapsulating 0.09M styrene and 0.10mM ACHN at 25ºC. The UV irradiation was turned on 10 min from the beginning of the photopolymerization run then turned off for further 10min. This exposure procedure kept alternating on and off every 10 min up to the end of the run when the structure stopped changing. It was shown that by keeping UV irradiation on, growth in the diffraction rings intensity was seen, while in the case where the UV irradiation was off, the intensity of these diffraction rings was paused.

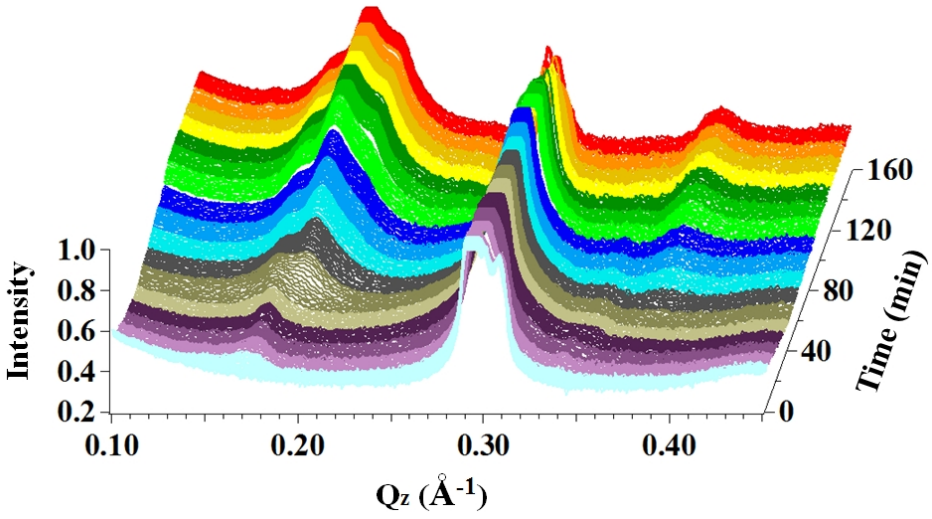

Figure 5.2.14: Line profiles from time-resolved GIXD patterns taken during photopolymerization of BDHAB/LPEI film encapsulating 0.09M styrene and 0.10mM ACHN at 25ºC. UV irradiation was alternated on and off every 10min. The Q_z lines profile were extracted from the GIXD patterns at Q_{xy} =0.01$Å^{-1}$.

This obvious relationship seen between UV exposure time and intensity of diffraction peaks proposed good evidence that photopolymerization process is dominated by UV exposure time. This changing in mesostructure was very obviously seen by using 245nm UV radiation, while at 365nm UV wavelength the changes in peaks intensities were very slow and gradual during the polymerization when the UV irradiation alternated on and off every 10min. This result suggests that 245nm UV radiation has more power to initiate the ACHN faster than 365nm and at the same time the 245nm radiation probably also enabled initiation of the styrene monomer directly to produce styrene free radicals, enhancing the polymerisation rate further [*74*]. Overall successfully managing switching the polymerization process on and off suggests a powerful method of controlling the rate of the photopolymerization process [*65*].

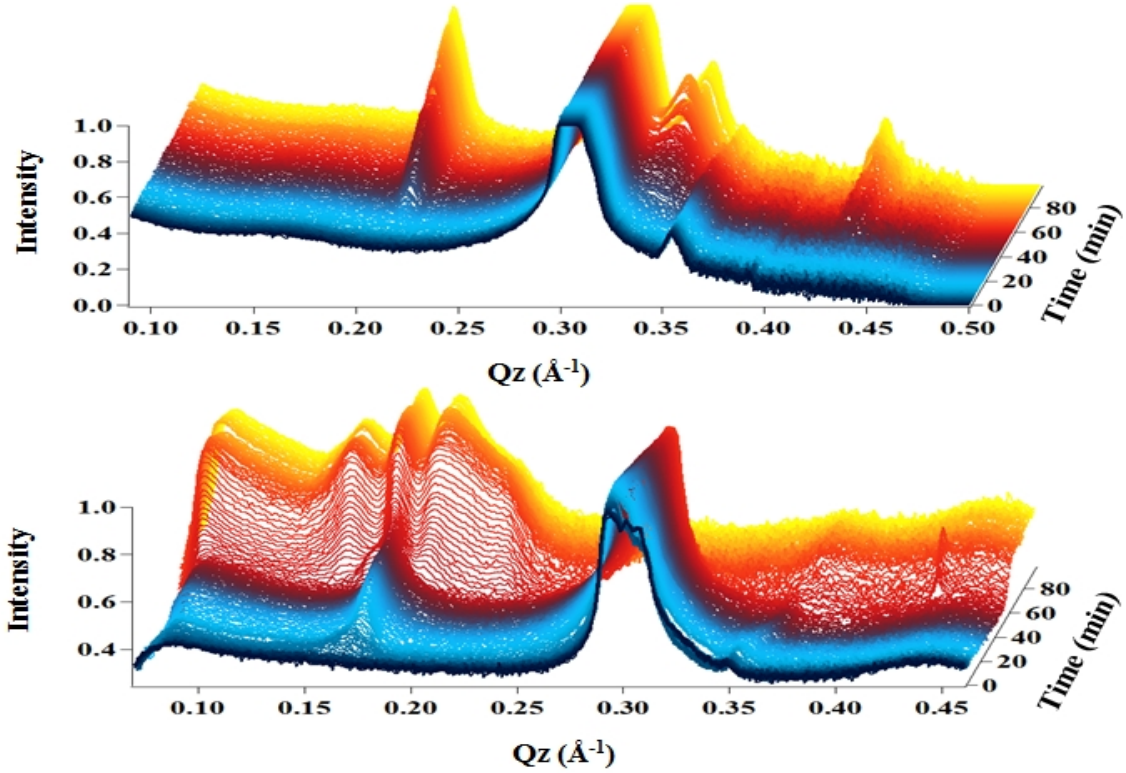

Figure 5.2.15: Line profiles from time-resolved GIXD patterns taken during photopolymerization of BDHAB/LPEI film encapsulating 0.09M styrene and 0.10mM ACHN at 25ºC. The photopolymerization occurred at 365nm (top graph) and 254nm (bottom graph). The Q_z lines profile were extracted from their GIXD patterns at Q_{xy} =0.01Å^{-1}.

Figure 5.2.15 show the film evolution during photopolymerization at two different UV wavelengths 254nm and 365nm with constant irradiation for the same film composition

with the same amount of styrene/ACHN. Photopolymerization at different wavelengths showed clearly differences in the size of the resulting polymerized structures. As mentioned above, the final structure in the photopolymerized film of BDHAB/LPEI at 254nm encapsulating 0.09M styrene and 0.10mM ACHN demonstrated a $Pm\bar{3}n$ cubic structure with an 82Å unit cell. The same film composition polymerized at 365nm still exhibited the same cubic phase structure but with a 43 Å unit cell. The first peak at Q_z 0.215 $Å^{-1}$ was seen in the 365nm polymerization to start growing after 30 min, whereas in the case of 254nm irradiation the peak at 0.195 $Å^{-1}$ started to grow after just 7 min irradiation time. These results suggest that the main reason behind these different polymerization performances is due to the variation in photopolymerization rate between short and mid wavelengths. Styrene is the one of photosensitive monomers able to produce radical species upon absorption of light [*75*]. Although the maximum absorption and recommended wavelength to initiate the ACHN is 360nm [*76*], using 254nm wavelength light showed a faster polymerization rate. Styrene monomer itself has a maximum UV absorption between 240-300nm, while at 360nm it does not show any UV absorbance (Chapter 4 Figure 4.2.1). Therefore styrene monomer is highly excited at 254nm which subsequently it is easier to produce direct free radical; in addition of presence ACHN (photosensitive initiator) could accelerate the photopolymerization rate many times. On the other hand due to variances in absorption of UV light, the polymerization rate of a photosensitive monomer is highly dependent on the wavelength of the irradiating light, where at lower wavelengths; the light is absorbed very fast, leading to a greater radical generation rate. Cramer *et al* polymerized a range of monomers including styrene using UV irradiation at 360nm and 254nm without any addition of initiator. This study illustrated very clearly that the photopolymerization rate of styrene at 254nm was four times faster than at 360nm. In this paper they concluded that polymerization rate for those system are highly dependent on the wavelength of the irradiating light [*74*].

5.2.3.3 Effect of PEI Molecular Weight

As stated in chapter 4, films grown at the water/air interface using an aromatic headgroup surfactant with LPEI showed better structure than surfactant/SPEI films. However aliphatic headgroup surfactants gave opposite results where low molecular weight PEI gave relatively highly ordered compared with high molecular weight of PEI [*7, 31*]. Photopolymerization of styrene in BDHAB/SPEI films also results in an enhancement in mesostructural ordering (figure 5.2.16).

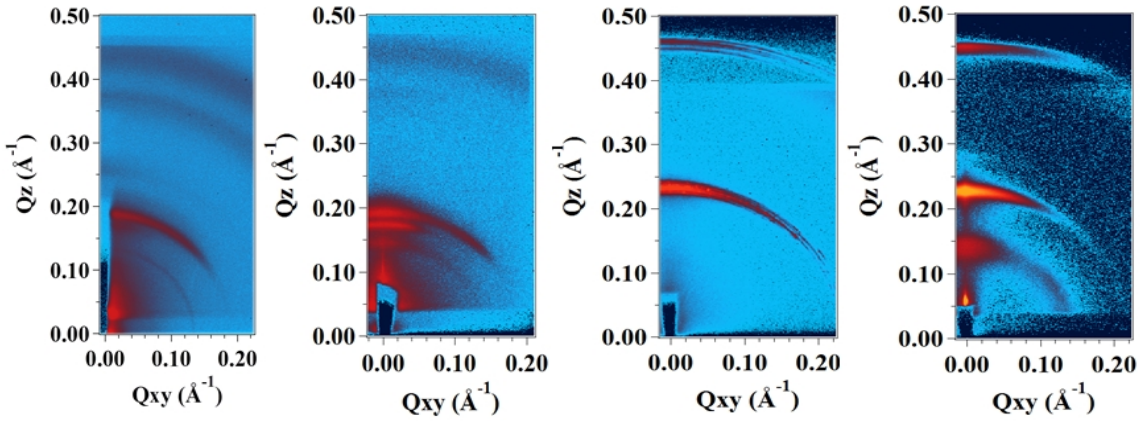

Figure 5.2.16: GIXD patterns of photopolymerized films encapsulating 0.09M styrene and 0.10mM ACHN at 25ºC from left to right; BDHAB/SPEI, BDHAB/LPEI, CPBr/SPEI and CPBr/LPEI. Patterns were taken after 60min of exposure to 254nm UV light.

The styrene/BDHAB/SPEI film before polymerization had a lamellar structure, while the final photopolymerized film has a GIXD pattern with rings suggesting formation of a $Pn\bar{3}m$ cubic structure with a 65Å unit cell. In the case of photopolymerization of styrene in CPBr/SPEI films, the initial lamellar structure did not significantly transform during the photopolymerization process, so the final film remained as a lamellar structure. However the final structure of photopolymerized styrene in CPBr/LPEI films as mentioned above showed an $Im\bar{3}m$ cubic phase. In general the final structure of photopolymerized styrene in surfactant/LPEI films provided bigger structures compared with the same films composition but with low molecular weight of PEI. The differences in lattice spacing between short and long PEI was ~9Å. This result agree with previous work within the group [*77-79*], where the SPEI has a lower molecular weight than LPEI and is less branched, consequently SPEI can fit more easily between the micelles, causing screening of the apparent charge on the micelles and thus decreases in lattice spacing.

5.2.3.4 Effect of Surfactant Chain Length

As demonstrated in chapter 4 most films formed at the water/air interface C_{14} hydrocarbon chain surfactants solubilising styrene did not show well-ordered structures. Most of these films showed a very broad diffraction feature in the GIXD patterns which indicates high polydispersity and poor ordering within the structure [*4*]. Figure 5.2.17 illustrates the time-resolved GIXD data taken during photopolymerization of styrene-containing C_{14} hydrocarbon chain surfactant/LPEI films.

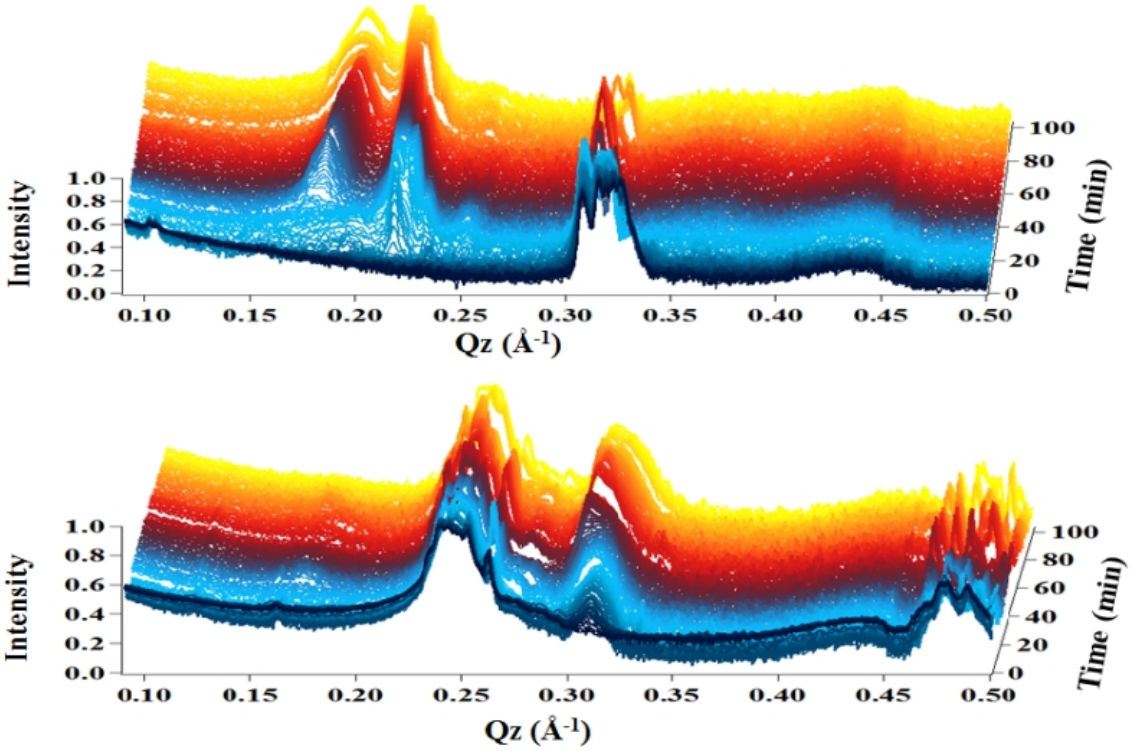

Figure 5.2.17: Line profiles from time-resolved GIXD patterns taken during photopolymerization of C_{14} tail BDTAB/LPEI (top graph) and TDPB/LPEI films (bottom graph) encapsulating 0.09M styrene and 0.10mM ACHN at 25ºC/254nm. The Q_z lines profile were extracted from their GIXD patterns at Q_{xy} =0.01Å^{-1}.

Both BDTAB and TDPB films showed, in the beginning, a lamellar structure, while after 90 min the styrene/LPEI/BDTAB photopolymerized film had a $Fm\bar{3}m$ cubic structure with a 56Å unit cell and GIXD data from the styrene/LPEI/TDPB film showed a $Pm\bar{3}n$ mesostructure with a 39Å unit cell. The styrene/LPEI/BDTAB photopolymerized films have bigger unit cell dimensions compared with those from the styrene/LPEI/TDPB films, as expected since for the C_{16} surfactant/LPEI

photopolymerized films formed using the BDHAB surfactant had bigger unit cell sizes than those formed using CPBr. However the C_{14} surfactant films have in general smaller unit cell compared with C_{16} surfactant films. These results agree with micelle size (Chapter 4) where the main reason is the hydrocarbon tail length. Subsequently this variation in the micelles size could affect the final molecular weight of polystyrene since it is correlated with shape and volume of the hosting medium [*80, 81*].

Changes in diffraction peak intensity for both BDTAB and TDPB films appear early during the photopolymerization process but the photopolymerized structures in the C_{14} films took more than 60 min to stabilize which indicates that there is more mobility of surfactant and growing polymer chains in the C_{14}-surfactant containing films compared with C_{16}-surfactant containing films. This behaviour may be related to variances of Krafft point between C_{14} and C_{16} hydrocarbon chain of these surfactants [*82*], where the long hydrocarbon tail increases the Krafft point. Therefore these surfactant with longer hydrocarbon tail have a greater tendency to form crystals than the C_{14} tail surfactants, subsequently increasing the viscosity and reduce the surfactant mobility [*83*].

5.1 Characterization of Polymerized Styrene in Organized systems.

Although the GC results discussed above demonstrate the polymerization of styrene in relatively high concentration cationic surfactant/PEI solutions, nevertheless polymerization of encapsulating monomer in the solid state (ie here in the films) is still not well established and more challenging to determine than in solution. Therefore it is very important to understand the characteristics of the final product in these reactions (polystyrene).

5.1.1 NMR, FT-IR and GPC Used to Identify and Study Polystyrene.

The first challenge in characterization of the polymerized styrene in solid polymer/surfactant films was how to extract the pure polystyrene from this mixture. Many attempts were made to purify polystyrene to make sure that the identification and characterization results are realistic. Since polystyrene is insoluble in water while the other materials forming the films are soluble, therefore extraction by pure water was the first choice. Unfortunately the solubilisation power of amphiphile molecules for hydrophobic organic compounds, made polystyrene extraction very difficult. Acid/water solutions, organic solvent and mixtures of organic solvent were also tried to purify the polystyrene from the film matrix. Finally a 7:3(*v/v*) mixture of water/ethanol solution was found the best way to purify polystyrene. However by using this solution more than half of the polystyrene weight is still lost during decantation of the centrifuged solution from the insoluble polymer. Figure 5.3.1 illustrated proton NMR and FT-IR spectrum of purified polystyrene from polymer/surfactant films.

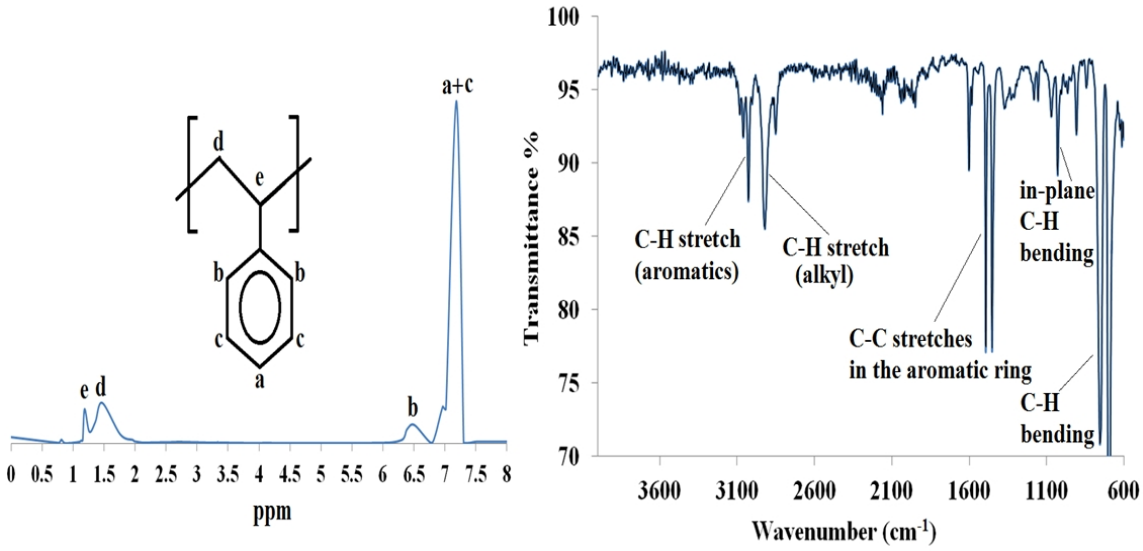

Figure 5.3.1: ^{1}H NMR (left) and FT-IR (right) spectra of purified polystyrene.

The ^{1}H NMR spectrum of purified polystyrene illustrated the typical proton resonance of standard polystyrene [*84*]. The peaks around 6.2 - 7.3 ppm belong to the C-H of the benzyl ring while the two peaks at 1.2 and 1.5 ppm belong to saturated aliphatic C-H and C-H_2 respectively. The two peaks at lower ppm confirm that double bonds of the styrene are completely converted and demonstrate formation of the polystyrene chain.

The IR spectrum of the purified polystyrene showed absorption bands at 3029 and 2931 cm^{-1} corresponding to aromatic and aliphatic C-H stretches respectively. The peaks at 1604 and 1494 cm^{-1} are allocated to aromatic C=C stretches. The C-H deformation vibration band of adjacent hydrogens in the benzene ring is observed at 758 cm^{-1}. The ring deformation vibration occurs at 697 cm^{-1} and the C-H stretching vibrations of those hydrogens occur at 3063 and 3089 cm^{-1} [*85*]. The small peaks around 2232 cm^{-1} corresponds to cyano (-C≡N) group which derive from the end group derived from the ACHN initiator [*86*]. Overall the assignment of NMR and FT-IR peaks indicates very clearly that the final product is pure polystyrene and nothing else.

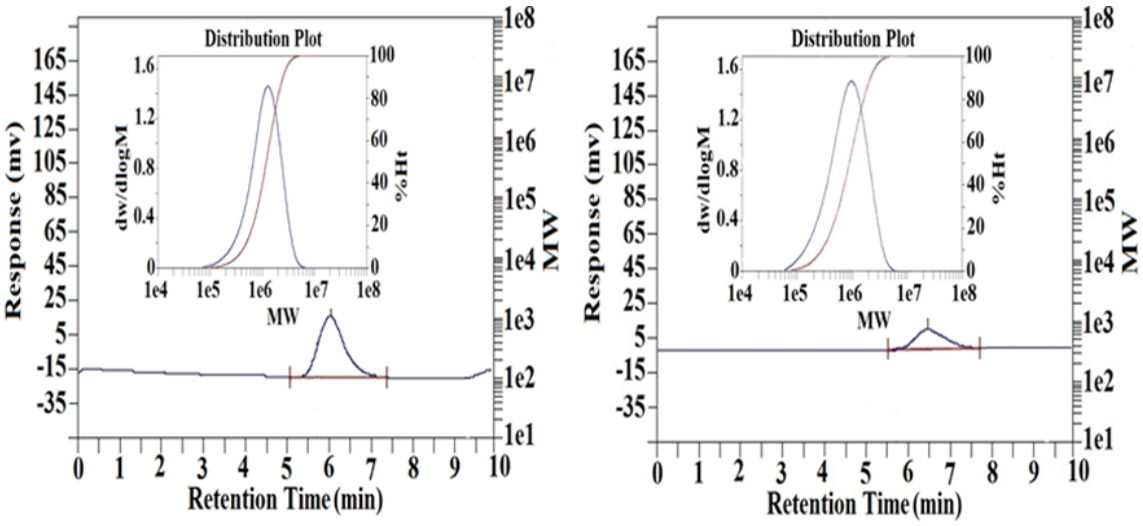

Figure 5.3.2: GPC curves of purified polystyrene extracted from films after photopolymerization in a styrene/BDHAB/LPEI film (left) and a styrene/CPBr/LPEI film (right).

GPC measurements were made to determine the molecular weight of the polymerised polystyrene. Although the same quantity of photopolymerized styrene/BDHAB/PEI and styrene/CPBr/PEI films were dissolved in equal amount of solvent, nevertheless the area under the peak for purified polystyrene extracted from styrene/BDHAB/LPEI films was bigger than that of purified polystyrene extracted from styrene/CPBr/LPEI films. As mentioned in the GC experiment the rate of conversion of styrene in BDHAB/PEI solution was very similar to CPBr/PEI solution. Therefore it must be assumed the quantity lost during purification of polystyrene from CPBr/LPEI films was greater than for polystyrene purified from BDHAB/LPEI films. The GPC results suggest that the proportion of low molecular weight (M_n) polystyrene resulting from photopolymerized styrene/CPBr/LPEI films was greater compared with that in photopolymerized styrene/BDHAB/LPEI films. There was therefore a risk that low molecular weight polystyrene, as well as any unpolymerised styrene was lost during the decanting process via solubilisation by CPBr surfactant. Therefore to obtain a more accurate M_n and M_w distribution of final photopolymerized polystyrene, fragments of whole surfactant/PEI films were dissolved in a known volume of THF. Using this method ensured that all polystyrene across the entire molecular weight distribution was dissolved in the THF solvent, but unfortunately THF also dissolved a portion of the surfactant molecules. That means that some surfactants molecules will pass through the GPC column, and

risks surfactant molecules blocking the column. Therefore only a few samples were able to be analysed using this technique. In future work a comprehensive analysis of the polystyrene M_n and M_w distribution for all of these photo and thermal polymerized films could be done using the MALDI-TOF mass spectroscopy technique [*87*]. Table 5.3.1 illustrates the average molecular weight, molecular number and polydispersity of polystyrene measured for styrene photopolymerized in cationic surfactant/LPEI films.

Table 5.3.1: M_n, M_w and PD of polystyrene were photopolymerized within surfactant/LPEI films encapsulating 0.09M styrene and 0.10mM ACHN.

Hosting surfactant/LPEI films	M_n	M_w	*PD*	ΔM_w (365nm/254nm)
BDHAB polymerized at 254nm	889000	1261000	1.42	1.12
BDHAB polymerized at 365nm	766000	1409000	1.84	
BDHAB polymerized at 254nm-purified	1463000	1760000	1.2	
CPBr polymerized at 254nm	607000	844000	1.39	1.12
CPBr polymerized at 365nm	568000	942000	1.66	
CPBr polymerized at 254nm-purified	849000	1161000	1.37	

Errors in the reported values are ±5%.

As can be seen from the table above the molecular weight of photopolymerized polystyrene in BDHAB/PEI films overall is higher than that polymerized in CPBr/PEI films. As stated before, all the BDHAB/PEI films had ordered structures with larger unit cell dimensions compared with CPBr/PEI films, so this indicates that the volume and shape of the hosting surfactant phase play a significant role in defining the molecular weight of the polymer templated in these organized systems. It is clear that photopolymerization using 365nm, for both BDHAB/PEI and CPBr/PEI films gives higher M_w compared with those films were polymerized at 254nm. These results demonstrate good agreement with the observed photopolymerization rate variation between short and medium wavelengths. More free radicals were produced at 254nm so consequently the photopolymerization rate at 365nm was slower compared with 254nm. In the end this suggests slower termination and so gives more chance for polystyrene chain growth (propagation) [*88*]. On the other hand polystyrene in films polymerized at 254nm display a narrower molecular weight distribution compared with those films that

were polymerized at 365nm. That means photopolymerization at short wavelength, particularly for this polymer/surfactant system, can produce controllable M_w/M_n and potentially nanostructured polystyrene. Overall this photopolymerization method also demonstrates narrow polydispersity compared with other free radical techniques used for polymerization in organized system [*13*].

The samples where polystyrene was purified before measurement showed the highest M_w and at the same time display the lowest polydispersity. This suggests that parts of their molecular weight distribution are chopped off, particularly those of low molecular weight, during the purification process.

This photopolymerization technique was used to polymerize encapsulating styrene in novel well-organized polymer/surfactant systems. In general these results demonstrated that polystyrene with very high molecular weight is formed. As mentioned in Chapter 4, theoretical calculation of the number of encapsulated styrene molecules for the $50\%_{v/v}$ styrene in BDHAB or CPBr micelles was 5440 and 429 molecules respectively (for samples without PEI). However in the case of surfactant/PEI solutions the number of encapsulated styrene molecules was dramatically decreased to 1587 molecules in case of BDHAB and 78 styrene molecules in case of CPBr micelle. That mean 'in the best case' the final polymerized polystyrene molecular weight should be 566576 and 44680 respectively (considering that 100% of conversion). These results do not match well with the actual GPC results although the correct trend is followed (ie the polymer formed in BDHAB-containing films has higher M_n than that formed in the CPBr micelles). As stated before, deformation and rearrangement of the surfactant micelles size and shape were seen by varying the water/surfactant/PEI concentrations. However the final GIXD patterns of surfactant/LPEI for photopolymerized films encapsulating 0.09M styrene and 0.1mM ACHN demonstrated a $Pm\bar{3}n$ structure in the case of BDHAB, where CPBr films showed an $Im\bar{3}m$ cubic structure. These 3D mesophases cubic structures were seen in the final photopolymerized films for both BDHAB and CPBr are thought to develop from lamellar phases as seen from figure 5.3.3. This means that substantial micelle rearrangement does occur during photopolymerization allowing styrene encapsulated in different micelles to merge during the polymerisation process, allowing higher molecular weights to form.

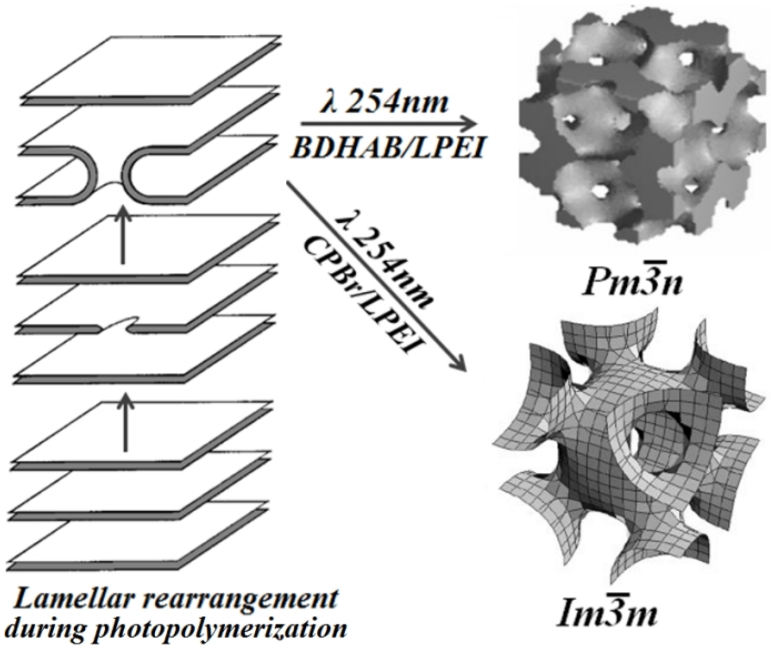

Figure 5.3.3: Schematic of theoretical phase change during photopolymerization of BDHAB and CPBr films encapsulating styrene monomer. Mesophases structures were redrawn from [54, 89].

The $Im\bar{3}m$ phase can be found as 3D micellar and bicontinuous (sponge) cubic structure [*90*]. The $Pm\bar{3}n$ cubic structure is formed from close-packed micelles, which, in the case of large headgroup cationic surfactants (such as BDHAB) forms as a clathrate packing micelles (identical to the melanophlogite silicate network) [*54, 90*]. This suggests that polymerization of styrene monomer in clathrate packing micelles or bicontinuous mesostructure phases leads to higher molecular weights when compared to polymerization of this monomer inside disconnected and small micelle volumes. Therefore the high polystyrene molecular weight found in these photopolymerized films supports the hypotheses that styrene was encapsulated and polymerized in a well-organized mesophases. Finally in this part, it is good to report that increases in molecular weight were found when these films were polymerized at 365nm, compared with 254nm, and the ratio of the increase in M_w between these two wavelengths was constant. This performance was seen for both of BDHAB and CPBr films which indicate that photopolymerization reactions in these systems are highly consistent (Table 5.3.1).

5.1.2 Electron microscopy studies of polystyrene

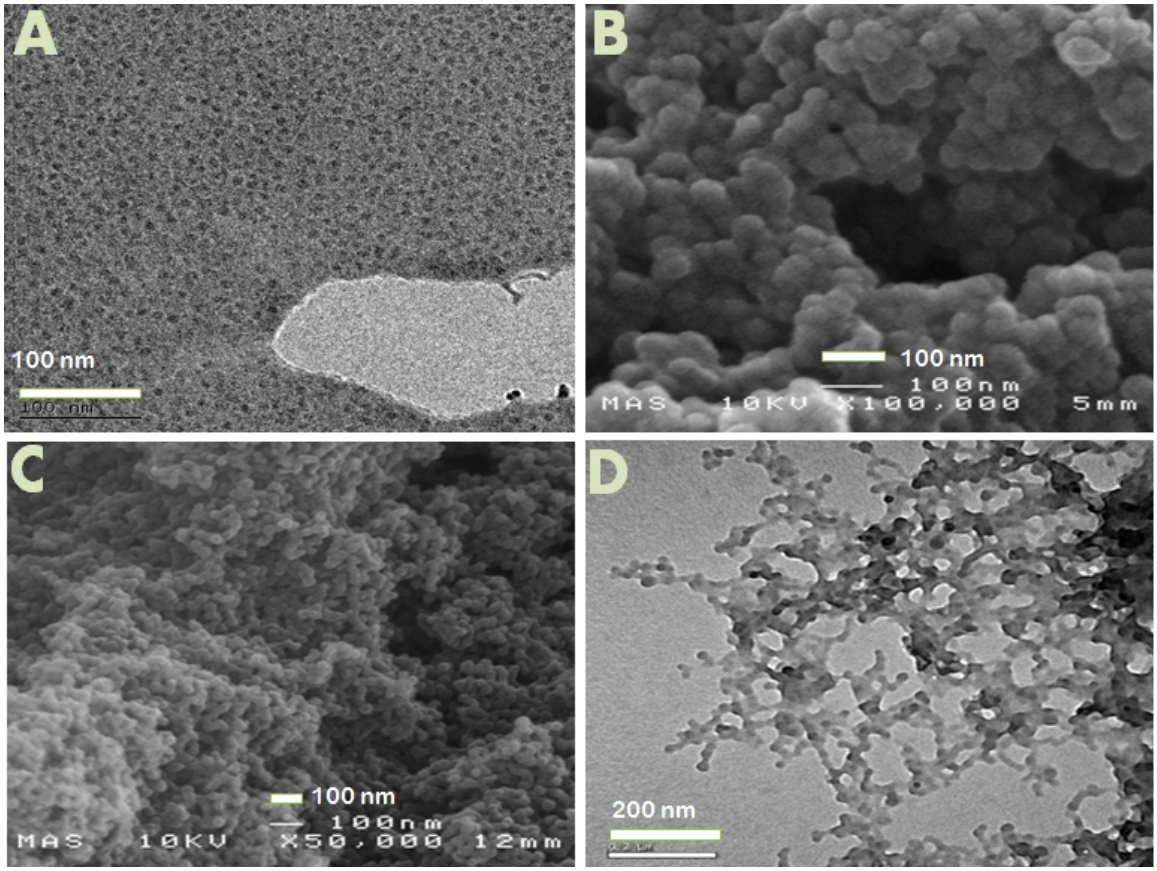

Figure 5.3.4: EM images for polystyrene resulting from photopolymerization of BDHAB/LPEI films encapsulating 0.09M styrene and 0.1mM ACHN. Cryo-TEM image of BDHAB/LPEI/styrene film polymerized at 254nm (A), FESM of purified polystyrene resulting from BDHAB/LPEI film polymerized at 365nm (B), FESM of purified polystyrene from BDHABLPEI film polymerized at 254nm (C) and TEM of purified polystyrene from BDHAB/LPEI film polymerized at 254nm (D).

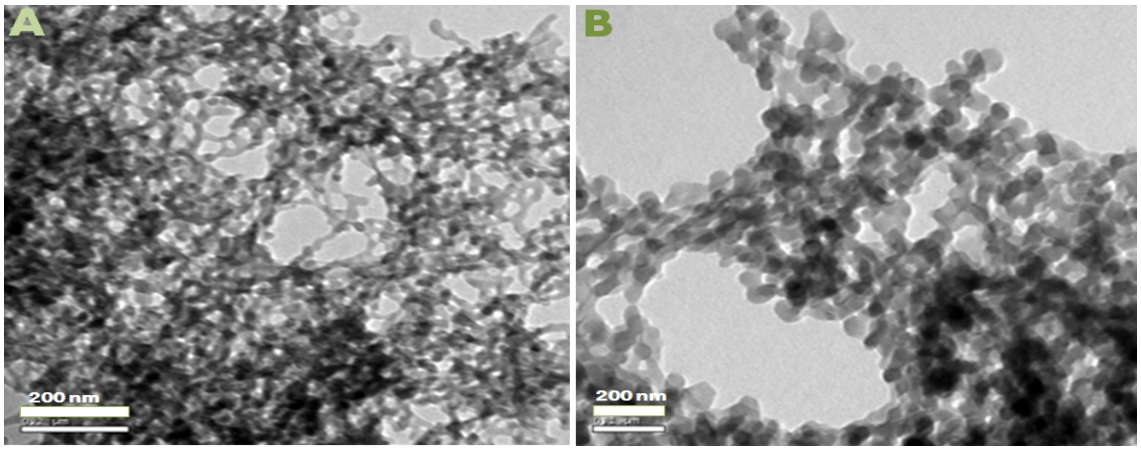

Figure 5.3.5: EM images for polystyrene resulting from photopolymerization of CPBr/LPEI films encapsulating 0.09M styrene and 0.1mM ACHN. TEM of purified polystyrene from CPBr/LPEI film polymerized at 365nm (A) and TEM of purified polystyrene from CPBr/LPEI film polymerized at 254nm (B.)

The above pictures show TEM and FESM images of the morphology of polystyrene that was photopolymerized in surfactant/PEI films. Cryo-TEM of a polymerized styrene/BDHAB/LPEI film showed small darker spots of polystyrene in the lower density PEI matrix. These spots show a uniform distribution nevertheless do not show any obvious identifiable order probably because the film, in areas which could be imaged, is only one layer of micelles thick. The soft PEI hydrogel may also be affected by the electron beam resulting in lower apparent ordering. In general the purified polystyrene morphology, after removal of the PEI hydrogel and the surfactant, demonstrated spherical parts connected with each other in a polymer network structure. These spheroidal parts suggesting that the styrene was encapsulated and polymerized inside surfactant micelles which prevented the growth of larger particles and reflects the proposed micellar cubic and bicontinuous structures seen in the GIXD. The polystyrene extracted from BDHAB/LPEI films show more compacted structures compared with polystyrene extracted from CPBr/LPEI films supporting the proposal that styrene polymerized in a different morphology in each type of film. The diameter of the polystyrene spheres was calculated and is summarized in Table 5.3.2.

Table 5.3.2: M_w and diameter of polystyrene photopolymerized in surfactant/LPEI films encapsulating 0.09M styrene and 0.10mM ACHN.

Hosting surfactant/LPEI films	Diameter (Å)	Δ Diameter (365nm/254nm)
BDHAB polymerized at 254nm	334 ±17	1.27
BDHAB polymerized at 365nm	418 ±21	
CPBr polymerized at 254nm	233 ±12	1.26
CPBr polymerized at 365nm	294 ±15	

20 particles were counted, to give good statistical results. Errors in these numbers are 4.2 times the standard deviation of the size distribution.

In general polystyrene polymerized at 365nm shows bigger particles diameters compared with those were polymerized at 254nm, which agrees with the larger M_w measured for polystyrene from films polymerized at 365nm above. In addition polystyrene extracted from BDHAB/LPEI films illustrated larger particle diameters than that which was polymerized in CPBr/LPEI films. Overall the diameters of extracted polystyrene particles are about four times bigger compared with average cell unit of

their corresponding final photopolymerized films. This result suggesting that each polystyrene sphere resulted from aggregation of polymer from four bicontinuous cubic unit cells. Since nanostructures have large surface energies, and the polymer purification process involved some heating it is possible that the structures fused during removal of the PEI matrix. The polystyrene particle diameters polymerized at 364nm and 254nm show a steady increase for both BDHAB and CPBr films which is compatible with the increase in M_w ratio. The consistent increase of M_w and polystyrene particle diameter ratio confirms that photopolymerization of polystyrene in these templated surfactant/polymer films is easy to control and is a tunable polymerization process.

Although the final purified polystyrene shows a nanocomposite structure however the aim of this experiment was to synthesis well-organized nanostructured polymer. Unfortunately the final purified polystyrene does not show a clear 1:1 copy of their hosting film structure. This could be due to a collapsing of polystyrene structure during the purification process. As mentioned earlier the removal of the PEI matrix was not easy so, involving warming to 40ºC ,then vigorous centrifugation was used to extract the polystyrene from surfactant and PEI, which could have caused fusion & distortion of the initially formed structure. Future work should try to develop an extraction and purification method which can maintain the initial structure. The second suggestion is to strengthen the polystyrene structure by building more supporting ‘scaffolds’, this step could be achieved by cross linking the polystyrene during polymerization.

5.2 Conclusion

In the previous chapter successful encapsulation of hydrophobic species in mesostructure polymer/surfactant films was demonstrated. These films were shown to contain an ordered array of micelles surrounded by polyethyleneimine. In this chapter, polymerization of the encapsulated styrene monomer in these films was investigated by GC and GIXD, while the resulting polystyrene was characterized by using FTIR, NMR, GPC and electron microscopy.

Styrene conversion studied by GC illustrated that styrene can be polymerized in cationic surfactant/PEI solutions using both thermal and photo irradiation techniques. However the most efficient conversion of styrene in these solutions was at high temperature (60ºC). Nevertheless polymerization of styrene in these solutions was successfully achieved at room temperature by using UV irradiation. Therefore polymerization styrene at room temperature by using UV irradiation can promote polymerisation in more viscous solutions thus reducing micelle re-arrangement through interdroplet diffusion and droplet exchange.

Thermal polymerization of styrene in both BDHAB/PEI/ and CPBr/PEI films showed variation in mesostructures and intermediate transition phases, where these changes in lyotropic phase were most likely due to temperature influences in these cationic surfactant films rather than polymerization effect. Both BDHAB/LPEI and CPBr/LPEI films showed a lamellar structure before thermal polymerization. However BDHAB/LPEI films transformed from a lamellar to a cubic structure as the polymerization temperature increased. Generally CPBr/LPEI films showed multilamellar structure with different d-spacings within the same film composition. These multilamellar structures are likely due to varying water/polyelectrolyte domain size and local variation in encapsulated styrene content within these films. The final polymerized CPBr/LPEI films structure illustrated in general lamellar and $Pm\bar{3}n$ cubic structures.

The main observation seen in photopolymerization of equivalent films was the stability of the intermediate phases compared with thermal polymerization. The final structure resulting from photopolymerization of films containing styrene in BDHAB/LPEI at different concentrations of styrene and ACHN was in general a $Pm\bar{3}n$ structure, while

the photopolymerization of styrene in LPEI/CPBr films resulted in $Im\bar{3}m$ cubic structures. However the initial structures of these films were again, in general, a lamellar structure. The photopolymerization using 245nm UV radiation has shown variation in mesostructure with time, while change in peak intensity was slow during photopolymerization using 365nm UV radiation. Also 254nm wavelength light showed a faster polymerization rate compared with 365nm which is due to the energetic 254nm wavelength being able to initiate both ACHN and styrene at the same time. In general the photopolymerization technique has been shown to be a powerful method of controlling the rate of the polymerization process by managing switching the polymerization process through alternating UV irradiation time and wavelength.

NMR and FT-IR confirmed the polymerization of styrene was achieved, and that the extracted white powder from surfactant/PEI films was pure polystyrene. However the extraction and purification of polymerized polystyrene from these polymer/surfactant films was big challenge, since the surfactant has high ability to solubilize part of the polystyrene, particularly the low molecular weight portion. In general the molecular weight of photopolymerized polystyrene in BDHAB/PEI films was higher than those were polymerized in CPBr/PEI films. On the other hand photopolymerization using 365nm in both BDHAB/PEI and CPBr/PEI films gives higher M_w compared with those films that were polymerized at 254nm. In addition electron microscopy illustrated that polystyrene were photopolymerized at 365nm had bigger particles diameters compared with those that were polymerized at 254nm. Also polystyrene extracted from BDHAB/LPEI films was larger particle diameters than that which was polymerized in CPBr/LPEI films. The final structure of extracted polystyrene does not reflect the hosted shape. Nevertheless successful templating of monomer in these polymer/surfactant films and polymerization of these monomer by thermal and photo initiaton process was achieved. Nanoscale polystyrene network were synthesised and have been shown to be a promising route to achieve 3D mesostructure polymers.

5.3 References

1. Quo, Q. (1999) *Polymer Blends and Alloys*, 155-187.
2. Pascault, J. P., and Williams, R. J. J. (2000) Formulation and characterization of thermoset-thermoplastic blends, *Polymer Blends 1*, 379-415.
3. Sakakibara, K., Hill, J. P., and Ariga, K. (2011) Thin-film-based nanoarchitectures for soft matter: Controlled assemblies into two-dimensional worlds, *Small 7*, 1288-1308.
4. Wasbrough, M. J., Edler, K. J., Hawley, A. M., Holdaway, J. A., and Price, G. J. (2012) Control of mesostructure in self-assembled polymer/surfactant films by rational micelle design, *Soft Matter 8*, 3357-3362.
5. Edler, K. J., and Yang, B. (2013) Formation of mesostructured thin films at the air-liquid interface, *Chemical Society Reviews 42*, 3765-3776.
6. Yan, F., and Texter, J. (2006) Polymerization of and in mesophases, *Advances in Colloid and Interface Science 128*, 27-35.
7. O'Driscoll, B. M. D., Hawley, A. M., and Edler, K. J. (2008) Incorporation of sparingly soluble species in mesostructured surfactant-polymer films, *J. Colloid Interface Sci. 317*, 585-592.
8. Zheng, A. N., Chen, B., Hu, D. H., Guan, Y., Wei, D. F., Li, S. Z., and Ji, D. D. (2013) A New View of the Initiation and Propagation in Anionic Polymerization, *Chinese J Chem 31*, 393-400.
9. Hong, H. L., Zhang, H. W., Mays, J. W., Visser, A. E., Brazel, C. S., Holbrey, J. D., Reichert, W. M., and Rogers, R. D. (2002) Conventional free radical polymerization in room temperature ionic liquids: a green approach to commodity polymers with practical advantages, *Chemical Communications*, 1368-1369.
10. Vaidhyanathan, V. S., and Santhappa, M. (1955) Chain Transfer Reactions and the Nature of Initiation in the Polymerization of Styrene, *Makromolekul Chem 16*, 140-156.
11. El-Aasser, M. S. L. P. A. (1997) *Emulsion polymerization and emulsion polymers*, J. Wiley, Chichester [u.a.
12. Fu, X. A., and Qutubuddin, S. (2002) Polymerization of styrene with a polymerizable cationic surfactant in three-component microemulsions, *Langmuir 18*, 5058-5063.
13. Faul, C., Antonietti, M., Sanderson, R., and Hentze, H. P. (2001) Directed polymerization in mesophases of polyelectrolyte-surfactant complexes, *Langmuir 17*, 2031-2035.
14. Petty, M. C. (2007) Molecular electronics from principles to practice, John Wiley & Sons, Chichester, England; Hoboken, NJ.
15. Meisburger, S. P., Warkentin, M., Chen, H., Hopkins, J. B., Gillilan, R. E., Pollack, L., and Thorne, R. E. (2013) Breaking the radiation damage limit with cryo-SAXS, *Biophysical Journal 104*, 227-236.
16. Ding, L. H., Park, S., Peyton, M., Girard, L., Xie, Y., Minna, J. D., and Story, M. D. (2013) Distinct transcriptome profiles identified in normal human bronchial epithelial cells after exposure to gamma-rays and different elemental particles of high Z and energy, *BMC Genomics*, 372.
17. Deymier-Black, A. C., Singhal, A., Yuan, F., Almer, J. D., Brinson, L. C., and Dunand, D. C. (2013) Effect of high-energy X-ray irradiation on creep

mechanisms in bone and dentin, *Journal of the Mechanical Behavior of Biomedical Materials 21*, 17-31.
18. Danauskas, S. M., Ratajczak, M. K., Ishitsuka, Y., Gebhardt, J., Schultz, D., Meron, M., Lin, B., and Lee, K. Y. C. (2007) Monitoring x-ray beam damage on lipid films by an integrated Brewster angle microscope/x-ray diffractometer, *Review of Scientific Instruments 78*.
19. Das, D., Kar, T., and Das, P. K. (2012) Gel-nanocomposites: Materials with promising applications, *Soft Matter 8*, 2348-2365.
20. Zhang, H., Liu, Y., Yao, D., and Yang, B. (2012) Hybridization of inorganic nanoparticles and polymers to create regular and reversible self-assembly architectures, *Chemical Society Reviews 41*, 6066-6088.
21. Rubingh, D. N., and Holland, P. M. (1991) *Cationic surfactants : physical chemistry*, M. Dekker, New York.
22. Salamone, J. C. (1996) *Polymeric materials encyclopedia*, CRC Press, Boca Raton.
23. Anthony, O., and Zana, R. (1994) Effect of temperature on the interactions between neutral polymers and a cationic and a nonionic surfactant in aqueous solutions, *Langmuir 10*, 4048-4052.
24. Wadekar, M. N., Pasricha, R., Gaikwad, A. B., and Kumaraswamy, G. (2005) Polymerization in surfactant liquid crystalline phases, *Chem. Mater. 17*, 2460-2465.
25. Hentze, H.-P., and Kaler, E. W. (2003) Morphosynthesis of Nanostructured Polymer Gels by Polymerization within Reverse Hexagonal Mesophases, *Chem. Mater. 15*, 708-713.
26. Tiddy, G. J. T. (1980) Surfactant-water liquid crystal phases, *Physics Reports 57*, 1-46.
27. Wypych, A., Szpotkowski, K., Jurga, S., Domka, L., and Kozak, M. (2013) Interactions of a cationic surfactant - (benzyloxymethyl) dodecyldimethylammonium chloride with model biomembrane systems, *Colloids and Surfaces B: Biointerfaces 108*, 212-218.
28. Filippova, S. N., Surgucheva, N. A., Ermakova, E. V., Kiselev, M. A., Terekhova, L. P., Sineva, O. N., Galatenko, O. A., Zabelin, A. V., and Gal'chenko, V. F. (2013) Structural organization and phase behavior of phospholipid fractions of actinobacteria in relation to storage conditions, *Microbiology (Russian Federation) 82*, 327-334.
29. Nielsen, M. M. B., and Simonsen, A. C. (2013) Imaging ellipsometry of spin-coated membranes: Mapping of multilamellar films, hydrated membranes, and fluid domains, *Langmuir 29*, 1525-1532.
30. Collings, P. J. H. M. (1997) *Introduction to liquid crystals chemistry and physics*, Taylor & Francis, London; Bristol, PA.
31. Edler, K., Wasbrough, M., Holdaway, J., and O'Driscoll, B. (2009) Self-assembled films formed at the air-water interface from CTAB/SDS mixtures with water-soluble polymers, *Langmuir 25*, 4047-4055.
32. Garstecki, P., and Hołyst, R. (2002) Scattering Patterns of Self-Assembled Cubic Phases. 1. The Model, *Langmuir 18*, 2519-2528.
33. Garstecki, P., and Hołyst, R. (2002) Scattering Patterns of Self-Assembled Cubic Phases. 2. Analysis of the Experimental Spectra, *Langmuir 18*, 2529-2537.
34. DePierro, M. A., Carpenter, K. G., and Guymon, C. A. (2006) Influence of polymerization conditions on nanostructure and properties of polyacrylamide

hydrogels templated from lyotropic liquid crystals, *Chem. Mater. 18*, 5609-5617.

35. Tattershall, C. E., Aslam, S. J., and Budd, P. M. (2002) Dimethylamino- and trimethylammonium-tipped oxyethylene-oxybutylene diblock copolymers and their use as structure-directing agents in the preparation of mesoporous silica, *J. Mater. Chem. 12*, 2286-2291.
36. Monteiro, M. J., and Cunningham, M. F. (2012) Polymer nanoparticles via living radical polymerization in aqueous dispersions: Design and applications, *Macromolecules 45*, 4939-4957.
37. Schuster, J., Köhn, R., Döblinger, M., Keilbach, A., Amenitsch, H., and Bein, T. (2012) In situ SAXS study on a new mechanism for mesostructure formation of ordered mesoporous carbons: Thermally induced self-assembly, *Journal of the American Chemical Society 134*, 11136-11145.
38. Kraineva, J., Narayanan, R. A., Kondrashkina, E., Thiyagarajan, P., and Winter, R. (2005) Kinetics of Lamellar-to-Cubic and Intercubic Phase Transitions of Pure and Cytochrome c Containing Monoolein Dispersions Monitored by Time-Resolved Small-Angle X-ray Diffraction, *Langmuir 21*, 3559-3571.
39. Tiwari, A. K., Sonu, and Saha, S. K. (2013) Aggregation behaviour and thermodynamics of mixed micellization of gemini surfactants with a room temperature ionic liquid in water and water-organic solvent mixed media, *Journal of Chemical Thermodynamics 60*, 29-40.
40. Cheng, X. H., Das, M. K., Diele, S., and Tschierske, C. (2002) Influence of semiperfluorinated chains on the liquid crystalline properties of amphiphilic polyols: Novel materials with thermotropic lamellar, columnar, bicontinuous cubic, and micellar cubic mesophases, *Langmuir 18*, 6521-6529.
41. Winter, R. (2001) Effects of hydrostatic pressure on lipid and surfactant phases, *Current Opinion in Colloid & Interface Science 6*, 303-312.
42. Lettow, J. S., Han, Y. J., Schmidt-Winkel, P., Yang, P., Zhao, D., Stucky, G. D., and Ying, J. Y. (2000) Hexagonal to Mesocellular Foam Phase Transition in Polymer-Templated Mesoporous Silicas, *Langmuir 16*, 8291-8295.
43. Kruk, M., Jaroniec, M., Kim, J. M., and Ryoo, R. (1999) Characterization of Highly Ordered MCM-41 Silicas Using X-ray Diffraction and Nitrogen Adsorption, *Langmuir 15*, 5279-5284.
44. Auvray, X., Petipas, C., Anthore, R., Rico, I., and Lattes, A. (1989) X-ray diffraction study of mesophases of cetyltrimethylammonium bromide in water, formamide, and glycerol, *Journal of Physical Chemistry 93*, 7458-7464.
45. Auvray, X., Petipas, C., Anthore, R., Rico, I., and Lattes, A. (1989) X-Ray-Diffraction Study of Mesophases of Cetyltrimethylammonium Bromide in Water, Formamide, and Glycerol, *Journal of Physical Chemistry 93*, 7458-7464.
46. Hotz, J., and Meier, W. (1998) Vesicle-templated polymer hollow spheres, *Langmuir 14*, 1031-1036.
47. Mayer, L. D., Hope, M. J., and Cullis, P. R. (1986) Vesicles of variable sizes produced by a rapid extrusion procedure, *BBA - Biomembranes 858*, 161-168.
48. Mata, J., Varade, D., and Bahadur, P. (2005) Aggregation behavior of quaternary salt based cationic surfactants, *Thermochimica Acta 428*, 147-155.
49. Jung, M., German, A. L., and Fischer, H. R. (2001) Polymerisation in lyotropic liquid-crystalline phases of dioctadecyldimethylammonium bromide, *Colloid and Polymer Science 279*, 105-113.
50. Borisch, K., Tschierske, C., Göring, P., and Diele, S. (1998) Molecular design of thermotropic liquid crystalline polyhydroxy amphiphiles exhibiting columnar

and cubic mesophases of the normal type, *Chemical Communications*, 2711-2712.
51. Seddon, J. M., and Templer, R. H. (1995) Chapter 3 Polymorphism of lipid-water systems, *Handbook of Biological Physics 1*, 97-160.
52. Luzzati, V., Delacroix, H., and Gulik, A. (1996) The micellar cubic phases of lipid-containing systems: Analogies with foams, relations with the infinite periodic minimal surfaces, sharpness of the polar/apolar partition, *J Phys Ii 6*, 405-418.
53. Auvray, X., Abiyaala, M., Duval, P., Petipas, C., Rico, I., and Lattes, A. (1993) X-ray diffraction and freeze-fracture electron microscopy study of the cubic phase in the cetylpyridinium chloride/formamide and cetyltrimethylammonium chloride/formamide systems, *Langmuir 9*, 444-448.
54. Sakamoto, Y., Kaneda, M., Terasaki, O., Zhao, D. Y., Kim, J. M., Stucky, G., Shin, H. J., and Ryoo, R. (2000) Direct imaging of the pores and cages of three-dimensional mesoporous materials, *Nature 408*, 449-453.
55. Fontell, K. (1990) Cubic phases in surfactant and surfactant-like lipid systems, *Colloid & Polymer Science 268*, 264-285.
56. Lindlbom, G., and Rilfors, L. (1989) Cubic phases and isotropic structures formed by membrane lipids. Possible biological relevance, *Biochimica et Biophysica Acta - Reviews on Biomembranes 988*, 221-256.
57. Esumi, K. U. M. (1997) *Structure-performance relationships in surfactants*, Marcel Dekker, New York.
58. Grosso, D., Babonneau, F., Soler-Illia, A., Albouy, P. A., and Amenitsch, H. (2002) Phase transformation during cubic mesostructured silica film formation, *Chemical Communications*, 748-749.
59. Odian, G. G. (2004) Principles of polymerization, Wiley, Hoboken, N.J.
60. Decker, C. (2002) Light-induced crosslinking polymerization, *Polym. Int. 51*, 1141-1150.
61. Kaur, M., and Srivastava, A. K. (2002) Photopolymerization: A review, *Journal of Macromolecular Science - Polymer Reviews 42*, 481-512.
62. DePierro, M. A., and Guymon, C. A. (2006) Photoinitiation and monomer segregation behavior in polymerization of lyotropic liquid crystalline systems, *Macromolecules 39*, 617-626.
63. Matuszewska-Czerwik, J., and Połowiński, S. (1991) Template photopolymerization of methacrylic acid-III. Determination of the rate constants ratio kt kp for elementary processes, *European Polymer Journal 27*, 743-746.
64. Matuszewska-Czerwik, J., and Polowiński, S. (1990) Template photopolymerization of methacrylic acid-II. Photopolymerization of methacrylic acid on poly(vinyl-pyrrolidone) in aqueous systems, *European Polymer Journal 26*, 549-552.
65. Clapper, J. D., Sievens-Figueroa, L., and Guymon, C. A. (2008) Photopolymerization in polymer templating, *Chem. Mater. 20*, 768-781.
66. Forney, B. S., and Guymon, C. A. (2010) Nanostructure Evolution during Photopolymerization in Lyotropic Liquid Crystal Templates, *Macromolecules 43*, 8502-8510.
67. McCormick, D. T., Stovall, K. D., and Guymon, C. A. (2003) Photopolymerization in pluronic lyotropic liquid crystals: Induced mesophase thermal stability, *Macromolecules 36*, 6549-6558.
68. Lester, C. L., and Guymon, C. A. (2002) Ordering effects on the photopolymerization of a lyotropic liquid crystal, *Polymer 43*, 3707-3715.

69. Amar-Yuli, I., Adamcik, J., Lara, C., Bolisetty, S., Vallooran, J. J., and Mezzenga, R. (2011) Templating effects of lyotropic liquid crystals in the encapsulation of amyloid fibrils and their stimuli-responsive magnetic behavior (vol 7, pg 3348, 2011), *Soft Matter 7*, 11547-11547.
70. Hartmann, P. C., and Sanderson, R. D. (2005) Templating polymerization of dodecylammonium surfactants with polymerizable (meth)acrylate counter ions, *Macromol. Symp. 225*, 229-237.
71. DePierro, M. A., Olson, A. J., and Guymon, C. A. (2005) Effect of photoinitiator segregation on polymerization kinetics in lyotropic liquid crystals, *Polymer 46*, 335-345.
72. El-Safty, S. A., and Hanaoka, T. (2004) Microemulsion liquid crystal templates for highly ordered three-dimensional mesoporous silica monoliths with controllable mesopore structures, *Chem. Mater. 16*, 384-400.
73. McCormick, D. T., Fordham, Z. W., Smith, J., McMullan, P. J., Thames, S. F., and Guymon, C. A. (2003) Polymer molecular weight and chain transfer during the photopolymerization of an aliphatic monoacrylate in a smectic liquid crystal, *Polymer 44*, 2751-2759.
74. Cramer, N. B., Scott, J. P., and Bowman, C. N. (2002) Photopolymerizations of thiol-ene polymers without photoinitiators, *Macromolecules 35*, 5361-5365.
75. Mishra, M. K. Y. Y. M. M. K. (2009) *Handbook of vinyl polymers : radical polymerization, process, and technology*, CRC Press/Taylor & Francis, Boca Raton.
76. GmbH, P. E. (2009) Methyl Methacrylate Casting & Embedding Kit, *Polysciences Europe GmbH Catalog Number 23679*, 1 of 4.
77. Yang, B., Jaber, R., and Edler, K. J. (2012) Silica-surfactant-polyelectrolyte film formation: Evolution in the subphase, *Langmuir 28*, 8337-8347.
78. O'Driscoll, D., Fernandez-Martin, C., Wilson , D., Knott, J., Roser, J., and Edler, J. (2007) Macroscopic, mesostructured cationic surfactant/neutral polymer films: structure and cross-linking, *Langmuir 23*, 4589-4598.
79. Edler, K. J., Goldar, A., Brennan, T., and Roser, S. J. (2003) Spontaneous free-standing nanostructured film growth in polyelectrolyte-surfactant systems, *Chemical Communications 9*, 1724-1725.
80. Dreja, M., and Tieke, B. (1998) Polymerization of styrene in ternary microemulsion using cationic gemini surfactants, *Langmuir 14*, 800-807.
81. Rao, J. P., and Geckeler, K. E. (2011) Polymer nanoparticles: Preparation techniques and size-control parameters, *Progress in Polymer Science 36*, 887-913.
82. Davey, T. W., Ducker, W. A., Hayman, A. R., and Simpson, J. (1998) Krafft temperature depression in quaternary ammonium bromide surfactants, *Langmuir 14*, 3210-3213.
83. Rosen, M. J. (1978) *Surfactants and interfacial phenomena*, Wiley, New York.
84. Coursan, M., Desvergne, J. P., and Deffieux, A. (1996) Reversible photodimerisation of ω-anthrylpolystyrenes, *Macromolecular Chemistry and Physics 197*, 1599-1608.
85. Kaniappan, K., and Latha, S. (2011) Certain investigations on the formulation and characterization of polystyrene/poly(methyl methacrylate) blends, *International Journal of ChemTech Research 3*, 708-715.
86. Horntvedt, H. T., and Klaeboe, P. (1975) Conformational spectroscopic studies of cyano- and isocyanatocyclohexane, *Acta Chem. Scand., Ser. A A29*, 528-536.

87. Pretorius, N. O., Rode, K., Simpson, J. M., and Pasch, H. Analysis of complex phthalic acid based polyesters by the combination of size exclusion chromatography and matrix-assisted laser desorption/ionization mass spectrometry, *Anal. Chim. Acta*.
88. Lopez, R. G., Trevino, M. E., Peralta, R. D., Cesteros, L. C., Katime, I., Flores, J., Mendizabal, E., and Puig, J. E. (2000) A Kinetic Description of the Free Radical Polymerization of Vinyl Acetate in Cationic Microemulsions, *Macromolecules 33*, 2848-2854.
89. Lynch, M., and Spicer, P. T. (2005) Bicontinuous liquid crystals, Taylor & Francis, Boca Raton.
90. Holmberg, K., Shah, O., and J., S. (2002) Handbook of applied surface and colloid chemistry, Wiley, Chichester, England; New York.

6. PAN-Pyrene Micelle Based Sensors for Metal Ions

Fluorescent sensors for metal cations are mainly based on multi-component molecules containing a fluorophore and a receptor covalently linked by a spacer [*1, 2*]. Recently synthesis of macromolecules consisting of a fluorophore/receptor a pair conjugated by a spacer have been proposed as new fluorescent sensors due to their high selectivity and sensitivity for the detection of metal cations [*3-5*]. However synthesis of these molecules is not easy and can be very expensive. In this chapter a method is demonstrated to combine these two parts (fluorescence and chelating molecules) in a simple way, by encapsulating the fluorescence part (pyrene) and chelating agent molecules (PAN) inside cationic surfactant micelles films [*6, 7*]. This method takes advantage of self-assembly and our robust polymer/surfactant films to encapsulate these fluorescence and chelating agent molecules inside the micelles where they can work together as a nanosensor. The solid nanostructured polyelectrolyte films formed through self-assembly at the air solution interface, discovered by Edler group can be promising hosts for many applications [*8*]. In the previous chapters it was successfully shown, using neutron reflectivity and small angle scattering, that hydrophobic molecules can be encapsulated within these surfactant/polyelectrolyte films, inside the micelles, so here this is used to prepare a metal ion sensor.

The species 1-(2-Pyridylazo)-2-naphthol (PAN) is a multipurpose organic chromogenic reagent that forms complexes with a numerous of transition metals in a wide range of pH and with different adsorbents. There are several reports of research that has used PAN-modified solid supports in the preconcentration of metal ions [*9-19*]. Also the good advantage of PAN is the absence of its affinity for alkali and alkaline earth metal ions [*6, 7, 20*]. PAN shows pH dependent behaviour but works best at high pH, so is compatible with the PEI-quaternary ammonium surfactant film-forming system. When used in combination with pyrene in micellar systems the fluorescence response of pyrene is modified in a quantitative manner in the presence of the chelator, and when it is bound to metal ions [*6*]. The response can thus be calibrated and used as a fluorescence sensor. Therefore it should be possible to develop micelle based metal-ion sensors using the PAN/pyrene system by incorporating these hydrophobic species, solubilized in micelles into the polyethyleneimine (PEI) films. Such films could be used

in dip stick testing, to provide a simple and sensitive method of monitoring metal ion content in aqueous samples. Figure 6.1 shows schematic of PAN/pyrene system incorporating in cationic surfactant micelles as metal-ion florescent sensor.

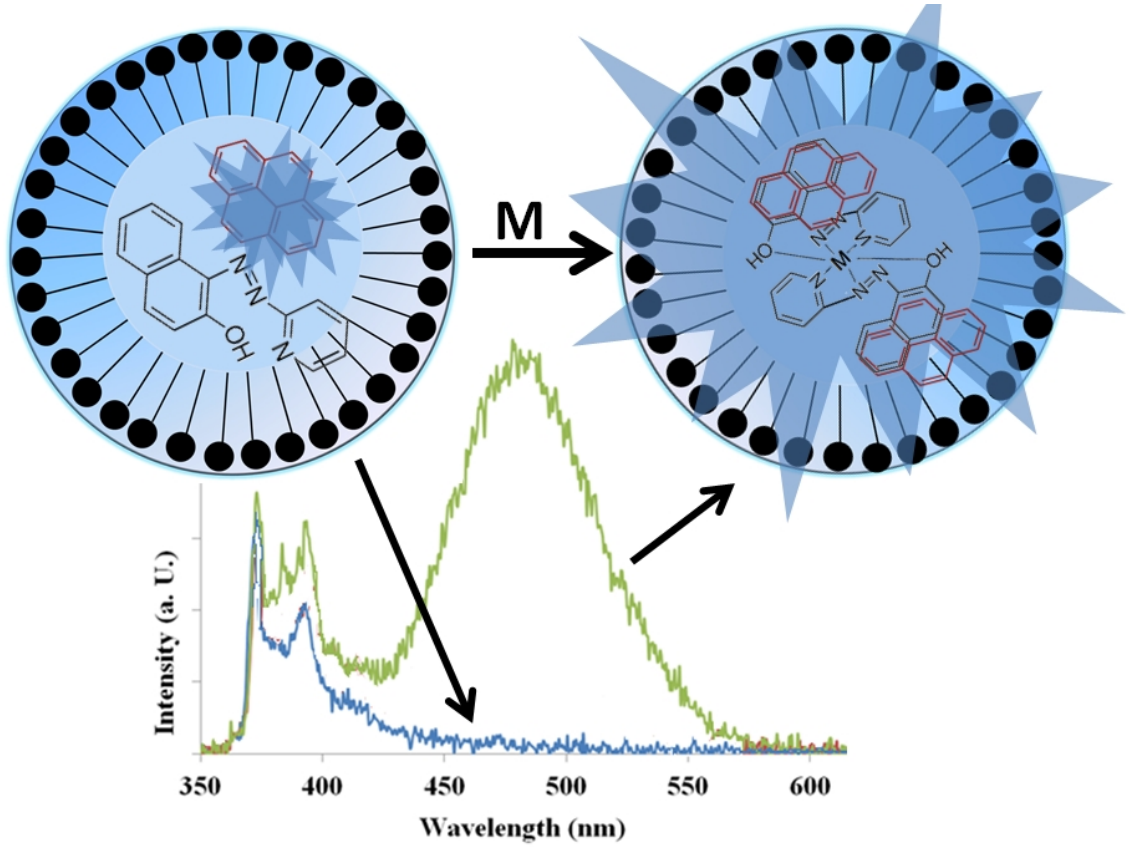

Figure 6.1: Schematic of metal-ion florescent sensor as PAN/pyrene system incorporating in cationic surfactant micelles. M is a metal ion.

6.1 Study of PAN and Pyrene Encapsulation in Micelles Using SANS

This section concentrates on studying incorporation of PAN and pyrene into surfactant-polymer film forming solutions. This by using contrast variation and small angle scattering to quantify the amount of pyrene present in the micelles, and to investigate how the micelle structure is affected by introducing PAN and pyrene into the surfactant micelles. From the previous chapters, studying styrene in PEI/surfactant systems, and other initial work on encapsulation of decane, cyclohexane and benzene in the same system [*21*]. It was suggested that hydrophobic molecules were successfully solubilized in cationic surfactant micelles, and that aromatic headgroups surfactants with a relatively long hydrocarbon tail. Consequently, improved mesostructures compared with those in films formed from surfactants with an aliphatic headgroup. Therefore this work focused on cationic surfactants with aromatic headgroup to encapsulate aromatic species such as pyrene and PAN in the surfactant micelles. Preliminary work on PEI/surfactant films containing PAN/pyrene showed that solid films formed at the air/solution interface in the presence of these species. However better structure was found for SPEI films compared with LPEI, which is opposite to the results found for the surfactant/PEI/styrene systems. Therefore low molecular weight ~2000Da was used at a concentration of 15g/L in these solution scattering experiments. A range of surfactants with aromatic headgroups were used in this experiment, covering C_{12},C_{14} and C_{16} hydrocarbon chain lengths, to study the chain-length effects on the solubilisation and the micelle geometry. Consequently dodecylpyridinium bromide (DPBr), tetradecylpyridinium bromide (TPBr), cetylpyridinium bromide (CPBr), benzyldimethyldodecylammonium bromide (BDDAB), benzyldimethyltetradecylammonium bromide (BDTAB) and benzyldimethylhexadecylammonium bromide (BDHAB) were synthesised as reported in Chapter 3 and used to solubilize PAN and pyrene. In addition tail deuterated benzyldimethylalkylammonium bromide and fully deuterated (tail and headgroup) cetylpyridinium bromide were synthesised and used for contrast experiments. All surfactant solutions were prepared at a concentration of 0.05M in 100% D_2O or 70% D_2O solution and the structures characterised in the presence and absence of PAN where final concentration of PAN was 1mM or 2mM. Fully deuterated and hydrogenated pyrene was used at concentration of 2mM or 4mM. All solutions were tested at 35ºC to avoid any surfactant crystallization.

The SANS experiments were performed on the LOQ instruments at the ISIS Rutherford Appleton Laboratories, Chilton, England. SANS patterns from micelles containing hydrogenated and deuterated additives were fitted simultaneously using the NIST SANS Analysis package within Igor PRO program (WaveMetrics) [*22*]. A uniform ellipsoid form factor with a Hayter-Penfold structure factor [*23*] for charged spheres used to fit the data, since this model gave the best fit, compared to other trialled models, based on the results giving the lowest χ^2. The temperature was fixed at 308 K, dielectric constant held at 78 and salt concentration was held at zero in this model. The variables fitted were the volume fraction, micelle radii, SLD ellipsoid contrast (between the centre of the micelle containing both surfactant tails and additives, and the solvent), micellar charge and incoherent background. The amounts of encapsulated additives and aggregation numbers of surfactant monomer (N_{agg}) were calculated based on the micelle radii and literature values for the volumes of the surfactant molecules. The molecular volume of pyrene (264 Å^3) and PAN (334 Å^3) was calculated as stated in chapter 4 [*24*]. N_{agg} of micelles [*21, 25*] were calculated in the same way as in Chapter 3. An alternative method was also used to calculate the aggregation number by evaluating the ratio of the total ellipsoid micelle area to the surfactant headgroup surface area (a_0) [*26, 27*]. The first method, using the ratio between the micelle volume and surfactant volume, could be accurate for the surfactant micelles without any additives but it is not necessarily true in the case of micelles solubilizing hydrophobic molecules. This because the total volume of the micelle encapsulating hydrophobic molecules is the sum of the volume of aggregated surfactant monomer plus the volume of these solubilized additives. Therefore the volume of micelles solubilized additives is measured as the same as the surfactant molecule volume, while calculating N_{agg} using the micelle surface area method neglects the contribution of encapsulated molecules to the overall volume. The approximate ellipsoid surface area was calculated by the following equation:

$$S \approx 4\pi \left(\frac{2(a^p b^p) + (b^p)^2}{3} \right)$$

where a and b are the micelle radii, $p \approx 1.6075$ which yields a relative error of at most 1.061% [*26, 27*].

6.1.1 Encapsulation of PAN and Pyrene

Figure 6.2 shows the simultaneous fitting of SANS data using the uniform ellipsoid with structure factor model for surfactants with C_{12}, C_{14} and C_{16} hydrocarbon chains containing 4mM of hydrogenated or deuterated pyrene. O'Driscoll [*21*] and Wasbrough [*28*] also found that the uniform ellipsoid model was the most appropriate model to fit cationic surfactant solutions solubilizing different species of additives in the presence and absence of PEI. Although scattering patterns for BDHAB micelles show the presence of long prolate ellipsoid (rod-like) micelles nevertheless the ellipsoid model was still much more suitable to fit these data than a cylinder with structure factor model, based on the relative χ^2 values.

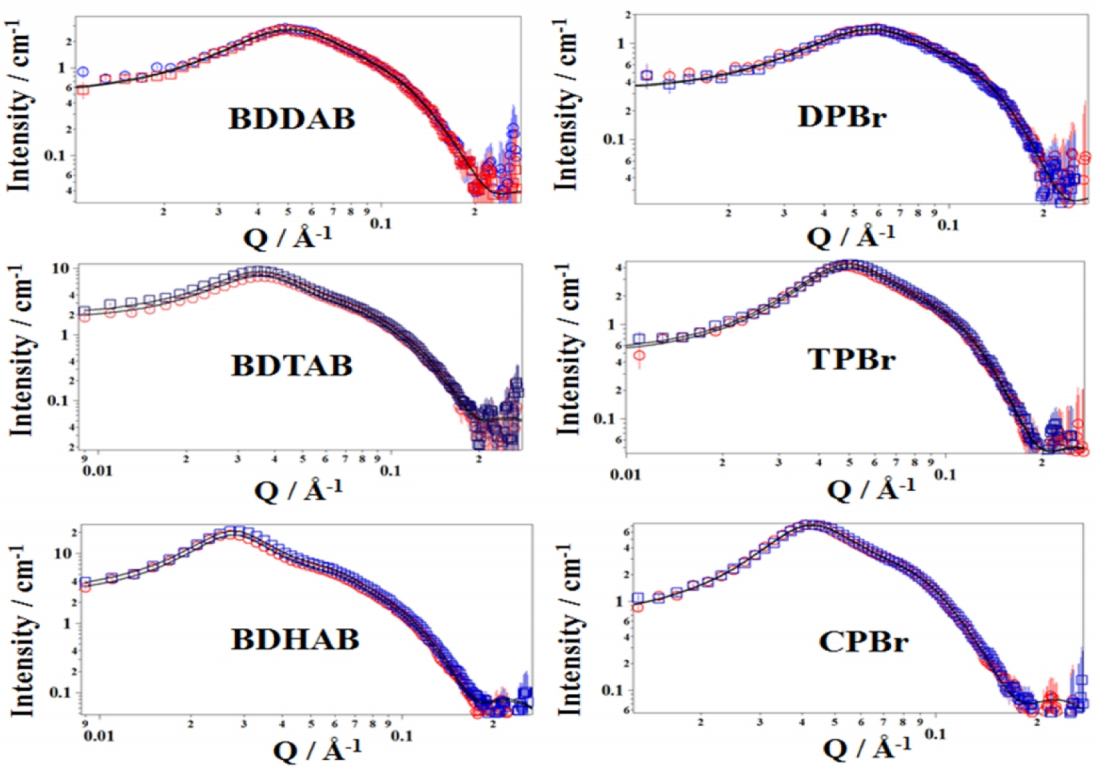

Figure 6.2: SANS data for surfactants with C_{12}, C_{14} and C_{16} hydrocarbon chains in D_2O solution solubilizing 4mM of hydrogenated pyrene (circles) and deuterated pyrene (squares). The solid lines are simultaneous fits to the data using the uniform ellipsoid with structure factor model.

Figure 6.2 shows clearly the variation of the SANS profiles curvature as the surfactant hydrocarbon chain length is increased. This suggests that shape and size of these surfactant micelles are highly dependent on the surfactant tail length as expected. However the total micellar widths and lengths for C_{12}, C_{14} and C_{16} of C_nTAB

surfactants found by O'Driscoll [*29*] were bigger than alkyl pyridinium and benzyldimethyl bromide surfactants, which indicates that aggregation number for these aliphatic surfactant headgroup (C_nTAB) are greater than aromatic surfactant were used in this experiment. Table 6.1 shows the micelle major and minor radii R_a and R_b from the modelled SANS parameters.

Table 6.1: Micelle radii (R_a and R_b), volume of micelle ellipsoid, numbers of encapsulated additives and aggregation numbers (N_{agg}).

Additives	*Surfactant*	R_a (Å)	R_b (Å)	*Vol. of Ellip. (Å^3)*	*Number of Encap. additive molecules*	N_{agg}
No Additives	BDDAB	31	18	43122	0	70
	BDTAB	49	20	82138	0	124
	BDHAB	75	22	153726	0	215
	DPBr	21	18	27836	0	58
	TPBr	31	19	47599	0	90
	CPBr	36	22	75503	0	131
2 *mM* Pyrene	BDDAB	36	18	49027	22	80
	BDTAB	60	20	100370	69	151
	BDHAB	134	23	291799	523	408
	DPBr	23	18	32541	18	68
	TPBr	31	20	54703	27	104
	CPBr	39	23	85709	39	148
4 *mM* Pyrene	BDDAB	36	18	47907	18	78
	BDTAB	67	21	119075	140	179
	BDHAB	143	23	325357	650	454
	DPBr	25	17	30391	10	64
	TPBr	33	21	58496	41	111
	CPBr	41	23	92822	66	161
1 *mM* PAN	BDDAB	31	18	43367	1	71
	BDTAB	51	20	86976	14	131
	BDHAB	126	23	277176	370	387
	DPBr	23	18	29447	5	62
	TPBr	31	20	50313	8	95
	CPBr	37	23	80634	15	140

The errors in micelle radii are ±2 Å, so the errors in the ellipsoid volume, number of encapsulated additives and N_{agg} were ±5% of the measured value.

The SANS data fits for these cationic surfactants solution in the presence and absence of additives shows that the micelles have a prolate ellipsoid shape. The micelles ellipsoid volume of these surfactants illustrate huge differences resulting from the changes in alkyl tail length, for instance in the case of alkyl-benzyldimethyl micelles without additives the micelle volume for the surfactant with a C_{16} hydrocarbon chain was 3.6 times bigger than the equivalent C_{12} surfactant, while in the presence of pyrene the micelles volume was 6.4 times bigger. The volume variation in the case of alkyl-pyridinium was less than that observed for the benzyldimethyl surfactants. In this case the average volume variation between C_{16}/C_{12} was 2.8 times (Table 6.1). This result indicates that both the surfactant hydrocarbon chain and surfactant headgroup play important roles in determining the micelle size and shape [*30*], and thus also the aggregation number (N_{agg}). Figure 6.3 illustrates the correlation between these cationic surfactants headgroup and their tail length with the micelle aggregation number.

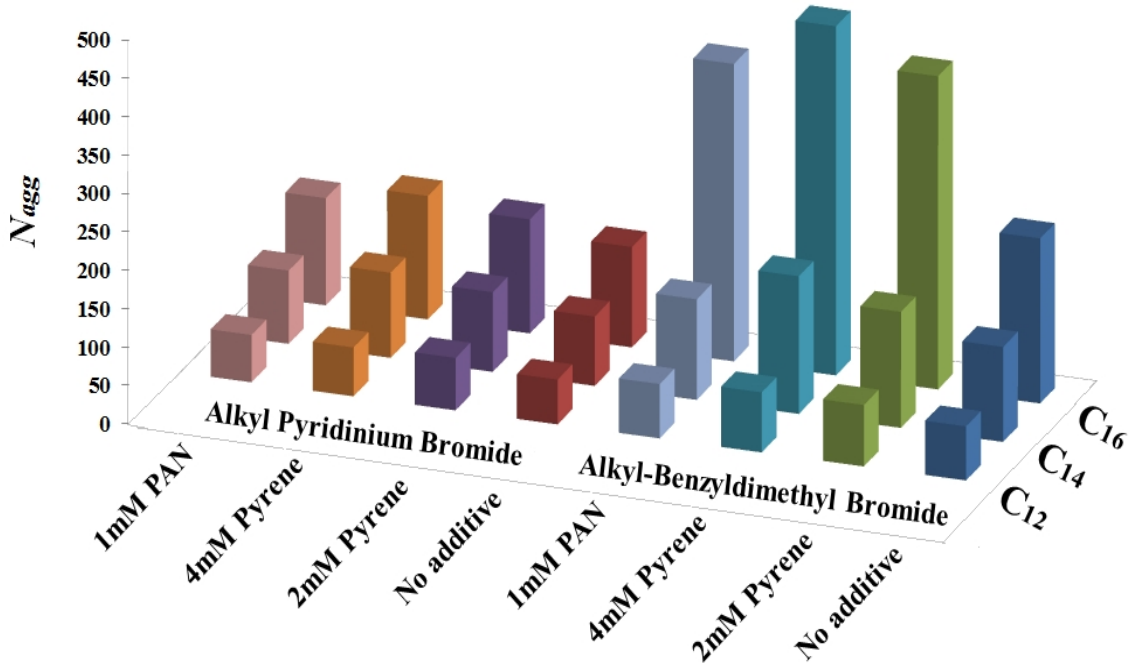

Figure 6.3: The aggregation number (N_{agg}) of 0.05M alkyl-benzyldimethyl bromide and alkyl-pyridinium bromide micelles solubilizing different amounts of PAN and pyrene. The errors in N_{agg} were ±5% of the measured value.

Figure 6.3 clearly shows that the aggregation number of surfactant molecules increases significantly as the surfactant hydrocarbon chain length is increased. However BDHAB

illustrated an extraordinary increase of N_{agg} compared with other surfactants, particularly when these micelles were used to solubilize PAN and pyrene. In general alkyl-benzyldimethyl bromide surfactants tend to form to form relatively bigger micelles compared with alkyl-pyridinium bromide surfactants. Mata *et al.* reported the aggregation number of DPBr, TPBr and CPBr at 30ºC in pure surfactant solution [*31*] where N_{agg} were 56, 81 and 111, respectively, which are close to the values found in this work for alkyl-pyridinium bromide micelles without additives. Malliaris *et al* studied the aggregation number of several cationic surfactants at a wide range of amphiphile concentrations up to 1 M [*32*]. The surfactants were alkylammonium chlorides with aliphatic chain length (n = 12, 14, 16). The author found that at low concentration, close to the critical micelle concentration the micelle shape was spherical while, as the concentration increased toward 1 M, the aggregation number increased linearly. However the surfactant micelles with a chloride counterion tend to stay spherical and smaller (at higher surfactant concentrations) than bromide micelles since Br^- binds to the surfactant headgroups neutralising them while chloride does not, therefore the aggregation number of bromide surfactants in micelles is larger as there is less charge repulsion [*33-35*]. Although some physical parameters such as concentration, temperature and pressure also affect the micellization process, nevertheless the nature of the surfactant molecules is the main factor controlling the size and micelle morphology [*25, 36, 37*]. Several authors reported growth in micelle size as the surfactant hydrocarbon chain is elongated [*38-40*]. However the bulkiness of the hydrophilic headgroup in amphiphilic molecules has complicated effects on aggregation performance, due to the interfacial free energy of the micelle which is affected by electrostatic and steric hindrance interactions between adjacent headgroups [*41, 42*]. It is well known that the packing parameter (p) decreases as the surfactant headgroup size is increased, based on the Israelachvili equation [$p = V/(al)$], where V is the volume of the hydrophobic chain, a, the headgroup area and l the average alkyl tail length [*43*]. Shrinkage in micelle size as the surfactant headgroups area increased was reported in several experiments [*42, 44, 45*]. However here in this experiment as shown in Figure 6.2, the alkyl-benzyldimethyl bromide surfactant with a relatively bulky surfactant headgroup demonstrated bigger micelles aggregation number compared with alkyl-pyridinum bromide surfactants. Zhang *et al*, pointed out two possible reasons behind why benzyldimethyl surfactants have this different behaviour [*46*]. Benzyldimethyl as a headgroup (apart from the alkyl tail) consists of three parts, which are the benzyl group

and two methyl groups where all of these three parts are conjugated at the nitrogen atom. The benzyl segment is relatively large, and the bond with the N is flexible, so due to their hydrophobicity, this part can potentially act as a second hydrocarbon tail which bends around to enter the micelle. In this case, the total volume of hydrocarbon chain expands, subsequently increasing the packing parameter. In addition, the asymmetry of the two hydrophobic chains in these molecules gives extra space to bend and rotate with higher conformational freedom for the main hydrocarbon tail, consequently reducing the total free energy of micellization. The second possibility related to the overall hydrophobicity of the micelle shell. The bulkiness of the benzyl group partially shields penetration of the water molecules and counterion into the surfactant micelle shell. Generally such behaviour increases the hydrophobicity of the micelle shell which subsequently leads to increase the micelle aggregation number. In general, micellar geometry and their size result from the balance of physical and thermodynamic interactions of the headgroups with themselves and with solvent/counterions, and the hydrophobic interactions of hydrocarbon chains in the micellar core [*41, 47-51*]. Encapsulation of hydrophobic molecules in the micellar core is one of the physical properties which influence this sensitive interaction between micellar components. Figure 6.4 shows a relationship between the capacity of the micelle to encapsulate hydrophobic molecules in cationic surfactants with different hydrocarbon tails and headgroups size.

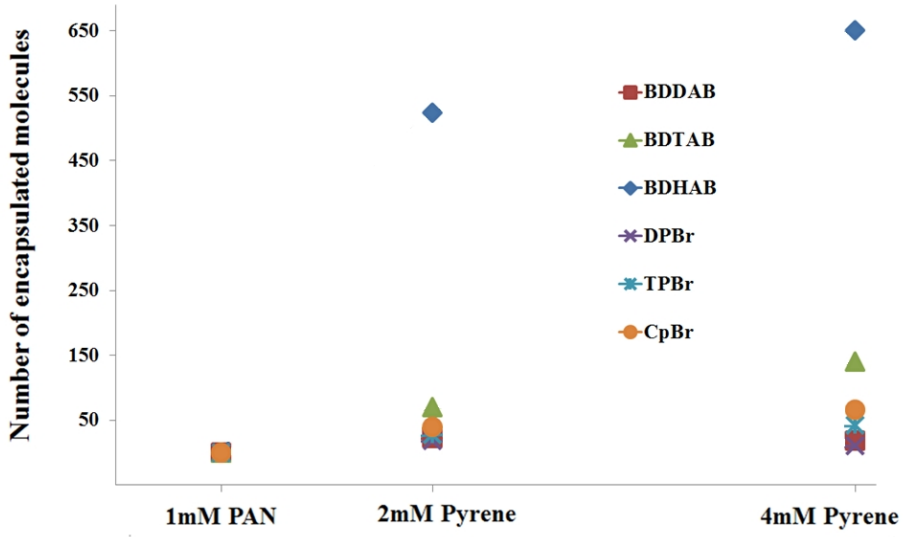

Figure 6.4: Calculated number of encapsulated hydrophobic molecules in cationic surfactant micelle solutions. The errors are ±5% of the measured value.

In general surfactants with C_{12} tails showed the lowest pyrene encapsulation capacity, while the long hydrocarbon chain enhanced solubilisation these hydrophobic molecules. However benzyldimethyl surfactants with C_{14} hydrocarbon chain had a higher pyrene encapsulation capacity compared with CPBr which has a C_{16} hydrocarbon tail. This result suggesting that encapsulation ability of these surfactant micelles varies, where the combination of properties of surfactant headgroup and their chain length both can affect the encapsulation capacity.

By doubling the concentration of pyrene, the micelle volume and number of encapsulated hydrophobic molecules increase. However this increase is not linear with the amount of pyrene added. Therefore it seems that encapsulation within the micelles depends on several factors, other than just surfactant structure, including ionic strength, temperature, and the nature and bulk of the solute [*52, 53*]. In general encapsulating these hydrophobic molecules in both alkyl-benzyldimethyl and alkyl-pyridinium bromide surfactant micelles transforms the micelles from long prolate to rod-like shape. O'Driscoll et al. also reported changes in micellar shape when solubilising *n*-decane, cyclohexane and cyclohexanol molecules within cationic surfactant solutions. He found that cyclohexane and decane consistently swelled the micelles leading to larger, spherical shapes, while cyclohexanol caused elongation of the prolate micelles along their long axis.

Encapsulation of PAN and pyrene was also studied here for these surfactants in the presence of SPEI. The data were fitted by the same model as above. Table 6.2 shows the micelle radii (R_a and R_b) resulting from fitting these data. The number of encapsulated molecules and surfactant aggregation numbers were calculated based on fitted data using the same two ways to calculate N_{agg} *as* described earlier.

In general, N_{agg} values calculated by the micelle surface area method give a higher aggregation number than those values which were calculated by micelle volume (Table 6.2). This is related to the difference between additive and surfactants volumes, where volumes of PAN or pyrene are less than of those of the cationic surfactants that were used in this experiment.

Table 6.2: Micelle radii (R_a and R_b), numbers of encapsulated additives and aggregation numbers (N_{agg}) for solutions containing both PAN and pyrene.

Additives	***Surfactant***	***R_a (Å)***	***R_b (Å)***	***Encap. additive***	***N_{agg} calc. by surface area***	***N_{agg} calc. by volume***
2mM Pyrene 1mM PAN	BDDAB	38	18	27	101	83
	BDTAB	65	20	98	188	166
	BDHAB	144	23	579	463	447
	DPBr	20	20	18	96	69
	TPBr	33	20	32	142	108
	CPBr	40	23	51	196	156
2mM Pyrene 1mM PAN 1.5% SPEI	BDDAB	40	17	10	98	75
	BDTAB	93	20	234	257	225
	BDHAB	149	23	563	468	441
	DPBr	20	20	20	97	70
	TPBr	30	21	25	137	104
	CPBr	40	23	50	196	155

The errors in micelle radii are ±2 Å, the errors of number of encapsulated additive molecules and N_{agg} (calculated by volume) were ±5% of the measured value and ±7% of N_{agg} (calculated by surface area).

The differences in N_{agg} for these surfactants, calculated by the two methods, display growth in BDDAB micelles by about 21 surfactant monomers, 27 for BDTAB and 22 for BDHAB solubilizing of both PAN and pyrene, whereas in the case of DPBr, TPBr and CPBr the differences in N_{agg} was 27, 34 and 41 surfactant molecules respectively. These differences were very close in both the cases of solubilizing a single additive or in the case of solubilizing PAN with a pyrene companion. Overall encapsulating mixtures of PAN and pyrene results in bigger micelle volumes and larger aggregation numbers compared with solubilizing 2mM pyrene or 1mM PAN as a single additive. Micelles containing pyrene at the concentration of 4mM showed variable N_{agg} values compared with those encapsulating a mixture of PAN and pyrene.

In general addition of SPEI to these surfactant solutions solubilising a mixture of PAN and pyrene does not show significant changes in N_{agg} of these surfactant micelles; except for BDTAB/SPEI which exhibited a slight growth in N_{agg} after addition of SPEI. As stated before BDHAB shows an extraordinary growth in N_{agg} compared with other surfactants which is related to the benzyl group performing as second tail [*46*]. This

phenomenon was however, not seen for BDTAB or BDDAB. It is possible that in the case of BDTAB/SPEI solubilising aromatic molecules, through the interaction between PEI and the nitrogen atom in the surfactant headgroups and the hydrophobicity of benzyl group improve the ability of the benzyl group to conjugate with encapsulated aromatic molecules. This thus increases the stability of BDTAB headgroups by forming π-cation bonds between the benzyl group and encapsulated PAN and pyrene [*21, 54*]. However it seems this process is balanced with surfactant tail length since BDDAB does not show this behaviour with SPEI.

6.1.2 Incorporation of Metal Ions into Surfactant/PAN/pyrene Micelle Systems.

Following the experiments on PAN/pyrene incorporation into cationic micelles, metal ions were added to the solutions. The purpose of these experiments was to determine changes in micelle shape and interactions with the polymer due to PAN binding metal ions, which will affect the structure and interactions of these species in the films and the sensor behaviour. Three different oxidation states metals Cu^{+}, Cu^{2+} and Fe^{3+} as metal chloride were added to the surfactant/PAN/pyrene solutions at two concentrations, 1 and 2 mM, in the presence and absence of SPEI. The micelle radii and aggregation numbers were calculated based on fitted data (Table 6.3). In general addition of metal ions was found to elongate the prolate micelles along their long axis but the effects of these three ions with different charge vary. Figure 6.5 shows the individual effect of these metal ions on the BDHAB/PAN/pyrene micelle aggregation number.

The first indication from Figure 6.5 is that pyrene concentration still has the most dominant effect on the aggregation behaviour of BDHAB, while adding PAN shows less effect. On the other hand addition of the Fe^{3+} ferric ion to the BDHAB/PAN/pyrene solutions in the absence of PEI has the largest effect on the aggregation number of all the ions trialled. At low concentrations of pyrene and a 1:1 molar ratio of PAN and to metal ion, addition of Cu^{+} has the lowest effect on N_{agg} while Cu^{2+} and Fe^{3+} give almost the same micelle size.

Table 6.4: Micelle radii (R_a and R_b) and aggregation numbers (N_{agg}) calculated by micelle volumes and micelle surface areas (S.A).

Surfactant 0.05M	***Additives***	***Metals added***		***R_a (Å)***	***R_b (Å)***	***N_{agg} By Vol.***	***N_{agg} By S.A***
BHHAB	2mM Pyrene 1mM PAN	1 mM	Fe^{3+}	149	23	463	479
			Cu^{+}	148	23	463	477
			Cu^{2+}	132	23	422	433
CPBr		1 mM	Fe^{3+}	43	23	166	207
			Cu^{+}	42	23	164	204
			Cu^{2+}	42	24	168	207
BHHAB	2mM Pyrene 2mM PAN	2 mM	Fe^{3+}	161	23	510	522
			Cu^{+}	151	23	451	476
			Cu^{2+}	150	23	464	481
CPBr		2 mM	Fe^{3+}	46	23	175	218
			Cu^{+}	43	23	167	208
			Cu^{2+}	37	24	153	190
BHHAB	4 mM Pyrene 1 mM PAN	1 mM	Fe^{3+}	177	23	566	576
			Cu^{+}	156	23	486	502
			Cu^{2+}	163	23	505	523
CPBr		1 mM	Fe^{3+}	55	22	196	245
			Cu^{+}	52	23	193	239
			Cu^{2+}	50	24	202	241
BHHAB	4 mM Pyrene 2 mM PAN	2 mM	Fe^{3+}	179	23	570	580
			Cu^{+}	176	23	551	566
			Cu^{2+}	176	23	559	571
CPBr		2 mM	Fe^{3+}	50	23	198	239
			Cu^{+}	50	23	197	238
			Cu^{2+}	52	23	203	245
BHHAB SPEI	2mM Pyrene 1mM PAN	1 mM	Fe^{3+}	191	22	547	587
			Cu^{+}	191	22	552	589
			Cu^{2+}	190	22	551	588
CPBr SPEI		1 mM	Fe^{3+}	50	22	182	228
			Cu^{+}	52	23	189	235
			Cu^{2+}	50	23	184	230
BHHAB SPEI	2mM Pyrene 2mM PAN	2 mM	Fe^{3+}	188	22	547	583
			Cu^{+}	185	22	538	573
			Cu^{2+}	184	22	537	571
CPBr SPEI		2 mM	Fe^{3+}	52	23	191	236

The errors in micelle radii are ±2 Å where the error of N_{agg} (calculated by volume) was ±5% of the measured value and ±7% of N_{agg} (calculated by surface area).

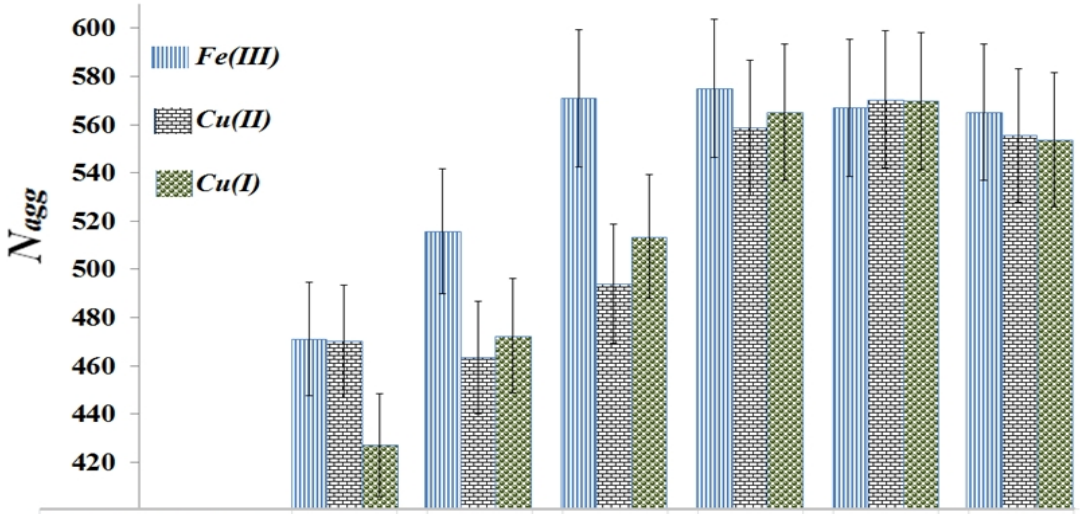

Pyrene Conc. (mM)	2	2	4	4	2	2
PAN Conc. (mM)	1	2	1	2	1	2
Metals Conc. (mM)	1	2	1	2	1	2
SPEI $\%_{w/v}$	0	0	0	0	1.5	1.5

Figure 6.5: Average aggregation numbers of BDHAB/PAN/pyrene micelles in the presence of different metal ions and SPEI.

When PEI is present using a 2:1:1 molar ratio of pyrene, PAN and metal ions respectively the micelles size almost doubles compared with the same mixture but without the polyelectrolyte. On the other hand no obvious change was seen of N_{agg} in the case of presence of PEI and metal ions. Nevertheless increasing the amount of the PAN and pyrene in this system reduces the overall micelle size. These results are particularly seen in the case of BDHAB micelles, however in the case of CPBr micelles a different behaviour in observed. Figure 6.6 shows the effect of the same metal ions on the CPBr/PAN/pyrene micelle aggregation numbers.

For the CPBr micelles, addition of PAN and pyrene showed the same effects as for BDHAB micelles overall, whereas the effects of metal ions addition is different. At low concentrations of pyrene and 1:1 molar ratios of PAN to metal ions, micelles in the presence of Cu^{2+} shows the lowest N_{agg} while those with Cu^{+} and Fe^{3+} have almost the same micelle size. However at 2:2:2 molar ratio, micelles in the presence of Fe^{3+} demonstrate the highest, while those with Cu^{+} exhibit the lowest $N_{agg.}$ At a high concentration of pyrene and 2:2 molar ratios of PAN and metal ions, Cu^{2+} containing solutions had the lowest micelle size but the micelles were still bigger than at low pyrene concentrations. When PEI was present, micelles in solutions containing Cu^{+} and Fe^{3+} showed almost the same micelle size while micelles in the presence of Cu^{+} had the highest N_{agg}.

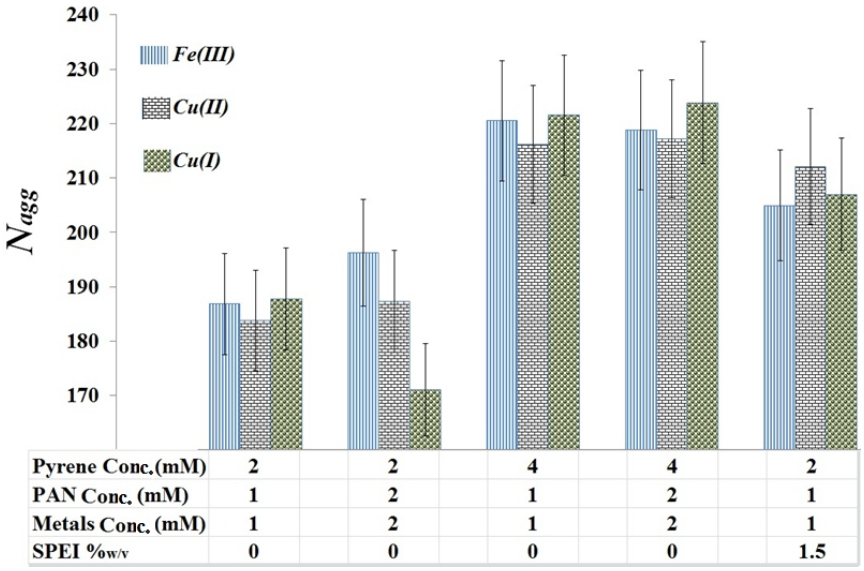

Figure 6.6: Average aggregation number of CPBr/PAN/pyrene micelles in the presence of different metal ions and SPEI.

From the data in Figures 6.3 and 6.4, it is apparent that there is a strong relationship between the metal ions used (Cu^{+}, Cu^{2+} and Fe^{3+}) and the micellar growth. There are two possibilities for the mechanism of influence of metal ions on the micellar aggregates. The first possibility relates to the effects of these metals ions as counterions. Several studies have highlighted the effects of surface electrostatic interactions on the aqueous micellar solutions [*55-57*]. Many of these studies demonstrated that addition of salt to a micellar solution of an oppositely charged surfactant enhances growth of the spherical micelles into long anisotropic aggregates. The main reason of this performance is related to the effect of the counterion, reducing the effective head group area of the surfactant molecules by neutralizing the charge on the micellar surface which increases the packing parameter. Enhanced screening of the repulsions between the charged head groups of the surfactant favours aggregation [*58-60*]. The surface electrostatic forces have a strong effect on the equilibrium size and shape of the micellar aggregates. Overall altering the charge on the head group and the counterion of the surfactant molecule changes the interfacial forces and the system properties. Here in this study different amounts of chloride counterion were added during the addition of Cu^{+}, Cu^{2+} and Fe^{3+} however although metal ion and chloride ratio are varied for these metal compounds, nevertheless no obvious trend were found for the N_{agg} of these cationic surfactant micelles with the concentration of chloride ions that were added.

The second possibility is related to the PAN/Metal interaction. Some authors reported changes in size and shape of the PAN molecule occurring during PAN-metal complex

formation [*61-63*]. PAN is a well-known ligand that can react with numerous metal ions, forming coloured chelate complexes. Generally there are two established PAN/Metal molar ratio complexes interactions. The first structure is observed for PAN/Metal ratios of 1:1. At this ratio the complex has the tetradentate ligand coordinating with the metal through the hydroxyl oxygen atom, the pyridine nitrogen atom, and one of the azo-group nitrogen atoms [*64*]. The second structure is found at a 2:1 PAN/Metal ratio, where the complex with the metal ion is coordinating to the ligand through two perpendicularly planar ligands [*63*] (Figure 6.7). On the other hand it has been suggested that when chelation forms between PAN and a metal ion like Fe^{3+}, two five-membered chelate rings are formed [*65*]. The heterocyclic nitrogen, the hydroxy-group and the nitrogen atom farthest from the pyridine ring are involved in the chelate formation. Szabó *et al.* found that the PAN molecule can take on different conformations, depending on the values of the dihedral angles [*61*]. Safari et al [*66*] reported a 2:1 molar ratio stoichiometry of PAN/Metal complexes for Co^{2+}, Ni^{2+} and Zn^{2+} ions in different solvent solutions.

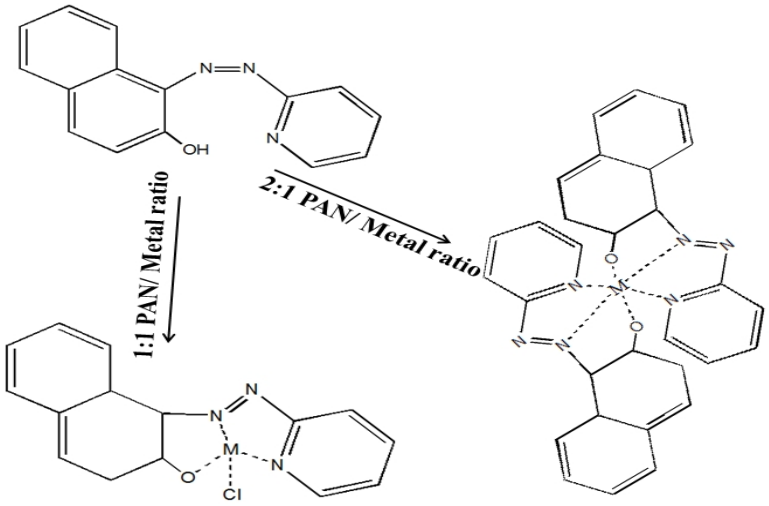

Figure 6.7: The optimized structure of 1:1 and 2:1 molar ratios of PAN/Metal complex interactions, where M is a metal ion.

The geometry of PAN/Metal complex structures and bonds lengths are reported in several published papers [*61, 63, 64, 67, 68*]. These papers showed overall that the size and structure of PAN/Metal complex compounds certainly are dissimilar to that of just the PAN molecule itself. That means that in general the new geometry and size of PAN after addition of metal ions is the most likely the main reason behind the variation in micelles volume of these cationic surfactants used in this experiment.

6.1.3 SANS Study Using Contrast Variation to Study Surfactant Micelles Solubilising Pyrene

The effects of PAN and pyrene encapsulation in the quaternary ammonium bromide surfactant micelles have been discussed above. In this section, by using contrast variation the aim was to find the relative locations of the pyrene and PAN in the micelles. This information could assist interpretation of fluorescence measurements on ion binding in this system and their performance as sensors. Therefore in this section both fully hydrogenated and tail-deuterated alkyl-benzyldimethyl bromide surfactants were synthesised and used to solubilise d_{10}-pyrene, h_{10}-pyrene and h-PAN. Fully hydrogenated, headgroup deuterated, tail deuterated and fully deuterated CPBr were also used to solubilise these additives. All of these surfactants and additives were dissolved in 100% D_2O solvent, except for tail and fully deuterated CPBr which were dissolved in 70%D_2O solution since there is no good contrast between this surfactant and 100% D_2O. Table 6.5 show the scattering length densities (SLDs) for the additives and hydrocarbon tails of these surfactants. Since the model used to fit the data was a simple uniform ellipsoid, the contribution of the surfactant headgroups to the scattering in 100% D2O has been neglected, and it was assumed that only the tail regions contributed significantly to the scattering in these fits.

Table: 6.5: Theoretical scattering length densities for all components used to fit the uniform ellipsoid model to the SANS data.

Component	**SLD ($Å^2$)**
Deuterated water D_2O	6.36×10^{-6}
70% D_2O Solution	4.29×10^{-6}
1.5% PEI in 100%D_2O	6.18×10^{-6}
1.5% PEI in 70%D_2O	4.16×10^{-6}
PEI alone (not in solution)	5.69×10^{-7}
Pyridine	1.78×10^{-6}
Pyridine-d_{10}	5.71×10^{-6}
1-(2-Pyridylazo)-2-naphthol (PAN)	2.77×10^{-6}
Hexadecyl	-3.53×10^{-7}
d_{33}-Hexadecyl	6.74×10^{-6}
Tetradecyl	-3.59×10^{-7}
d_{29}-Tetradecyl	6.66×10^{-6}
Dodecyl	-3.67×10^{-7}
d_{25}-Dodecyl	6.59×10^{-6}

Table 6.6: Micelle radii and SLDs values of the uniform ellipse resulting from fitting SANS data from alkyl-benzyldimethyl bromide surfactant with different neutron contrast solubilizing hydrogenated or deuterated pyrene and hydrogenated PAN.

Surfactant	***Additives***	***SLD (Å^2)***	***R_a (Å)***	***R_b (Å)***
BDDAB	2mM Pyrene	-3.37×10^{-7}	36	18
	2mM Pyrene-d_{10}	9.94×10^{-8}		
BDTAB	2mM Pyrene	-3.55×10^{-7}	60	20
	2mM Pyrene-d_{10}	6.82×10^{-7}		
BDHAB	2mM Pyrene	1.19×10^{-7}	134	23
	2mM Pyrene-d_{10}	1.39×10^{-6}		
d_{25}-BDDAB	2mM Pyrene	4.86×10^{-6}	34	21
	2mM Pyrene-d_{10}	5.17×10^{-6}		
d_{29}-BDTAB	2mM Pyrene	5.72×10^{-6}	60	31
	2mM Pyrene-d_{10}	5.81×10^{-6}		
d_{33}-BDHAB	2mM Pyrene	5.84×10^{-6}	132	34
	2mM Pyrene-d_{10}	5.86×10^{-6}		
BDDAB	1mM PAN and 2mM Pyrene	-3.31×10^{-7}	38	18
	1mM PAN and 2mM Pyrene-d_{10}	1.32×10^{-7}		
BDTAB	1mM PAN and 2mM Pyrene	-3.50×10^{-7}	65	20
	1mM PAN and 2mM Pyrene-d_{10}	1.99×10^{-8}		
BDHAB	1mM PAN and 2mM Pyrene	1.23×10^{-7}	144	23
	1mM PAN and 2mM Pyrene-d_{10}	1.77×10^{-6}		
d_{25}-BDDAB	1mM PAN and 2mM Pyrene-d_{10}	5.54×10^{-6}	38	26
d_{29}-BDTAB	1mM PAN and 2mM Pyrene-d_{10}	5.78×10^{-6}	65	31
d_{33}-BDHAB	1mM PAN and 2mM Pyrene-d_{10}	5.88×10^{-6}	144	34
BDDAB SPEI	1mM PAN and 2mM Pyrene	-1.57×10^{-7}	40	18
	1mM PAN and 2mM Pyrene-d_{10}	-2.75×10^{-8}		
BDTAB SPEI	1mM PAN and 2mM Pyrene	-9.28×10^{-8}	93	20
	1mM PAN and 2mM Pyrene-d_{10}	1.86×10^{-7}		
BDHAB SPEI	1mM PAN and 2mM Pyrene	-1.06×10^{-7}	149	23
	1mM PAN and 2mM Pyrene-d_{10}	1.10×10^{-6}		
d_{25}-BDDAB SPEI	1mM PAN and 2mM Pyrene-d_{10}	5.87×10^{-6}	39	26
d_{29}-BDTAB SPEI	1mM PAN and 2mM Pyrene-d_{10}	5.94×10^{-6}	91	31
d_{33}-BDHAB SPEI	1mM PAN and 2mM Pyrene-d_{10}	6.13×10^{-6}	145	34

The errors in micelle radii are ±2 Å and the error in the SLD is ±7.92 × 10^{-8}.

Several attempts were made to determine the location of these encapsulated additives in presence and absence of PEI in the micelle through the use of more complex models, such as core-shell spheres and core-shell prolate ellipses but use of these models was not justified by the data available. Therefor all of the contrast data was fitted using the uniform ellipsoid model with a structure factor as described previously. Table 6.6 shows the micelle radii and SLDs values that were obtained from fitting the different contrasts of alkyl-benzyldimethyl bromide surfactant micelles containing solubilized PAN and either hydrogenated/deuterated pyrene. Simultaneous fitting was performed in the case of hydrogenated and deuterated pyrene; however the resulting fits were poor. Subsequently it was found from many trials that the ellipsoid micelle radii of hydrogenated alkyl-benzyldimethyl surfactant are not equivalent to that of the tail-deuterated surfactant. From the data in Table 6.6, it is apparent that the lengths of R_b (minor axis) for the tail-deuterated alkyl-benzyldimethyl surfactant are in general are bigger than those of the full hydrogenated surfactant while R_a (major axis) are closer in length. Candau et al. investigated the solubilisation behaviour of 1-pentanol by hydrogenated and deuterated alkyl chain of tetradecyltrimethylammonium bromide. They reported also differences in the micelles radius and aggregation number in case of hydrogenated and deuterated alkyl chain of the same surfactant. Moreover the solubilisation coefficient of 1-pentanol by these surfactants was different [*69*]. Another possibility for the micelle size variation observed in this case could be related to impurity variation between hydrogenated and tail deuterated alkyl-benzyldimethyl arising during synthesis of these surfactants. However a similar purification procedure was followed for both deuterated and hydrogenated surfactants, also NMR, LC-MS and TLC showed high purity of these synthesised surfactants nevertheless the exact quantity of impurity in these synthesised surfactants are unknown.

In general the C_{12} and C_{14} tail regions of benzyldimethyl surfactant micelles have small SLD differences between micelles containing pyrene -d10 or pyrene- h10, while the maximum SLD difference was seen for the C_{16} micelles (1.65×10^{-6} Å^2). Figure 6.6 displays the average percentage of the ratio between numbers of encapsulated hydrophobic molecules to the surfactant monomer. The ratio of solubilised additive to surfactant molecules were calculated by dividing of numbers encapsulated molecules over the number of surfactant molecules forming the micelle (N_{agg}). The SLD contrasts between micelles containing pyrene-d_{10} and pyrene-h_{10} are compatible with pyrene/surfactant percentage ratio (Figure 6.8) calculated from Tables 6.1and 6.6.

Hydrocarbon Tail	C_{12}	C_{14}	C_{16}
Δ SLDs of contrast pyrene	4.36E-07	1.04E-06	1.27E-06

Figure 6.8: The percentage ratio of numbers encapsulated hydrophobic molecules to alkyl-benzyldimethyl ammonium bromide surfactant monomer compared to the difference in SLD between micelles with h-pyrene and micelles containing d-pyrene. The errors in encapsulating values are ±5% and the error in the SLD is ±7.92×10^{-8} Å^{-2}

The differences in SLDs for micelles containing -h10 or –d10 pyrene in the case of tail deuterated alkyl-benzyldimethyl surfactants showed less variation compared with a similar comparison for fully hydrogenated surfactant. This could be related to the small contrast between tail deuterated surfactant and the solvent (D_2O) or it could be related to the variation in encapsulation capacity between hydrogenated and deuterated surfactant as stated above [*69*].

Several authors have reported the location of pyrene inside cationic surfactant micelles. A number of authors reported that an attractive interaction exists between pyrene and quaternary ammonium headgroups [*70-72*]. Mainly this is due to an electrostatic interaction that occurs between the π-electrons surrounding the pyrene molecules and the positive charge of the quaternary ammonium headgroup. Consequently pyrene molecules would prefer to be situated in the palisade layer because of the greater charge density on their surface and less hydrophobicity due to occupancy of the largest free space area in the micelle geometry [*73*]. In this experiment solubilizing the combination of PAN and pyrene in the cationic micelles shows that some micellar swelling is observed, with small variation in the SLDs but the data could not be fitted to core-shell models so the location of the PAN and pyrene could not be determined directly by this method [*74*].

The SLD of the cores of h-tail micelles containing pyrene-d10 and –h10 in the presence of PEI is lower than those without PEI, while for tail deuterated BDHAB with PEI the SLD is higher compared with the same system without PEI. These suggest that PEI in solution allows removal of some of the hydrophobic species from the micelle cores possibly stabilizing them in the headgroup region of the micelle, or removing them entirely into solution via binding to the polymer. However some PAN and pyrene must remain, as the core SLD remains higher than that expected for the pure h-alkyl tails, and lower than that of pure d-alkyl tails. This is backed up by the fact that fully hydrogenated alkyl-benzyldimethyl surfactants encapsulating pyrene in presence of PEI are roughly the same size (within the errors of the measurement) as those with tail deuterated alkyl-benzyldimethyl, and both are similar to the size of the same micelles without PEI.

Table 6.7 SLD results from contrast variation experiments using cetylpyridinium bromide surfactants solubilizing hydrogenated or deuterated pyrene and hydrogenated PAN.

CPBr Contrast	Full-h	Head-d	Full-d	Tail-d	Full-h	Full-d
Additive	2mM Pyrene	2mM Pyrene	2mM Pyrene	2mM Pyrene	2mM Pyrene 1mM PAN	2mM Pyrene 1mM PAN
SLD ($Å^2$) h10-pyrene	-1.11×10^{-7}	2.16×10^{-8}	3.52×10^{-6}	3.14×10^{-6}	-3.50×10^{-7}	3.63×10^{-6}
SLD ($Å^2$) d10-pyrene	-1.71×10^{-8}	1.29×10^{-7}	3.61×10^{-6}	3.21×10^{-6}	1.64×10^{-8}	3.69×10^{-6}

The SLD errors are $\pm 8 \times 10^{-8}$ $Å^2$

The results from fitted SLD contrast variation data for CPBr solubilizing different contrasts of pyrene are summarized in Table 6.7. In general the differences in SLDs for different contrasts using pyrene shows relatively very small values, when the maximum SLD contrasts of pyrene were obtained from fitting this data compared with theoretical differences of SLDs expected between deuterated and hydrogenated pyrene in these micelles.

This result is compatible with calculations of micelles size for both CPBr and BDHAB, since CPBr shows a lower encapsulated amount of pyrene. The SLD differences in case of CPBr with a deuterated headgroup encapsulating –h10 or –d10 pyrene was greater than for tail or full deuterated of CPBr solubilizing pyrene. Fully deuterated CPBr encapsulating PAN and pyrene had in general larger differences in SLD than the fully hydrogenated CPBr encapsulating the same contrasts of hydrophobic additives. In general small differences in SLDs were found in case of CPBr and BDHAB but this difference in SLD indicates there are some of these additives in the core of micelles. This result is in good agreement with several studies which found that hydrophobic molecules such as pyrene prefer to locate in the region between the micellar core and shell region, close to the surfactant headgroup, in the palisade layer [*69, 73-77*].

6.2 Incorporation of PAN/Pyrene Swollen Micelles in Cross-Linked Polyelectrolyte Films

As mentioned earlier solid nanostructured polyelectrolyte films prepared through spontaneous self-assembly at the air-solution interface [*8*], retain their nanoscale structure after removal from the solution surface [*78, 79*]. These films are self-supporting [*29, 78, 80*] and they can be lifted from the solution surface after cross-linking onto either solid substrates or as membranes on an open mesh. O'Driscoll found that cetyltrimethylammonium bromide and polyethylenimine films can be significantly reinforced by cross linking the polymer after the film has formed, using ethylene glycol diglycidyl ether (EGDGE) [*78*]. The PEI/cationic surfactant films were crosslinked at room temperature under ambient conditions simply by including EGDGE in the sub-phase solutions. The higher concentration of polymer in the films allowed the membrane at the surface of the solution to be crosslinked well before the bulk solution in the sub-phase. This crosslinking allowed the films to be removed from the solution surface on an open mesh for drying or transfer onto a substrate (Figure 6.2.1). The extent of crosslinking directly affects the robustness of the film, and also the organisation of the micellar array encapsulated within the polymer hydrogel membrane. If the crosslinker concentration is too high it disrupts micelle organisation and the ordered mesostructure is lost [*78*].

To operate efficiently, the sensor containing films will require rapid diffusion of water and metal ions through the polymer hydrogel to the sensor sites, thus the crosslinker density and its effect on the micelles containing the sensor species is crucially important to this application. Therefore in this section films were prepared using BDHAB and CPBr at 0.05M to solubilise PAN and pyrene at three concentrations (1, 2 and 3mM) and (2, 4 and 6mM) respectively. The molar ratio of solubilised pairs of PAN/Pyrene was kept at 2:1 since the preliminary work showed that stable solid films formed with relatively good mesostructures at this ratio of PAN/Pyrene. The films were crosslinked using ethylene glycol diglycidyl ether EGDGE) at a fixed concentration (30mM). This amount was found to be a suitable concentration from preliminary experiments and from previous work in the group [*78, 81*].

The aim from this study is to characterise the in-plane structure of these cationic surfactant/PEI films as they grow at the air-water interface, encapsulating PAN/pyrene

in the micelles and to determine changes in the mesostructure in the films due to the crosslinking, and incorporation of the pyrene and PAN species.

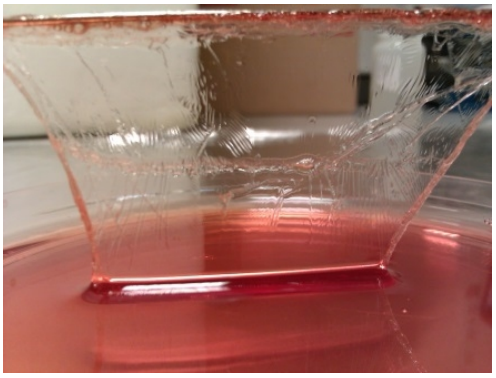

Figure 6.2.1: Fresh film grown on a solution of 0.05M BDHAB and 1.5% S-PEI solubilising 4.0mM pyrene and 2.0mM PAN containing 30.0mM of EGDGE, lifted from the top of this solution.

6.2.1 Solubilisation of Pyrene in Surfactant/PEI Films.

Neutron reflectivity experiments were performed on SURF at the ISIS Pulsed Neutron Source, [*82*]. The incident angle used for the reflectometry experiments was 1.5°, with data being collected between Q =0.048 and 0.600 $Å^{-1}$. Film formation was observed by collecting the reflectivity patterns every 15 min up to 90 min. Figure 6.2.2 shows the time-resolved neutron reflectivity patterns of BDHAB/SPEI and CPBr/SPEI films solubilising 4.0mM of pyrene.

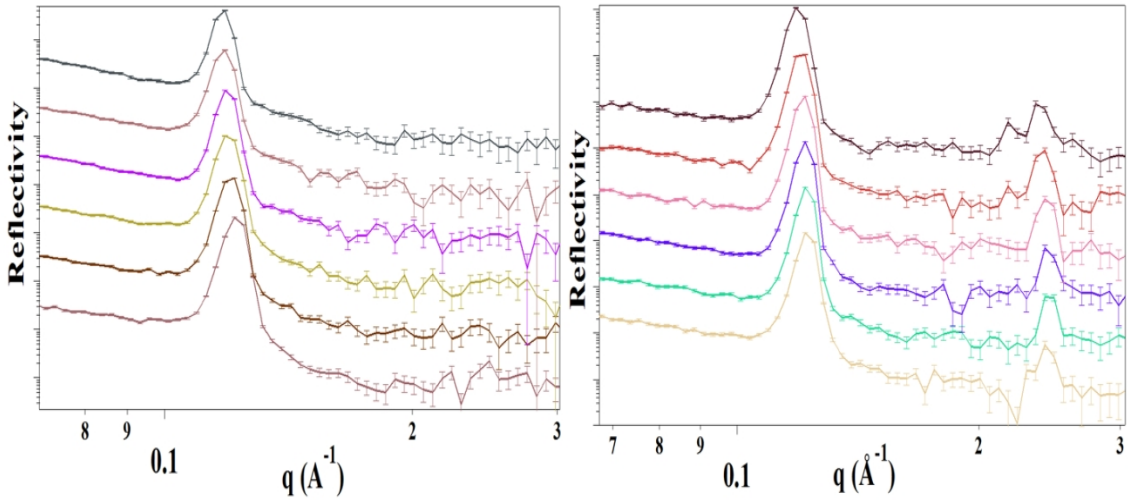

Figure 6.2.2: Time resolved neutron reflectivity patterns of films formed on 0.05M BDHAB with 1.5wt% SPEI solubilising 4.0mM of pyrene (left) and 0.05M CPBr with S-PEI solubilising 2.0mM of pyrene (right). The patterns were collected every 15min from bottom to top.

In general, BDHAB/SPEI films solubilising different amount of pyrene demonstrate a systematic shift of the high intensity peak to lower Q values with time. This shift indicates that the spacing between adjacent repeat units of these films is increasing about 1.0Å every 15 min. CPBr/SPEI films solubilising different concentrations of pyrene show an overall stable d-spacing during the time-resolved measurements compared with the BDHAB/SPEI films suggesting film formation is completed within the first 15 minutes when this surfactant is used. Figure 6.2.3 display more details of films formation on solutions of BDHAB and CPBr solubilising 2.0, 4.0 and 6.0 mM of pyrene during the first 90 min of these films formation.

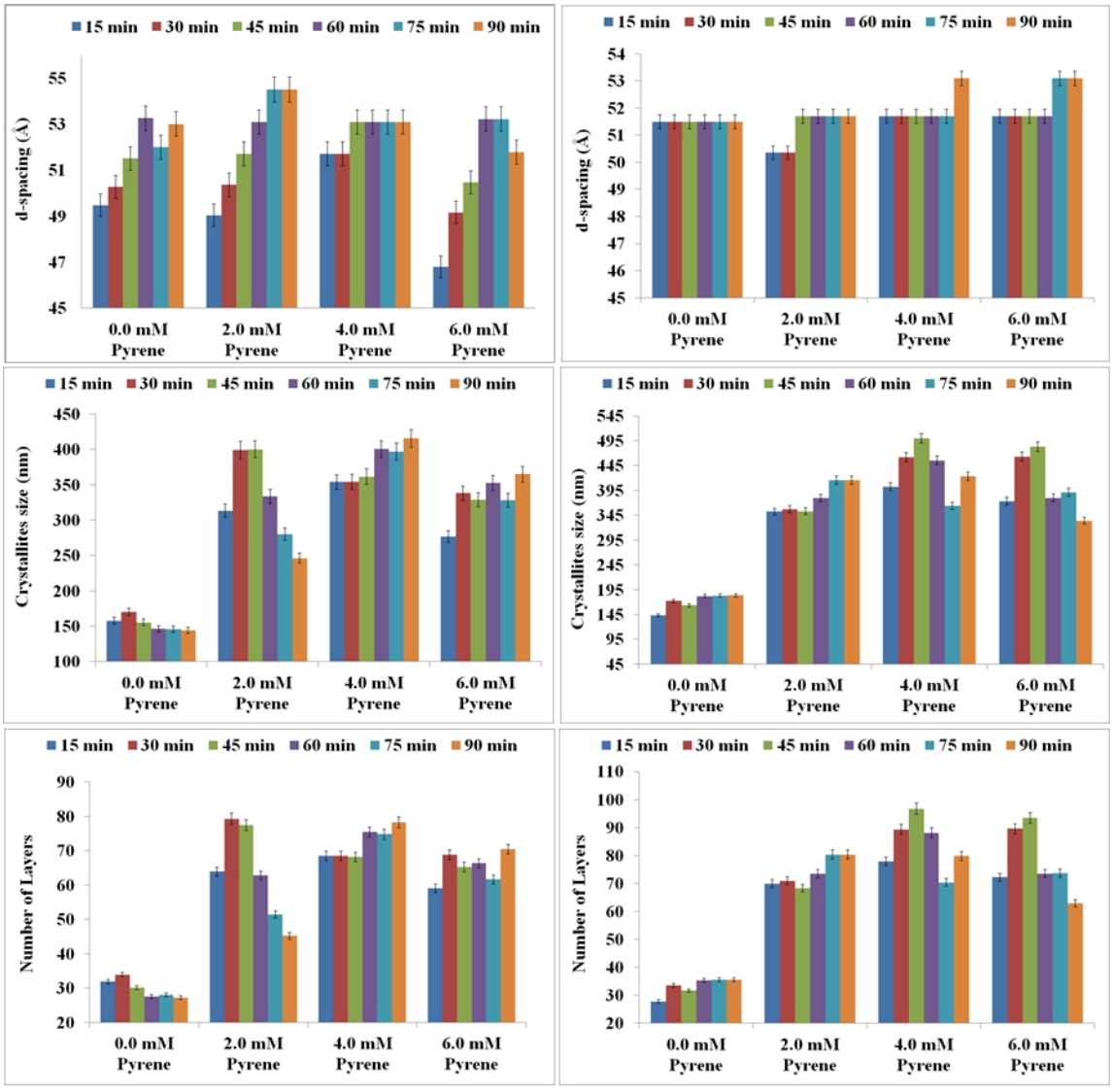

Figure 6.2.3: d-spacing, crystallite size and number of layers formed in films composed of BDHAB/SPEI solubilising different amount of pyrene (left 3 charts) and for films formed from CPBr/SPEI solubilising different amount of pyrene (right 3 charts).

The d-spacing, crystallite size and number of layers were calculated from peak position and peak width at half height of the high intensity peaks from the neutron reflectivity data as mentioned in Chapter 4. In general BDHAB/SPEI films solubilising different amount of pyrene have a slightly bigger spacing between adjacent repeat units than CPBr/SPEI films solubilising the same amounts of pyrene. Although the d-spacing of BDHAB/SPEI and CPBr/SPEI films solubilising different amount of pyrene does not show significant variation, however these results demonstrate an obvious increase in crystallite size and an increase in the number of layers in the film compared with BDHAB/SPEI and CPBr/SPEI films without pyrene. This result is in good agreement with SANS fitting data for the micelle solutions used to grow these films. In the previous section BDHAB and CPBr solubilising different amounts of pyrene illustrated stable and similar values for the elliptical micelle short axis (R_b), around 22.2Å – 23.3Å. On the other hand these ellipsoid micelles increased in size in the long axis (R_a) compared to those for the same surfactant without pyrene. For instance, BDHAB micelles solubilising 4.0 mM of pyrene were about double the length of the same surfactant micelle without pyrene. The long and relatively thin micelles were found from SANS data suggesting that the structure of these films most likely are made up of rod-like micelles packing parallel to the solution surface [*28*].

Interestingly, as shown in Chapter 4; solubilising styrene in BDHAB/SPEI and CPBr/SPEI films does not result in significant variation in crystallite size and number of layers for those films before and after solubilising styrene. The crystallites size for films of both surfactants solubilising 50vol% of styrene in the micelles was between 160 to 200Å and the maximum number of layers for those systems was 33 layers. Thus the mean number of repeating layers and final thickness of BDHAB/SPEI or CPBr/SPEI films solubilising different amount of pyrene are two times bigger than similar films without pyrene or solubilising different amount of styrene. This results suggesting that nature and properties of encapsulated hydrophobic molecules have a crucial influence in the final structure size and thickness of these films. As mentioned before that these aromatics tend to be encapsulated into the palisade layer of the micelle, which leads to formation of π-cation interactions between the polarisable benzene ring of the solute [*54*] and the surfactant headgroups. This correlation increases the average space between the surfactant headgroups, leading to a decrease in charge density on the micelle thus reducing the micellar curvature [*83, 84*]. This could be related to varying interactions between polyelectrolyte and surfactant headgroups in the micelles during

solubilisation of hydrophobic molecules [*21, 85*]. As stated before there is an interaction between PEI and the polar part of these cationic surfactants and the strength of this interaction may vary as the micelle morphology changes. In other words, when the micelles transform from spherical to ellipsoid then to rod-like during solubilisation of hydrophobic additives, this changes the overall micelles curvature, hence the micelle surface area exposing points where PEI can bind will increase, leading also to increases in the interaction strength. Consequently the significant increases occurring in crystallite size and number of layers for these films solubilising pyrene could be due to an increase in surfactant micelle and PEI interaction. On the other hand the polyelectrolyte in solution can act as a counterion to the surfactant also causing changes in the curvature of surfactant/water interfaces. The strong interaction between surfactant micelles and polyelectrolyte binds the micelles to each other and brings them closer together. This bridging will change the distances between micelles, and cause them to phase-separate, in our case into a thicker film [*85*].

6.2.2 Solubilisation of PAN in Surfactant/PEI Films.

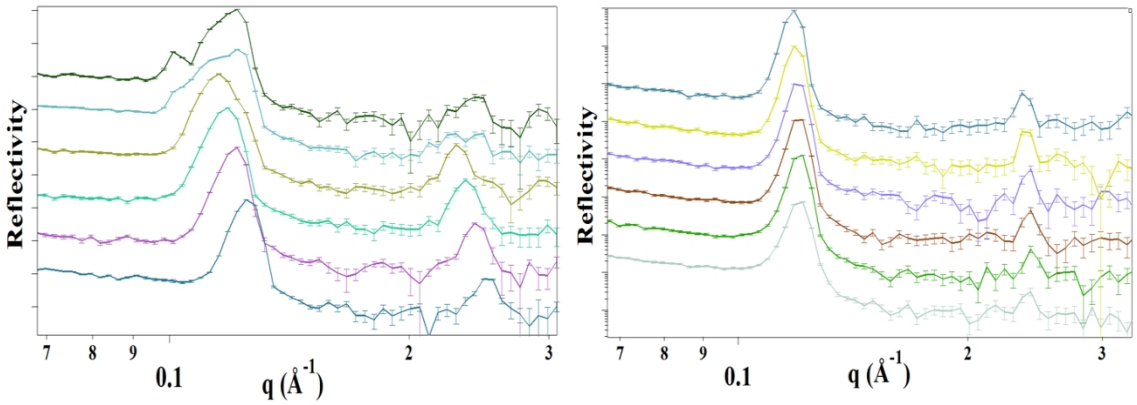

Figure 6.2.4: Time resolved neutron reflectivity patterns of films formed on 0.05M BDHAB with 1.5wt% S-PEI solubilising 2.0mM of PAN (left) and 0.05M CPBr with S-PEI solubilising 2.0mM of PAN (right). The patterns were collected every 15min from bottom to top.

Films grown from solutions of BDHAB with 1.5wt% S-PEI solubilising 1.0, 2.0 or 3.0mM of PAN show different reflectivity patterns compared with the same film composition solubilising pyrene and also compared with CPBr/SPEI solubilising PAN

(Figure 6.2.4). During the first 45min after pouring the solution into the trough, the high intensity peak observed at Q = 0.118 $Å^{-1}$ became broader and less intense, while after 60min two overlapping peaks were seen at Q = 0.10 $Å^{-1}$ and 0.12 $Å^{-1}$. These two overlapping peaks could be due to a rearrangement of the micelle structure into different phases, meaning two different mesostructures are present in the films at the same time. CPBr/SPEI films solubilising different concentration of PAN show, in general, stable d-spacings, indicating little change in the distance between adjacent repeat units during the time-resolved measurements. However the film thickness, suggested increases in crystallite size with time (Figure 6.2.5).

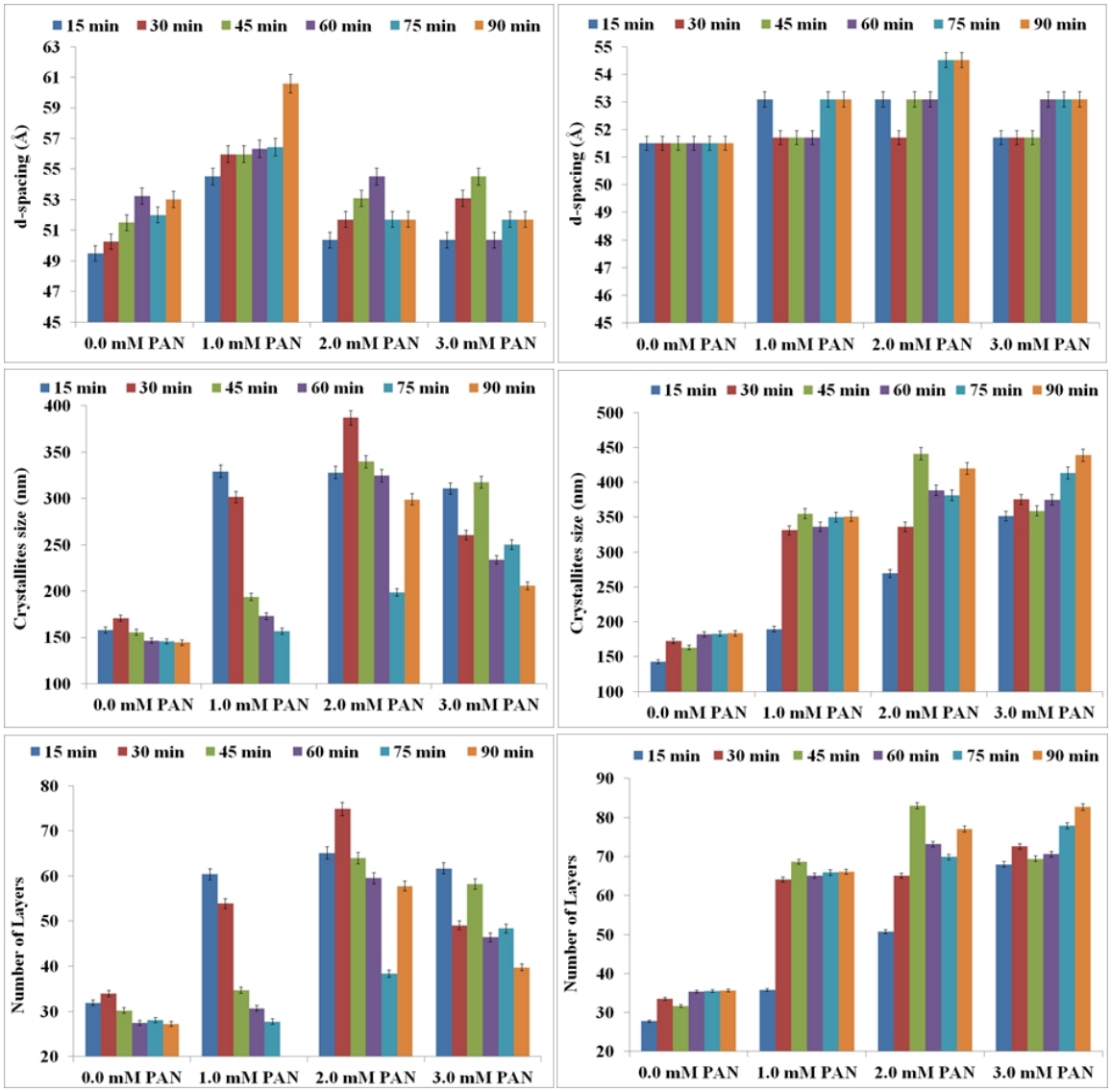

Figure 6.2.5: d-spacing, crystallite size and number of layers formed in films composed of BDHAB/SPEI solubilising different amount of PAN (left 3 charts) and for films formed from CPBr/SPEI solubilising different amount of PAN (right 3 charts).

Overall neutron reflectivity patterns of BDHAB/SPEI films solubilising PAN contained more than two diffraction peaks, which indicate that these films are forming from repeated of mesostructured layers. The mesostructures of these films will be discussed in more detail in GIXD section. BDHAB/SPEI films solubilising different amount of PAN show in general a growth in the d-spacing of these films during the time-resolved measurements of these films formation. However when the amount of PAN in the solution is increased, the BDHAB/SPEI films illustrate a shrinkage in d-spacing which suggests that the micelles re-arrange in the films. A second reason for this change could be due to a reduction in the amount of water or PEI in the water-PEI layer between the micelles within the film. Unfortunately there is not enough SANS data to support whether this change in shape of the BDHAB micelles solubilising PAN occurred just in the solid state films or also in the micelle solutions.

However, for a given PAN concentration, despite the fact that BDHAB/SPEI films show a growth in d-spacing throughout the time of film formation, nevertheless the apparent crystallite size and number of layers for these films exhibits a reduction during the measurement. This behaviour was also typically seen in the case of BDHAB/PEI solubilising styrene monomer (Chapter 4), where it was suggested that the reason behind loss in the film thickness with time is related to the dissolution rate of BDTAB/SPEI films being faster than the accumulative rate. The other possibility for decreases in crystallites size and number of layers for these films could be due to formation of a second mesostructure within the same film as mentioned earlier. The broadening of first diffraction peak seen in the time resolved neutron reflectivity patterns of BDHAB/SPEI films support that there is more than one mesophases structure within the same film, where one of these mesophases are shrinking and the other is growing [*29, 80, 81*].

CPBr/SPEI films solubilising different amounts of PAN on the other hand, show a growth in crystallite size and number of layers during these films formation. However there are no significant variations in CPBr/SPEI films thickness through solubilising different amounts of PAN. This suggests that CPBr/SPEI films solubilising different amounts of PAN are more stable compared with BDHAB/SPEI films solubilising similar amount of PAN.

6.2.3 Solubilisation of Combinations of PAN/Pyrene.

Solubilising combinations of different amounts of both PAN and pyrene together gives different neutron reflectivity patterns compared with those films solubilising individual of each of these additives (Figure 6.2.6).

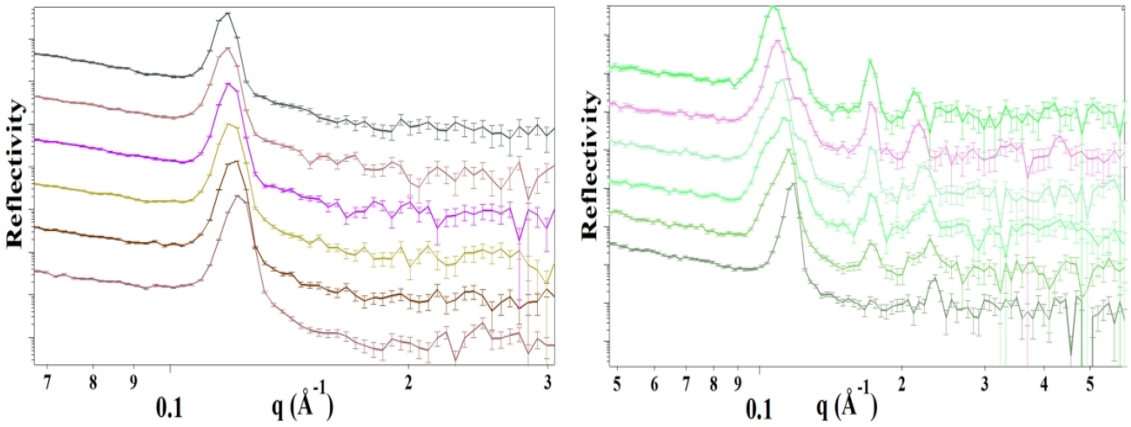

Figure 6.2.6: Time resolved neutron reflectivity patterns of films formed on 0.05M BDHAB with 1.5wt% S-PEI solubilising a combination of 4.0mM pyrene and 2.0mM PAN (left), and right, films on a similar solution using CPBr. The patterns were collected every 15min from bottom to top.

Reflectivity patterns for BDHAB/SPEI and CPBr/SPEI films solubilising different concentrations of pyrene showed very intense diffraction peaks. However, whereas reflectivity patterns of BDHAB/SPEI films solubilising different amount of PAN had two overlapping peaks, patterns from CPBr/SPEI films showed only the two peaks of a single lamellar or oriented 2D hexagonal phase. However, time resolved neutron reflectivity patterns of CPBr/SPEI films solubilising both PAN and pyrene shows in the beginning two discrete diffraction peaks at Q = 0.118 $Å^{-1}$ and 0.235 $Å^{-1}$. After 90 min from starting measurements, four diffraction peaks were seen at Q = 0.112, 0.125, 0.171 and 0.217 $Å^{-1}$ where the first two peaks overlapped. These diffraction peaks suggesting that CPBr/SPEI films solubilising combination of PAN and pyrene form a complex mesostructure. In contrast, BDHAB/SPEI films solubilising different concentrations of PAN and pyrene show only one diffraction peak, although that does not necessarily mean that these films have a simple structure. O'Driscoll et al. reported loss in the intensity of neutron reflectivity diffraction peaks over time for CTAB/SPEI films. This was suggested to be due to increasing disorder in the mesophase present in these films [*29*]. Hillhouse et al. demonstrated the expected variation in the diffraction peaks from

p6mm hexagonal mesophases by calculating the patterns for different orientations of the mesophase relative to the direction of the X-ray beam. In the case where the mesophase was oriented with the direction of the long axis of the micelles parallel to the substrate face, and the X-ray beam is reflected from the surface, 2 peaks should be seen in the reflectivity pattern corresponding to the 100 and 200 reflections of the 2D hexagonal phase. This pattern cannot be distinguished from that of a lamellar phase in the same orientation. However no diffraction peak should be seen in the reflectivity pattern for the same film structure if the mesophase was oriented with the direction of the long axis of the micelles perpendicular to the substrate. Thus the number of diffraction peaks are related to the beam direction with orientation of mesophases ordering [*86*].

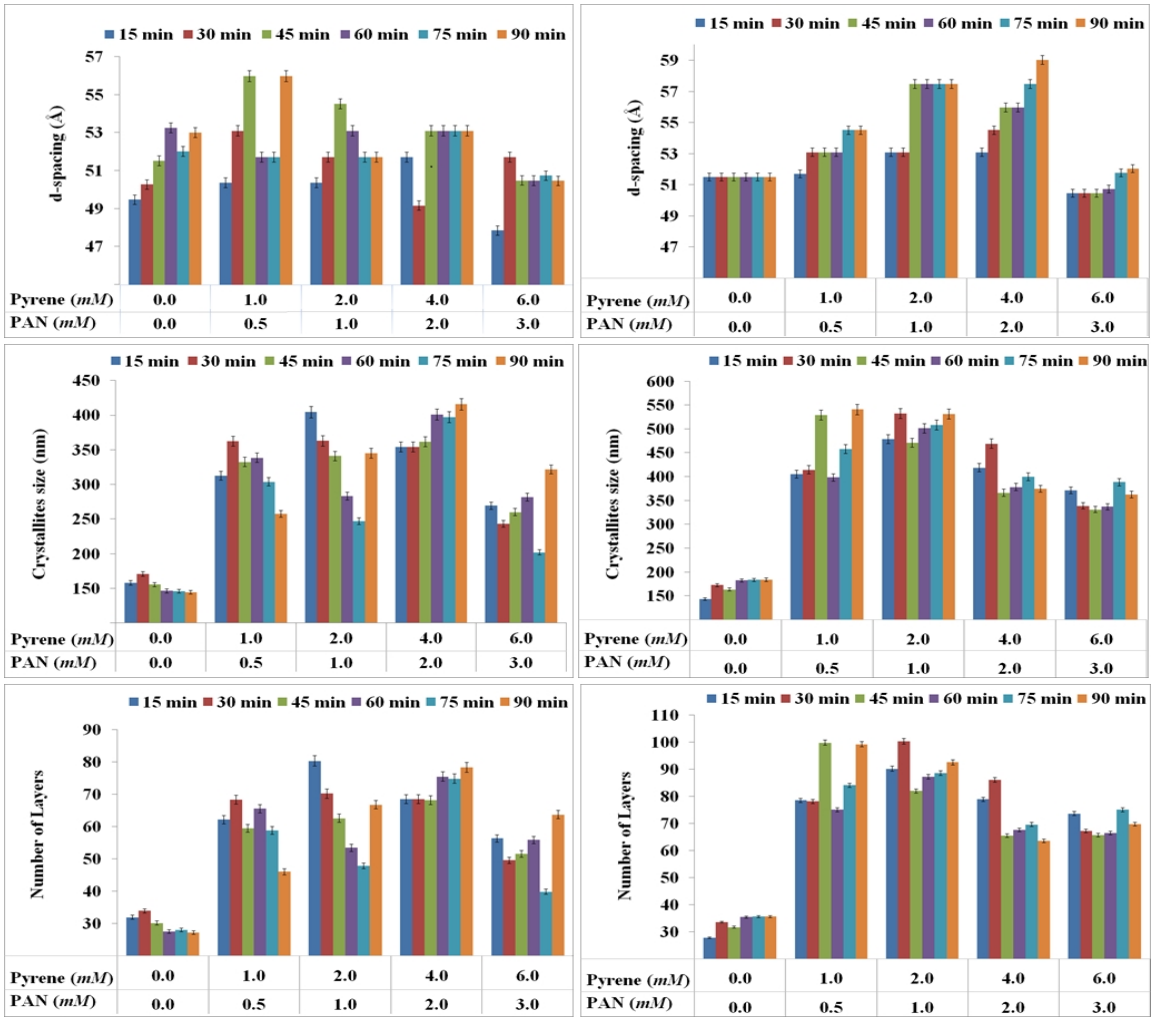

Figure 6.2.7: d-spacing, crystallite size and number of layers formed in films composed of BDHAB/SPEI solubilising combinations of PAN and pyrene (left 3 charts) and for films formed from CPBr/SPEI solubilising combinations of PAN and pyrene (right 3 charts).

Reflectivity patterns from BDHAB/SPEI films solubilising relatively low concentrations of PAN and pyrene (0.5/1.0 *mM* and 1.0/2.0 *mM*) show in general greater variation in d-spacing during the time of these films formation, compared to those solubilizing high concentration of PAN and pyrene (Figure 6.2.7). This behaviour could be related to micelle rearrangement in these films, consequently changing their mesophases over time. Overall increases in the concentration of solubilising PAN and pyrene in BDHAB/SPEI films shows decreases in d-spacing. CPBr/SPEI solubilising different concentrations of PAN and pyrene generally show an increase in d-spacing and number of repeat units during the time of those films formation. In addition increases in the amount of PAN and pyrene in the CPBr/SPEI films increased the d-spacing. However at high concentration of PAN/Pyrene (3.0 mM PAN and 6.0 mM pyrene), the d-spacing decreased by about 7Å (±2Å). This behaviour could be related to the solubilisation capacity of CPBr micelles, where this surfactant shown cleavage into small micelles when the amount of styrene solubilized in the micelles is increased (Chapter 4). The other possibility is related to loss of water molecules in the water/PEI layer between the micelles within the film due to solubilising high amount of hydrophobic molecules.

The SANS fitting data showed that BDHAB/SPEI micelles solubilising 1.0 *mM* of PAN and 2.0 *mM* of pyrene were bigger 3.7 times in the longer micelles axis (R_a) than CPBr/SPEI solubilising similar amount of PAN and pyrene. The smaller micelle axis (R_b) for both BDHAB/SPEI and CPBr/SPEI solubilising 1.0 mM of PAN and 2.0 mM of pyrene did not change (around 22.5-23.1 Å). However the lowest d-spacing for these self-assembled films solubilising different concentration of PAN and pyrene was 48Å, which is twice as large as the small micelles axis (R_b). This result suggests that the micelles might be re-arranged into a different phase with smaller dimensions in the film compared to the micelles in solution.

In general BDHAB/SPEI and CPBr/SPEI films solubilising combinations of PAN and pyrene or even solubilising PAN or pyrene individually show relatively large crystallite sizes and high numbers of repeating layers in these films. These results suggest a high potential surface area will be available on the micelle surfaces within the films for sensor interactions [*87*]. In addition the neutron reflectivity data suggests that these films are formed with ordered mesostructures. GIXD for those films solubilising PAN

and pyrene support this and enable structure determination, as will be demonstrated in the next section.

Mainly there are two crucial factors for any good metal ion sensors. First the time of response including the accuracy during the experiment time measurement, and second a high sensitivity which indicates the detection limits [*88, 89*]. Jung et al. reported that thicker sensing layers demonstrate higher sensitivity and a wider range of analyte concentrations detection, but in the other hand caused a longer response time [*90*], since the time of response is related to the diffusion rate of the metal ions [*89*]. Well-organised mesostructured films also can give extra advantage for these prospective surfactant/SPEI/PAN/Pyrene metal ion sensor films by improving the diffusion in short times. Another advantage for well-ordered nanostructured film is increasing the overall surface area of micelles within the film. This means the chance of metal ion interactions with PAN molecules will increase which subsequently will increase the sensitivity of the sensor [*91*].

6.2.4 Cross-Linking of Surfactant/PEI Films Solubilising PAN/Pyrene.

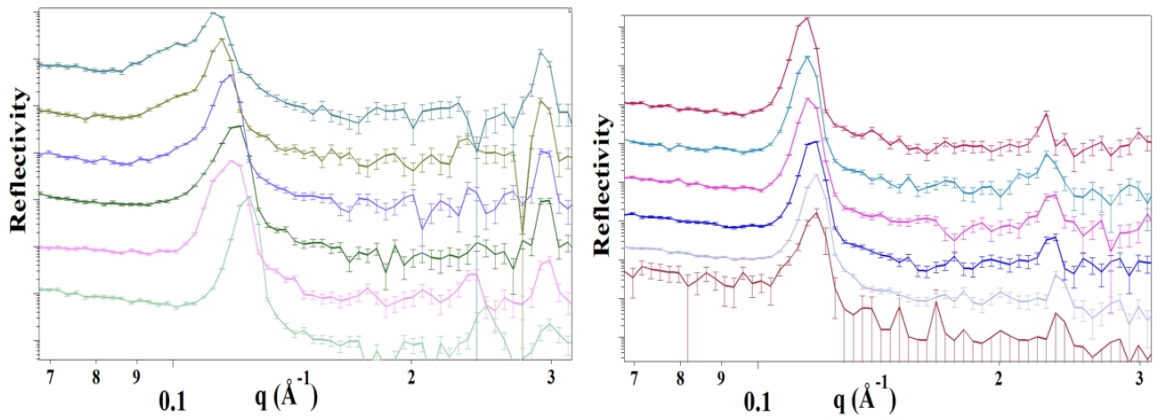

Figure 6.2.8: Time resolved neutron reflectivity patterns of films formed on 0.05M BDHAB with 1.5wt% S-PEI solubilising a combination of 4.0mM pyrene and 2.0mM PAN (left), and right, films on a similar solution using CPBr. Both films were cross-linked using 30.0mM EGDGE. The patterns were collected every 15min from bottom to top.

As stated earlier the main purpose of this sensor is to provide a simple and sensitive method of monitoring metal ion content in aqueous samples in a format such as a metal ion dip stick testing kit. Therefore to strengthen the polymer/surfactant films by using

the crosslinker, ethylene glycol diglycidyl ether, is very important for two reasons; first to maintain the templated structure of these self-assembled nanostructured films, second to prevent these solid films from dissolution during contact with aqueous media. Therefore EGDGE was used at 30.0mM to crosslink and improve the robustness of these films. Although the extent of crosslinking affects the robustness of the film, it could also disturb the organisation of the micellar array encapsulated within the polymer hydrogel membrane. O'Driscoll reported that in the case of CTAB/PEI films with high concentrations of EGDGE as cross linker, he micelle organisation was disrupted and the ordered mesostructures were lost [*78*]. Figure 6.2.8 shows the evolution of neutron reflectivity patterns from films prepared from BDHAB/SPEI and CPBr/SPEI solubilising both pyrene and PAN, where these films were cross-linked by EGDGE. The patterns from both films started with sharp peak around Q = 0.12Å, while after 90min the pattern for BDHAB/SPEI had very broad overlapped peaks, whereas the pattern for the CPBr/SPEI film still showed a single sharp peak. This result shows that reflectivity patterns of these films with EGDGE behave in a different way compared with those from films solubilising the same amount of PAN and pyrene but without cross linker. EGDGE reacts with the PEI through nucleophilic addition reactions involving the amine groups on the polymer, since EGDGE has two epoxide groups. This interaction between EGDGE and PEI reduces the number of primary amine groups in PEI which decreases the strength of the dipole formed across the amine group, subsequently the interaction between PEI and the cationic surfactant will decrease [*78*]. However via crosslinking the effective molecular weight of the polymer is increased so the films made from SPEI become thicker and more stable while retaining their mesoscale ordering. The structure of the films may change due to crosslinking altering the size of gaps between polymer strands in the water-gel network surrounding the micelles but at the level of crosslinker investigated here, this process does not adversely affect the mesostructure. Therefore the structure of films containing surfactant/PEI micelles solubilising PAN and pyrene in the presence of EGDGE has different reflectivity behaviour than those films without EGDGE, but the films are still ordered.

In general the d-spacing, crystallite size and number of layers for the films solubilising a combination of PAN/pyrene then cross-linked by EGDGE show a slight increase in these values compared with those for films that were not cross-linked. This change could be related to rearrangement of micelles during the film formation to form bigger micelles, however this is unlikely since the micelle size in the layer is largely

determined by the surfactant tail-length (as the amounts of PAN and pyrene are small) which is not changing.

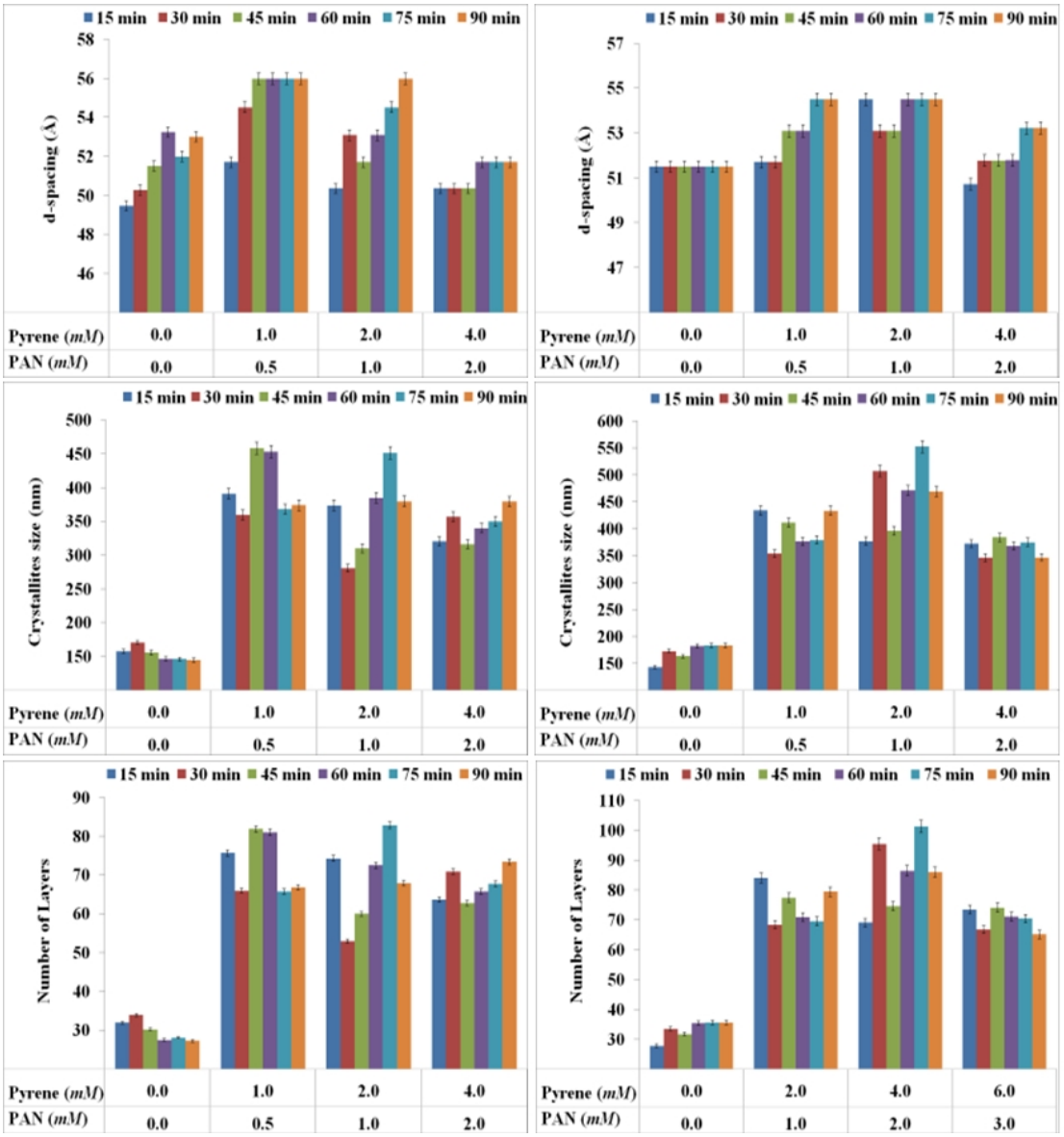

Figure 6.2.9: d-spacing, crystallite size and number of layers formed in films composed of BDHAB/SPEI solubilising combinations of PAN and pyrene cross-linked by 30.0mM of EGDGE (left 3 charts) and for films formed from CPBr/SPEI solubilising combinations of PAN and pyrene cross-linked by 30.0mM of EGDGE (right 3 charts).

The other possibility for this growth in lattice spacing and in the films thickness is related to the growing polymer molecular weight of the PEI between these micelles due to the cross-linking interaction between EGDGE and polymer. Overall the growth behaviour of these cross-linked films shows a similar performance to those films without EGDGE although grown with a slightly higher molecular weight PEI. In

general for low concentrations of PAN and pyrene the films contain the highest crystallite size and number of layers while at high concentration of PAN and pyrene the crosslinked films have more layers than those films solubilising the same amount of PAN and pyrene but without crosslinking.

6.2.5 Effects of Metal Ions on Cross-Linked Films Solubilised PAN/Pyrene.

In the previous section, the effects of metals ions such as Fe^{3+} and Cu^{2+} on micellar shape and size has been studied by using SANS. In the last part here, on neutron reflectivity from films made from cationic surfactant/PEI solubilising PAN and pyrene, the films were investigated in presence of 2.0mM of these metal ions to observe their effects on the final surfactant/PEI/PAN/pyrene film structures. Neutron reflectivity patterns of cross-linked films formed on BDHAB or CPBr solutions with 1.5wt% SPEI solubilising a combination of 4.0mM pyrene, 2.0mM PAN and mixed with either Fe^{3+} or Cu^{2+} show intense diffraction peaks which indicates that these films still maintain their mesostructure even in presence of these metal salts (Figure 6.2.10). The main variation seen between these cross-linked films before and after addition of metal ions is a broadening of diffraction peaks in the case of films without metal ions, while the cross-linked films incorporating metal ions show an almost stable peak width. This result suggesting that incorporation of metal ions in these films reduces the polydispersity in the layer thickness [*28*] and stabilizes them against changes in mesostructure during formation.

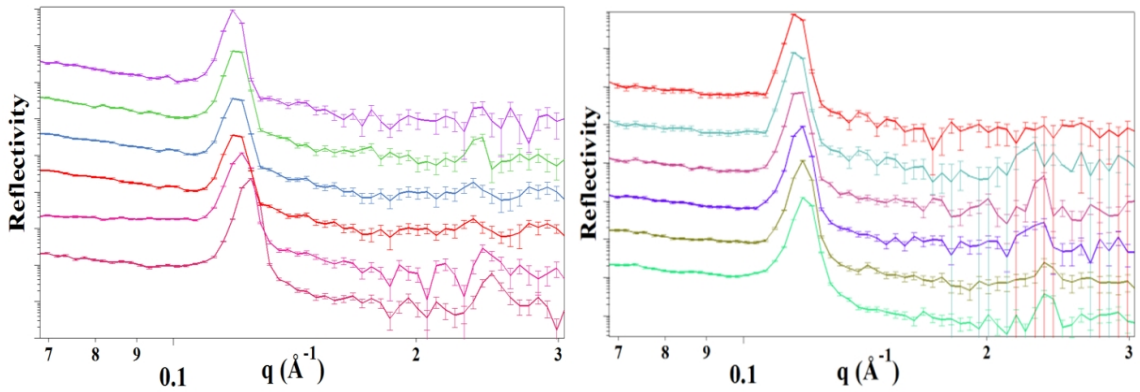

Figure 4.2.10: Time resolved neutron reflectivity patterns of (left) a cross-linked film formed on 0.05M BDHAB solution with 1.5wt% S-PEI, solubilising a combination of 4.0mM pyrene, 2.0mM PAN and mixed with 2.0mM Cu^{2+} and (right), a cross-linked film formed from 0.05M CPBr with S-PEI solubilising a combination of 4.0mM pyrene, 2.0mM PAN and mixed with 2.0mM Cu^{2+}. The patterns were collected every 15min from bottom to top.

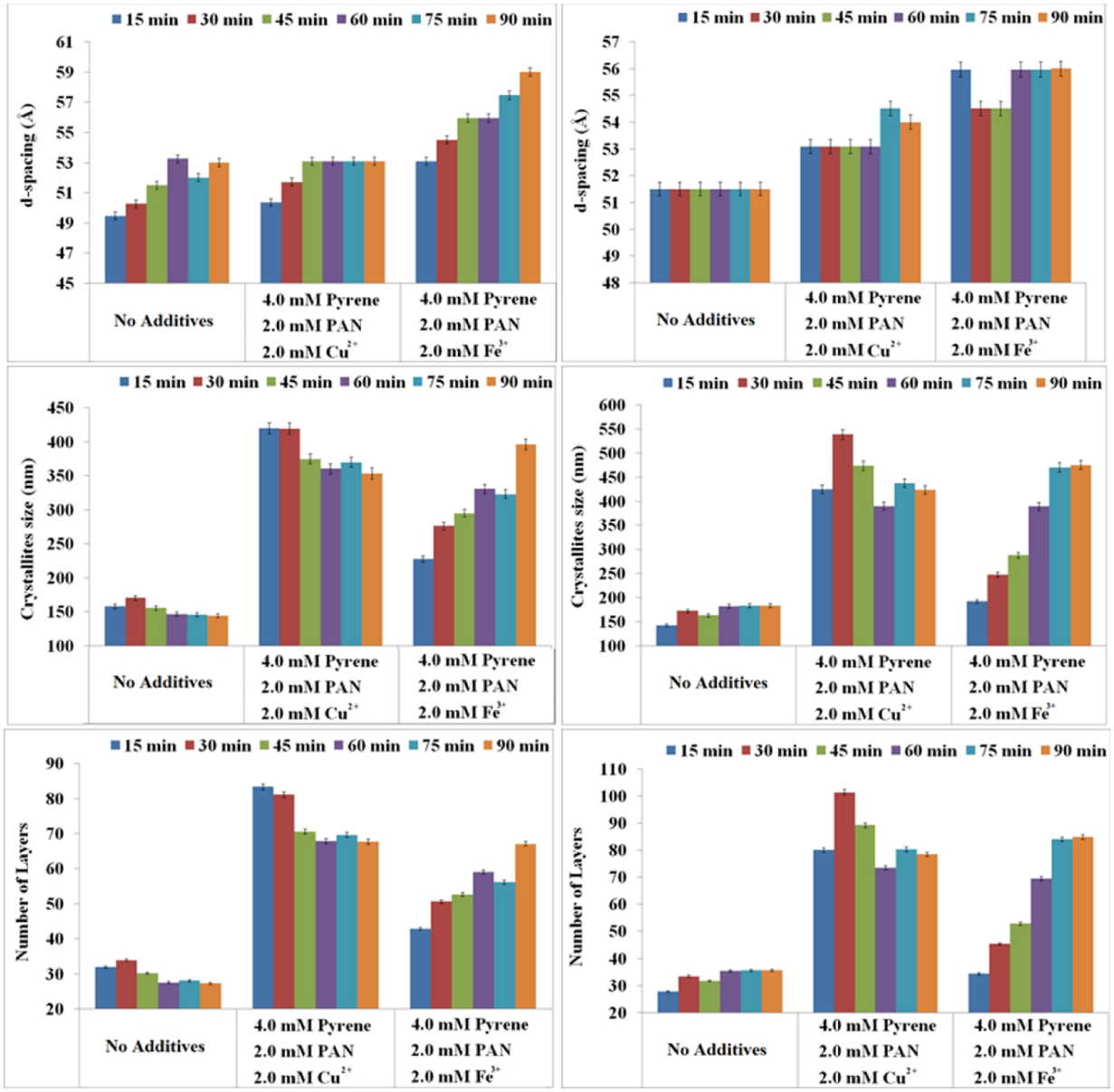

Figure 6.2.11: d-spacing, crystallite size and number of layers formed in cross-linked films composed of BDHAB/SPEI solubilising combinations of PAN and pyrene where the film forming solutions were mixed with metals salts (left 3 charts) and for films formed from CPBr/SPEI solubilising combinations of PAN and pyrene cross-linked by 30.0mM of EGDGE and with metals salts mixed into the film forming solutions (right 3 charts).

The adjacent repeat units for both films in the presence of ferric ions demonstrates a higher lattice spacing value compared with the case of copper ions (Figure 6.2.11). This result is in a good agreement with SANS fitting data, since both BDHAB and CPBr solubilising PAN and pyrene showed bigger micelles in the presence of ferric ions compared with copper ions. Both BDHAB/SPEI and CPBr/SPEI films solubilising PAN/pyrene show in general an increase in their d-spacing with time during the

formation of these films. However the total thickness and number of layers for both BDHAB and CPBr films tended to decrease with time in the presence of Cu^{2+} ions, while they increased with time in the case of addition Fe^{3+} ions during these films formation.

This variation in number of repeating units and number of layers during film grown is related to either the influence of the chloride counterions. The chloride counterions could alter the apparent charge on the surfactant headgroup when present at higher concentrations hence enhancing growth of the micellar aggregates in the case of Fe^{3+} ions [*92*]. The second possibility is due to a transformation in the size, shape and hydrophobicity of the PAN molecule during the complex formation between PAN and metal ions [*61-63*]. However, in general 90min after these films form on solutions containing metal ions the values of d-spacing, crystallites size and numbers of layers were very similar compared with those cross-linked films solubilising PAN and pyrene but without metals. Thus the presence of metal ions in general did not affect the final film structure or properties of these films.

The next section will discuss the final mesostructured films formed from cationic surfactant/PEI films solubilising PAN and pyrene as individual additives and the structure of these films solubilising a combination of PAN and pyrene.

6.3 Grazing Incidence X-ray Diffraction of Cationic Surfactant/PEI Films Solubilising PAN and Pyrene

Film forming solutions were made up from BDHAB or CPBr with low molecular weight PEI at the same concentrations as discussed above, solubilising either a combination of PAN and pyrene or solubilising individual components. These films show at least three diffraction spots rather than rings which suggest that all of these films contain very well ordered mesostructures (Figure 6.3.1). All of these diffraction spots can be indexed as the (010), (100), (110), (120) and (200) reflections [*93*], which indicate a highly ordered 2D hexagonal mesostructure. SANS data for the surfactant micelle solutions used to form these films showed that the micelles transformed from long prolate ellipsoid to rod-like micelles when solubilising either single components or combinations of PAN and pyrene.

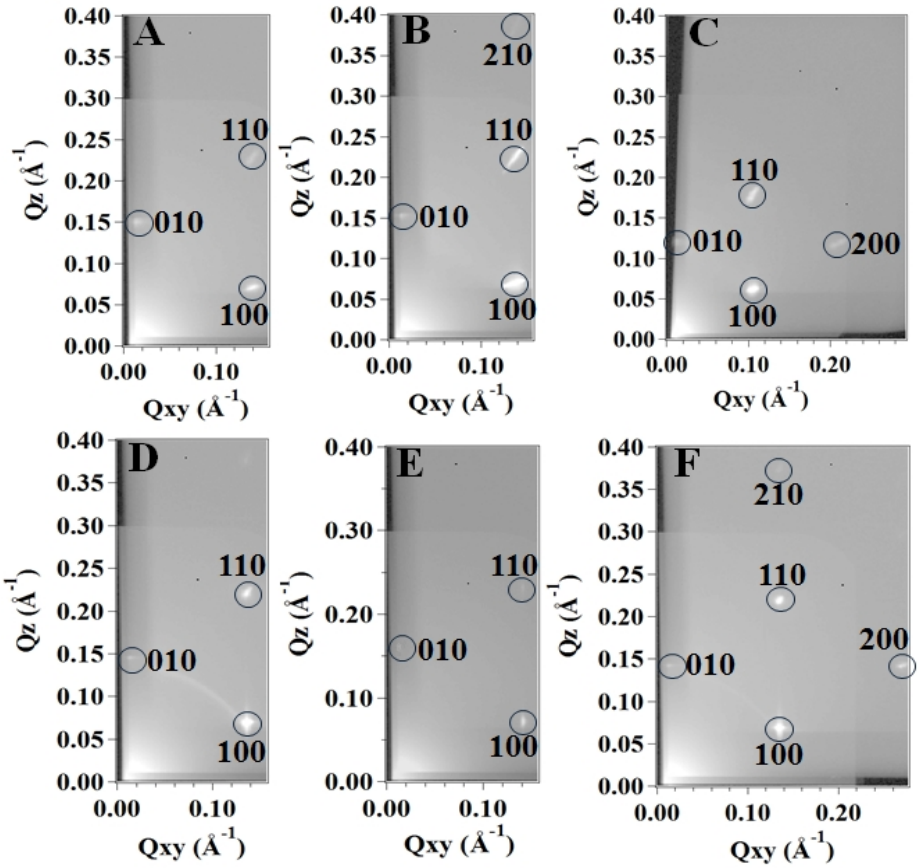

Figure 6.3.1: GIXD patterns of BDHAB/SPEI films solubilising 4.0mM pyrene (A), 2.0mM PAN (B), cross-linked BDHAB/SPEI film solubilising a combination of 4.0mM pyrene and 2.0mM PAN (C), CPBr/SPEI films solubilising 4.0mM pyrene (D), 2.0mM PAN (E) and CPBr/SPEI cross-linked film solubilising a combination of 4.0mM pyrene and 2.0mM PAN (F).

The neutron reflectivity patterns illustrated diffraction peaks for those films with an apparent lamellar spacing, since the specular pattern only crosses the Ewald sphere on the Q_{xy} = 0 line, while GIXD shows the full in-plane structure. The diffraction spots seen in the GIXD patterns suggest that the micelles are packed at the air-liquid interface to form highly ordered arrays, with a final 2D hexagonal mesostructure where the cylindrical micelles are oriented with the long axis of the cylinders parallel to the air–solution interface [*28, 86*].

Table 6.3.1: *The Q positions, d_{100}-spacing and unit cell dimensions of surfactant/SPEI films solubilising different amount of PAN and pyrene, calculated from GIXD patterns showing a 2D hexagonal micelle packing geometry. When EGDGE was used it was at a concentration of 30.0mM.*

Surfactant	**Conc. of Pyrene (*mM*)**	**Conc. of PAN (*mM*)**	**Q for *(100)* spot ($Å^{-1}$)**	***d_{100}*-spacing (Å)**	**Unit cell dimension (Å)**
BDHAB	0.0	0.0	0.144	44	50
CPBr	0.0	0.0	0.140	45	52
BDHAB	2.0	0.0	0.150	42	48
BDHAB	4.0	0.0	0.150	42	48
BDHAB	6.0	0.0	0.153	41	47
CPBr	2.0	0.0	0.163	39	45
CPBr	4.0	0.0	0.155	41	47
CPBr	6.0	0.0	0.150	42	48
BDHAB	0.0	1.0	0.154	41	47
BDHAB	0.0	2.0	0.152	41	48
BDHAB	0.0	3.0	0.152	41	48
CPBr	0.0	1.0	0.165	38	44
CPBr	0.0	2.0	0.153	41	47
CPBr	0.0	3.0	0.152	41	48
BDHAB	2.0	1.0	0.140	45	52
BDHAB	4.0	2.0	0.128	49	57
BDHAB	6.0	3.0	0.150	42	48
CPBr	2.0	1.0	0.135	47	54
CPBr	4.0	2.0	0.151	42	48
CPBr	6.0	3.0	0.150	42	48
BDHAB with EGDGE	2.0	1.0	0.122	52	59
BDHAB with EGDGE	4.0	2.0	0.118	53	61
BDHAB with EGDGE	6.0	3.0	0.130	48	56
CPBr with EGDGE	2.0	1.0	0.124	51	59
CPBr with EGDGE	4.0	2.0	0.120	52	60
CPBr with EGDGE	6.0	3.0	0.122	52	59

Error for the spot positions is ± 0.02 $Å^{-1}$ and for the d-spacing and unit cell dimension is ±2 Å.

The Edler group have previously reported the 2D hexagonal structure as the final film structure over a wide composition range for films made from cationic surfactants mixed with polyethylenimine solutions [*28, 78, 94, 95*] . For instance O'Driscoll et al. found that CTAB/SPEI films assemble into 2D hexagonal arrays of rod-like surfactant micelles templated by polymer [*78*]. Yang et al. found that a mixture of CTAB/PEI/silicate films also formed 2D hexagonal phases [*81*]. Wasbrough et al reported that self-assembled films formed from a mixture of DDAB/CTAB/PEI solution and demonstrated a 2D hexagonal structure as packed cylinders arranged with a unit cell size of 46Å [*28*]. These results are therefore comparable with the earlier work, and the presence of PAN, pyrene and cross-linker does not alter the expected structure, although they do appear to improve the ordering in the films.

It is important to note here that the structures seen for the films solubilising PAN and pyrene is identical to the 2D hexagonal mesostructure seen in previous work (Figure 6.3.1). The average of d-spacing for these films calculated from GIXD patterns (Table 6.3.1) is close to the d-spacings seen in neutron reflectivity patterns from similar films. Cross-linked films solubilising a combination of PAN and pyrene have the highest d_{100}-spacing and unit cell values which agree with neutron reflectivity data discussed above. This results support the proposal that the cross-linker is connecting the polyelectrolyte molecules with each other, subsequently strengthening the mesostructure templated in these films. In general all of these films show well-ordered 2D hexagonal mesostructures.

These highly-ordered mesostructured materials have potential applications in the field of metal ion sensors. The well-ordered materials are highly desirable because they have a big micelle surface area displaying PAN binding sites, and highly networked connectivity through the surrounding polymer hydrogel leads to high sensitivity and selective detection [*96-98*]. Chandra et al. fabricated highly ordered 2D-hexagonal mesoporous organosilica fluorophore grafted materials are found that this material had a very strong affinity for metal cations such as Zn^{2+}, $Fe3^{+}$, Hg^{2+} and Cd^{2+}, and thus can be very efficiently used for the removal of these heavy metal ions from wastewater. This well-ordered material also could have possible application in optical sensors [*96*]. Xia et al. proposed that a carbon paste electrode modified with hexagonal mesoporous silica demonstrated improved sensitivity and high selectivity toward the detection of cadmium, lead and copper [*97*]. Sherif and Shenashen identify several advantages of the

highly-ordered mesoporous metal sensors which include long-term stability of signalling and recognition functionalities that in general provide extraordinary sensitivity, selectivity and reusability [*98*].

However these metal ion sensor research examples are synthesised from either silicate or metal nanocomposite substrates, nevertheless all of these papers confirmed that the efficiency and sensitivity of these sensors are significantly increased by enhancing the surface area of these sensors. On the other hand 3D hydrogel sensors for specific metal ion sensing have also proven to have high sensitivity and very low background noise [*99, 100*], where trapping of target cations causes shrinkage of the hydrogels causing blue shift of the refraction peak wavelength with a detection limit lower than 1^{-9} M. Also three dimensional hydrogel based sensors showed about 100 times increase in signal density due to the advanced immobilization ability of sensing moieties within the matrix [*101*]. In general hydrogel sensors have good advantages since the response rate is dependent on the hydrogel composition, shape and size which can be controlled. Modified hydrogel with small rectangular monocrystalline silicon tips have been used as well for ion-sensing [*102*]. Zhang et al. [*103*] used a hydrogel layer based on acrylamide and (3- acrylamidopropyl) triethyl ammonium chloride, this system shown high selectivity to $CrO4^{-2}$ with a sensitivity as low as 10^{-11} M.

6.4 Characterization of cationic surfactant/PEI films solubilising PAN/Pyrene.

Several approaches and techniques for the detection of toxic metal ions have been developed and published. Some of these techniques such as atomic absorption spectroscopy [*104*], potentiometric or colorimetric titration [*105*] and fluorescence spectrometry [*106*] exhibited high sensitivity and low limit of detection. But on the other hand some of these techniques are expensive, hard to handle and have high operation costs. Simple methods for metal ion determination which can be used with minimal equipment costs are therefore still needed.

6.4.1 Surfactant/PEI/PAN/Pyrene films as an electrochemical metal ion sensor.

Recently, many experiments are being performed using electrochemical techniques and sensors to detect toxic metal ions at low concentrations. There are many advantages of the electrochemical approach for detection of metal ions such as simplicity, suitability, and fast response for the preparation of inexpensive and portable instrumentations [*107*]. Cyclic voltammetry (CV) is one of the particularly sensitive electrochemical technique for measuring trace metals and also can carry out simultaneous detection of many metals in different matrices [*108, 109*]. Figure 6.4.1 shows the setup of the electrochemical cell that was used in this experiment.

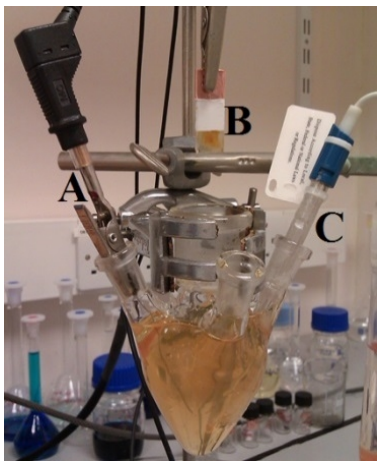

Figure 6.4.1: Electrochemical cell formed from three electrodes where A is the counter electrode, B is the working electrode and C is the reference electrode.

The three-electrode cell used in this experiment consisted of a working electrode prepared from tin-doped indium oxide (ITO) coated glass slides. The spontaneously self-assembled film formed from BDHAB/SPEI solubilising 2.0mM and 4.0mM PAN/Pyrene cross-linked by EGDGE was deposited on a 1cm × 1cm ITO glass slide. A platinum (Pt) wire was used as counter electrode while a silver/silver chloride couple (Ag/AgCl, 3 M KCl) was used as reference electrode (Figure 6.4.1). Two metals ions (Fe^{3+} and Cu^{2+}) as chloride salts at 10 ppm final concentration were investigated. The metals salts were dissolved in 10mM H_2SO_4 as electrolyte solution. The electrochemical measurements were implemented by an electrochemical analyser microAutolab II potentiostat system (EcoChemie, Netherlands) with GPES software [*110*]. All scans were conducted at room temperature but the system was not thermostated. Figure 6.4.2 shows the cyclic voltammetry curves from the BDHAB/SPEI film coated electrodes in the 10mM H_2SO_4 electrolyte solution.

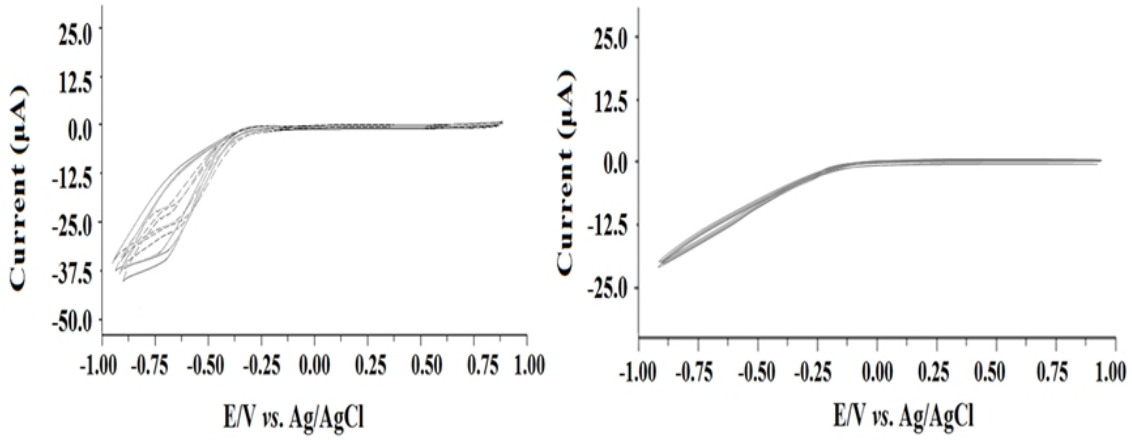

Figure 6.4.2: CV curves of BDHAB/SPEI/PAN/Pyrene coated electrodes in the 10mM H_2SO_4 electrolyte solution (left) and BDHAB/SPEI electrode without PAN/pyrene in the 10mM H_2SO_4 electrolyte solution containing 10ppm Cu^{2+}. The potential was scanned between −0.95 and +0.95 V with scan rate of 30 mV per second for 8 scan cycles.

The CV measurement curves for the acidic electrolyte solution without any metals ions using BDHAB/SPEI/PAN/Pyrene as the working electrode showed flat lines at all positive potentials in the voltage scan. The shoulder in the curves at negative potentials (-0.25 to -0.95V) could be attributed to reduction of H^+ in the acidic solution [*111*]. When a BDHAB/SPEI films on electrodes without PAN and pyrene was scanned in presence of 10ppm Cu^{2+} no obvious oxidation/reduction process was seen, confirming the fact that the PAN/pyrene sensor was required to observe any electrochemical activity in the films. Overall no significant anodic or cathodic peaks were found during

the scan of the blank 10mM H_2SO_4 electrolyte solution for both BDHAB/SPEI/PAN/Pyrene electrode without metal ions or for BDHAB/SPEI electrode without PAN/Pyrene in presence of Cu^{2+}.

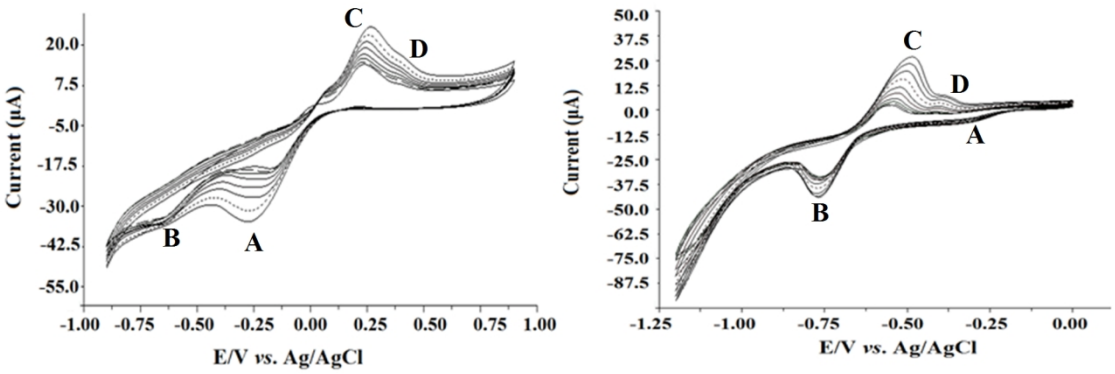

Figure 6.4.3: Cyclic voltammetry curves of BDHAB/SPEI/PAN/pyrene as the working electrode measured in an acidic solution containing 10ppm Cu^{2+} where the measurements of the potential was scanned between −0.95 and 0.95 V with a potential scan rate of 30 mV s^{-1} for 9 scan cycles (left image). The right image is the cyclic voltammetry curves of BDHAB/SPEI/PAN/pyrene as the working electrode measured in an acidic solution containing 10ppm Fe^{3+} where the measurements of the potential was scanned between −0.12 and 1.25 V with a potential scan rate of 30 mV s^{-1} for 10 scan cycles.

The I/E curves of copper ion solution when using an electrode coated in the BDHAB/SPEI/PAN/pyrene film show a peak (A) starting at -0.13V, then after 8 cycles end up at -0.25V. This peak corresponds to the reduction of Cu^{2+} to Cu^{+1} and this peak show increases in the current value with time. As the potential becomes more negative, a peak B, is also exhibited at -0.66V. This peak is related to the reduction of Cu^{+1} to Cu. When the potential changes toward more positive values, the metallic copper is oxidized on the electrode surface resulting in a change in the observed current. The broad peak around +0.25V contains two overlapping peaks at +0.26V (peak C) and +0.40 (peak D) which corresponds to oxidation of Cu^{+1} and Cu^{2+} respectively (Figure 6.4.3 left image) [*111, 112*].

CV scans of ferric ion solutions using an electrode coated in the BDHAB/SPEI/PAN/pyrene film show small peak (A) at -0.30V related to the reduction of Fe^{3+} to Fe^{2+}. The second reduction occurred at potential -0.75V (B) where the two

peaks around -0.50V (peak C) and -0.37 (peak D) corresponds to oxidation of ferric and ferrous iron ions (Figure 6.4.3 right image) [*107, 113*]. Figure 6.4.3 shows clearly that CV scans using BDHAB/SPEI/PAN/pyrene as a working electrode in presence of metal ions exhibited obvious anodic or cathodic peaks while CV scans without the metal ions do not show these features. The second observation from the CV scans for both Cu^{2+} and Fe^{3+} metal ions is that the current signal increases with time for both reduction and oxidation peaks. This increase is proportional to time however the scan rate was fixed ($30mVs^{-1}$). This result suggests that metal ions are diffusing and accumulating at the BDHAB/SPEI/PAN/pyrene electrode therefore causing an increase the current signal [*114*].

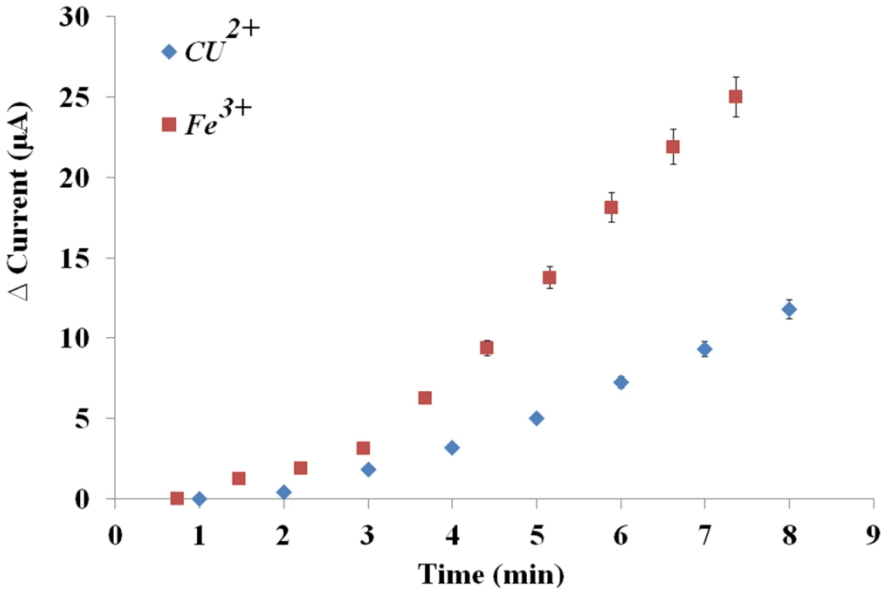

Figure 6.4.4: The differential of cyclic voltammetric current for the first oxidation peak measurement at BDHAB/SPEI/PAN/Pyrene electrode in 10ppm Cu^{2+} solution and 10ppm Fe^{3+} solution for 8 min.

The increase of CV current during scan time was calculated and plotted as seen in Figure 6.4.4. This increase of CV current corresponds to an increase of metal ions concentration at the BDHAB/SPEI/PAN/Pyrene electrode and differs for Cu^{2+} and Fe^{3+} ions which indicates that diffusion rate for these ions in the film varied [*115*]. Also, the maximum CV current of Fe^{3+} ions was 27µA after 8 min while CV current of Cu^{2+} ions was 24µA suggesting that the affinity and sensitivity detection of these metal ions at the BDHAB/SPEI/PAN/Pyrene working electrode was different [*113*]. Overall this variation in behaviour of these metal ions at the BDHAB/SPEI/PAN/Pyrene working

electrode suggests that this electrode could be used as a metal ion sensor to detect several metal ions at the same time.

This preliminary cyclic voltammetry study focused on the performance of a cross-linked surfactant/SPEI film solubilising PAN and pyrene as a metal ion sensor and it showed clearly differences between CV measurements for this electrode in presence and absence of metal ions, which demonstrate the effective voltammetry activity of this system. However there is no function of solubilised pyrene in this electrode, nevertheless pyrene molecules was kept in these electrodes to ensure that the final structures were retained, also to demonstrate the possibility to prepare a multifunctional electrode which might be working as electrochemically active sensor, as well as allowing simultaneous UV-Vis and fluorescence measurements.

In future work full comparison of these surfactant/SPEI films solubilising different concentrations of PAN and pyrene should be investigated using the cyclic voltammetry method to determine the influence of the mesostructure and composition of these films on the electrochemical activity.

6.4.2 Fluorescence and UV-Vis of surfactant/PEI/PAN/Pyrene films.

Fluorescence spectroscopy is widely used for detection of a broad range of chemical compounds since it is highly sensitive, simple to apply, and uses low cost instrumentation [*116-118*]. Recently several methods to detect and quantify transition metal ions have been developed using fluorescence sensors. This technique has advantages, because it does not need extensive sample preparation and it is a relatively fast technique [*119-121*]. In this work fluorescence spectroscopy was performed on a Perkin Elmer LS 50B Spectrometer. The excitation wavelength was used at 300nm and the spectrum was recorded between 350nm and 660nm. Different concentrations of Cu^{2+} as copper chloride ($CuCl_2$) was added gradually to a solution consisting of BDHAB, SPEI, PAN, pyrene and EGDGE at concentrations of 10.0, 1.2, 0.6 and 2.0 mM respectively. The emission wavelength was 337nm ±2nm, where the spectra and the intensity at the maxima (372nm) were recorded. Figure 6.4.5 illustrates the fluorescence spectra of a BDHAB/SPEI/PAN/Pyrene solution with increasing amounts of Cu^{2+} ions. From this Figure it shows that by increasing the concentration of copper

ions the intensity of fluorescence increases proportionally. However the interaction of copper ions with BDHAB/SPEI/PAN/pyrene solutions does not show any new fluorescence peak as expected [*122*]. This could be related to the complex formation between copper ions and PAN and also intramolecular π-π interactions, between PAN and pyrene inside BDHAB micelles [*123*]. Fluorescence scans at a relatively high concentration of BDHAB/PAN/Pyrene solutions display low signal/noise ratio while the curves from solutions at low concentrations of BDHAB/PAN/pyrene solutions have lower signals in the Cu^{2+} calibration curve.

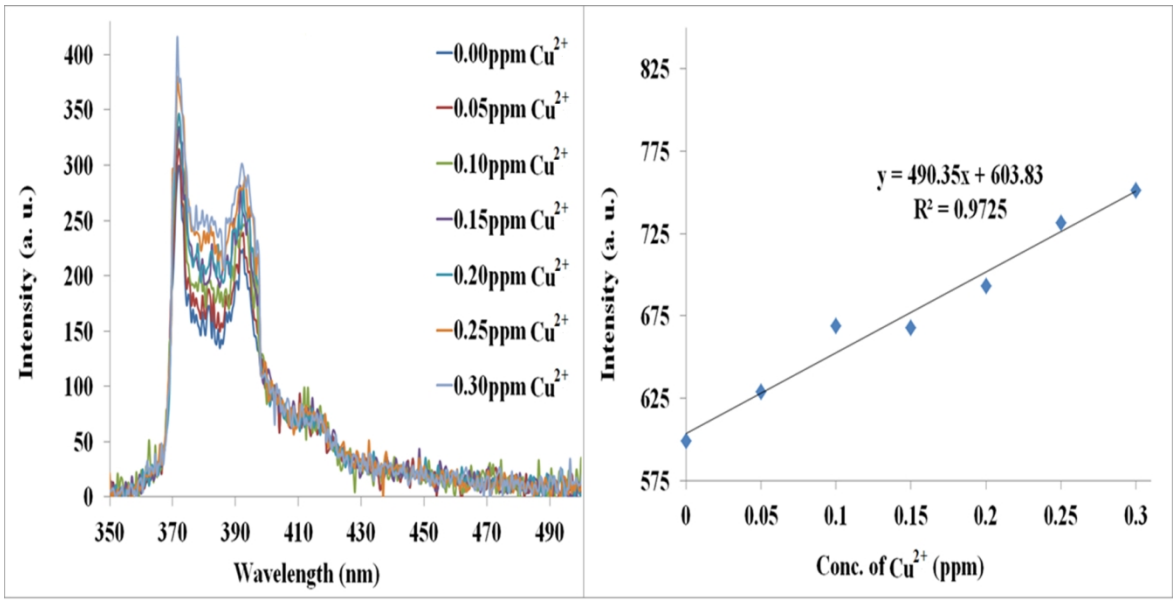

Figure 6.4.5: Fluorescence spectra of a BDHAB/SPEI/PAN/Pyrene solution with increasing amounts of Cu^{2+} ions (left) and the calibration curve for Cu^{2+} addition calculated from fluorescence spectra at the intensity maxima of 372nm.

The calibration curve of Cu^{2+} using BDHAB/SPEI/PAN/Pyrene solutions as the fluorescent metal ion sensor shows a detection range from 0.05ppm up to 3.0ppm which is about three times higher (for instance) than results found by Lan et al. [*124*] however the fluorescent probes made by this author were selective and sensitive for detection of copper ions. Figure 6.4.6 shows fluorescence spectra of BDHAB/SPEI/PAN/Pyrene solution with Zn^{2+} and with Co^{2+} ions.

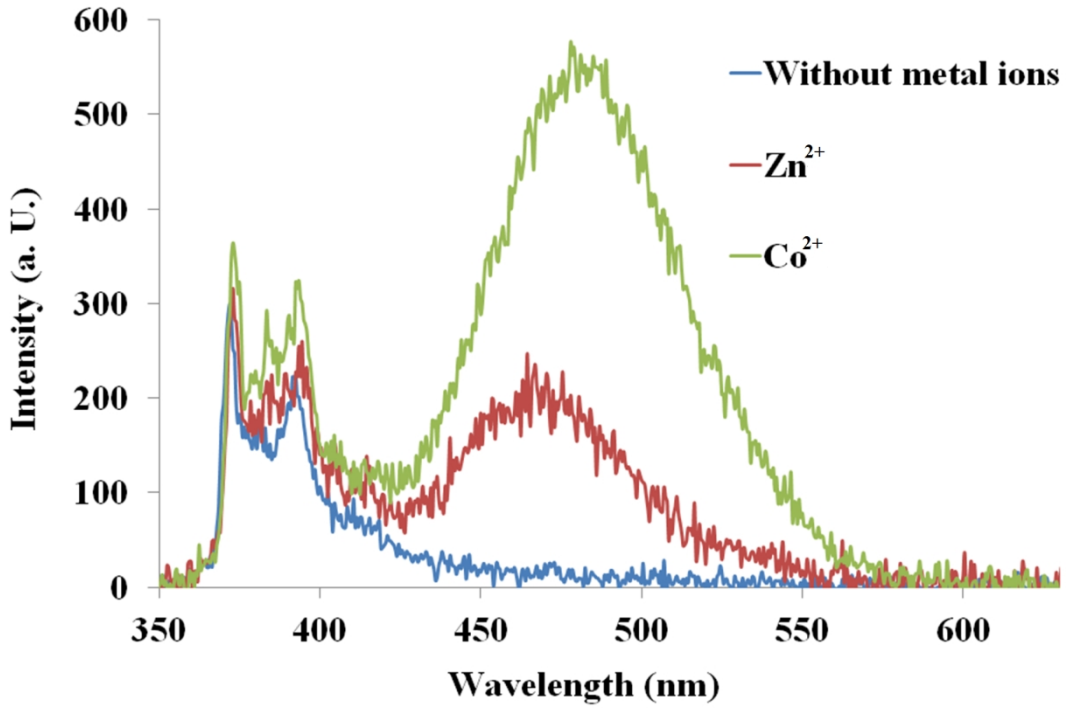

Figure 6.4.6: Fluorescence spectra of BDHAB/SPEI/PAN/Pyrene solutions with 10ppm Zn^{2+} or 10ppm Co^{2+} at an excitation wavelength of 342 nm.

As seen from the previous Figure 6.4.6 the fluorescence spectra of BDHAB/SPEI/PAN/pyrene solution with Cu^{2+} ions did not show any peak between 400nm-500nm. However the fluorescence spectra of BDHAB/SPEI/PAN/Pyrene solutions interacting with 10 ppm of Zn^{2+} showed a broad peak between 420nm-520nm, while the same concentration of Co^{2+} produces a very intense and broad peak in the same region (Figure 6.4.6). These peaks found in the case of Zn^{2+} and Co^{2+} are possibly due to strong intramolecular π–π interaction between PAN and pyrene units which result in an increase in the excimer emission [*125*]. This result agrees with the conclusion of Safari et al [*66*] that the stoichiometry of PAN/Metal complexes molar ratio for Co^{2+}, Ni^{2+} and Zn^{2+} ions was 2:1 as stated before (section 3.1.2 Figure 6.6). This result suggests that the BDHAB/SPEI/PAN/Pyrene system can work as a selective fluorescence sensor for those two metal ions and the high peak intensity shown for the fluorescence spectrum with Co^{2+} ions suggests a high relative sensitivity for this metal ion.

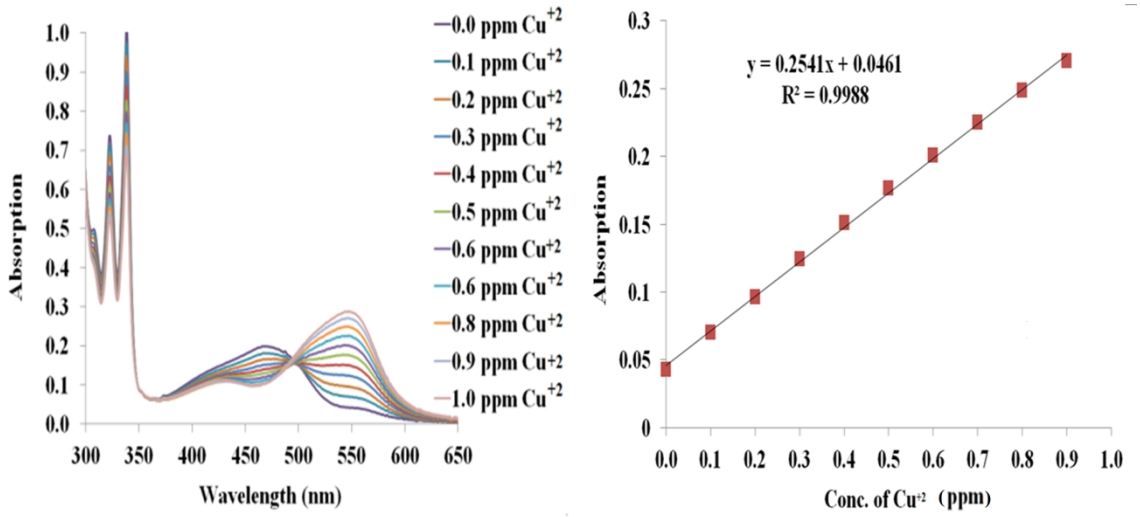

Figure 6.4.7: UV-Vis spectra of BDHAB/SPEI/PAN/pyrene solution with increasing amounts of Cu^{2+} ions (left) and calibration curve of Cu^{2+}addition where calculated from the Vis. region spectra at the intensity maxima of 545nm.

The same concentrations of BDHAB/SPEI/PAN/Pyrene solutions were tested by UV-Vis spectroscopy in the presence of metal ions. The experiment was carried out in a Hewlett Packard HP spectrometer with linear diode array. Scan measurements were recorded between 200-800 nm^{-1} with the addition of different concentrations of Cu^{2+} ions. The UV-Vis spectra of the BDHAB/SPEI/PAN/pyrene solution shows growth of a new peak at 545nm as the Cu^{2+} concentration increases, while the peak at 465nm exhibits a decrease in intensity at the same time (Figure 6.4.7). This change in UV-Vis absorption for these two bands is due to the n-π* electronic transitions arising from Cu^{2+} and PAN interaction [*126*]. On the other hand, peaks in the UV region at 309, 322 and 337 nm show an increasing intensity with increase of Cu^{2+} concentration. The calibration curve of UV-Vis measurements for BDHAB/SPEI/PAN/Pyrene in the presence of Cu^{2+} ions shows a linear detection range from 0.10ppm up to 1.0ppm with good R-squared values when fitting a straight line. This result suggests that the BDHAB/SPEI/PAN/pyrene system can also be used as metal ion sensor by using UV-Vis detection. The detection range found here using UV-Vis spectroscopy with the BDHAB/SPEI/PAN/Pyrene solution is 5 times more efficient than the detection range of Cu^{2+} found by Shvoeva et al, however they used direct UV-Vis measurements for PAN/Cu^{2+} ions in organic solutions [*127*]. Yun et al. on the other hand demonstrated 0.023ppm detection limits of Cu^{2+} also by using UV-Vis micellar colorimetric determination of metal ions complexes but using Tween 80 micellar medium as the

surfactant micelles rather than the BDHAB used here. However interference effects were found among different analytes ions when using Tween 80 micelle solutions to host the PAN. [*128*].

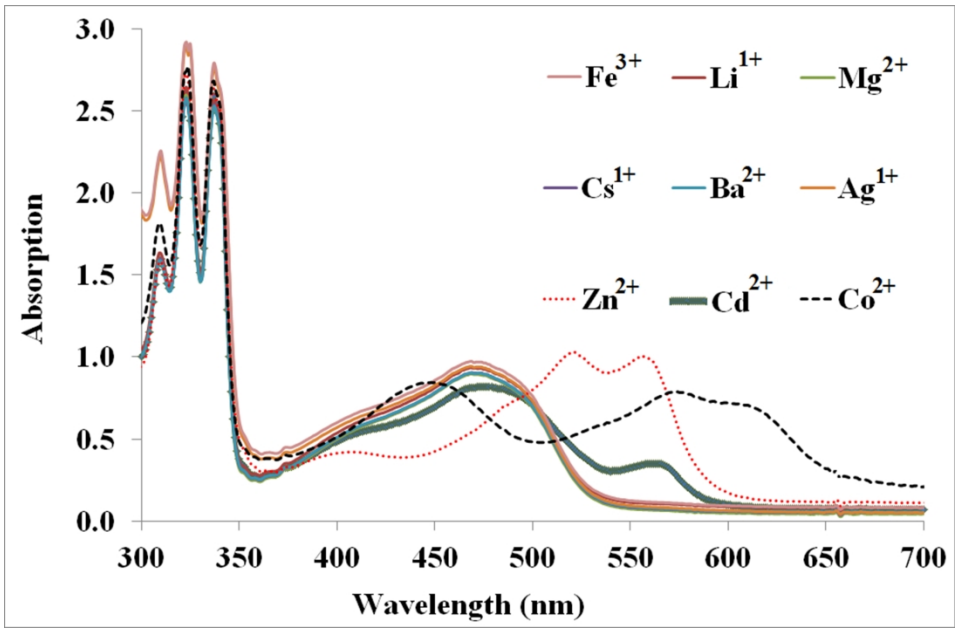

Figure 6.4.8: UV-Vis spectra of BDHAB/SPEI/PAN/Pyrene solutions with a broad range of metal ions.

The UV-Vis scan of BDHAB/SPEI/PAN/pyrene solutions without metal ions shows three peaks at the range between 300nm – 350nm and a broad peak at 465nm. As stated above by adding Cu^{2+} to BDHAB/SPEI/PAN/pyrene solutions a new peak arose at 545nm (Figure 6.4.8). This behaviour was not seen when 10ppm of each of Fe^{3+}, Li^{+1}, Mg^{2+}, Cs^{+1}, Ba^{2+} and Ag^{+1} were mixed with the BDHAB/SPEI/PAN/Pyrene solution. These solutions did not alter the UV-Vis scan compared to that of the BDHAB/SPEI/PAN/Pyrene solution without any metal ions, as seen in Figure 6.4.8. On the other hand Zn^{2+}, Cd^{2+} and Co^{2+} gave different UV-Vis scan features. This result agreed with fluorescence experiment since addition of Zn^{2+} and Co^{2+} showed different fluorescence spectra compared with Cu^{2+} ions. As mentioned above this behaviour is due to the n-π^* electronic transitions during metal/PAN complex interaction as seen in Figure 6.4.8 [*126*]. This variation in the UV-Vis absorption for these metal ions suggests that the UV-Vis spectroscopy method can be used for the selective detection of Zn^{2+}, Cd^{2+} and Co^{2+} ions using BDHAB/SPEI/PAN/pyrene solutions. Unfortunately attempts to use UV-Vis spectroscopy on similar systems supported in films did not

succeed due to light scattering by the film and insufficient time was available to find a solution to this problem.

In general, the electrochemical cell using BDHAB/SPEI/PAN/Pyrene films as the working electrode showed a good sensitivity for metal ions so may be one way to develop a sensor from these films. UV-Vis and fluorescence spectra illustrated sensitivity and selectivity for BDHAB/SPEI/PAN/pyrene solutions but insufficient time was available to optimise the films as optical sensors. From these results it can be said that the BDHAB/SPEI/PAN/Pyrene system could work as a multifunctional sensor with high selectivity and sensitivity for detection of metal ions. However one of the purposes of these films was to use it in dip stick testing to offer a simple and sensitive method of measuring metal ion content in aqueous samples, and this was not achieved. Investigation directly of solid films using UV-Vis or fluorescence spectroscopy did not provide accurate and reasonable results so far. This could be related to the high concentration of surfactant in solid state films which cause the films to become opaque and which shields the signals from the other components. In future work different concentrations of surfactant, PEI and PAN/Pyrene should be tested to find the best concentration to prepare solid films as sensors with maintains a good 3D nanostructure.

6.5 Conclusion

In this chapter it was successfully shown that solid nanostructured polyelectrolyte films formed through self-assembly at the air solution interface are promising hosts for metal ions sensors. A combine of fluorescence and chelating molecules was achieved in a simple way by encapsulating pyrene and PAN inside cationic surfactant micelles.

The SANS data of the cationic surfactants solutions in the presence and absence of PAN and pyrene illustrated a prolate ellipsoid micelle shape. The micelle volume of C_{16} hydrocarbon chain of benzyldimethyl-headgroup micelles without PAN/Pyrene was 3.6 times bigger than that of the equivalent C_{12} surfactant, while in the presence of pyrene the micelle volume was 6.4 times bigger. These results emphasise that morphology of these surfactant micelles are highly dependent on the surfactant tail length. Alkyl-pyridinium bromide surfactants showed lower micelle volumes and encapsulation capacities than alkyl- benzyldimethyl bromide surfactants with an equivalent hydrocarbon tail length.. This indicates that both the surfactant hydrocarbon chain and surfactant headgroup play important roles in determining the micelle size and shape, and thus the aggregation number of these cationic surfactants. BDHAB showed extraordinary increase of N_{agg} compared with other surfactants which supports the idea that in this molecule benzyl group can potentially act as a second hydrocarbon tail. In general encapsulating hydrophobic molecules in both alkyl-benzyldimethyl and alkyl-pyridinium bromide surfactant micelles changes the micelles from long prolate to rod-like shapes.

Addition of metal ions into surfactant/PEI/PAN/Pyrene solutions resulted in formation of new micelle geometries and changes in micelle volume. This was mainly due to direct interaction between PAN and metal ions forming complexes, and this interaction overall influences the micelles aggregation behaviour when solubilizing PAN in the micelles.

In general BDHAB/SPEI and CPBr/SPEI films solubilising PAN and pyrene were shown to have relatively high numbers of layers and large crystallite sizes within these films. This suggests that they should be an ideal sensor with multiple interaction sites due to the high potential surface area which will be available on the micelle surfaces. Also GIXD confirmed that the micelles in these surfactant systems are packed in films

at the air-liquid interface to form highly ordered arrays, with a final 2D hexagonal mesostructure where the cylindrical micelles are oriented with the long axis of the cylinders parallel to the air–solution interface. This structure also supports the goal of high surface interactions and rapid ion diffusions which should thus increase the sensor sensitivity.

Electrochemical characterization of cationic surfactant/PEI films solubilising PAN/Pyrene proved that metal ions are diffusing and accumulating at the BDHAB/SPEI/PAN/Pyrene electrode therefore causing an increase the current signal. The signal differed for different metal ions which suggests that these electrodes can be used as a metal ion sensor to detect several metal ions at the same time. Both fluorescence and UV-Vis spectroscopy illustrated high sensitivity and selectivity of BDHAB/SPEI/PAN/Pyrene solutions as metal ions sensors but further work is required to incorporate this system into films to prepare an optical sensor. All of these multifunctional detection methods suggest that the surfactant/PEI/PAN/Pyrene system can work as a multifunctional sensor with high selectivity and sensitivity for detection of metal ions, if further development is carried out.

6.6 References

1. Rurack, K. (2001) Flipping the light switch 'ON' - The design of sensor molecules that show cation-induced fluorescence enhancement with heavy and transition metal ions, *Spectrochimica Acta - Part A Molecular and Biomolecular Spectroscopy 57*, 2161-2195.
2. De Silva, A. P., Fox, D. B., Moody, T. S., and Weir, S. M. (2001) Luminescent sensors and photonic switches, *Pure Appl Chem 73*, 503-511.
3. El-Betany, A. M. M., Vachova, L., Bezzu, C. G., Pope, S. J. A., and McKeown, N. B. (2013) The synthesis and study of fluorescent PAMAM-based dendritic molecules, *Tetrahedron 69*, 8439-8445.
4. Lin, G., Xu, H., Cui, Y., Wang, Z., Yang, Y., and Qian, G. (2013) An ortho-methylated fluorescent chemosensor based on pyrromethene for highly selective and sensitive detection of Ag+ and Hg2+ ions, *Materials Chemistry and Physics 141*, 591-595.
5. Wang, F., Peng, R., and Sha, Y. (2008) Selective dendritic fluorescent sensors for Zn(II), *Molecules 13*, 922-930.
6. Díaz-Fernández, Y., Péres-Gramatges, A., Rodríguez-Calvo, S., Mangano, C., and Pallavicini, P. (2004) Structure and dynamics of micelle-based fluorescent sensor for transition metals, *Chem. Phys. Lett. 398*, 245-249.
7. Perez-Gramatges, A., and Chatt, A. (2006) Preconcentration neutron activation analysis of lanthanides by cloud point extraction using PAN, *Journal of Radioanalytical and Nuclear Chemistry 269*, 491-497.
8. Edler, K. J., Goldar, A., Brennan, T., and Roser, S. J. (2003) Spontaneous free-standing nanostructured film growth in polyelectrolyte-surfactant systems, *Chemical Communications 9*, 1724-1725.
9. Kenawy, I. M. M., Hafez, M. A. H., Akl, M. A., and Lashein, R. R. (2000) Determination by AAS of some trace heavy metal ions in some natural and biological samples after their preconcentration using newly chemically modified chloromethylated polystyrene-PAN ion-exchanger, *Analytical Sciences 16*, 493-500.
10. Shemirani, F., and Akhavi, B. T. S. (2001) Preconcentration and determination of trace cadmium using 1-(2-pyridylazo)-2-naphthol (PAN) immobilized on surfactant-coated alumina, *Analytical Letters 34*, 2179-2188.
11. Bermejo-Barrera, P., Martínez Alfonso, N., Díaz López, C., and Bermejo Barrera, A. (2003) Use of Amberlite XAD-2 loaded with 1-(2-pyridylazo)-2-naphthol as a preconcentration system for river water prior to determination of Cu 2+, Cd2+ and Pb2+ by flame atomic absorption spectroscopy, *Mikrochimica Acta 142*, 101-108.
12. Narin, I., and Soylak, M. (2003) The uses of 1-(2-pyridylazo) 2-naphtol (PAN) impregnated Ambersorb 563 resin on the solid phase extraction of traces heavy metal ions and their determinations by atomic absorption spectrometry, *Talanta 60*, 215-221.
13. Yang, L., Hu, B., Jiang, Z., and Pan, H. (2004) On-line separation and preconcentration of trace metals in biological samples using a microcolumn loaded with PAN-modified nanometer-sized titanium dioxide, and their determination by ICP-AES, *Microchim Acta 144*, 227-231.

14. Tuzen, M., Parlar, K., and Soylak, M. (2005) Enrichment/separation of cadmium(II) and lead(II) in environmental samples by solid phase extraction, *J Hazard Mater 121*, 79-87.
15. Tokalioğlu, Ş., Büyükbaş, H., and Kartal, Ş. (2006) Preconcentration of trace elements by using 1-(2-pyridylazo)-2-naphthol functionalized amberlite XAD-1180 resin and their determination by FAAS, *Journal of the Brazilian Chemical Society 17*, 98-106.
16. Afzali, D., and Mostafavi, A. (2008) Potential of modified multiwalled carbon nanotubes with 1-(2-pyridylazo)-2-naphtol as a new solid sorbent for the preconcentration of trace amounts of cobalt(II) ion, *Analytical Sciences 24*, 1135-1139.
17. Afzali, D., and Mostafavi, A. (2008) Determination of trace amounts of Cu2+, Ni2+, and Mn2+ ions after preconcentration onto PAN-immobilized organo nanoclay as a new sorbent, *Journal of AOAC International 91*, 1430-1434.
18. Kaur, A., and Gupta, U. (2009) Preconcentration of zinc and manganese using 1-(2-pyridylazo)-2-naphthol anchored SiO2 nanoparticles, *Eurasian J. Anal. Chem. 4*, 234.
19. Tavallali, H. (2011) Determination of Pb (II) in some real samples based on alumina-coated magnetite nanoparticles solid phase extraction method, *International Journal of ChemTech Research 3*, 1641-1646.
20. Jaggi, S., and Gupta, U. (2013) Solid phase extraction and preconcentration of Ni(II) using 1-(2-pyridylazo)-2-naphthol) (PAN) modified β-cyclodextrin butanediol diglycidyl ether polymer as a solid phase extractant, *Macedonian Journal of Chemistry and Chemical Engineering 32*, 57-67.
21. O'Driscoll, B. M. D., Hawley, A. M., and Edler, K. J. (2008) Incorporation of sparingly soluble species in mesostructured surfactant-polymer films, *J. Colloid Interface Sci. 317*, 585-592.
22. Kline, S. R. (2006) Reduction and analysis of SANS and USANS data using IGOR Pro, *Journal of Applied Crystallography 39*, 895-900.
23. Hayter, J. B., and Penfold, J. (1981) An analytic structure factor for macroion solutions, *Mol. Phys. 42*, 109-118.
24. Shipman, J., Wilson, J. D., Todd, A., and Higgins Jr, C. A. (2012) *An introduction to physical science*, Brooks/Cole Publishing Company.
25. Peyre, V., Bouguerra, S., and Testard, F. (2013) Micellization of dodecyltrimethylammonium bromide in water-dimethylsulfoxide mixtures: A multi-length scale approach in a model system, *J. Colloid Interface Sci. 389*, 164-174.
26. Klamkin, M. S. (1976) Corrections to "Elementary Approximations to the Area of N-Dimensional Ellipsoids", *The American Mathematical Monthly 83*, 478.
27. Klamkin, M. S. (1971) Elementary Approximations to the Area of N-Dimensional Ellipsoids, *The American Mathematical Monthly 78*, 280-283.
28. Wasbrough, M. J., Edler, K. J., Hawley, A. M., Holdaway, J. A., and Price, G. J. (2012) Control of mesostructure in self-assembled polymer/surfactant films by rational micelle design, *Soft Matter 8*, 3357-3362.
29. O'Driscoll, B. M. D., Milsom, E., Fernandez-Martin, C., White, L., Roser, S. J., and Edler, K. J. (2005) Thin films of polyethylenimine and alkyltrimethylammonium bromides at the air/water interface, *Macromolecules 38*, 8785-8794.
30. Rosen, M. J. (1978) *Surfactants and interfacial phenomena*, Wiley, New York.

31. Mata, J., Varade, D., and Bahadur, P. (2005) Aggregation behavior of quaternary salt based cationic surfactants, *Thermochimica Acta 428*, 147-155.
32. Malliaris, A., Lang, J., and Zana, R. (1986) Micellar aggregation numbers at high surfactant concentration, *J. Colloid Interface Sci. 110*, 237-242.
33. Berr, S., Jones, R. R. M., and Johnson, J. S., Jr. (1992) Effect of counterion on the size and charge of alkyltrimethylammonium halide micelles as a function of chain length and concentration as determined by small-angle neutron scattering, *Journal of Physical Chemistry 96*, 5611-5614.
34. Aswal, V. K., and Goyal, P. S. (2002) Role of different counterions and size of micelle in concentration dependence micellar structure of ionic surfactants, *Chem. Phys. Lett. 368*, 59-65.
35. Aswal, V. K., and Goyal, P. S. (2003) Role of different counterions and size of micelle in concentration dependence micellar structure of ionic surfactants, *Chem. Phys. Lett. 368*, 59-65.
36. Tiwari, A. K., Sonu, and Saha, S. K. (2013) Aggregation behaviour and thermodynamics of mixed micellization of gemini surfactants with a room temperature ionic liquid in water and water-organic solvent mixed media, *Journal of Chemical Thermodynamics 60*, 29-40.
37. Sarkar, B., Ravi, V., and Alexandridis, P. (2013) Micellization of amphiphilic block copolymers in binary and ternary solvent mixtures, *J. Colloid Interface Sci. 390*, 137-146.
38. Krishna, A. K., and Flanagan, D. R. (1989) Micellar solubilization of a new antimalarial drug, β-arteether, *journal of pharmaceuticals sciences. 78*, 574-576.
39. Rangel-Yagui, C. O., Pessoa, A., Jr., and Tavares, L. C. (2005) Micellar solubilization of drugs, *8*, 147-165.
40. Chaiko, M. A., Nagarajan, R., and Ruckenstein, E. (1984) Solubilization of single-component and binary mixtures of hydrocarbons in aqueous micellar solutions, *J. Colloid Interface Sci. 99*, 168-182.
41. Evans, D. F., Mukherjee, S., Mitchell, D. J., and Ninham, B. W. (1983) Surfactant diffusion: New results and interpretations, *J. Colloid Interface Sci. 93*, 184-204.
42. Okano, L. T., Quina, F. H., and El Seoud, O. A. (2000) Fluorescence and light-scattering studies of the aggregation of cationic surfactants in aqueous solution: Effects of headgroup structure, *Langmuir 16*, 3119-3123.
43. Israelachvili, J. N., Mitchell, D. J., and Ninham, B. W. (1976) Theory of self-assembly of hydrocarbon amphiphiles into micelles and bilayers, *Journal of the Chemical Society, Faraday Transactions 2: Molecular and Chemical Physics 72*, 1525-1568.
44. Haldar, J., Aswal, V. K., Goyal, P. S., and Bhattacharya, S. (2004) Small-angle neutron scattering study of aggregate structures of multi-headed pyridinium surfactants in aqueous solution, *Pramana - Journal of Physics 63*, 303-307.
45. Carnero Ruiz, C., Díaz-López, L., and Aguiar, J. (2007) Self-assembly of tetradecyltrimethylammonium bromide in glycerol aqueous mixtures: A thermodynamic and structural study, *J. Colloid Interface Sci. 305*, 293-300.
46. Zhang, Y., Qi, Y., and Zakin, J. L. (2005) Headgroup effect on drag reduction and rheological properties of micellar solutions of quaternary ammonium surfactants, *Rheologica Acta 45*, 42-58.
47. Chachaty, C., Warr, G. G., Jansson, M., and Li, P. (1991) Influence of the polar head size on the dynamics of micellized surfactants, *Journal of Physical Chemistry 95*, 3830-3836.

48. Chachaty, C. (1987) Applications of NMR methods to the physical chemistry of micellar solutions, *Progress in Nuclear Magnetic Resonance Spectroscopy 19*, 183-222.
49. Buckingham, S. A., Garvey, C. J., and Warr, G. G. (1993) Effect of head-group size on micellization and phase behavior in quaternary ammonium surfactant systems, *Journal of Physical Chemistry 97*, 10236-10244.
50. Blackmore, E. S., and Tiddy, G. J. T. (1988) Phase behaviour and lyotropic liquid crystals in cationic surfactant-water systems, *Journal of the Chemical Society, Faraday Transactions 2: Molecular and Chemical Physics 84*, 1115-1127.
51. Bacaloglu, R., Blasko, A., Bunton, C. A., Cerichelli, G., and Shirazi, A. (1991) Segmental motions of free and micellized cationic surfactants, *Langmuir 7*, 1107-1111.
52. Khan, M. N. (2007) Micellar catalysis, CRC/Taylor & Francis, Boca Raton.
53. Attwood, D., and Florence, A. T. (1983) Surfactant systems, *Their Chemistry, Pharmacy and Biology*.
54. McCurdy, A., Jimenez, L., Stauffer, D. A., and Dougherty, D. A. (1992) Biomimetic catalysis of SN2 reactions through cation-pi interactions. The role of polarizability in catalysis, *Journal of the American Chemical Society 114*, 10314-10321.
55. Kuperkar, K., Abezgauz, L., Prasad, K., and Bahadur, P. (2010) Formation and growth of micelles in dilute aqueous CTAB solutions in the presence of NaNO3 and NaClO3, *Journal of Surfactants and Detergents 13*, 293-303.
56. Ranganathan, R., Okano, L. T., Yihwa, C., and Quina, F. H. (1999) Growth of cetyltrimethylammonium chloride and acetate micelles with counterion concentration, *J. Colloid Interface Sci. 214*, 238-242.
57. Aswal, V. K., and Goyal, P. S. (2000) Counterions in the growth of ionic micelles in aqueous electrolyte solutions: A small-angle neutron scattering study, *Physical Review E - Statistical Physics, Plasmas, Fluids, and Related Interdisciplinary Topics 61*, 2947-2953.
58. Hoffman, H., Loebl, M., Rehage, H., and Wunderlich, I. (1985) RHEOLOGY OF SURFACTANT SOLUTIONS, *Tenside Detergents 22*, 290-298.
59. Missel, P. J., Mazer, N. A., Benedek, G. B., Young, C. Y., and Carey, M. C. (1980) Thermodynamic analysis of the growth of sodium dodecyl sulfate micelles, *The Journal of Physical Chemistry 84*, 1044-1057.
60. Eastoe, J., Fragneto, G., Robinson, B. H., Towey, T. F., Heenan, R. K., and Leng, F. J. (1992) Variation of surfactant counterion and its effect on the structure and properties of Aerosol-OT-based water-in-oil microemulsions, *J. Chem. Soc., Faraday Trans. 88*, 461-471.
61. Szabó, L., Herman, K., Mircescu, N. E., Fălămaş, A., Leopold, L. F., Leopold, N., Buzumurgă, C., and Chiş, V. (2012) SERS and DFT investigation of 1-(2-pyridylazo)-2-naphthol and its metal complexes with Al(III), Mn(II), Fe(III), Cu(II), Zn(II) and Pb(II), *Spectrochimica Acta Part A: Molecular and Biomolecular Spectroscopy 93*, 266-273.
62. Pramanik, K., and Adhikari, B. (2010) 1-(2′-Pyridylazo)-2-naphtholate (PAN) complexes of rhodium(III): Synthesis, structure and spectral studies, *Polyhedron 29*, 1015-1022.
63. Basu, S., Halder, S., Pal, I., Samanta, S., Karmakar, P., Drew, M. G. B., and Bhattacharya, S. (2008) 1-(2′-Pyridylazo)-2-naphtholate complexes of

ruthenium: Synthesis, characterization, and DNA binding properties, *Polyhedron 27*, 2943-2951.

64. Adams, H., Bucknall, R. M., Fenton, D. E., Garcia, M., and Oakes, J. (1998) Self association in the structures of two copper (II)-Azo-dye complexes, *Polyhedron 17*, 4169-4177.
65. Shibata, S. (1961) Solvent extraction and spectrophotometric determination of metals with 1-(2-pyridylazo)-2-naphthol, *Anal. Chim. Acta 25*, 348-359.
66. Safari, Z., Gholivand, M. B., and Hosseinzadeh, L. (2011) Spectrophotometric study of complex formations between 1-(2-pyridylazo)-2-naphthol (PAN) and some metal ions in organic solvents and the determination of thermodynamic parameters, *Spectrochimica Acta Part A: Molecular and Biomolecular Spectroscopy 78*, 1606-1610.
67. Kuźniarska-Biernacka, I., Biernacki, K., Magalhães, A. L., Fonseca, A. M., and Neves, I. C. (2011) Catalytic behavior of 1-(2-pyridylazo)-2-naphthol transition metal complexes encapsulated in y zeolite, *J. Catal. 278*, 102-110.
68. Desiraju, G. R., Luss, H. R., and Smith, D. L. (1978) Resonance interactions in metal chelates of o-hydroxyazo compounds. Crystal growth, structure, and spectra of 1-(2-pyridylazo)-2-naphtholatochlorocopper(II), *Journal of the American Chemical Society 100*, 6375-6382.
69. Candau, S., Hirsch, E., and Zana, R. (1982) Effect of alcohol on the properties of micellar systems: IV. Effect of the isotopic composition of the system on the micellar properties in the presence and absence of 1-pentanol, *J. Colloid Interface Sci. 88*, 428-436.
70. Sabaté, R., Gallardo, M., and Estelrich, J. (2001) Location of pinacyanol in micellar solutions of N-alkyl trimethylammonium bromide surfactants, *J. Colloid Interface Sci. 233*, 205-210.
71. Lianos, P., Viriot, M. L., and Zana, R. (1984) Study of the solubilization of aromatic hydrocarbons by aqueous micellar solutions, *Journal of Physical Chemistry 88*, 1098-1101.
72. Bacaloglu, R., Bunton, C. A., and Ortega, F. (1989) Micellar enhancements of rates of SN2 reactions of halide ions. The effect of headgroup size, *Journal of Physical Chemistry 93*, 1497-1502.
73. Benrraou, M., Bales, B. L., and Zana, R. (2003) Effect of the nature of the counterion on the properties of anionic surfactants. 1. Cmc, ionization degree at the Cmc and aggregation number of micelles of sodium, cesium, tetramethylammonium, tetraethylammonium, tetrapropylammonium, and tetrabutylammonium dodecyl sulfates, *J. Phys. Chem. B 107*, 13432-13440.
74. Masrat, R., Maswal, M., and Dar, A. A. (2013) Competitive solubilization of naphthalene and pyrene in various micellar systems, *J Hazard Mater 244-245*, 662-670.
75. Dong, B., Zhao, X., Zheng, L., Zhang, J., Li, N., and Inoue, T. (2008) Aggregation behavior of long-chain imidazolium ionic liquids in aqueous solution: Micellization and characterization of micelle microenvironment, *Colloids and Surfaces A: Physicochemical and Engineering Aspects 317*, 666-672.
76. Zheng, O., and Zhao, J. X. (2006) Solubilization of pyrene in aqueous micellar solutions of gemini surfactants C12-s-C12ś2Br, *J. Colloid Interface Sci. 300*, 749-754.

77. Lianos, P., and Zana, R. (1981) Fluorescence probe studies of the effect of concentration on the state of aggregation of surfactants in aqueous solution, *J. Colloid Interface Sci. 84*, 100-107.
78. O'Driscoll, D., Fernandez-Martin, C., Wilson , D., Knott, J., Roser, J., and Edler, J. (2007) Macroscopic, mesostructured cationic surfactant/neutral polymer films: structure and cross-linking, *Langmuir 23*, 4589-4598.
79. O'Driscoll, B. M. D., Nickels, E. A., and Edler, K. J. (2007) Formation of robust, free-standing nanostructured membranes from catanionic surfactant mixtures and hydrophilic polymers, *Chemical Communications*, 1068-1070.
80. O'Driscoll, B. M. D., Fernandez-Martin, C., Wilson, R. D., Roser, S. J., and Edler, K. J. (2006) Effect of micelle composition on the formation of surfactant-templated polymer films, *J. Phys. Chem. B 110*, 5330-5336.
81. Yang, B., and Edler, K. J. (2009) Free-standing ordered mesoporous silica films synthesized with surfactant-polyelectrolyte complexes at the air/water interface, *Chem. Mater. 21*, 1221-1231.
82. Penfold, J., Richardson, R. M., Zarbakhsh, A., Webster, J. R. P., Bucknall, D. G., Rennie, A. R., Jones, R. A. L., Cosgrove, T., Thomas, R. K., Higgins, J. S., Fletcher, P. D. I., Dickinson, E., Roser, S. J., McLure, I. A., Hillman, A. R., Richards, R. W., Staples, E. J., Burgess, A. N., Simister, E. A., and White, J. W. (1997) Recent advances in the study of chemical surfaces and interfaces by specular neutron reflection, *J. Chem. Soc., Faraday Trans. 93*, 3899-3917.
83. Hedin, N., Sitnikov, R., Furo, I., Henriksson, U., and Regev, O. (1999) Shape Changes of C16TABr Micelles on Benzene Solubilization, *J. Phys. Chem. B 103*, 9631-9639.
84. Luechinger, M., Pirngruber, G. D., and Prins, R. (2004) Solubilization of Aromatic Molecules in Templating Micelles of Mesoporous Silicas Followed by 1H NMR, *J. Phys. Chem. B 108*, 10903-10910.
85. Ilekti, P., Martin, T., Cabane, B., and Piculell, L. (1999) Effects of polyelectrolytes on the structures and interactions of surfactant aggregates, *J. Phys. Chem. B 103*, 9831-9840.
86. Hillhouse, H. W., van Egmond, J. W., Tsapatsis, M., Hanson, J. C., and Larese, J. Z. (2001) The interpretation of X-ray diffraction data for the determination of channel orientation in mesoporous films, *Microporous Mesoporous Mater. 44-45*, 639-643.
87. Burns, A., Ow, H., and Wiesner, U. (2006) Fluorescent core-shell silica nanoparticles: Towards "lab on a particle" architectures for nanobiotechnology, *Chemical Society Reviews 35*, 1028-1042.
88. Bagher-Gholivand, M., Babakhanian, A., Mohammadi, M., Moradi, P., and Kiaie, S. H. (2013) Novel optical bulk membrane sensor and its application for determination of iron in plant and cereal samples, *Journal of Food Composition and Analysis 29*, 144-150.
89. Vaseashta, A., Dimova-Malinovska, D., and Marshall, M. (2005) Nanostructured and advanced materials for applications in sensor, optoelectronic and photovoltaic technology, Springer, Dordrecht; [Great Britain].
90. Jung, S. A., Lee, T. S., Kim, W. M., Lee, K. S., Jeong, D. S., Lee, W. S., and Kim, I. (2013) Thickness dependence of surface plasmon resonance sensor response for metal ion detection, *Journal of Physics D: Applied Physics 46*.
91. Wang, X., Drew, C., Lee, S. H., Senecal, K. J., Kumar, J., and Samuelson, L. A. (2002) Electrospun Nanofibrous Membranes for Highly Sensitive Optical Sensors, *Nano Lett. 2*, 1273-1275.

92. Goyal, P. S., and Aswal, V. K. (2001) Micellar structure and inter-micelle interactions in micellar solutions: Results of small angle neutron scattering studies, *Current Science 80*, 972-979.
93. Hudson, S., Tanner, D. A., Redington, W., Magner, E., Hodnett, K., and Nakahara, S. (2006) Quantitative TEM analysis of a hexagonal mesoporous silicate structure, *Phys. Chem. Chem. Phys. 8*, 3467-3474.
94. Edler, K. J., and Yang, B. (2013) Formation of mesostructured thin films at the air-liquid interface, *Chemical Society Reviews 42*, 3765-3776.
95. Yang, B., Holdaway, J. A., and Edler, K. J. (2013) Robust ordered cubic mesostructured polymer/silica composite films grown at the air/water interface, *Langmuir 29*, 4148-4158.
96. Chandra, D., Das, S. K., and Bhaumik, A. (2010) A fluorophore grafted 2D-hexagonal mesoporous organosilica: Excellent ion-exchanger for the removal of heavy metal ions from wastewater, *Microporous Mesoporous Mater. 128*, 34-40.
97. Xia, F., Zhang, X., Zhou, C., Sun, D., Dong, Y., and Liu, Z. (2010) Simultaneous determination of copper, lead, and cadmium at hexagonal mesoporous silica immobilized quercetin modified carbon paste electrode, *Journal of Automated Methods and Management in Chemistry 2010*.
98. Sherif A. El-Safty, M. A. S. (2012) High-Order Mesoporous (HOM) Sensors for Visual Recognition of Toxic Metal Ions from Drinking Water, *The 14th International Meeting on Chemical Sensors IMCS 2012*, 725 - 725.
99. Meiring, J. E., Schmid, M. J., Grayson, S. M., Rathsack, B. M., Johnson, D. M., Kirby, R., Kannappan, R., Manthiram, K., Hsia, B., Hogan, Z. L., Ellington, A. D., Pishko, M. V., and Willson, C. G. (2004) Hydrogel biosensor array platform indexed by shape, *Chem. Mater. 16*, 5574-5580.
100. Hong, W., Li, W., Hu, X., Zhao, B., Zhang, F., and Zhang, D. (2011) Highly sensitive colorimetric sensing for heavy metal ions by strong polyelectrolyte photonic hydrogels, *J. Mater. Chem. 21*, 17193-17201.
101. Guschin, D., Yershov, G., Zaslavsky, A., Gemmell, A., Shick, V., Proudnikov, D., Arenkov, P., and Mirzabekov, A. (1997) Manual Manufacturing of Oligonucleotide, DNA, and Protein Microchips, *Analytical Biochemistry 250*, 203-211.
102. Ji, H. F., Thundat, T., Dabestani, R., Brown, G. M., Britt, P. F., and Bonnesen, P. V. (2001) Ultrasensitive detection of CrO4 2- using a microcantilever sensor, *Analytical Chemistry 73*, 1572-1576.
103. Zhang, Y., Ji, H. F., Brown, G. M., and Thundat, T. (2003) Detection of CrO4 2- using a hydrogel swelling microcantilever sensor, *Analytical Chemistry 75*, 4773-4777.
104. Carballo, S., Terán, J., Soto, R. M., Carlosena, A., Andrade, J. M., and Prada, D. (2013) Green approaches to determine metals in lubricating oils by electrothermal atomic absorption spectrometry (ETAAS), *Microchemical Journal 108*, 74-80.
105. Jisha, B., Resmi, M. R., Maya, R. J., and Varma, R. L. (2013) Colorimetric detection of Al(III) ions based on triethylene glycol appended 8-propyloxy quinoline ester, *Tetrahedron Lett 54*, 4232-4236.
106. Tan, D., He, Y., Xing, X., Zhao, Y., Tang, H., and Pang, D. (2013) Aptamer functionalized gold nanoparticles based fluorescent probe for the detection of mercury (II) ion in aqueous solution, *Talanta 113*, 26-30.
107. International Symposium on Electrochemistry in, M., Metal Processing, D. F. M. K. G. H. W. R. E. S. I. E., and Electrochemical Engineering, D.

Electrochemistry in mineral and metal processing VII, Electrochemical Society, Pennington, NJ.
108. Sebez, B., Ogorevc, B., Hocevar, S. B., and Veber, M. (2013) Functioning of antimony film electrode in acid media under cyclic and anodic stripping voltammetry conditions, *Anal. Chim. Acta 785*, 43-49.
109. Choi, C., Jeong, Y., and Kwon, Y. (2013) Detection of trace copper metal at carbon nanotube based electrodes using squarewave anodic stripping voltammetry, *Bulletin of the Korean Chemical Society 34*, 801-809.
110. Rassaei, L., Jaber, R., Flower, S. E., Edler, K. J., Compton, R. G., James, T. D., and Marken, F. (2010) Microwave-electrochemical formation of colloidal zinc oxide at fluorine doped tin oxide electrodes, *Electrochim Acta 55*, 7909-7915.
111. Popescu, A. M., Constantin, V., Cojocaru, A., and Olteanu, M. (2011) Electrochemical behaviour of Copper (II) chloride in choline chloride-urea deep eutectic solvent, *Revista de Chimie 62*, 206-211.
112. Trnkova, L., Zerzankova, L., Dycka, F., Mikelova, R., and Jelen, F. (2008) Study of copper and purine-copper complexes on modified carbon electrodes by cyclic and elimination voltammetry, *Sensors 8*, 429-444.
113. Van Staden, J. F., and Matoetoe, M. C. (1998) Simultaneous determination of traces of iron(II) and iron(III) using differential pulse anodic stripping voltammetry in a flow-through configuration on a glassy carbon electrode, *Anal. Chim. Acta 376*, 325-330.
114. Salaün, P., and Van Den Berg, C. M. G. (2006) Voltammetric detection of mercury and copper in seawater using a gold microwire electrode, *Analytical Chemistry 78*, 5052-5060.
115. Liu, M., Deng, J., Chen, Q., Huang, Y., Wang, L., Zhao, Y., Zhang, Y., Li, H., and Yao, S. (2013) Sensitive detection of rutin with novel ferrocene benzyne derivative modified electrodes, *Biosensors and Bioelectronics 41*, 275-281.
116. Qiu, B., zhang, Y. S., Lin, Y. B., Lu, Y. J., Lin, Z. Y., Wong, K. Y., and Chen, G. N. (2013) A novel fluorescent biosensor for detection of target DNA fragment from the transgene cauliflower mosaic virus 35S promoter, *Biosensors and Bioelectronics 41*, 168-171.
117. Olivo, M., Ho, C. J. H., and Fu, C. Y. (2013) Advances in fluorescence diagnosis to track footprints of cancer progression in vivo, *Laser and Photonics Reviews 7*, 646-662.
118. Jeong, H. J., Ohmuro-Matsuyama, Y., Ohashi, H., Ohsawa, F., Tatsu, Y., Inagaki, M., and Ueda, H. (2013) Detection of vimentin serine phosphorylation by multicolor Quenchbodies, *Biosensors and Bioelectronics 40*, 17-23.
119. Li, M., Lv, H. S., Luo, J. Z., Miao, J. Y., and Zhao, B. X. (2013) An effective "turn-on" rodamine-based fluorescent chemosensor for Cu (II) in living cells, *Sens. Actuators, B 188*, 1235-1240.
120. Ganjali, M. R., Hosseini, M., Ghafarloo, A., Khoobi, M., Faridbod, F., Shafiee, A., and Norouzi, P. (2013) Selective recognition of Pr3 + based on fluorescence enhancement sensor, *Materials Science and Engineering C 33*, 4140-4143.
121. Ding, L., Wang, S., Liu, Y., Cao, J., and Fang, Y. (2013) Bispyrene/surfactant assemblies as fluorescent sensor platform: Detection and identification of Cu2+ and Co2+ in aqueous solution, *J Mater Chem A 1*, 8866-8875.
122. Zhao, C. L., Winnik, M. A., Riess, G., and Croucher, M. D. (1990) Fluorescence probe techniques used to study micelle formation in water-soluble block copolymers, *Langmuir 6*, 514-516.

123. Moriuchi-Kawakami, T., Hisada, Y., and Shibutani, Y. (2010) A Cu 2+ion-selective fluoroionophore with dual off/on switches, *Chemistry Central Journal 4*.
124. Lan, G. Y., Huang, C. C., and Chang, H. T. (2010) Silver nanoclusters as fluorescent probes for selective and sensitive detection of copper ions, *Chemical Communications 46*, 1257-1259.
125. Yang, R. H., Chan, W. H., Lee, A. W. M., Xia, P. F., Zhang, H. K., and Li, K. (2003) A ratiometric fluorescent sensor for Ag1 with high selectivity and sensitivity, *Journal of the American Chemical Society 125*, 2884-2885.
126. Karipcin, F., Dede, B., Percin-Ozkorucuklu, S., and Kabalcilar, E. (2010) Mn(II), Co(II) and Ni(II) complexes of 4-(2-thiazolylazo)resorcinol: Syntheses, characterization, catalase-like activity, thermal and electrochemical behaviour, *Dyes Pigments 84*, 14-18.
127. Shvoeva, O. P., Dedkova, V. P., Gitlits, A. G., and Savvin, S. B. (1997) Test methods for semiquantitative determination of heavy metals, *Journal of Analytical Chemistry 52*, 76-80.
128. Yun, J., and Choi, H. (2000) Micellar colorimetric determination of iron, cobalt, nickel and copper using 1-nitroso-2-naphthol, *Talanta 52*, 893-902.

7 Summery, Conclusions and Future Work

The overall aims of this project were threefold. First, to improve the understanding of cationic surfactant and polyelectrolyte interactions responsible for forming particular nanoscale structures in free-standing polymer amphiphile films, second to use the films as a template to form insoluble nanostructured polymers and third to use the films as supports for a metal ion sensor.

In the first section, the interactions in polyelectrolyte-cationic surfactant solutions and the relationship between these and the materials properties of the films were investigated by using different chain lengths and headgroups of cationic surfactants. The critical micellar concentration of surfactants was been used to study the free energy of micellization and degree of ionization of the surfactants by using conductivity measurements. SANS experiments were also used to study the micellar volume and aggregation number of cationic surfactants with and without addition of the film forming polyelectrolyte, polyethylenimine. Chapter 3 discussed the micellization behaviour of a wide range of cationic surfactants with varied head groups and hydrocarbon chain lengths. The results demonstrated that the nature and bulkiness of the surfactant headgroup and hydrocarbon chain length all play significant roles in surfactant micellization. Both aromatic and aliphatic headgroup cationic surfactants with three different hydrocarbon chains length (C_{12}, C_{14} and C_{16}) showed an exponential correlation between hydrocarbon chain length and critical micelle concentration, where increases in the number of methyl groups in the surfactant hydrocarbon tail reduced the critical micelle concentration. In addition thermodynamically it was more favourable for longer hydrocarbon chain surfactants to form micelles. On the other hand interactions between the polyelectrolyte PEI, and the cationic surfactants drives the surfactants to form micelles at lower concentrations.

SANS studies in Chapter 3 confirmed that the aggregation number in the presence and absence of PEI for the wide range of cationic surfactants increases with increased surfactant hydrocarbon chain length. The bulkiness of the surfactant headgroup however

caused a relative decrease in the N_{agg}. In general the influence of PEI on the broad range of cationic surfactants investigated was dissimilar. Therefore the structures formed by combining these cationic surfactants and PEI were driven by a complex interaction affected by several factors such as surfactant tail length, hydrophobicity and bulkiness of headgroup of these surfactants.

In this Chapter, only one type of polyelectrolyte (PEI) with different molecular weights were used with a variety of cationic surfactants to investigate the polymer/surfactant interaction. To extend our understanding of polymer/surfactant interactions further, different type of polyelectrolyte such as polyacrylamide, polyacrylic acid, polystyrene sulfonate, could be used with the same cationic surfactants as were used in this Chapter to compare the aggregation behaviour and the nature of these polymer /surfactant interactions.

The aim in Chapter 4 was to select PEI/cationic surfactant films with well-organized mesostructures as a first step towards synthesising nanoscale insoluble polymer membranes which could be used as supports for catalysis and size selective membranes. Therefore the encapsulation of hydrophobic monomers into cationic surfactant micelles in solutions and in solid polymer/surfactant films was investigated to determine the structure of the micelles formed in those systems which also provided good formation of the films at the interface, since there is a close relationship between the solution structures and the final structure of the films.

The solubilisation studies of styrene in cationic surfactant solutions by using UV-Vis spectroscopy in Chapter 4 demonstrated shifts in styrene λ_{max} from surfactant/styrene mixture solutions compared with a styrene/water scan. This shift is due to changes in the $\pi \rightarrow \pi^*$ transitions band due to attractive polarisation forces between the surfactant hydrocarbon chain and styrene hydrophobic monomer, which lower the energy levels of both the excited and unexcited states. This interaction between the surfactant hydrocarbon chain and styrene molecules indicates that styrene preferred to encapsulate inside the micelles at the hydrophobic tail region. SANS investigations of the encapsulated styrene monomer locations inside cationic surfactant micelles suggested

that styrene was encapsulated mainly in the palisade layer, although some of the encapsulated styrene was also located in the micelle core associated with the surfactant tails.

The influence of PEI on cationic surfactant micelle solutions encapsulating styrene demonstrated that there is an attractive complex interaction between the cationic surfactant micelles and PEI. Polyethylenimine binds to the cationic surfactant micelle headgroup through electrostatic interactions between the PEI amino group and the positive charge on the cationic headgroup. At the same time PEI interacts with water molecules close to the surfactant headgroup and also with PEI itself by hydrogen bonding.

The extent of encapsulated styrene was calculated and showed that cationic surfactants with aromatic headgroups have more solubilisation capacity for styrene than those with aliphatic surfactant headgroups. BDHAB with and without PEI had the highest encapsulation capacity compared with the other surfactants that were used in this project. Overall SANS results from polymer/surfactant solutions encapsulating styrene demonstrated that the surfactant headgroup plays an essential role in determining the micellar volume and thus can determine the polyelectrolyte/surfactant interaction and its influence on these micelles encapsulating hydrophobic molecules. On the other hand the influence of PEI on these cationic surfactants encapsulating styrene was greater for BDHAB then CPBr while CTAB showed the least effect. Both BDHAB and CPBr showed micellar cleavage into smaller micelles in the case of micelles encapsulating styrene in presence of PEI.

The second part of Chapter 4 studied the formation of solid polymer/surfactant films at the air-solution interface. A range of surfactants with aliphatic and aromatic headgroups and three hydrocarbon chain lengths C_{12}, C_{14} and C_{16} were used to select the films with the best mesostructures for the next polymerization step.

In general cationic surfactants with C_{14} and C_{16} hydrocarbon tails formed robust films on the top of the water/air interface of the solution while C_{12} surfactants did not show any obvious solid films on their solutions surface. The cationic surfactants having a C_{12} hydrocarbon tail with SPEI formed a simple adsorbed layer rather than forming ordered

structures. On the other hand pyridinium headgroup surfactants showed a more attractive interaction with PEI compared with the benzyldimethylammonium group due to the effects of steric bulk in the headgroup and hydrophobicity effects.

Time resolved studies of polymer/surfactant films encapsulating styrene demonstrated that the crystallite size of the TDPB/SPEI system grew with time while the thickness of BDTAB/SPEI films was reduced during the films formation. This behaviour mainly is due to the dissolution rate of BDTAB/SPEI films which was faster than the accumulative rate for the same system therefore loss in the film thickness was seen with time. The accumulative rate of TDPB/SPEI system was higher than dissolution rate, thus built thicker films with time.

The layer thicknesses for both BDHAB/SPEI and CPBr/SPEI films without styrene overall were thicker than in case of presence of styrene. This indicates that solubilising styrene in the cationic surfactant/PEI films decreases the attraction between PEI and micelles thus leading to closer packing of these micelles. Overall the number of layers and the films thickness of films formed from surfactants with long hydrocarbon tail and benzyldimethyl and pyridinium headgroups encapsulating hydrophobic monomer suggested that these films were the most suitable host media for polymerization of monomers inside these templating films.

Grazing incidence X-ray diffraction was used to show that surfactants with a C_{16} hydrocarbon chain for both headgroups (benzyldimethyl and pyridinium) solubilising different concentration of styrene formed more well-organized structures compared with those formed from surfactants with a C_{14} hydrocarbon chain. Also BDHAB/LPEI films encapsulating different concentration of styrene formed well-organized structures compared with SPEI films, as solubilising styrene in BDHAB/LPEI films enhanced the mesostructures of BDHAB/LPEI films.

Overall Chapter 4 demonstrated from SANS results of micellar solutions and neutron - X-ray reflectivity of polymer/surfactant films that surfactant with an aromatic headgroup and a relatively long hydrocarbon tail were suitable mesostructured hosts for templating hydrophobic monomers into these surfactant/PEI films. Therefore in the next Chapter on polymerization of encapsulated styrene the work mainly focused on surfactants with aromatic headgroup with a C_{16} hydrocarbon tail since this formed the most well-ordered structures and the most robust films.

Chapter 5 focused on polymerization of the encapsulated styrene monomer in surfactant/PEI films. This investigation was achieved by using GC and GIXD. Polymerized of polystyrene was also characterized in by using FTIR, NMR, GPC and transmission electron microscopy.

The preliminary study of conversion of styrene into polymer in the micelles confirmed that styrene can be polymerized in cationic surfactant/PEI solutions using both thermal and photo-irradiation techniques. Polymerization of styrene in PEI/surfactant solutions could be successfully achieved at room temperature by using UV irradiation, which avoided thermal disruption to the micelles.

Thermal polymerization of styrene in both BDHAB/PEI/ and CPBr/PEI films exhibited changes in the initial mesostructures to produce new structures after polymerisation and intermediate transition phases. This change in lyotropic phases was mainly due to temperature effects in these cationic surfactant films. The initial structure for both BDHAB/LPEI and CPBr/LPEI films encapsulating styrene before polymerization displayed a lamellar structure. BDHAB/LPEI films transformed from a lamellar to a cubic structure as the polymerization temperature increased. Generally a multilamellar structure, containing several different layer spacings at the same film composition was seen for the initial CPBr/LPEI films encapsulating styrene. The multilamellar structure was due to local changes in water/polyelectrolyte domain size and variations in the amount of encapsulated styrene within these films. The final polymerized CPBr/LPEI film structures demonstrated, in general, lamellar and $Pm\bar{3}n$ cubic structures. The main advantage seen in photopolymerization of equivalent films was the stability of the mesophases compared with thermal polymerization.

In general a $Pm\bar{3}n$ cubic structure was found in the final films resulting from photopolymerization of styrene in BDHAB/LPEI films, while photopolymerization of styrene in LPEI/CPBr films showed $Im\bar{3}m$ cubic structures. Using 245nm UV radiation showed differences in the mesostructures which evolved with time, while 365nm UV radiation gave stabile mesostructures during photopolymerization. Also 254nm wavelength light showed a faster polymerization rate compared with 365nm which is due to the energetic 254nm wavelength being able to initiate both ACHN and styrene radicals at the same time. Overall photopolymerization in this system system has been shown to be a powerful method of controlling the rate of the polymerization process by

managing switching the polymerization through alternating UV irradiation time and wavelength.

Polymerized styrene and purity of polystyrene was confirmed by NMR and FT-IR. In general the molecular weight of photopolymerized polystyrene in BDHAB/PEI films was greater than those polymerized in CPBr/PEI films. On the other hand photopolymerization using 365nm in both BDHAB/PEI and CPBr/PEI films illustrated higher M_w compared with those films that were polymerized at 254nm. In addition transmission electron micrographs of polystyrene that was photopolymerized at 365nm showed interconnected particles which had bigger particle diameters compared with those that were polymerized at 254nm. Polystyrene extracted from BDHAB/LPEI films also had larger particle diameters than that which was polymerized in CPBr/LPEI films.

Overall successful templating of hydrophobic monomer in polymer/surfactant films and polymerization this monomer by thermal and photo initiation process, was achieved in this work. The resulting nanoscale polystyrene network demonstrated that this is a promising route to achieve 3D mesostructured polymers.

From both Chapters 4 and 5 it was been suggested that the extent of water molecules in polymer/surfactant films can determine the final mesostructure of these films. In future work it would be interesting to monitor the exact percentage of water and PEI during formation of these films. Extension of the work to different hydrophobic monomers would also be required to demonstrate the universality of the technique. Attempts to create different surfactant phases after swelling by monomer would also be needed to demonstrate that it would be possible to generate different nanoscale structures using this technique

In Chapter 6 it was successfully shown that solid nanostructured polyelectrolyte films are promising hosts for metal ions sensors by encapsulating a combination of fluorescent and chelating molecules in a simple way inside cationic surfactant micelles.

Prolate ellipsoid micelles shape was seen for the cationic surfactants micelle solutions in the presence and absence of PAN and pyrene. The shape and size of these micelles are elongated as the encapsulated amount of PAN and pyrene was increased. BDHAB

showed an extraordinary increase of N_{agg} compared with other surfactants which support that benzyl group is potentially act as a second hydrocarbon tail.

Overall encapsulating hydrophobic molecules in both alkyl-benzyldimethyl and alkyl-pyridinium bromide surfactant micelles changes the micelles from long prolate to rod-like shape. Addition of metal ions in surfactant/PEI/PAN/Pyrene solution system also changed the micelle geometry due to direct interaction between PAN and metal ions. The result of this interaction overall was to increase the micelles aggregation number.

In general BDHAB/SPEI and CPBr/SPEI films solubilising PAN and pyrene formed films with relatively high numbers of layers and large crystallite size within the films. These films are ideal for sensor interactions due to high accessible surface area on the micelle surfaces within the open polymer hydrogel network. Also these surfactant systems formed highly ordered arrays, with a final 2D hexagonal mesostructure with the cylindrical micelles oriented with the long axis of the cylinders parallel to the air–solution interface which also support high surface interaction and good ion diffusion within the films thus potentially increasing the sensor sensitivity.

Electrochemical studies of cationic surfactant/PEI films solubilising PAN/Pyrene illustrated that metal ions are diffusing preferentially into the films and accumulating at these electrodes causing an increase the current signal. Different metal ions produced signals at different potentials so these electrodes could be used as a metal ion sensor to detect several metal ions at the same time. Fluorescence and UV-Vis spectroscopy confirmed high sensitivity and selectivity of BDHAB/SPEI/PAN/Pyrene micelle solutions for metal ion sensing which suggesting these systems could eventually act as a multifunctional electrochemical and optical sensor with high selectivity and sensitivity for detection of metal ions. However the optical signal from the film was not sufficient to use the films directly as sensors, and further optimisation of this system is required to reduce opacity and scattering in the films by possibly reducing the thickness or removing micron scale defects which scatter light.

Other future work required for the development of BDHAB/SPEI/PAN/Pyrene films to work as a dipstick kit for metal ion would be to find the best combination of concentrations and structures of the films and the limits of detection possible in these polymer/surfactant/PEI/Pyrene systems.

Conclusions

Overall, polymer/surfactant films was discovered by Edler group are very promising in wide range of applications such as targeted delivery including as membranes for topical drug delivery for wound dressings and bandages as well as other encapsulation and release systems such as agrochemicals, flavour components, odourants and nutrients, and also for instrumental application like sensors and responsive membrane. In this work clearly showed that styrene monomer encapsulated inside cationic surfactant micelles mainly in the palisade layer and in the micelle core associated with the surfactant tails. The influence of PEI on cationic surfactant micelle solutions encapsulating styrene demonstrated that there is an attractive complex interaction between the cationic surfactant micelles and PEI, where templating of hydrophobic monomer in polymer/surfactant films and polymerization this monomer by thermal and photo initiation process, effectively was achieved in this work. The resulting nanoscale polystyrene network demonstrated that this is a promising route to achieve 3D mesostructured polymers. On the other hand, these polymer/surfactant films demonstrate very appropriate hosts for metal ions sensors by encapsulating a combination of fluorescent and chelating molecules in a simple way inside cationic surfactant micelles.

The overall future work based on this project could also include:

1- Using polymerisable surfactants within highly ordered polymer/surfactant films to create reproducible solid polymer nanostructures within the water soluble polymer film. These polymer networks will reinforce the film making it more robust and suitable for applications requiring unsupported membranes. Also, depending on the nanoscale structure of the surfactant liquid crystalline network within the film, the encapsulated polymer strands could be aligned in a unidirectional manner or connected in a 3D network. The particular liquid crystalline phase used will therefore provide either isotropic or anisotropic networks, which will affect the materials properties of the resulting membranes. Testing of film strength and elastic properties would be of interest.

2- Synthesis of responsive polymer films by using responsive polymers such as polyNIPAM (which has a thermoreversable phase transition around 37 °C). PEI is itself responsive to changes in pH as the nitrogen groups can reversibly take up positive charge. The swelling and collapse of cross-linked cationic surfactant/PEI films should be investigated as a function of pH.

3- Combination of the solid polymer network, with responsive hydrogel matrices into responsive films and the incorporation of sensor species into in the films. In the final stage this could produce a responsive hydrogel network reinforced with a polymerised nanostructured backbone which contains the sensor molecule system to provide a robust material for application in real-world sensor applications.

Appendix A: Chemicals used in this thesis.

Aliphatic Surfactant Headgroup

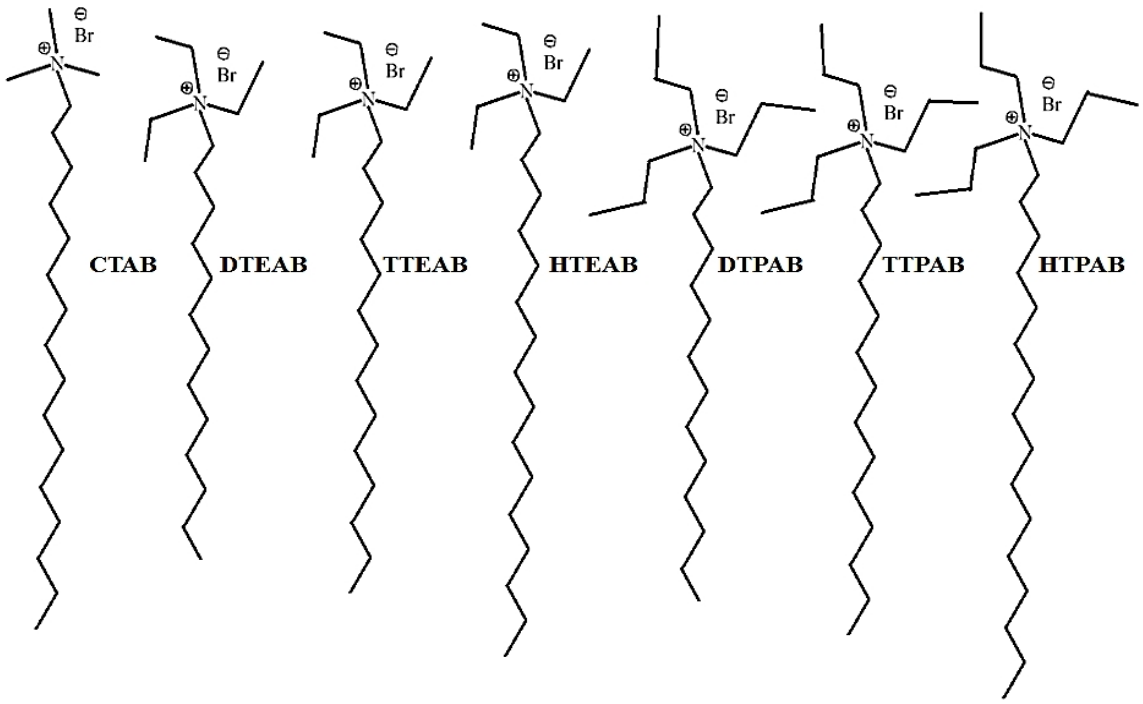

Aromatic Surfactant Headgroup

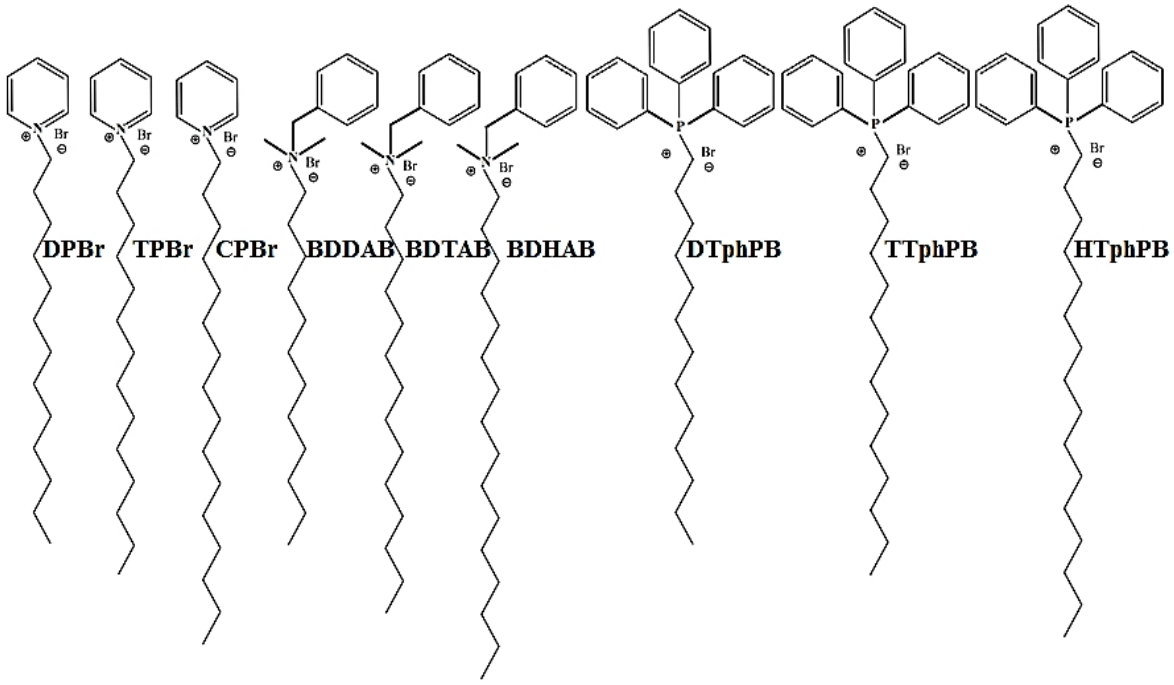

Other Chemicals

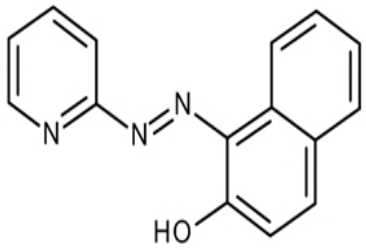

1-(2-Pyridylazo)-2-naphthol (PAN)

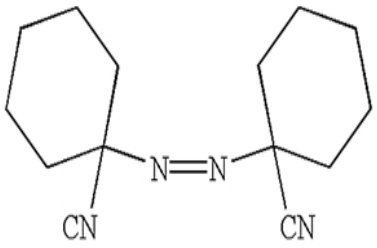

1,1′-Azobis(cyclohexanecarbonitrile) ACHN

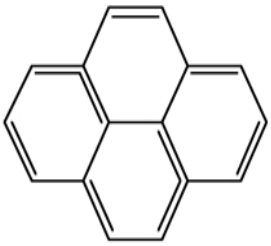

Pyrene

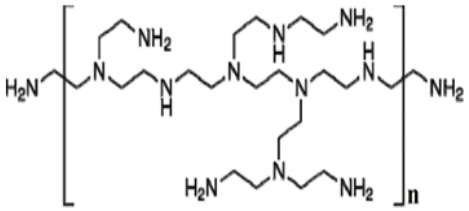

Polyethyleneimine (PEI)

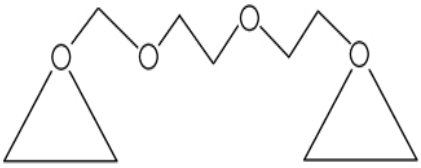

Ethylene glycol diglycidyl ether (EGDGE)

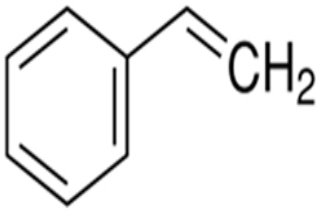

Styrene

Appendix B: Uniform Ellipsoid Model with a Hayter Penfold Structure Factor.

Table B: Measured value of micelle charge and SLD of micelle core with h/d-styrene for BDMHAB, CPBr and CTAB with and without of 1.5% LPEI. Calculated by global fitting used a uniform ellipsoid model with a Hayter Penfold structure factor.

Solution	Amount of styrene added (vol%)	*Micelle charge*	*SLD of micelle core with h-styrene*	*SLD of micelle core with d-styrene*
BDHAB	30	33	-1.20×10^{-6}	-4.6×10^{-7}
	40	32	2.21×10^{-6}	7.96×10^{-6}
	50	30	2.12×10^{-6}	7.89×10^{-6}
BDHAB/LPEI	30	9	-3.12×10^{-7}	5.03×10^{-8}
	50	7	-8.73×10^{-7}	4.92×10^{-7}
CPBr	30	23	-8.81×10^{-8}	4.82×10^{-7}
	40	27	-1.83×10^{-7}	5.85×10^{-7}
	50	30	1.25×10^{-7}	1.15×10^{-6}
CPBr/LPEI	30	4	-1.83×10^{-7}	3.78×10^{-7}
	50	6	-5.20×10^{-7}	-1.54×10^{-7}
CTAB	50	12	5.87×10^{-8}	2.20×10^{-7}
CTAB /LPEI	50	5	1.18×10^{-6}	2.73×10^{-6}

The errors of SLD core are $\pm 3.51 \times 10^{-8}$ $Å^{-2}$ and ±5% of micelle charge

Appendix C: Principal mesostructures mentioned in this work

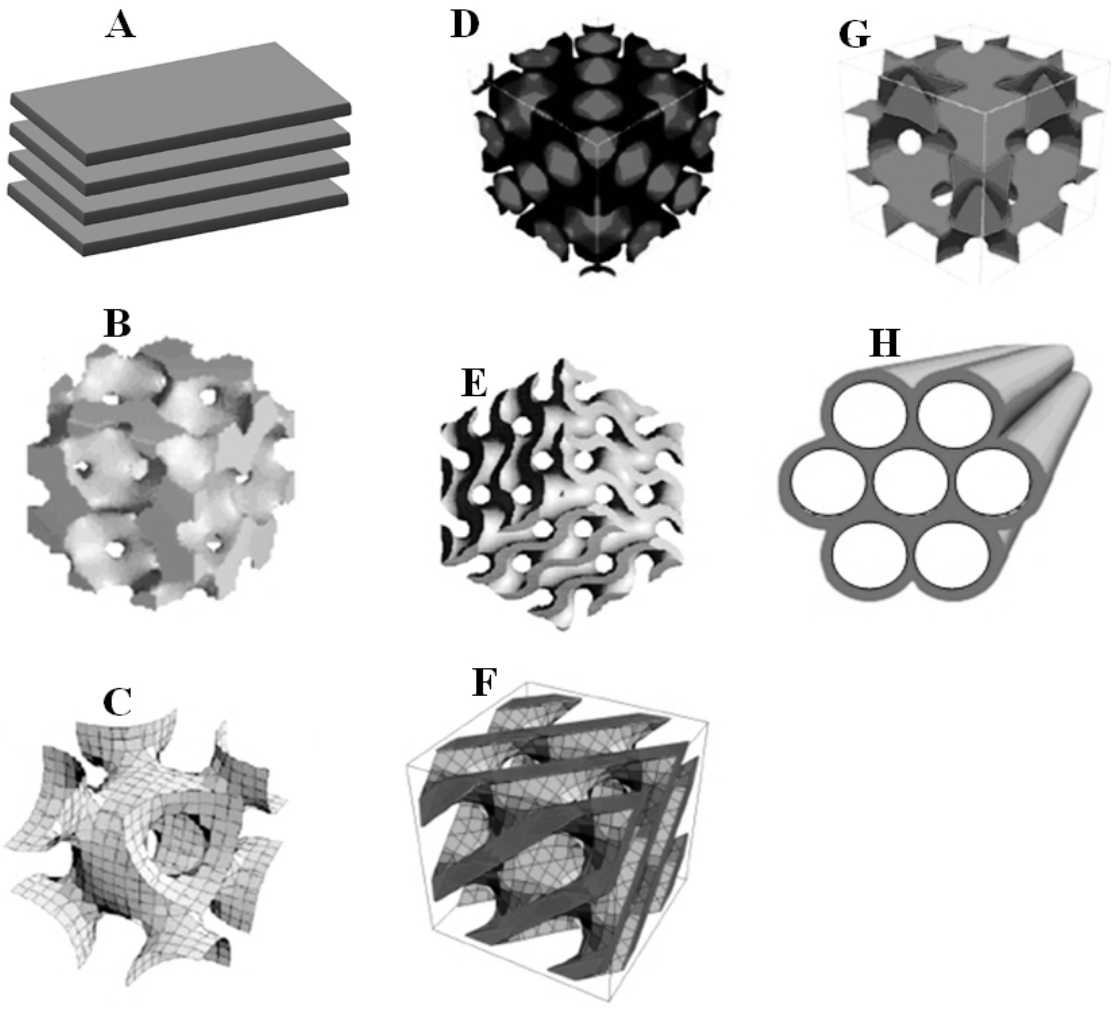

Figure C: Schematics of mesostructures with symmetric of (A) Lamellar (B) $Pm\bar{3}n$ [1] (C) $Im\bar{3}m$ [1] (D) $Fd\bar{3}m$ [2] (E) $Ia\bar{3}d$ [3] (F) $Pn\bar{3}m$ [4] (G) $Fm\bar{3}m$ [5] (H) p6mm

References

1. *Sakamoto, Y., Kaneda, M., Terasaki, O., Zhao, D. Y., Kim, J. M., Stucky, G., Shin, H. J., and Ryoo, R. (2000) Direct imaging of the pores and cages of three-dimensional mesoporous materials, Nature 408, 449-453.*
2. *Garcia-Bennett, A. E., Miyasaka, K., Terasaki, O., and Che, S. (2004) Structural solution of mesocaged material AMS-8, Chem. Mater. 16, 3597-3605.*
3. *Kaneda, M., Tsubakiyama, T., Carlsson, A., Sakamoto, Y., Ohsuna, T., Terasaki, O., Joo, S. H., and Ryoo, R. (2002) Structural study of mesoporous MCM-48 and carbon networks synthesized in the spaces of MCM-48 by electron crystallography, J. Phys. Chem. B 106, 1256-1266.*
4. *Gao, C., Sakamoto, Y., Sakamoto, K., Terasaki, O., and Che, S. (2006) Synthesis and Characterization of Mesoporous Silica AMS-10 with Bicontinuous Cubic Pn$\bar 3$m Symmetry, Angewandte Chemie 118, 4401-4404.*
5. *Yu, T., Zhang, H., Yan, X., Chen, Z., Zou, X., Oleynikov, P., and Zhao, D. (2006) Pore structures of ordered large cage-type mesoporous silica FDU-12s, J. Phys. Chem. B 110, 21467-21472.*